Spin-wave excitations and electron-magnon scattering in elementary ferromagnets from *ab initio* many-body perturbation theory

Mathias Christian Thomas David Müller

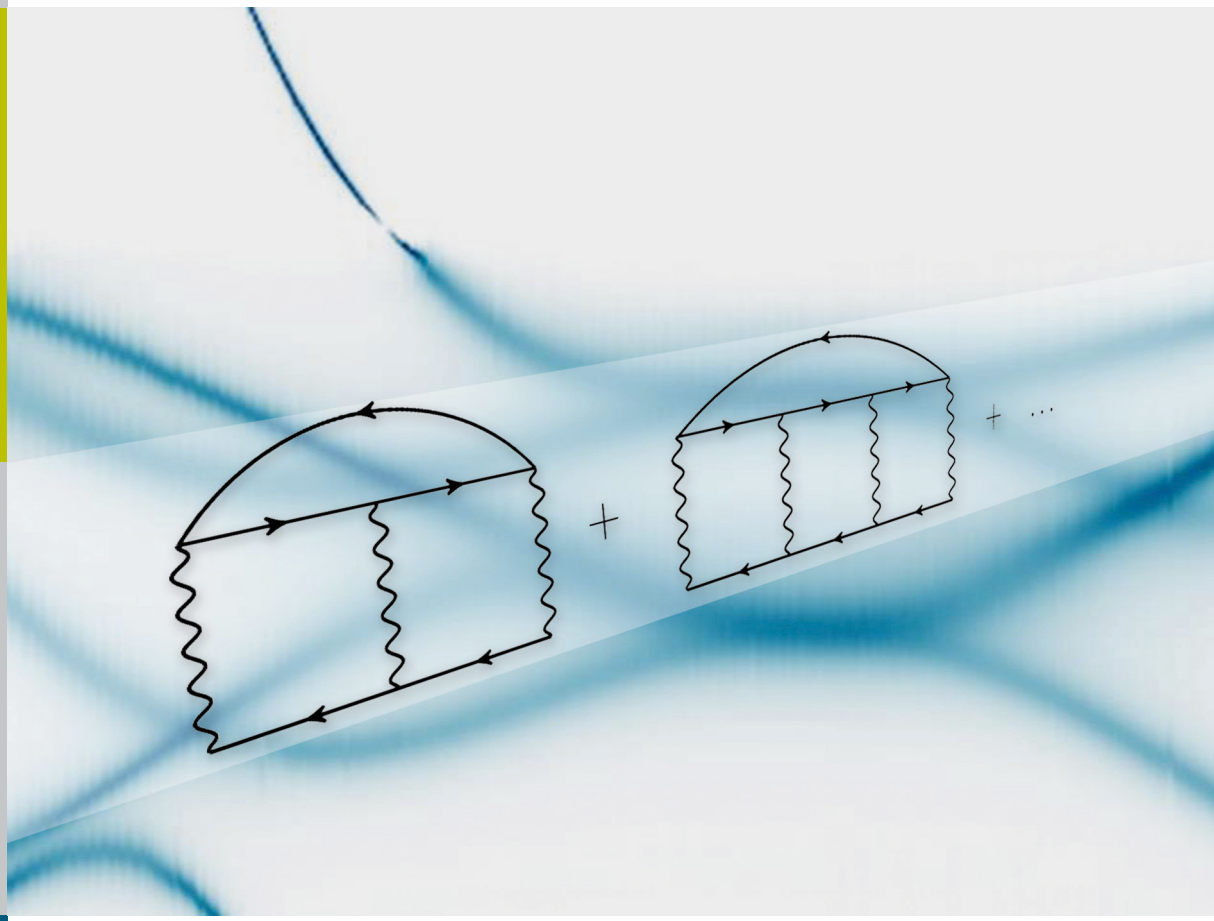

Member of the Helmholtz Association

Schlüsseltechnologien / Key Technologies
Band / Volume 146
ISBN 978-3-95806-242-9

JÜLICH
FORSCHUNGSZENTRUM

Schriften des Forschungszentrums Jülich
Reihe Schlüsseltechnologien / Key Technologies Band / Volume 146

Forschungszentrum Jülich GmbH
Peter Grünberg Institute (PGI)
Quantum Theory of Materials (PGI-1 / IAS-1)

Spin-wave excitations and electron-magnon scattering in elementary ferromagnets from *ab initio* many-body perturbation theory

Mathias Christian Thomas David Müller

Schriften des Forschungszentrums Jülich
Reihe Schlüsseltechnologien / Key Technologies Band / Volume 146

ISSN 1866-1807 ISBN 978-3-95806-242-9

Bibliographic information published by the Deutsche Nationalbibliothek.
The Deutsche Nationalbibliothek lists this publication in the Deutsche
Nationalbibliografie; detailed bibliographic data are available in the
Internet at http://dnb.d-nb.de.

Publisher and Distributor:	Forschungszentrum Jülich GmbH Zentralbibliothek 52425 Jülich Tel: +49 2461 61-5368 Fax: +49 2461 61-6103 Email: zb-publikation@fz-juelich.de www.fz-juelich.de/zb
Cover Design:	Grafische Medien, Forschungszentrum Jülich GmbH
Printer:	Grafische Medien, Forschungszentrum Jülich GmbH
Copyright:	Forschungszentrum Jülich 2017

Schriften des Forschungszentrums Jülich
Reihe Schlüsseltechnologien / Key Technologies, Band / Volume 146

D 82 (Diss. RWTH Aachen University, 2017)

ISSN 1866-1807
ISBN 978-3-95806-242-9

The complete volume is freely available on the Internet on the Jülicher Open Access Server (JuSER)
at www.fz-juelich.de/zb/openaccess.

Abstract

In this thesis, an *ab initio* theoretical framework for the investigation of spin excitations and the electron-magnon scattering is developed within many-body perturbation theory and implemented in the full-potential linearized augmented-plane-wave method. The spin excitations, including single-particle Stoner excitations and collective spin waves, are accessible through the magnetic response function, which is obtained by the solution of a Bethe-Salpeter equation employing four-point functions. These four-point functions are represented in a Wannier-function basis, which allows to exploit the short-range behavior of the screened interaction in metallic systems by truncating the matrices in real space. The spin excitation spectrum of ferromagnetic materials contains an acoustic magnon mode whose energy, in the absence of spin-orbit coupling, vanishes in the long-wavelength limit as a consequence of the spontaneously broken spin-rotation symmetry in these materials according to the Goldstone theorem. However, in numerical realizations of the magnetic response function the acoustic magnon mode exhibits a small but finite gap in the Goldstone-mode limit. We investigate this violation of the Goldstone theorem and present an approach that implements the magnetic response function employing the properly renormalized Green function instead of the Kohn-Sham one. This much more expensive approach shows a substantial reduction of the gap error. In addition, we discuss a correction scheme motivated by the one-band Hubbard model that cures the fundamental inconsistency of using the Kohn-Sham Green function by adjusting the exchange splitting. We present corrected magnon spectra for the elementary ferromagnets iron, cobalt, and nickel. We then employ the T-matrix approach for the description of the electron-magnon interaction within the GT approximation, which can be combined with the GW approximation without the need of double-counting corrections. The multiple-scattering T matrix is part of the four-point magnetic response function and describes the correlated propagation of electron-hole pairs with opposite spins from which the collective spin excitations arise. We apply the GT

approximation to Fe, Co, and Ni and present renormalized spectral functions. The *GT* approximation leads to a pronounced spin-dependent lifetime broadening of the quasiparticle states to the extent that the quasiparticle character is virtually lost in certain energy regions. In iron, the spectral functions exhibit an additional quasiparticle peak indicating the emergence of a new quasiparticle. We discuss the features of this quasiparticle state that forms out of a superposition of single-particle and magnon excitations. In addition, we find kink structures in the quasiparticle dispersion of free-electron-like bands of cobalt and nickel.

Zusammenfassung

In dieser Arbeit werden theoretische Verfahren für die *ab initio* Untersuchung von Spinanregungen und der Elektron-Magnon-Streuung innerhalb der Vielteilchenstörungstheorie entwickelt und in der *full-potential linearized augmented-plane-wave* Methode implementiert. Die Spinanregungen, einschließlich der Einteilchen-Stoner-Anregungen und kollektiver Spinwellen, sind durch die magnetische Antwortsfunktion zugänglich, die durch das Lösen einer Bethe-Salpeter-Gleichung unter Verwendung von Vierpunktsfunktionen gewonnen wird. Diese Vierpunktsfunktionen werden in einer Wannierfunktionsbasis dargestellt, die es erlaubt das kurzreichweitige Verhalten der abgeschirmten Wechselwirkung in metallischen Systemen auszunutzen, indem die Matrizen im Realraum begrenzt werden. Das Spinanregungsspektrum von ferromagnetischen Materialien beinhaltet eine akustische Magnonenmode, deren Energie unter Vernachlässigung der Spin-Bahn-Kopplung im Grenzfall unendlich großer Wellenlängen verschwindet. Entsprechend des Goldstone-Theorems ist dies eine Konsequenz der spontan gebrochenen Spinrotationssymmetrie in diesen Materialien. In der numerischen Realisierung der magnetischen Antwortsfunktion beinhaltet die akustische Magnonenmode jedoch eine kleine aber endliche Lücke in der Goldstone-Mode. Wir untersuchen die Verletzung des Goldstone-Theorems und präsentieren einen Ansatz, der die magnetische Antwortsfunktion unter Verwendung der geeignet renormalisierten Greensfunktion anstelle der Kohn-Sham-Greensfunktion implementiert. Dieser wesentlich aufwendigere Ansatz zeigt eine substantielle Reduktion des Lückenfehlers. Darüber hinaus diskutieren wir ein Korrekturschema, motiviert vom Ein-Band-Hubbard-Modell, das die fundamentale Inkonsistenz der Verwendung der Kohn-Sham-Greensfunktion durch das Anpassen der Austauschaufspaltung heilt. Wir zeigen korrigierte Magnonspektren für die elementaren Ferromagneten Eisen, Kobalt und Nickel. Wir verwenden dann den T-Matrix-Ansatz für die Beschreibung der Elektron-Magnon-Wechselwirkung in der GT-Näherung, die additiv mit der GW-Näherung kombiniert werden kann ohne

die Notwendigkeit von Doppelzählkorrekturen. Die T-Matrix ist Teil der magnetischen Vierpunkt-Antwortsfunktion und beschreibt die korrelierte Propagation von Elektron-Loch-Paaren mit entgegengesetztem Spin von der die kollektiven Spinanregungen herrühren. Wir wenden die GT-Näherung auf Eisen, Kobalt und Nickel an und präsentieren renormalisierte Spektralfunktionen. Die GT-Näherung führt zu einer ausgeprägten spin-abhängigen Lebensdauerverbreiterung der Quasiteilchenzustände, was dazu führen kann, dass der Quasiteilchencharakter in bestimmten Energiebereichen praktisch verloren geht. In Eisen zeigen die Spektralfunktionen einen zusätzlichen Quasiteilchenpeak, der die Entstehung eines neuen Quasiteilchens anzeigt. Wir diskutieren die Eigenschaften dieses Quasiteilchenzustands, der sich aus einer Überlagerung von Einteilchen- und Magnonanregungen ergibt. Darüber hinaus finden wir in der Quasiteilchendispersion von Bändern in Kobalt und Nickel, die ähnlich zu freien Elektronen dispergieren, Knickstellenstrukturen.

Contents

1. Introduction

Nowadays, information technology and its applications affect almost all aspects of human life, and it is expected to become even more important with the advent of big data concepts, cloud computing, and the internet of things. Information technology is based on three basic operations: the storage, the processing, and the transfer of information [1, 2]. Progress in information technology is particularly propelled by fundamental research on novel physical concepts and emerging materials. For example, the discovery of the giant magnetoresistance (GMR) [3,4] has been a breakthrough for storing information magnetically. The GMR effect was measured first in layered magnetic structures consisting of iron and chromium layers independently by Albert Fert and Peter Grünberg, both awarded with the Nobel prize in physics in 2007. Grünberg demonstrated in his Nobel lecture entitled *From spin waves to giant magnetoresistance and beyond* [5] the importance of the concept of spin waves for the understanding of layered magnetic structures. It was the measurement of the spin-wave spectrum by means of Brillouin light scattering (BLS) experiments [6] that, for the first time, gave evidence for an antiferromagnetic interlayer exchange coupling, which is important for the GMR effect. The discovery of the GMR effect, in turn, has opened up the possibility for a tremendous increase of the data storage density on a hard disk drive (HDD).

Traditionally, nonvolatile memory and logic devices for information processing are realized by different technologies. While information is typically stored in magnetic domains, information processing nowadays relies practically always on charge-based switching devices among which the complementary metal-oxide-semiconductor (CMOS) technology is the most successful one. Charge-based switching devices, e.g., field-effect transistors differentiate between a logic 0 and 1 by charging and discharging the transistor gate, which regulates the source-drain conduc-

tivity. Consequently, the switching capabilities of a charge-based device requires charge transport, which is accompanied by fundamental limits concerning the minimum switching energy and the switching speed [7]. There are attempts to overcome these fundamental limits by replacing the electron as information carrier. Recently, magnons, which are the quanta of collective spin excitations, have been proposed as information carrier for a logic device [8, 9]. The proposed magnon transistor is an all-magnon device entirely avoiding electron transport. Such an all-magnon device has the advantage that the waste heat generation can be drastically reduced, and its size can potentially be scaled down to the sub-ten nanometer scale [8,10] while being capable of ultra-fast data processing reaching the THz range [8, 11–13].

Clearly, the understanding of spin waves is essential for fundamental research and application in technology. Spin waves can be studied experimentally, e.g., by the Brillouin light scattering technique, which allows to extract information about the magnetic properties with spatial and time resolution [14]. Neutron scattering experiments can be used to probe bulk properties due to the high penetration depth of the neutron. While neutron diffraction allows to extract information about the magnetic structure of a solid, inelastic neutron scattering (INS) techniques [15] are able to measure the momentum and energy resolved spin-wave excitation spectrum. INS experiments measure the scattering cross section of the neutrons, which can be related to the spectral function of the magnetic response function of linear response theory [16, 17]. The magnetic response function accounts for the dynamical linear response of a magnetic material due to an external perturbing B field. The magnetic response function provides information about the complete magnetic excitation spectrum and is therefore the central quantity of interest to study spin excitations theoretically.

In the past 30 years, the density-functional theory (DFT) [18] in the Kohn-Sham (KS) formulation [19], employing a local-spin-density approximation (LSDA) or a semilocal generalized gradient approximation (GGA) for the unknown exchange-correlation functional, has developed into a powerful *ab initio* approach for the description of ground-state properties of materials. Even though excited-state properties are beyond the scope of DFT, total-energy calculations allow to obtain magnon excitation energies for systems with localized moments employing an adiabatic treatment that separates the fast motion of the electrons and the slow motion of the magnetic moments [20–24]. In the adiabatic treatment, the magnon excitation energy is related to the magnetic ground-state energy of a system whose spins are aligned in

a frozen spin-wave configuration, employing the constraint density-functional theory [25]. However, the adiabatic treatment is strictly speaking only applicable to systems with rather localized moments and it is not a good approximation for itinerant magnetic materials.

Going beyond the adiabatic treatment is a non-trivial task. More sophisticated approaches treat the magnetic response for bulk systems, surfaces, or adatoms on surfaces within the multi-band Hubbard model with effective tight-binding parameters [26–30], which was recently extended by the inclusion of spin-orbit coupling [31,32]. First-principles calculations of the magnetic response function that take into account realistic band structures, wave functions, and Coulomb interactions are scarce in the literature as they demand a tremendous implementational and computational effort. Yet, these treatments give the most reliable and most precise results for spin-wave excitations. Only recently, the first *ab initio* calculations of the magnetic response function have been published. Savrasov [33], Buczek *et al.* [34–37], Lounis *et al.* [38–41], and Rousseau *et al.* [42] calculated the magnetic response function within the time-dependent density-functional theory (TDDFT). Alternatively, the magnetic response function can be treated from first principles within the many-body perturbation theory (MBPT). The first full *ab initio* study of spin-wave spectra of the bulk transition metals within MBPT was published by Şaşıoğlu *et al.* [43]. In contrast to earlier works [44,45] that employed model potentials, Şaşıoğlu *et al.* [43] calculated the screened interaction, which mediates the correlation between the electron-hole pairs, explicitly from the random-phase approximation (RPA). The short spatial range of the correlation in the partially filled $3d$ orbitals can be exploited by employing a projection onto maximally localized Wannier functions [46,47] for an efficient treatment of the four-point multiple-scattering T matrix describing the electron-hole pair interaction. The implementation is based on the all-electron full-potential linearized-augmented-planewave (FLAPW) method [48–50], one of the most precise electronic structure methods for crystalline solids. The FLAPW method treats core and valence electrons on an equal footing, avoids any shape approximation of the charge density or the potential, and is applicable to all elements of the periodic table.

The magnetic response function calculated within TDDFT or MBPT allows to access single-particle excitations as well as collective spin-wave excitations simultaneously. The spin excitation lifetimes, which result from the mixing of single-particle and collective excitations, are accessible in these approaches as well. However, it has turned out that a problem arises related to the acoustic magnon mode. In the

absence of spin-orbit coupling, the acoustic magnon mode can be understood as the consequence of the Goldstone theorem, which requires that the magnon excitation energy vanishes in the long-wavelength limit due to the spontaneously broken spin-rotation symmetry in collinear magnetic systems. Usually, in *ab initio* calculations of the magnetic response function employing either TDDFT or MBPT a gap error occurs in the magnon dispersion, i.e., the magnon excitation energy does not vanish in the long-wavelength limit numerically violating the Goldstone-mode condition. While in TDDFT the origin of the violation is attributed to the numerical realization of the magnetic response function [38, 42], the violation of the Goldstone-mode condition in the MBPT is more fundamental.

In this thesis, we have investigated the violation of the Goldstone-mode condition in MBPT [51]. We found that the fundamental inconsistency which arises in MBPT calculations of the magnetic response function is related to the use of the Kohn-Sham Green function. We have lifted this inconsistency by employing the properly renormalized Green function within the magnetic response function calculation. Furthermore, to bypass the computationally much more expensive approach of calculating the self-consistently renormalized Green function, we have proposed a correction scheme for the Kohn-Sham Green function for ferromagnetic materials that cures the Goldstone violation and opens up the possibility for efficient *ab initio* MBPT calculations of spin excitations and, in particular, their coupling to the electronic excitations.

The interaction of electrons and spin excitations plays a fundamental role for a wide variety of phenomena. For example, in spintronics spin-polarized currents depolarize due to their interaction with magnons [52], the electron scattering by magnons is responsible for the characteristic temperature dependence of the tunneling magnetoresistance (TMR) [53], and in nanospintronics the spin and charge currents that flow through nanostructures deposited on surfaces can be strongly affected by the electron-magnon interaction [54–57]. Recent angle-resolved photoemission spectroscopy (ARPES) experiments on an iron surface state [58] and a nickel bulk state [59] found a kink structure in the quasiparticle band dispersion, which was attributed to the coupling of electrons to spin excitations. These findings together with further experiments on the $3d$ transition metals [60–64] has revived the scientific interest to understand correlation effects in bulk transition metals from a theoretical point of view, for example by employing dynamical mean-field theory (DMFT) within the LDA+DMFT approach [62–66] or diagrammatic techniques [67–70].

In this thesis we have proposed a self-energy correction within many-body per-

turbation theory that explicitly accounts for spin-flip excitations and can be combined with the *GW* approximation [71] without the need for a double-counting correction. This self-energy relies on the multiple-scattering *T* matrix and is termed *GT* self-energy. The *GT* self-energy has been implemented in the SPEX code [72], which is a FLAPW implementation of the *GW* approach. We have illustrated the capabilities of the *GT* self-energy by investigating the bulk elementary ferromagnets iron, cobalt, and nickel. The coupling of electrons to spin excitations leads to a pronounced spin-dependent lifetime broadening of the quasiparticle states. The lifetime broadening, which is particularly strong in iron, can even lead to a loss of quasiparticle resonances in the spectrum. In iron, a new quasiparticle emerges from the coupling of electrons to magnons that leaves its footprint in the electronic spectral function as an additional quasiparticle peak. A similar effect, though less pronounced, is found in cobalt and nickel. In these materials, the electron-magnon scattering gives rise to an anomalous quasiparticle dispersion behavior of free-electron-like bands in the vicinity of the Fermi level.

The thesis is organized as follows. Chapter 2 introduces the many-body perturbation theory and the density-functional theory as the theoretical foundations of this thesis. The acoustic magnon mode is discussed in Chapter 3 in terms of the magnetic response function within many-body perturbation theory. The derivation and the implementation of the magnetic response function are presented. The coupling of electrons to spin excitations is investigated in Chapter 4 in terms of the *GT* approximation. The *GT* self-energy is derived in Section 4.2, and the implementational details are shown in Section 4.3. Results of the *GT* self-energy calculations applied to iron, cobalt, and nickel are presented in Section 4.7. Finally, the conclusions in Chapter 5 summarize our findings.

2. Theoretical Foundations

In the last decades, numerical first-principles calculations of material properties have become increasingly important in the fields of theoretical condensed-matter physics, quantum chemistry, and computational material science. In these approaches, one tries to solve the Schrödinger equation with the many-body Hamiltonian that characterizes the solid-state system. The many-body Hamiltonian is composed of the kinetic energy of the electrons, the kinetic energy of the atomic nuclei, the electron-electron interaction, the nucleus-nucleus interaction, and the electron-nucleus interaction. The many-body Hamiltonian is too complex to allow a straightforward solution of the Schrödinger equation. However, the problem can be drastically simplified by the fact that the electron mass is by orders of magnitude smaller than the nuclear mass. Therefore, the electrons react almost instantaneously to a change of the nuclear positions and, as a result, the electrons can be assumed in their many-body ground state for a given set of nuclear positions. The Born-Oppenheimer approximation [73] exploits the large difference between the electron and nuclear mass to decouple the electron motion from that of the nuclei. As a consequence, the quest of solving the Schrödinger equation with the many-body Hamiltonian of the electrons and the nuclei simplifies to a Schrödinger equation with a many-electron Hamiltonian in which the nuclear positions appear merely as parameters. Still, the problem cannot be solved exactly and approximate approaches are required. The many-body perturbation theory is an approach to find an approximate solution to the interacting system in terms of the Green function that allows to access excited state properties. The Green function is obtained as the solution of a Dyson equation to an energy-dependent and nonlocal potential that plays the role of a self-energy. The self-energy accounts for exchange and correlation effects within the system. Although the exact form of the self-energy is unknown, it can be approximated in terms of an expansion

in powers of the interaction between the particles of the system [71,74]. The density-functional theory is another approach, which uses the ground-state density as its basic variable. In the Kohn-Sham formalism the density-functional theory reduces the calculation of ground-state properties to the iterative solution of single-particle Schrödinger-like equations [75,76]. In the present work, density-functional theory calculations serve as a starting point for subsequent many-body perturbation theory calculations. We introduce both theories, the many-body perturbation theory in Section 2.1 and the density-functional theory in Section 2.2. Our implementation relies on the full-potential linearized augmented-plane-wave (FLAPW) method, which is introduced in Section 2.3.

2.1 Many-Body Perturbation Theory

The many-body perturbation theory allows to determine excitation spectra in solids from first principles. The excitation spectrum of a solid is accessible via the electronic Green function, which is the solution of a Dyson equation to a nonlocal and frequency-dependent self-energy. The self-energy is a central ingredient to the many-body perturbation theory, it contains in principle all exchange and correlation effects. In practice, however, the self-energy must be approximated. The formulation of many-body perturbation theory in terms of the Hedin equations allows the self-energy to be expanded in terms of a screened Coulomb interaction. The screened Coulomb interaction takes into account dynamical screening effects due to charge fluctuations. The first-order expansion of the self-energy leads to the *GW* approximation. For the introduction of the many-body perturbation theory the Hamiltonian written in first quantization is transformed into the second quantization. The Green function is defined in Section 2.1.1 and with the Hamiltonian in second quantization the Green function's equation of motion, which leads to the Hedin equations, is derived in Section 2.1.2.

The electronic structure theory is based on the Born-Oppenheimer approximation [73], which decouples the electrons from the nuclei. The fundamental Hamiltonian of the electronic structure theory, written in atomic units, has the form

$$H = \sum_{i=1}^{N} h(\mathbf{r}_i) + \frac{1}{2} \sum_{i \neq j}^{N} v(\mathbf{r}_i, \mathbf{r}_j) \tag{2.1.1}$$

with the single-particle Hamiltonian

$$h(\mathbf{r}_i) = -\frac{1}{2}\nabla^2_{\mathbf{r}_i} + v_{\text{ext}}(\mathbf{r}_i), \tag{2.1.2}$$

where $v_{\text{ext}}(\mathbf{r})$ is the external potential created by the atomic nuclei and

$$v(\mathbf{r}_i, \mathbf{r}_j) = \frac{1}{|\mathbf{r}_i - \mathbf{r}_j|} \tag{2.1.3}$$

is the Coulomb interaction between the electrons. The many-electron wave function $\Phi(\mathbf{r}_1, \mathbf{r}_2, \ldots, \mathbf{r}_N)$ is the ground-state eigenfunction of the Hamiltonian (2.1.1), i.e., the wave function is formally the solution of the Schrödinger equation

$$H\Phi(\mathbf{r}_1, \mathbf{r}_2, \ldots, \mathbf{r}_N) = E\Phi(\mathbf{r}_1, \mathbf{r}_2, \ldots, \mathbf{r}_N) \tag{2.1.4}$$

with the total energy E. Due to the Pauli exclusion principle the wave function has to be anti-symmetric under the exchange of two electron positions, i.e.,

$$\Phi(\mathbf{r}_1, \mathbf{r}_2, \ldots, \mathbf{r}_N) = -\Phi(\mathbf{r}_2, \mathbf{r}_1, \ldots, \mathbf{r}_N). \tag{2.1.5}$$

The Schrödinger equation of a non-interacting single-particle Hamiltonian of the form of Eq. (2.1.2) can be solved exactly and its solutions are the single-particle wave functions denoted by $\phi_i(\mathbf{r})$. The corresponding many-electron wave function of the non-interacting system can be written as the sum over all possible permutations of the single-particle wave functions

$$\Phi(\mathbf{r}_1, \ldots, \mathbf{r}_N) = \frac{1}{N!}\sum_{\mathcal{P}}(-1)^{\mathcal{P}}\phi_{i_1}(\mathbf{r}_{\mathcal{P}(1)})\phi_{i_2}(\mathbf{r}_{\mathcal{P}(2)})\cdots\phi_{i_N}(\mathbf{r}_{\mathcal{P}(N)}), \tag{2.1.6}$$

where $\mathcal{P}(i)$ gives the rearrangement with respect to a permutation $\mathcal{P}$. The summation over all permutations $\mathcal{P}$ ensures that the resulting wave function is anti-symmetric as required by the Pauli exclusion principle (2.1.5). The expression (2.1.6) is known as the Slater determinant of a non-interacting system [77]. If the Slater determinant is used as a wave-function ansatz to solve the Schrödinger equation (2.1.4) with the Hamiltonian (2.1.1), this leads to the Hartree-Fock approach [78]. Other wave-function based approaches, for example, the configuration interaction, the Moeller-Plesset perturbation theory [79], or the coupled-cluster methods [80], go beyond the Hartree-Fock approach by using linear combinations of Slater determinants as an approximation to the many-electron wave function.

In the present thesis, however, the many-body perturbation theory, which relies on the Green function method, is employed. The Green function approach of many-body perturbation theory makes use of a formulation in second quantization. The second quantization is a formulation that describes the many-electron state in the occupation number representation. The state vector in the occupation number representation

$$|n_1 n_2 \dots n_N\rangle \tag{2.1.7}$$

counts the number of particles in each state, i.e., the state vector (2.1.7) means that there are n_1 particles in state 1, n_2 particles in state 2, and so on. In an electron system the Pauli exclusion principle restricts the occupation number for each state i to $n_i = 0, 1$. The occupation number representation sets up a complete and normalized basis set. The electron creation $a_\nu^\dagger$ and annihilation a_ν operators of second quantization increase and lower the occupation number of the ν-th state by one electron, respectively. The electron creation and annihilation operators satisfy the anti-commutation relations

$$[a_\nu, a_{\nu'}]_+ = [a_\nu^\dagger, a_{\nu'}^\dagger]_+ = 0, \tag{2.1.8}$$

and

$$[a_\nu, a_{\nu'}^\dagger]_+ = \delta_{\nu,\nu'}, \tag{2.1.9}$$

where ν and ν' denote full sets of quantum numbers to describe uniquely the electronic states. For example, in lattice-periodic systems without spin-orbit coupling an eigenstate $\varphi_{\mathbf{k}m}^\alpha$ can be characterized by its Bloch momentum $\mathbf{k}$, its band label m, and a spin α according to the Bloch theorem [81]. The operators $a_{\mathbf{k}m}^{\alpha\,\dagger}$ and $a_{\mathbf{k}m}^\alpha$ create and destroy an electron in the state $\nu = \mathbf{k}m\alpha$, respectively. It is advantageous to use a formulation in terms of field operators $\psi_\alpha^\dagger(\mathbf{r})$ and $\psi_\alpha(\mathbf{r})$, which create and destroy an electron with spin α at a particular point in space, respectively. The field operators are related to the creation and annihilation operators by

$$\psi_\alpha^\dagger(\mathbf{r}) = \sum_{\mathbf{k}m} a_{\mathbf{k}m}^{\alpha\,\dagger} \varphi_{\mathbf{k}m}^{\alpha *}(\mathbf{r}), \tag{2.1.10}$$

and

$$\psi_\alpha(\mathbf{r}) = \sum_{\mathbf{k}m} \varphi_{\mathbf{k}m}^\alpha(\mathbf{r}) a_{\mathbf{k}m}^\alpha, \tag{2.1.11}$$

where $\varphi_{\mathbf{k}m}^{\alpha *}(\mathbf{r}) = \langle \mathbf{k}m\alpha|\mathbf{r}\rangle$. The field operators fulfill anti-commutation relations of the same form as (2.1.8) and (2.1.9). The Hamiltonian in second quantization takes

the form

$$H = \sum_{\alpha} \int \mathrm{d}\mathbf{r}\, \psi_{\alpha}^{\dagger}(\mathbf{r}) h(\mathbf{r}) \psi_{\alpha}(\mathbf{r}) + \frac{1}{2} \sum_{\alpha,\beta} \int \mathrm{d}\mathbf{r}\, \mathrm{d}\mathbf{r}'\, \psi_{\alpha}^{\dagger}(\mathbf{r}) \psi_{\beta}^{\dagger}(\mathbf{r}') v(\mathbf{r},\mathbf{r}') \psi_{\beta}(\mathbf{r}') \psi_{\alpha}(\mathbf{r}), \tag{2.1.12}$$

where the ordering of the field operators is important to ensure the Hamiltonian to be Hermitian. In second quantization the fields turn into operator quantities, while the one-particle Hamiltonian and the interaction among the particles turn into complex functions. In principle, the Hamiltonian (2.1.12) can be used in the Schrödinger equation (2.1.4) to solve for the many-electron wave function using the so-called Schrödinger representation of quantum mechanics. In contrast, many-body perturbation theory is based on the Green function technique, which makes a treatment within the Heisenberg representation more convenient. In the Heisenberg representation the dynamics of the system is incorporated into the operators instead of the many-electron wave functions, i.e., while the wave functions are time-independent, the operators take the time dependence. For example the field operator defined in the Heisenberg representation has a time dependence of the form

$$\psi_{\alpha}(\mathbf{r}t) = e^{\mathrm{i}Ht} \psi_{\alpha}(\mathbf{r}) e^{-\mathrm{i}Ht}. \tag{2.1.13}$$

Instead of the Schrödinger equation one has to solve the equation of motion for the operators in the Heisenberg representation, e.g., the field operator obeys the equation of motion

$$\mathrm{i}\partial_t \psi_{\alpha}(\mathbf{r}t) = [\psi_{\alpha}(\mathbf{r}t), H]_{-}. \tag{2.1.14}$$

The many-body perturbation theory allows to calculate ground-state and excited-state properties. The calculation of these properties, for example, the charge or spin density, usually involves the calculation of expectation values of one-particle operators. One-particle operators, in turn, correspond to combinations of creation and annihilation field operators. The Green function can be written as an expectation value of a creation and annihilation operator, too.

2.1.1 Green Function

The one-particle Green function is defined by the equation

$$G_{\alpha\beta}(\mathbf{r}t, \mathbf{r}'t') = -\mathrm{i}\langle \mathcal{T} \psi_{\alpha}(\mathbf{r}t) \psi_{\beta}^{\dagger}(\mathbf{r}'t') \rangle, \tag{2.1.15}$$

where $\mathcal{T}$ is the time-ordering operator, which ensures that the field operators are ordered such that their time arguments increase from right to left, and $\langle \ldots \rangle$ denotes the expectation value with respect to the ground state of the interacting system. The Green function is the probability amplitude for the propagation of an additional electron ($t > t'$) or an additional hole ($t' > t$) in the many-body system described by the Hamiltonian (2.1.12). The Green function is a very important quantity because expectation values of any one-particle operator can be written as a known functional of the Green function. For example, the electron density can be expressed in terms of the Green function

$$n(\mathbf{r}t) = -\mathrm{i}\sum_{\alpha} G_{\alpha\alpha}(\mathbf{r}t, \mathbf{r}t + \eta), \tag{2.1.16}$$

where $\eta \to 0^+$ is a positive infinitesimal number. In addition, Galitskii and Migdal [82, 83] showed that the ground-state total energy of a system is determined by the Green function as well. Furthermore, the Green function contains information about the excited states, i.e., it carries information about the $(N \pm 1)$-electron system. The excitation spectrum of the system is accessible via the Lehmann representation [84] of the Green function. Provided that the Hamiltonian is not explicitly time dependent, the Green function depends only on the time difference $\tau = t - t'$ of the field operator's action. The ν-th state $|N \pm 1, \nu\rangle$ of the $(N \pm 1)$-electron system is an eigenstate of the full Hamiltonian, i.e., $H|N \pm 1, \nu\rangle = E_\nu^{N\pm1}|N \pm 1, \nu\rangle$. The Green function's Lehmann representation results from inserting the closure relation of the $(N \pm 1)$-electron system

$$\sum_{\nu} |N \pm 1, \nu\rangle\langle N \pm 1, \nu| = 1 \tag{2.1.17}$$

between the field operators of the Green function (2.1.15) and applying a Fourier transformation to the frequency domain

$$\begin{aligned} G_{\alpha\beta}(\mathbf{r}, \mathbf{r}'; \omega) = \sum_{\nu} & \frac{\langle N, 0|\psi_\alpha(\mathbf{r})|N+1, \nu\rangle\langle N+1, \nu|\psi_\beta^\dagger(\mathbf{r}')|N, 0\rangle}{\omega - (E_\nu^{N+1} - E^N) + \mathrm{i}\eta} \\ & + \frac{\langle N, 0|\psi_\beta^\dagger(\mathbf{r}')|N-1, \nu\rangle\langle N-1, \nu|\psi_\alpha(\mathbf{r})|N, 0\rangle}{\omega - (E^N - E_\nu^{N-1}) - \mathrm{i}\eta}, \end{aligned} \tag{2.1.18}$$

where E^N is the energy of the N-electron system. Thus, the excitation energies of the $(N \pm 1)$-electron system are the poles of the Green function in the Lehmann representation. As the Green function contains the excitation energies of the $(N \pm 1)$-electron system, it is related to (inverse) photoemission spectroscopy experiment. In a system of non-interacting electrons, the amplitudes $\langle N-1, \nu|\psi_\alpha(\mathbf{r})|N, 0\rangle$ and

$\langle N+1,\nu|\psi^\dagger_\beta(\mathbf{r}')|N,0\rangle$ correspond to the occupied and unoccupied single-particle wave functions, respectively.

2.1.2 Hedin Equations

The Green function can be obtained as the solution of its equation of motion

$$\begin{aligned}\mathrm{i}\partial_t G_{\alpha\beta}(\mathbf{r}t,\mathbf{r}'t') = \delta(\mathbf{r}-\mathbf{r}')\delta(t-t')\delta_{\alpha\beta} + h(\mathbf{r})G_{\alpha\beta}(\mathbf{r}t,\mathbf{r}'t') \\ - \mathrm{i}\sum_\gamma \int \mathrm{d}\mathbf{r}''\, v(\mathbf{r},\mathbf{r}'')\langle \mathcal{T}\psi^\dagger_\gamma(\mathbf{r}''t)\psi_\gamma(\mathbf{r}''t)\psi_\alpha(\mathbf{r}t)\psi^\dagger_\beta(\mathbf{r}'t')\rangle, \quad (2.1.19)\end{aligned}$$

which results from the equation of motion of the field operator (2.1.14). However, a straightforward solution of the one-particle Green function's equation of motion is not possible because the equation of motion leads to a hierarchy of Green functions of higher order, i.e., the one-particle Green function depends on the two-particle Green function

$$G^{(2)}_{\alpha\beta\gamma\delta}(12,34) = -\langle \mathcal{T}\psi_\alpha(1)\psi_\beta(2)\psi^\dagger_\delta(4)\psi^\dagger_\gamma(3)\rangle, \quad (2.1.20)$$

which in turn depends on the three-particle Green function, and so on. Here and in the following, we abbreviate the space and time arguments by $1 = \mathbf{r}_1 t_1$, and 1^+ indicates that the time argument is increased by an infinitesimal positive amount η, i.e., $1^+ = \mathbf{r}_1 t_1 + \eta$. The equation of motion of the one-particle Green function leads to a hierarchy of equations of Green functions of ever increasing order. Formally, the hierarchy of equations can be truncated by relating the two-particle Green function to a functional derivative of the one-particle Green function, which leads to the Hedin equations. The Hedin equations are a set of five integro-differential equations that solve the many-body problem in principle exactly. For its derivation an auxiliary external field $U_{\mathrm{ext}}(1)$ is incorporated into the one-particle Hamiltonian $h(1) \to h(1) + U_{\mathrm{ext}}(1)$. The external field acts as an external perturbation. The limit $U_{\mathrm{ext}}(1) \to 0$ is taken at the end of the derivation. The introduction of such an external perturbation allows to employ the Schwinger functional derivative technique [85]. The functional derivative of the Green function with respect to the external perturbation is connected to the two-particle Green function [85]

$$\left.\frac{\delta G_{\alpha\beta}(12)}{\delta U_{\mathrm{ext}}(3)}\right|_{U_{\mathrm{ext}}=0} = \sum_\gamma \left[G_{\alpha\beta}(12)G_{\gamma\gamma}(33^+) - G^{(2)}_{\alpha\gamma\beta\gamma}(13,23^+)\right], \quad (2.1.21)$$

which turns Eq. (2.1.19) into

$$\mathrm{i}\partial_t G_{\alpha\beta}(12) = \delta(12)\delta_{\alpha\beta} + h_0(1)G_{\alpha\beta}(12) + \sum_\gamma \int \mathrm{d}3\, \Sigma_{\alpha\gamma}(13)G_{\gamma\beta}(32), \tag{2.1.22}$$

where

$$h_0(1) = h(1) + U_{\mathrm{ext}}(1) + v_{\mathrm{H}}(1), \tag{2.1.23}$$

is the Hartree Hamiltonian with the Hartree potential

$$v_{\mathrm{H}}(1) = -\mathrm{i}\sum_\gamma \int \mathrm{d}2\, v(12)G_{\gamma\gamma}(22^+), \tag{2.1.24}$$

and

$$\Sigma_{\alpha\beta}(12) = \mathrm{i}\sum_\gamma \int \mathrm{d}3\,\mathrm{d}4\, v(1^+3)\frac{\delta G_{\alpha\gamma}(14)}{\delta U_{\mathrm{ext}}(3)}G^{-1}_{\gamma\beta}(42) \tag{2.1.25}$$

is the nonlocal and time-dependent self-energy, which accounts for the interaction of a particle with the rest of the system. The self-energy vanishes in a non-interacting system and the corresponding solution of the Green function's equation of motion (2.1.22) is called the non-interacting Green function G_0

$$[\mathrm{i}\partial_t - h_0(1)]\, G_{0,\alpha\beta}(12) = \delta(12)\delta_{\alpha\beta}. \tag{2.1.26}$$

With this definition the solution of the Green function's equation of motion (2.1.22) can be written in terms of a Dyson equation

$$G_{\alpha\beta}(12) = G_{0,\alpha\beta}(12) + \sum_{\gamma,\delta}\int \mathrm{d}3\,\mathrm{d}4\, G_{0,\alpha\gamma}(13)\Sigma_{\gamma\delta}(34)G_{\delta\beta}(42). \tag{2.1.27}$$

The external perturbation U_{ext} causes a change of the density (2.1.16) that leads in turn to a response of the system resulting in the total effective potential

$$U_{\mathrm{eff}}(1) = U_{\mathrm{ext}}(1) + \int \mathrm{d}2\,\mathrm{d}3\, v(13)\left.\frac{\delta n(3)}{\delta U_{\mathrm{ext}}(2)}\right|_{U_{\mathrm{ext}}=0} U_{\mathrm{ext}}(2). \tag{2.1.28}$$

The change of the effective potential with respect to the external perturbation equals the inverse dielectric function

$$\epsilon^{-1}(12) = \left.\frac{\delta U_{\mathrm{eff}}(1)}{\delta U_{\mathrm{ext}}(2)}\right|_{U_{\mathrm{ext}}=0} \tag{2.1.29}$$

characterizing the polarizability of the system. With this, the self-energy can be rearranged such that

$$\Sigma_{\alpha\beta}(12) = \mathrm{i}\sum_{\gamma}\int \mathrm{d}3\,\mathrm{d}4\, G_{\alpha\gamma}(14)W(1^{+}3)\Gamma_{\gamma\beta}(42;3), \tag{2.1.30}$$

with the vertex correction

$$\begin{aligned}\Gamma_{\alpha\beta}(12;3) = -\left.\frac{\delta G^{-1}_{\alpha\beta}(12)}{\delta U_{\mathrm{eff}}(3)}\right|_{U_{\mathrm{ext}}=0} &= \delta(12)\delta(13)\delta_{\alpha\beta} \\ &- \sum_{\gamma,\delta,\nu,\mu}\int \mathrm{d}4\,\mathrm{d}5\,\mathrm{d}6\,\mathrm{d}7\,\frac{\delta\Sigma_{\alpha\beta}(12)}{\delta G_{\gamma\delta}(45)}G_{\delta\nu}(56)\Gamma_{\nu\mu}(67;3)G_{\mu\gamma}(74),\end{aligned} \tag{2.1.31}$$

and the screened interaction

$$W(12) = \int \mathrm{d}3\,\epsilon^{-1}(13)v(32) = v(12) + \int \mathrm{d}3\,\mathrm{d}4\, v(13)P(34)W(42), \tag{2.1.32}$$

where

$$P(12) = -\mathrm{i}\sum_{\alpha}\frac{\delta G_{\alpha\alpha}(11^{+})}{\delta U_{\mathrm{eff}}(2)} = -\mathrm{i}\sum_{\alpha,\beta,\gamma}\int \mathrm{d}3\,\mathrm{d}4\, G_{\alpha\beta}(13)\Gamma_{\beta\gamma}(34;2)G_{\gamma\alpha}(41^{+}), \tag{2.1.33}$$

is the polarization of the system. The coupled set of integro-differential equations (2.1.27), (2.1.30), (2.1.31), (2.1.32), and (2.1.33) constitute the Hedin equations. The self-consistent solution of the Hedin equations, in principle, solves the many-body problem exactly. The vertex function (2.1.31) is responsible for the coupling of the set of equations. Therefore, the Hedin equations cannot be solved straightforwardly and in practice, approximations are needed. A commonly used approach starts with a non-interacting Green function G_0 and iterates the Hedin equations once. In case of a non-interacting system the self-energy vanishes so that the vertex function simplifies to

$$\Gamma_{\alpha\beta}(12;3) = \delta(12)\delta(13)\delta_{\alpha\beta}, \tag{2.1.34}$$

and the polarization is given by

$$P(12) = -\mathrm{i}\sum_{\alpha,\beta} G_{0,\alpha\beta}(12)G_{0,\beta\alpha}(21^{+}), \tag{2.1.35}$$

which leads to the random-phase approximation (RPA) for the screened interaction W (2.1.32). Iterating the Hedin equations once results in the *GW* self-energy

$$\Sigma_{\alpha\beta}(12) = \mathrm{i}G_{0,\alpha\beta}(12)W(1^{+}2), \tag{2.1.36}$$

and the renormalized Green function is obtained by solving the Dyson equation (2.1.27) with the *GW* self-energy. We analyze the magnetic response function in the framework of the *GW* approximation in Chapter 3. In addition, we propose a new self-energy approximation starting from the Hedin equations that accounts for the coupling of spin excitations to electronic degrees of freedom in Chapter 4. In practical applications of the many-body perturbation theory the non-interacting Green function is conveniently obtained from the density-functional theory, in which G_0 is the solution to the Hartree Hamiltonian (2.1.23) plus a local and energy independent approximation to the exchange-correlation self-energy.

2.2 Density-Functional Theory

The density-functional theory (DFT) is nowadays one of the most widely used methods in theoretical condensed-matter physics, quantum chemistry, and computational material science [76]. Density-functional theory allows to calculate ground-state properties such as the total energy, the charge density, the magnetization density, lattice constants, and so on, in good agreement with experimental findings. Hohenberg and Kohn [18] developed the density-functional theory for a non-degenerate ground state of an interacting electron gas in an external potential. The density-functional theory is based on two fundamental theorems. First, the wave function $\Psi[n(\mathbf{r})]$ of the ground state is a unique functional of the density $n(\mathbf{r})$. Secondly, they proved the existence of the ground-state energy functional $E[n(\mathbf{r})]$, which is stationary with respect to the density, i.e., the energy functional $E[n(\mathbf{r})]$ takes its minimum at the true ground-state density $n_0(\mathbf{r})$. While the proof of Hohenberg and Kohn was by *reductio ad absurdum*, Levy [86, 87] gave a constructive proof in analogy to the Rayleigh-Ritz variational principle. The Rayleigh-Ritz variational principle ensures that the ground-state wave function Ψ_0 minimizes the total energy

$$E[\Psi] = \langle\Psi|H|\Psi\rangle \geq E[\Psi_0], \tag{2.2.1}$$

of a many-electron system described by the Hamiltonian $H = T + U + V$ containing the kinetic energy T, the Coulomb interaction between the electrons U and the external potential energy V due to the interaction between the electrons and the nuclei. In addition, the many-electron wave function Ψ is related to the density

$$n(\mathbf{r}) = \langle \Psi | \sum_{\alpha} \psi_{\alpha}^{\dagger}(\mathbf{r}) \psi_{\alpha}(\mathbf{r}) | \Psi \rangle, \tag{2.2.2}$$

with the subsidiary condition that the charge density integrates to the total number of electrons

$$N = \int \mathrm{d}\mathbf{r}\, n(\mathbf{r}), \tag{2.2.3}$$

so that the minimization of the energy functional for a given density n subject to the many-electron wave function Ψ

$$E[n] = \min_{\Psi \to n} \langle \Psi[n] | T + U + V | \Psi[n] \rangle = T[n] + U[n] + V[n], \tag{2.2.4}$$

yields an energy higher than the ground-state energy if the density n is different from the ground-state density n_0 and accordingly the wave function Ψ is not the ground-state wave function Ψ_0. The kinetic energy functional $T[n]$ forms, together with the Coulomb interaction functional $U[n]$, a functional $F[n] = T[n] + U[n]$, which is universal in the sense that it does not refer to the actual external potential energy functional [76, 88]

$$V[n] = \int \mathrm{d}\mathbf{r}\, n(\mathbf{r}) v_{\mathrm{ext}}(\mathbf{r}). \tag{2.2.5}$$

The theorems of Hohenberg and Kohn were generalized to the spin-dependent case by the generalization of the density to a spin density matrix

$$n_{\alpha\beta}(\mathbf{r}) = \langle \Psi | \psi_{\alpha}^{\dagger}(\mathbf{r}) \psi_{\beta}(\mathbf{r}) | \Psi \rangle \tag{2.2.6}$$

by von Barth and Hedin [89]. The existence of the energy functional (2.2.4) is, however, of little practical use as the functional form of $F[n] = T[n] + U[n]$ remains unspecified.

2.2.1 Kohn-Sham Formalism

Kohn and Sham [19] proposed a separation of the energy functional (2.2.4) guided by the picture of non-interacting particles moving in an effective potential. This approach greatly simplifies the search for the functional form of the universal func-

tional $F[n]$. The following formulas are given for the collinear spin-polarized case. Kohn and Sham proposed a separation of the energy functional

$$E[n] = T_0[n] + U_{\mathrm{H}}[n] + E_{\mathrm{xc}}[n] + V[n] \tag{2.2.7}$$

into the kinetic energy of a system of non-interacting particles

$$T_0[n] = \sum_{\alpha} \sum_{i} \int \mathrm{d}\mathbf{r}\, \varphi_i^{\alpha *}(\mathbf{r}) \left(-\frac{1}{2} \nabla_{\mathbf{r}}^2 \right) \varphi_i^{\alpha}(\mathbf{r}) \tag{2.2.8}$$

with the single-particle orbitals $\varphi_i^{\alpha}(\mathbf{r})$ of spin α and the spin density

$$n_{\alpha}(\mathbf{r}) = \sum_{i}^{\mathrm{occ.}} |\varphi_i^{\alpha}(\mathbf{r})|^2, \tag{2.2.9}$$

the Hartree energy, i.e., the electrostatic interaction energy due to the charge distribution

$$U_{\mathrm{H}}[n] = \frac{1}{2} \int \mathrm{d}\mathbf{r}\, \mathrm{d}\mathbf{r}'\, \frac{n(\mathbf{r}) n(\mathbf{r}')}{|\mathbf{r} - \mathbf{r}'|}, \tag{2.2.10}$$

and the exchange-correlation energy $E_{\mathrm{xc}}[n]$, which accounts for the difference of the electron-electron interaction and the Hartree energy $U[n] - U_{\mathrm{H}}[n]$ and for the difference that stems from the kinetic energy in an interacting and a non-interacting system $T[n] - T_0[n]$. The stationarity of the total energy with respect to the ground state density can be recast into a variational principle for the single-particle wave functions $\varphi_i^{\alpha}[n(\mathbf{r})]$, which are themselves functionals of the density, i.e., the variation of the total energy functional (2.2.7) with respect to the single-particle wave functions leads to the Kohn-Sham equations

$$\left(-\frac{1}{2} \nabla_{\mathbf{r}}^2 + v_{\mathrm{eff}}^{\alpha}(\mathbf{r}) \right) \varphi_i^{\alpha}(\mathbf{r}) = \epsilon_i^{\alpha} \varphi_i^{\alpha}(\mathbf{r}), \tag{2.2.11}$$

where the Lagrange parameters ϵ_i^{α} account for the subsidiary condition that the Kohn-Sham wave functions are normalized

$$\int \mathrm{d}\mathbf{r}\, \varphi_i^{\alpha *}(\mathbf{r}) \varphi_i^{\alpha}(\mathbf{r}) = 1. \tag{2.2.12}$$

Strictly speaking, neither the Lagrange parameter ϵ_i^{α} nor the Kohn-Sham wave functions $\varphi_i^{\alpha}(\mathbf{r})$ can be interpreted in a physical manner. Yet, in practice ϵ_i^{α} is commonly taken as the true excitation energy of an interacting electron system and $\varphi_i^{\alpha}(\mathbf{r})$ is interpreted as the corresponding quasiparticle wave function. The Kohn-Sham equa-

tions describe non-interacting particles $\varphi_i^\alpha(\mathbf{r})$ moving in an effective spin-dependent potential

$$v_{\text{eff}}^\alpha(\mathbf{r}) = v_{\text{H}}(\mathbf{r}) + v_{\text{xc}}^\alpha(\mathbf{r}) + v_{\text{ext}}(\mathbf{r}), \tag{2.2.13}$$

with the Hartree potential $v_{\text{H}}(\mathbf{r})$ and the exchange-correlation potential

$$v_{\text{xc}}^\alpha(\mathbf{r}) = \frac{\delta E_{\text{xc}}[n]}{\delta n_\alpha(\mathbf{r})}, \tag{2.2.14}$$

which contains in principle all the many-body effects of the interacting systems. In practice, however, the exchange-correlation potential has to be approximated. Commonly, the local-spin-density approximation (LSDA) to the exchange-correlation energy

$$E_{\text{xc}}^{\text{LSDA}}[n] = \int \mathrm{d}\mathbf{r}\, n(\mathbf{r}) \varepsilon_{\text{xc}}^{\text{LSDA}}(n(\mathbf{r})) \tag{2.2.15}$$

or its semilocal generalization, the generalized gradient approximation (GGA)

$$E_{\text{xc}}^{\text{GGA}}[n] = \int \mathrm{d}\mathbf{r}\, n(\mathbf{r}) \varepsilon_{\text{xc}}^{\text{GGA}}(n(\mathbf{r}), \nabla n(\mathbf{r})) \tag{2.2.16}$$

is used. The (semi-) local approximations to the exchange-correlation potential are exact in the limit of a homogeneous electron gas. For the present work the self-consistent solution of the Kohn-Sham equations (2.2.11) serves as starting point for a subsequent many-body perturbation theory calculation. We employ either the LSDA in the parameterization of Perdew and Zunger [90] or the GGA in the parameterization of Perdew, Burke, and Ernzerhof [91].

2.3 Full-Potential Linearized Augemented-Plane-Wave Method

The full-potential linearized augmented-plane-wave (FLAPW) method [48–50] is the basis for the implementation of the density-functional theory realized in the FLEUR code [92] as well as the implementation of the many-body perturbation theory realized in the SPEX code [72]. Besides the FLAPW method, there is a wide variety of electronic structure methods, each of which is optimized for a particular situation. While there are methods which solve the electronic structure problem on a real-space grid [93], frequently the wave functions are expanded into a linear combination of basis functions. The basis functions are chosen such that the electronic structure problem can be solved efficiently. Therefore, the choice of the basis functions depends

on a) the problem under consideration, e.g., periodic solids, solids with surfaces, or clusters of atoms and molecules, and b) the treatment of the external potential due to the atomic nuclei [94].

In chemistry, localized basis functions such as the Slater-type orbitals or Gaussian-type orbitals are widely used for a linear-combination of atomic orbitals (LCAO) to treat clusters and molecules [95]. In lattice-periodic systems without spin-orbit coupling, the wave functions follow the Bloch theorem [81] and consequently they can be labeled by a Bloch vector $\mathbf{k}$, a band index m, and a spin α. Provided that the effective potential of the Kohn-Sham equation is a smoothly varying function, the plane-wave basis is a good choice for the representation of the wave function. This is because the kinetic energy and also the solution to the Poisson equation, which is necessary for the calculation of the Hartree potential, contains the Laplace operator $\Delta_{\mathbf{r}}$, which is diagonal in the plane-wave basis. In addition, the charge density is easily expandable in plane waves. However, the plane-wave basis does not converge if the full $1/r$-Coulomb potential stemming from the atomic nuclei is taken into account. Pseudopotential methods bypass the problematic $1/r$-like behavior and replace the external potential by an effective smoothly varying potential that acts on the valence states and assumes the core states to be frozen. There are various ways to construct an effective potential, e.g., the norm-conserving pseudopotentials [96], the ultrasoft Vanderbilt-type pseudopotentials [97], or the projector-augemented wave (PAW) method [98, 99].

In contrast, full potential all-electron methods treat core and valence electrons on equal footing by accounting for the full $1/r$-Coulomb potential of the atomic nuclei without any shape approximations. To this end, the space is partitioned into non-overlapping spheres around the atoms called muffin-tin spheres and the interstitial region. Within the muffin-tin spheres all-electron methods work with basis functions which treat the singularity of the Coulomb potential exactly, i.e., the basis functions are chosen as the solution of the radial Schrödinger equation

$$\left[-\frac{1}{2}\frac{\mathrm{d}^2}{\mathrm{d}r^2}+\frac{l(l+1)}{2r^2}+v_{\mathrm{eff}}^{a,\alpha}(r)-E_{a,l}^{\alpha}\right] r u_{a,l}^{\alpha}(r,E_{a,l}^{\alpha})=0 \tag{2.3.1}$$

with a predetermined energy parameter $E_{a,l}^{\alpha}$ for each atom a and angular momentum l. Generally, the solutions of the radial Schrödinger equation (2.3.1) depend on the predetermined energy parameter $E_{a,l}^{\alpha}$. In practice, the energy parameters are chosen as close as possible to the Kohn-Sham energy eigenvalues. Nevertheless, the

energy eigenvalues of a lattice-periodic system are dispersive and depend on the band index. In contrast, the energy parameters dependent on the atom a and angular momentum l. Therefore, deviations between the energy parameters and the actual band energies are unavoidable. Therefore, a basis constituting only of the solution to the radial Schrödinger equation (2.3.1) with a predetermined energy parameter are usually too stiff in the sense that such a basis provides too little variational freedom for an accurate description of the wave functions. To solve this problem, the linear augmented-plane-wave (LAPW) method includes in addition to the solutions $u^{\alpha}_{a,l}(r, E^{\alpha}_{a,l})$ of the radial Schrödinger equation (2.3.1), their energy derivatives $\dot{u}^{\alpha}_{a,l}(r, E^{\alpha}_{a,l})$. The solutions within the muffin-tin spheres are matched to energy-independent plane waves as envelope functions in the interstitial region [100]. The flexibility of the basis to accurately describe states in the vicinity of the chosen energy parameter is increased as the representation error scales quadratically [101, 102]

$$u^{\alpha}_{a,l}(r, E) \approx u^{\alpha}_{a,l}(r, E^{\alpha}_{a,l}) + \dot{u}^{\alpha}_{a,l}(r, E^{\alpha}_{a,l})(E - E^{\alpha}_{a,l}) + \mathcal{O}(E - E^{\alpha}_{a,l})^2. \tag{2.3.2}$$

The expression suggests that the basis set can be improved further by incorporating also the second energy derivative $\ddot{u}^{\alpha}_{a,l}(r, E^{\alpha}_{a,l})$. This is, however, not the case: Singh [103] showed that the inclusion of the second energy derivative makes the basis set less flexible as another matching condition at the muffin-tin sphere boundary must be fulfilled. Instead of that he proposed to use local orbitals that are entirely confined to the muffin-tin sphere. The inclusion of local orbitals allow an accurate description of semi core states, i.e., high-lying core states that extend to the interstitial region and high-lying unoccupied states. The local orbitals are a linear combination of the functions $u^{\alpha}_{a,l}(r, E^{\alpha}_{a,l})$ and $\dot{u}^{\alpha}_{a,l}(r, E^{\alpha}_{a,l})$ plus an additional function $u^{\alpha,\mathrm{LO}}_{a,l}(r)$ that is either another solution to the radial Schrödinger equation (2.3.1) with a different energy parameter or the second energy derivative $\ddot{u}^{\alpha}_{a,l}(r, E^{\alpha}_{a,l})$ [101, 102, 104]. The local orbitals are constructed such that their values as well as their derivatives vanish at the muffin-tin sphere boundary. It has been shown that the inclusion of local orbitals substantially reduces the dependence of the basis set on the predetermined energy parameters $E^{\alpha}_{a,l}$ as well as the dependence on the chosen muffin-tin sphere radius [101, 102]. In particular, calculations that rely on the summation of unoccupied states such as the optimized-effective potential method or the GW approximation require the convergence of the basis set in terms of local orbitals to ensure an accurate description of the high-lying unoccupied states [104–108].

To sum up, the full-potential linearized augmented-plane-wave method [48–50]

accounts for the full potential of the atomic nuclei without any shape approximations. The Bloch wave functions $\varphi^{\alpha}_{\mathbf{k}n}(\mathbf{r})$ are expanded within the LAPW method piecewise in the muffin-tin region by atomic orbitals and in the interstitial region by plane waves, that is

$$\varphi^{\alpha}_{\mathbf{k}n}(\mathbf{r}) = \sum_{v} \kappa^{\alpha}_{\mathbf{k}n,v} A^{\alpha}_{\mathbf{k},v}(\mathbf{r}) + \sum_{\mathbf{G}} \beta^{\alpha}_{\mathbf{k}n,\mathbf{G}} P^{\alpha}_{\mathbf{k},\mathbf{G}}(\mathbf{r}), \tag{2.3.3}$$

where $v \equiv (a, p, l, m)$ is a composite index containing the atom number a in the unit-cell, index p specifying the atomic orbitals, and the angular momentum l as well as its z component m, and $\mathbf{G}$ are the reciprocal lattice vectors. The first term represents the wave function in the muffin-tin (MT) sphere, whereas the second term is non-zero only in the interstitial region (IR). Both are related by the continuity condition of the Bloch function and its radial derivative at the muffin-tin sphere boundary determining the coefficients κ and β in Eq. 2.3.3. The atomic orbitals are defined as

$$A^{\alpha}_{\mathbf{k},aplm}(\mathbf{r}) = \begin{cases} \frac{1}{\sqrt{N}} \sum_{\mathbf{R}} \phi^{\alpha}_{apl}(|\mathbf{r} - \mathbf{R} - \mathbf{R}_a|) Y_{lm}(\widehat{\mathbf{r} - \mathbf{R} - \mathbf{R}_a}) e^{i\mathbf{k}\mathbf{R}} & \text{if } \mathbf{r} \in \text{MT} \\ 0 & \text{elsewhere} \end{cases}, \tag{2.3.4}$$

where the functions $\phi^{\alpha}_{apl}(r = |\mathbf{r}|)$ represent the radial character of the atomic orbitals. The atomic orbitals include three different types of functions: for $p = 0$ the functions ϕ are the solutions $u^{\alpha}_{a,l}$ to the radial Schrödinger equation (2.3.1), $p = 1$ labels the energy derivates $\dot{u}^{\alpha}_{a,l}$, and $p \geq 2$ are local orbitals augmenting the basis function. The angular dependence of the atomic orbitals is represented in terms of spherical harmonics $Y_{lm}(\widehat{\mathbf{r}})$. N is the (infinite) number of unit cells. The interstitial region is described by plane waves

$$P^{\alpha}_{\mathbf{k},\mathbf{G}}(\mathbf{r}) = \begin{cases} \frac{1}{\sqrt{V}} e^{i(\mathbf{k}+\mathbf{G})\mathbf{r}} & \text{if } \mathbf{r} \in \text{IR} \\ 0 & \text{elsewhere} \end{cases}, \tag{2.3.5}$$

where V is the (infinite) crystal volume. The FLAPW method is employed for the implementation of the Kohn-Sham density-functional theory and the many-body perturbation theory. The representation of the wave functions in terms of the LAPW basis functions turns the differential Kohn-Sham equations (2.2.11) into a generalized eigenvalue problem that can be solved efficiently. The resulting wave function and energies are used for the subsequent many-body perturbation theory calculations.

3. Spin-Wave Excitations

3.1 Introduction

Collective spin excitations form an important class of excitations in magnetic materials. As their energy reaches from a few hundreds meV down to a few meV, they play a fundamental role for the physical properties of magnetic solids at all temperatures. For example, the specific heat [109] exhibits a characteristic $T^{3/2}$ behavior that can be attributed to the low-energy spin-wave excitations (magnons). The spin-wave excitations are as well responsible for the temperature dependence of the macroscopic magnetization [110, 111]. As the temperature increases, another type of spin excitations, the single-particle spin-flip excitations become increasingly important. These excitations, known as Stoner excitations, give an important contribution to the damping of the collective spin excitations and they further change the temperature dependence of the magnetization.

The coupling of spin excitations to electronic states leads to a renormalization of the quasiparticles. Recent, high-resolution angle-resolved photoemission spectroscopy (ARPES) experiments [58, 59] found a pronounced renormalization in the quasiparticle band dispersion at high binding energies. While one experiment studied a minority spin surface state of iron, the other experiment analyzed a minority spin bulk state of nickel. In both cases the significant deviation of the experimental data compared to a calculated band structure can be described by a self-energy accounting for the coupling of spin excitations to electronic excitations. Similar coupling processes might be relevant for superconducting materials. ARPES experiments on high-temperature superconductors reveal an unusual line shape within the spectra of the superconducting state [112–114]. The unusual line shape is called a peak-dip-hump feature as it emerges from the presence of two features in the spec-

tra. At the same time, neutron scattering experiments [115–120] find a magnetic resonance in the superconducting state. The effect of the magnetic resonance on the electronic spectra has been discussed theoretically by Eschrig *et al.* [121–123]. They found that the corresponding self-energy can explain various dispersion anomalies seen experimentally. Similar peak-dip-hump features are found in the spectra of the superconducting state of iron-based superconductors by ARPES experiments [124–128] leading to kink structures in the quasiparticle band dispersion. Magnons are proposed as mediating boson for the attractive electron-electron interaction that leads to the superconducting state in the high-temperature superconductors [129–131]. A recently conducted analysis of ARPES and an inelastic neutron scattering (INS) experiment on the same high-temperature superconductor [132] supports this scenario. The analysis demonstrates that the coupling strength of spin fluctuations to electronic quasiparticles is sufficiently large to explain superconducting transition temperatures exceeding 150 K.

Recently, spin-wave excitations have been proposed for technical applications. An exciting proposal is to use spin waves as information carriers for nanoscale logic devices [8, 133, 134]. Employing the spin wave as information carrier might overcome fundamental drawbacks of traditional transistor technology in electronics like the complementary metal-oxide-semiconductor (CMOS) technology. A traditional field effect transistor makes use of the motion of electrons to implement its switching capabilities. The resulting waste heat increases the transistor's power consumption. Even worse, the generation of waste heat increases with increasing data processing speed. In a recently proposed magnon transistor [8], the spin waves replace the electrons as the information carriers. Consequently, the waste heat generation is reduced because such a magnon transistor does not require charge transport. The proposed magnon transistor is an all-magnon device entirely forgoing the use of electrons for switching purposes, i.e., the magnon flow from the transistor's source to its drain is controlled by the injection of magnons into the transistor's gate. An all-magnon device might have the potential advantage that its size can be scaled down to the subten nanometer scale [8, 10] while it is capable of ultra-fast data processing reaching the THz range [8, 11–13].

Clearly, spin excitations are equally interesting for their relevance in fundamental research and for their potential technical applications. Spin excitations can be experimentally studied by neutron-scattering experiments. Typical neutron-scattering techniques, such as the triple-axis spectroscopy (TAS) or the time-of-flight spectrom-

etry, allow to measure the neutron-scattering cross section directly. Spin excitations manifest themselves as peaks in the scattering cross section [15–17, 135–140], which is related to the spectral function of the transverse magnetic response function. The magnetic response function describes the dynamical linear response of a magnetic material to an external magnetic perturbation. Therefore, the magnetic response function is the central quantity of interest to study spin excitations theoretically. It allows to obtain the complete excitation spectrum, including Stoner excitations, collective spin-wave excitations, and combinations thereof. Its spectral function exhibits peaks at the spin-excitation energies with a certain width, which is associated with the inverse lifetime of the spin excitations.

Collinear magnetic systems without spin anisotropy exhibit a spontaneously broken global rotational symmetry in spin space. As a consequence, the global spin polarization can be rotated by a homogeneous magnetic field perpendicular to the magnetization axis without a cost of energy. This, in turn, corresponds to an acoustic magnon mode with vanishing excitation energy in the long-wavelength limit, a consequence of the Goldstone theorem. This theorem states that the spontaneously broken spin-rotation symmetry leads to the appearance of a gapless magnon dispersion curve, a condition to which we refer to as the Goldstone condition. The Goldstone condition is often numerically violated in *ab initio* realizations of the magnetic response function.

For a theoretical description of spin excitations various formalisms have been established. A frequently used approach employs a separation of the slow magnetic degrees of freedom and the fast motion of the electrons [20–24]. It is realized in the classical Heisenberg model, which allows to study the collective spin excitations in systems with localized moments. The Heisenberg model relies on parameters, the so-called Heisenberg exchange parameters, which can be obtained from constrained density-functional theory [25]. The Goldstone condition is identically fulfilled in this approach. However, single-particle Stoner excitations are missing in the Heisenberg model and, as a consequence, magnon lifetimes are inaccessible. In addition, the local-moment approximation of the Heisenberg model is only justified for insulators and rare-earth elements but not for metallic magnets such as the 3*d* ferromagnets [15]. Even though the Heisenberg model captures the long-wavelength spin dynamics of the 3*d* ferromagnets reasonably well, it gives unsatisfactory results for the short-wavelength spin excitations.

To overcome the shortcomings of the Heisenberg model, one needs a more gen-

eral theoretical framework that works for systems with localized moments and for itinerant-electron magnets alike. For example the many-body perturbation theory (MBPT) provides such a framework in which the single-particle Stoner excitations and the collective spin excitations appear simultaneously as poles in the transverse magnetic response function, which describes the correlated motion of an electron-hole pair with opposite spins coupled by an effective electron-electron interaction. First applications to metallic magnets [141–143] employed a tight-binding description of the electronic bands. In this approach, the single-particle propagator and the effective interaction derive from the same Hamiltonian so that the Goldstone condition is fulfilled by construction.

Parameter-free calculations of the magnetic response function based on *ab initio* electronic structure methods are scarce in the literature. This is because such calculations demand a tremendous computational cost. Apart from MBPT calculations [43–45] another method that is often used is time-dependent density-functional theory (TDDFT). Usually, calculations of the magnetic response function within TDDFT [33–42] have to account for the violation of the Goldstone condition. The origin of this violation is attributed to approximations in the numerical scheme [39, 42], i.e., the exchange-correlation kernel and the non-interacting magnetic response function are derived from different ground-state calculations. To ensure the proper long-wavelength limit of the spin-wave spectrum, Lounis *et al.* [38–41] deduce the exchange-correlation kernel from a magnetic sum rule. Based on similar grounds, Rousseau *et al.* [42] construct a correction scheme for the magnetic response function, while the exchange-correlation kernel remains unchanged. Another correction scheme is implemented by Buczek *et al.* [34, 37], they set the smallest eigenvalue of the enhancement matrix equal to zero to account for the Goldstone condition.

First studies of spin-wave excitations based on the *ab initio* electronic structure of itinerant ferromagnets using MBPT were performed by Karlsson and Aryasetiawan [44]. However, they employed a model potential for the effective interaction among the electron-hole pairs. Kotani and van Schilfgaarde [45] studied spin-wave spectra based on quasiparticle self-consistent *GW* calculations [144–147]. The effective interaction is determined from a magnetic sum rule, similar to the approach used by Lounis *et al.* [39], ensuring the fulfillment of the Goldstone condition. The first who performed a full *ab initio* study of spin-wave spectra within MBPT was Şaşıoğlu *et al.* [43]. What contrasts their study from previous works is that they calculated the screened interaction explicitly from the random-phase approximation (RPA). They

ensure the Goldstone condition by introducing a scaling factor for the screened interaction. In most cases the scaling factor was relatively close to 1, but it could reach 1.5 for bulk nickel, unless the exchange splitting was adjusted to the experimental value as an *ad hoc* correction.

The violation of the Goldstone condition in the MBPT calculations is more fundamental compared to the case of TDDFT. The present chapter investigates the Goldstone violation in MBPT. Parts and results of this chapter have been published recently [51]. We argue that the Goldstone violation originates to a large degree from the inconsistency between the non-interacting magnetic response function, which is constructed from the single-particle Green function, and the RPA screened interaction. The inconsistency stems from the fact that the two quantities derive from different Hamiltonians. While the single-particle Green function derives from the Kohn-Sham density-functional theory within the local-spin-density approximation (LSDA) or the generalized gradient approximation (GGA), the screened interaction derives from the *GW* self-energy [71] with an additional static approximation. We argue that constructing the single-particle Green function from a self-consistent Coulomb-hole screened exchange (COHSEX) self-energy [71] instead should lift the inconsistency. We perform self-consistent calculations of the COHSEX self-energy for the bulk 3*d* transition metals iron, cobalt, and nickel. The results, in turn, are employed as starting point for the calculation of the magnetic response function. Within this approach, we find, in fact, a substantial reduction of the Goldstone violation.

The application of the COHSEX self-energy is considerably more time-consuming compared to standard Kohn-Sham density-functional theory calculations. In order to bypass the additional computational effort needed for the self-consistent COHSEX calculation, we discuss a correction scheme for the Kohn-Sham Green function of ferromagnetic materials. The Goldstone condition can be analyzed in detail by means of the spin-wave solution of the one-band Hubbard model. The analysis reveals that the magnetization, the exchange splitting, and the interaction among the electron-hole pairs are intimately connected [148,149]. With this in mind, we propose a correction scheme for the non-interacting magnetic response function to resolve the Goldstone violation. We show that the corrected LSDA spin-wave spectra and the corrected GGA spin-wave spectra for the 3*d* transition metals iron, cobalt, and nickel are close to the results obtained from the much more expensive COHSEX approach and to experimental measurements.

The next section gives an overview of the theoretical framework of the magnetic

response function, and the details of its implementation are summarized in Section 3.3. The magnetic response function is analyzed in view of the Goldstone condition in Section 3.4. The violation of the Goldstone condition in MBPT and the starting-point dependence of the spin-wave spectra of iron, cobalt, and nickel is discussed in Section 3.5. We conclude the discussion with a summary in Section 3.6.

3.2 Theory

Inelastic neutron scattering (INS) experiments are commonly used to study the magnetic properties of bulk materials [15,140,141,150–154]. The neutron as a charge neutral particle is able to scatter with the nuclei without electrostatic interaction. As a consequence, the neutron probes, on the one hand, phonon excitations. On the other hand, the magnetic spin of the neutron interacts with the spins of the system giving rise to spin excitations. The neutron scattering cross section coming from the spin excitations is related to the magnetic response function of the system. The magnetic response function describes the change of the spin density due to an external magnetic perturbation. The Green function of the interacting many-body system carries the information about the average spin density of its ground state

$$\langle \sigma^i(\mathbf{r}t)\rangle = -\mathrm{i}\sum_{\alpha,\beta}\sigma^i_{\beta\alpha}G_{\alpha\beta}(\mathbf{r}t,\mathbf{r}t^+), \tag{3.2.1}$$

where $\sigma^i_{\beta\alpha}$ is the i-th Pauli matrix with $i = \mathrm{x},\mathrm{y},\mathrm{z}$, Greek letters denote spin indices, and $t^+ = t + \eta$ with a positive infinitesimal time η provides the correct time ordering of the field operators in the Green function. The neutrons in a neutron scattering experiment can be prepared such that their magnetic perturbation corresponds to that of a circularly polarized magnetic field $B^+ = B_\mathrm{x} + \mathrm{i}B_\mathrm{y}$. A magnetic perturbation $\delta B^+(\mathbf{r}'t')$ gives rise to spin excitations $\delta\langle\sigma^+\rangle = \delta\langle\sigma_\mathrm{x}\rangle + \mathrm{i}\delta\langle\sigma_\mathrm{y}\rangle$ which are described by the transverse magnetic response function

$$R^{+-}(\mathbf{r}t,\mathbf{r}'t') = \frac{\delta\langle\sigma^+(\mathbf{r}t)\rangle}{\delta B^+(\mathbf{r}'t')}. \tag{3.2.2}$$

This function accounts for the linear response of the magnetic system to an external circularly polarized magnetic perturbation. The magnetic response function (3.2.2) can be written as a time-ordered correlation function [111]

$$R^{+-}(\mathbf{r}t,\mathbf{r}'t') = -\mathrm{i}\langle\mathcal{T}S^+(\mathbf{r}t)S^-(\mathbf{r}'t')\rangle. \tag{3.2.3}$$

Given that the Hamiltonian is not explicitly time-dependent, the response function depends only on the time-difference $\tau = t - t'$ between the action of the spin-ladder operators $S^{\pm} = \sigma^{\pm}/2$, and we write for the magnetic response function $R^{+-}(\mathbf{r}, \mathbf{r}'; \tau)$. The time-ordering operator $\mathcal{T}$ ensures that the operators are ordered with increasing time arguments from right to left, i.e.,

$$R^{+-}(\mathbf{r}, \mathbf{r}'; \tau) = -\mathrm{i} \begin{cases} \langle S^{+}(\mathbf{r}\tau) S^{-}(\mathbf{r}'0) \rangle, & \tau > 0 \\ \langle S^{-}(\mathbf{r}'0) S^{+}(\mathbf{r}\tau) \rangle, & \tau < 0 \end{cases} . \tag{3.2.4}$$

The response function is not uniquely defined for equal times $t = t'$ due to the time-ordering operator, and the response function's limiting values $\tau \to 0^{\pm}$ from left and right differ. As a result, the response function has a step at equal times $\tau = 0$. The size of the step amounts to the magnetization of the system. The magnetization can be formally written in terms of the commutation relation of the spin-ladder operators. It can be constructed by means of the time-ordered magnetic response function

$$2\langle S_z(\mathbf{r}) \rangle = \mathrm{i} \int \mathrm{d}\mathbf{r}' \left(\lim_{\tau \to 0^{+}} R^{+-}(\mathbf{r}, \mathbf{r}'; \tau) - \lim_{\tau \to 0^{-}} R^{+-}(\mathbf{r}, \mathbf{r}'; \tau) \right) \delta(\mathbf{r} - \mathbf{r}'). \tag{3.2.5}$$

Also, the anti-commutation relation of the spin-ladder operator allows a physical interpretation. The anti-commutation relation of the spin-ladder operators yields the transverse spin fluctuations

$$2\langle [S_x^2 + S_y^2](\mathbf{r}) \rangle = \mathrm{i} \int \mathrm{d}\mathbf{r}' \left(\lim_{\tau \to 0^{+}} R^{+-}(\mathbf{r}, \mathbf{r}'; \tau) + \lim_{\tau \to 0^{-}} R^{+-}(\mathbf{r}, \mathbf{r}'; \tau) \right) \delta(\mathbf{r} - \mathbf{r}'). \tag{3.2.6}$$

The sum rule of the magnetization (3.2.5) and that of the transverse spin fluctuations (3.2.6) has been implemented by means of the magnetic response function.

For a treatment of the magnetic response function within MBPT the expression (3.2.2) together with Eq. (3.2.1) forms the starting point. The formalism has been introduced by Aryasetiawan and Karlsson [155], it relies on the Schwinger functional derivative technique [85]. Şaşıoğlu *et al.* [43] have implemented the formalism in an all-electron Wannier function formulation employing the *GW* approximation for the exchange and correlation self-energy. In this case, the magnetic response function obeys a Bethe-Salpeter equation that yields an infinite summation of ladder diagrams. The ladder diagrams are a special type of Feynman diagrams that describe the correlated motion of an electron-hole pair with opposite spins. The correlation among the electron-hole pairs is mediated by the screened Coulomb interac-

tion W that derives from the GW approximation. The spin excitations, i.e., the collective spin-wave excitations, the renormalized Stoner excitations, and combinations thereof, emerge from the correlated motion of the electron-hole pairs. The derivation of the magnetic response function within MBPT employing the GW approximation has been presented by Şaşıoğlu *et al.* [43] and in more general terms by Friedrich *et al.* [72]. For the sake of completeness, we give a brief summary of the derivation here. We abbreviate the space and time argument by its corresponding index, i.e., we write $1 = \mathbf{r}_1 t_1$.

The Green function is the solution of the Dyson equation [156]

$$G^{-1}_{\alpha\beta}(12) = G^{-1}_{0,\alpha\beta}(12) - \Sigma_{\alpha\beta}(12), \tag{3.2.7}$$

with the inverse non-interacting Green function

$$G^{-1}_{0,\alpha\beta}(12) = \left[-\mathrm{i}\frac{\partial}{\partial t_1} - \frac{1}{2}\nabla^2_{\mathbf{r}_1} - v_{\mathrm{ext}}(\mathbf{r}_1) - v_{\mathrm{H}}(\mathbf{r}_1)\right]\delta(12)\delta_{\alpha\beta} - \left[\sum_i \sigma^i_{\alpha\beta} B^i(1)\right]\delta(12), \tag{3.2.8}$$

and the exchange-correlation self-energy $\Sigma_{\alpha\beta}(12)$. The non-interacting Green function is the solution of the Hartree Hamiltonian that contains the kinetic energy, the external potential $v_{\mathrm{ext}}(\mathbf{r}_1)$, the Hartree potential $v_{\mathrm{H}}(\mathbf{r}_1)$, and the Zeeman term

$$\sum_i \sigma^i_{\alpha\beta} B^i(1) = \frac{1}{2}\left[\sigma^+_{\alpha\beta} B^-(1) + \sigma^-_{\alpha\beta} B^+(1)\right] + \sigma^z_{\alpha\beta} B^z(1), \tag{3.2.9}$$

which describes the coupling of the system to an external magnetic perturbation. We employ the GW approximation [71] for the exchange-correlation self-energy

$$\Sigma_{\alpha\beta}(12) = \mathrm{i} G_{\alpha\beta}(12) W(1^+2), \tag{3.2.10}$$

where

$$W(12) = v(12) + \int \mathrm{d}3\,\mathrm{d}4\, v(13) P(34) W(42) \tag{3.2.11}$$

is the screened interaction. The screening of the bare Coulomb interaction $v(12) = \delta(t_1 - t_2)/|\mathbf{r}_1 - \mathbf{r}_2|$ is described by the random-phase approximation (RPA) to the polarization function

$$P(12) = -\mathrm{i}\sum_{\alpha,\beta} G_{\alpha\beta}(12) G_{\beta\alpha}(21^+). \tag{3.2.12}$$

We note that a conserving implementation of the magnetic response function requires

that the Dyson equation (3.2.7) is solved self-consistently. To expand the magnetic response function (3.2.2) in terms of an effective interaction, the functional derivative of the Green function itself is needed. It is related to the functional derivative of the inverse Green function

$$\frac{\delta G_{\alpha\beta}(12)}{\delta B^i(3)} = -\sum_{\gamma,\delta}\int \mathrm{d}4\,\mathrm{d}5\, G_{\alpha\gamma}(14)\frac{\delta G^{-1}_{\gamma\delta}(45)}{\delta B^i(3)}G_{\delta\beta}(52), \tag{3.2.13}$$

which allows to employ the Dyson equation (3.2.7) for its evaluation. We restrict ourselves to collinear magnetic systems, i.e., the Green function is diagonal in spin space. The functional derivative of the inverse Green function contains two contributions

$$\frac{\delta G^{-1}_{\downarrow\uparrow}(12)}{\delta B^+(3)} = -\delta(13)\delta(12) - \frac{\delta\Sigma_{\downarrow\uparrow}(12)}{\delta B^+(3)}, \tag{3.2.14}$$

the first term on the right-hand side stems from the Zeeman term of the non-interacting Green function's equation of motion (3.2.8). The second term involves the functional derivative of the GW self-energy, it derives from the Dyson equation (3.2.7) itself. To sum up, the functional derivative of the inverse Green function (3.2.14) in combination with Eq. (3.2.13) yields the transverse magnetic response function

$$R^{+-}(12) = -2\mathrm{i}\left[G_\downarrow(12)G_\uparrow(21^+) + \int \mathrm{d}3\,\mathrm{d}4\, G_\downarrow(13)\frac{\delta\Sigma_{\downarrow\uparrow}(34)}{\delta B^+(2)}G_\uparrow(41^+)\right]. \tag{3.2.15}$$

In case of a collinear magnetic system, the functional derivative of the GW self-energy is

$$\frac{\delta\Sigma_{\downarrow\uparrow}(12)}{\delta B^+(3)} = \mathrm{i}W(1^+2)\left[G_\downarrow(13)G_\uparrow(32) + \int \mathrm{d}4\,\mathrm{d}5\, G_\downarrow(14)\frac{\delta\Sigma_{\downarrow\uparrow}(45)}{\delta B^+(3)}G_\uparrow(52)\right]. \tag{3.2.16}$$

Here, we have used that the spin indices of the Green function are either both up or both down, i.e., $G_{\alpha\alpha} = G_\alpha$. The successive reinsertion of $\delta\Sigma/\delta B$ on the right-hand side of Eq. (3.2.15) yields terms of ever increasing order leading to the Bethe-Salpeter equation of the magnetic response function. The generalization of the magnetic response function to an auxiliary four-point quantity has the advantage that the Bethe-Salpeter equation can be solved by matrix inversion. The auxiliary four-point quantity $R^{(4)}_{\alpha\alpha'}(12,34)$ is implicitly defined via

$$\frac{\delta\Sigma_{\downarrow\uparrow}(12)}{\delta B^+(3)} = W(1^+2)R^{(4)}_{\downarrow\uparrow}(12,33). \tag{3.2.17}$$

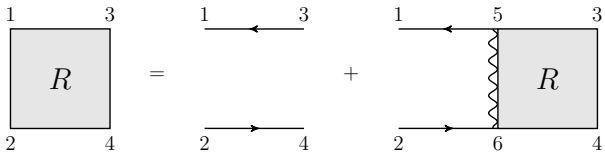

Figure 3.1: Feynman diagram of the magnetic response function in the ladder approximation. The wiggly line denotes the screened interaction in the random-phase approximation (RPA) and the single-particle Green function is denoted by an arrow.

In addition to that, we have to generalize the two-particle propagator to a four-point quantity

$$K_{\downarrow\uparrow}(12,34) = \mathrm{i}G_{\downarrow}(13)G_{\uparrow}(42). \tag{3.2.18}$$

The generalization of the magnetic response function to a four-point quantity turns the Bethe-Salpeter equation into a matrix equation

$$R^{(4)}_{\downarrow\uparrow}(12,34) = K_{\downarrow\uparrow}(12,34) + \int \mathrm{d}5\,\mathrm{d}6\, K_{\downarrow\uparrow}(12,56)W(5^{+}6)R^{(4)}_{\downarrow\uparrow}(56,34), \tag{3.2.19}$$

and its solution gives the magnetic response function in the ladder approximation, shown in Fig. 3.1. While the rungs of the ladder correspond to the screened interaction W, its rails describe the propagation of the electron-hole pairs with opposite spins. The physically meaningful magnetic response function, however, is the two-point magnetic response function. It is obtained by contraction of the auxiliary four-point magnetic response function

$$R^{+-}(12) = -2R^{(4)}_{\downarrow\uparrow}(11,22). \tag{3.2.20}$$

We have implemented the magnetic response function in the many-body perturbation theory. The details of the implementation are discussed in the next section.

3.3 Implementation

The implementation of the magnetic response function within many-body perturbation theory is realized in the SPEX code [72] and relies on the full-potential linearized augment-plane-wave (FLAPW) method. The starting point of a magnetic response function calculation is a mean-field solution provided by the FLEUR [92] code, which is a FLAPW implementation of the density-functional theory [18, 19]. The implementation of the magnetic response function makes use of the fact that the Hamil-

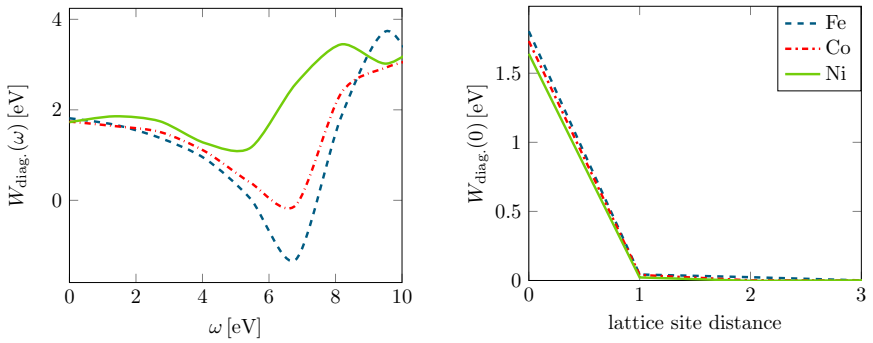

Figure 3.2: Average diagonal element of the screened interaction projected onto a lattice site **R** employing a basis of Wannier function consisting of s, p, and d orbitals for iron (blue dashed), cobalt (red dash-dotted), and nickel (green solid). The left and right panel show the frequency dependence of the screened interaction and the spatial dependence of the static screened interaction, respectively.

tonian is not explicitly time dependent. As a consequence, the magnetic response function $R^{(4)}$, see Fig. 3.1, depends on three independent time arguments. However, the calculation of the magnetic response function from the four-point function $R^{(4)}$ is still too complex. Since spin-wave excitations are low-energy excitations, it is reasonable to approximate the frequency dependent screened interaction W by its static limit, compare the frequency dependence of the screened interaction shown in the left panel of Fig. 3.2. The static approximation implies that the interaction is instantaneous in time, i.e., $W(12) = W(\mathbf{r}_1, \mathbf{r}_2)\delta(t_1 - t_2)$. With this approximation the magnetic response function depends only on a single time or frequency argument. After a Fourier transformation, Eq. (3.2.19) turns into the Bethe-Salpeter equation in the frequency domain

$$R^{(4)}_{\downarrow\uparrow}(\mathbf{r}_1, \mathbf{r}_2; \mathbf{r}_3, \mathbf{r}_4; \omega) = K_{\downarrow\uparrow}(\mathbf{r}_1, \mathbf{r}_2; \mathbf{r}_3, \mathbf{r}_4; \omega) + \int \mathrm{d}\mathbf{r}_5\, \mathrm{d}\mathbf{r}_6\, K_{\downarrow\uparrow}(\mathbf{r}_1, \mathbf{r}_2; \mathbf{r}_5, \mathbf{r}_6; \omega) W(\mathbf{r}_5, \mathbf{r}_6) R^{(4)}_{\downarrow\uparrow}(\mathbf{r}_5, \mathbf{r}_6; \mathbf{r}_3, \mathbf{r}_4; \omega). \quad (3.3.1)$$

Here, we have used that the two-particle propagator K depends only on the time difference $\tau = t - t'$ with $t = t_1 = t_2$ and $t' = t_3 = t_4$,

$$K_{\alpha\alpha'}(\mathbf{r}_1, \mathbf{r}_2; \mathbf{r}_3, \mathbf{r}_4; \tau) = \mathrm{i}\, G_\alpha(\mathbf{r}_1, \mathbf{r}_3; \tau)\, G_{\alpha'}(\mathbf{r}_4, \mathbf{r}_2; -\tau). \quad (3.3.2)$$

The Bethe-Salpeter equation (3.3.1) is still too complex for a numerical treatment as the interaction $W(\mathbf{r}, \mathbf{r}')$ is non-zero for all separations $\mathbf{r}$ and $\mathbf{r}'$. In metallic systems,

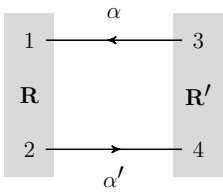

Figure 3.3: Feynman diagram of the non-interacting magnetic response function. The non-interacting magnetic response function describes the independent propagation of an electron-hole pair with opposite spins $\alpha \neq \alpha'$. The screened interaction within the on-site approximation restricts the points $\mathbf{r}_1$ and $\mathbf{r}_2$ as well as $\mathbf{r}_3$ and $\mathbf{r}_4$ to be at the same lattice site $\mathbf{R}$ and $\mathbf{R}'$, respectively. An electron is depicted by an arrow from right to left for $\tau > 0$.

however, screening is very effective so that the screened interaction is short-range. We utilize the short-range behavior of the screened interaction W and introduce an on-site approximation. The on-site approximation means that the electron-hole pairs interact with each other only if they are located at the same atomic site. Off-site contributions to the interaction are neglected. Especially in metallic systems the on-site approximation is a good approximation as the off-site contributions fall off sufficiently fast, compare the spatial dependence of the static screened interaction shown in the right panel of Fig. 3.2. The short-range behavior of the screened interaction W motivates a formulation in a basis of maximally localized Wannier functions [46, 47].

3.3.1 Formulation in a Wannier Basis

The formulation in the Wannier basis allows an efficient real-space truncation of the magnetic response function. The truncation is realized by projecting the magnetic response function onto maximally localized Wannier functions. They are defined as Fourier transforms of the single-particle wave functions that serve as starting point of the many-body perturbation theory calculation

$$w^{\alpha}_{\mathbf{R}n}(\mathbf{r}) = \frac{1}{N} \sum_{\mathbf{k}} e^{-\mathrm{i}\mathbf{k}\mathbf{R}} \sum_{m} U^{\alpha}_{\mathbf{k}m,n} \varphi^{\alpha}_{\mathbf{k}m}(\mathbf{r}), \tag{3.3.3}$$

where n labels the Wannier functions per atomic site $\mathbf{R}$, and N is the number of $\mathbf{k}$ points used in the calculation. Here, we restrict ourselves to crystals with a single atom in the unit cell. The Wannier functions are constructed from linear combinations of single-particle states. The Wannier functions are calculated with the method proposed by Marzari and Vanderbilt [46], which is implemented in the WANNIER90

code [47]. The Wannier functions are calculated such that the transformation matrix $U^{\alpha}_{\mathbf{k}m,n}$ minimizes their spread. The two-particle propagator, as product of two Green functions in the time domain (3.3.2), turns into a convolution in the frequency domain. With the Lehman representation of the Green function

$$G_{\alpha}(\mathbf{r},\mathbf{r}';\omega) = \frac{1}{N}\sum_{\mathbf{k}m}^{\text{all}} \frac{\varphi^{\alpha}_{\mathbf{k}m}(\mathbf{r})\varphi^{\alpha *}_{\mathbf{k}m}(\mathbf{r}')}{\omega - \epsilon^{\alpha}_{\mathbf{k}m} + \mathrm{i}\eta\mathrm{sgn}(\epsilon^{\alpha}_{\mathbf{k}m} - \epsilon_{\mathrm{F}})}, \tag{3.3.4}$$

where ϵ_{F} denotes the Fermi energy, the two-particle propagator evaluates to

$$\begin{aligned} K_{\alpha\alpha'}(\mathbf{r}_1,\mathbf{r}_2;\mathbf{r}_3,\mathbf{r}_4;\omega) = \frac{1}{N^2}\sum_{\mathbf{k}m}^{\text{occ.}}\sum_{\mathbf{k}'m'}^{\text{unocc.}} \Bigg(& \frac{\varphi^{\alpha}_{\mathbf{k}m}(\mathbf{r}_1)\varphi^{\alpha *}_{\mathbf{k}m}(\mathbf{r}_3)\varphi^{\alpha' *}_{\mathbf{k}'m'}(\mathbf{r}_2)\varphi^{\alpha'}_{\mathbf{k}'m'}(\mathbf{r}_4)}{\omega + \epsilon^{\alpha'}_{\mathbf{k}'m'} - \epsilon^{\alpha}_{\mathbf{k}m} - \mathrm{i}\eta} \\ & - \frac{\varphi^{\alpha}_{\mathbf{k}'m'}(\mathbf{r}_1)\varphi^{\alpha *}_{\mathbf{k}'m'}(\mathbf{r}_3)\varphi^{\alpha' *}_{\mathbf{k}m}(\mathbf{r}_2)\varphi^{\alpha'}_{\mathbf{k}m}(\mathbf{r}_4)}{\omega + \epsilon^{\alpha'}_{\mathbf{k}m} - \epsilon^{\alpha}_{\mathbf{k}'m'} + \mathrm{i}\eta} \Bigg) \end{aligned} \tag{3.3.5}$$

in the frequency domain. The on-site approximation to the screened interaction restricts the points $\mathbf{r}_1$ and $\mathbf{r}_2$ as well as $\mathbf{r}_3$ and $\mathbf{r}_4$ to be at the same lattice site, say $\mathbf{R}$ and $\mathbf{R}'$, see Fig 3.3. The two-particle propagator projected onto the maximally localized Wannier functions

$$\begin{aligned} K^{\alpha\alpha'}_{\mathbf{R}n_1\mathbf{R}n_2,\mathbf{R}'n_3\mathbf{R}'n_4}(\omega) = \frac{1}{N^2}\sum_{\mathbf{k}m}^{\text{occ.}}\sum_{\mathbf{k}'m'}^{\text{unocc.}} \Bigg(& \frac{U^{\alpha *}_{\mathbf{k}m,n_1}U^{\alpha}_{\mathbf{k}m,n_3}U^{\alpha'}_{\mathbf{k}'m',n_2}U^{\alpha' *}_{\mathbf{k}'m',n_4}}{\omega + \epsilon^{\alpha'}_{\mathbf{k}'m'} - \epsilon^{\alpha}_{\mathbf{k}m} - \mathrm{i}\eta} e^{\mathrm{i}(\mathbf{k}-\mathbf{k}')(\mathbf{R}-\mathbf{R}')} \\ & - \frac{U^{\alpha *}_{\mathbf{k}'m',n_1}U^{\alpha}_{\mathbf{k}'m',n_3}U^{\alpha'}_{\mathbf{k}m,n_2}U^{\alpha' *}_{\mathbf{k}m,n_4}}{\omega + \epsilon^{\alpha'}_{\mathbf{k}m} - \epsilon^{\alpha}_{\mathbf{k}'m'} + \mathrm{i}\eta} e^{-\mathrm{i}(\mathbf{k}-\mathbf{k}')(\mathbf{R}-\mathbf{R}')} \Bigg) \end{aligned} \tag{3.3.6}$$

depends only on the lattice site difference $\Delta\mathbf{R} = \mathbf{R} - \mathbf{R}'$. This allows to apply a (lattice) Fourier transformation into the Bloch momentum space

$$\begin{aligned} K^{\alpha\alpha'}_{n_1n_2,n_3n_4}(\mathbf{q},\omega) &= \sum_{\mathbf{R}\mathbf{R}'} e^{-\mathrm{i}\mathbf{q}(\mathbf{R}-\mathbf{R}')} K^{\alpha\alpha'}_{\mathbf{R}n_1\mathbf{R}n_2,\mathbf{R}'n_3\mathbf{R}'n_4}(\omega) \\ &= \frac{1}{N}\sum_{\mathbf{k}}\sum_{m}^{\text{occ.}}\sum_{m'}^{\text{unocc.}} \Bigg(\frac{U^{\alpha *}_{\mathbf{q}+\mathbf{k}m,n_1}U^{\alpha}_{\mathbf{q}+\mathbf{k}m,n_3}U^{\alpha'}_{\mathbf{k}m',n_2}U^{\alpha' *}_{\mathbf{k}m',n_4}}{\omega + \epsilon^{\alpha'}_{\mathbf{k}m'} - \epsilon^{\alpha}_{\mathbf{q}+\mathbf{k}m} - \mathrm{i}\eta} \\ & \qquad - \frac{U^{\alpha *}_{\mathbf{q}+\mathbf{k}m',n_1}U^{\alpha}_{\mathbf{q}+\mathbf{k}m',n_3}U^{\alpha'}_{\mathbf{k}m,n_2}U^{\alpha' *}_{\mathbf{k}m,n_4}}{\omega + \epsilon^{\alpha'}_{\mathbf{k}m} - \epsilon^{\alpha}_{\mathbf{q}+\mathbf{k}m'} + \mathrm{i}\eta} \Bigg). \end{aligned} \tag{3.3.7}$$

For the Brillouin zone integration we employ the tetrahedron method [157]. Unlike the two-particle propagator, the screened interaction $W(\mathbf{r},\mathbf{r}')$ is a two-point function.

Its representation in the Wannier product basis reads

$$W^{\alpha\alpha'}_{\mathbf{R}n_1\mathbf{R}n_2,\mathbf{R}n_3\mathbf{R}n_4} = \frac{N}{\mathcal{N}} \int \mathrm{d}\mathbf{r}\, \mathrm{d}\mathbf{r}'\, w^{\alpha *}_{\mathbf{R}n_1}(\mathbf{r}) w^{\alpha}_{\mathbf{R}n_3}(\mathbf{r}) W(\mathbf{r},\mathbf{r}') w^{\alpha'}_{\mathbf{R}n_2}(\mathbf{r}') w^{\alpha' *}_{\mathbf{R}n_4}(\mathbf{r}'). \tag{3.3.8}$$

As the screened interaction $W(\mathbf{r},\mathbf{r}')$ is non-zero for all separations $\mathbf{r}$ and $\mathbf{r}'$ the integrals run over the whole space. While the single-particle wave functions are normalized to the unit cell, the Wannier functions are normalized to the supercell. To avoid double counting the integral is normalized by the normalization factor $\mathcal{N}/N$ which accounts for the (infinite) number of supercells taken into account, where $\mathcal{N}$ counts the (infinite) number of unit cells. The spin-dependence of the interaction matrix is inherited from the spin-dependence of the Wannier functions, while the interaction itself is independent of the spin. With the definition of the Wannier functions the screened interaction reads

$$\begin{aligned} W^{\alpha\alpha'}_{\mathbf{R}n_1\mathbf{R}n_2,\mathbf{R}n_3\mathbf{R}n_4} = \frac{1}{N^3} \sum_{\mathbf{k},\mathbf{k}',\mathbf{k}''} \sum_{m_1,m_2,m_3,m_4} & U^{\alpha *}_{\mathbf{k}+\mathbf{k}'m_1,n_1} U^{\alpha}_{\mathbf{k}m_3,n_3} U^{\alpha'}_{\mathbf{k}'+\mathbf{k}''m_2,n_2} U^{\alpha' *}_{\mathbf{k}'m_4,n_4} \\ \times \frac{1}{\mathcal{N}} \int \mathrm{d}\mathbf{r}\, \mathrm{d}\mathbf{r}'\, & \varphi^{\alpha *}_{\mathbf{k}+\mathbf{k}''m_1}(\mathbf{r}) \varphi^{\alpha}_{\mathbf{k}m_3}(\mathbf{r}) W(\mathbf{r},\mathbf{r}') \varphi^{\alpha'}_{\mathbf{k}'+\mathbf{k}''m_2}(\mathbf{r}') \varphi^{\alpha' *}_{\mathbf{k}'m_4}(\mathbf{r}'), \end{aligned} \tag{3.3.9}$$

Here, we have used that the screened interaction depends only on the separation $\mathbf{r}-\mathbf{r}'$. The screened interaction is independent of the atomic site $\mathbf{R}$ so that we write $W^{\alpha\alpha'}_{\mathbf{R}n_1\mathbf{R}n_2,\mathbf{R}n_3\mathbf{R}n_4} = W^{\alpha\alpha'}_{n_1n_2,n_3n_4}$.

With the two-particle propagator K and the screened interaction W projected onto the Wannier basis, we are prepared to solve the Bethe-Salpeter equation (3.3.1) for the auxiliary four-point magnetic response function

$$\begin{aligned} R^{(4)\alpha\alpha'}_{\mathbf{R}n_1\mathbf{R}n_2,\mathbf{R}'n_3\mathbf{R}'n_4}(\omega) = K^{\alpha\alpha'}_{\mathbf{R}n_1\mathbf{R}n_2,\mathbf{R}'n_3\mathbf{R}'n_4}(\omega) + \sum_{\mathbf{R}''} \sum_{n_5,n_6,n_7,n_8} & K^{\alpha\alpha'}_{\mathbf{R}n_1\mathbf{R}n_2,\mathbf{R}''n_5\mathbf{R}''n_6}(\omega) \\ \times W^{\alpha\alpha'}_{n_5n_6,n_7n_8} & R^{(4)\alpha\alpha'}_{\mathbf{R}''n_7\mathbf{R}''n_8,\mathbf{R}'n_3\mathbf{R}'n_4}(\omega). \end{aligned} \tag{3.3.10}$$

Just as the two-particle propagator K discussed above, the four-point magnetic response function depends only on the difference $\Delta\mathbf{R} = \mathbf{R}-\mathbf{R}'$. This allows to apply a (inverse) lattice Fourier transformation yielding the Bethe-Salpeter equation

$$\begin{aligned} R^{(4)\alpha\alpha'}_{n_1n_2,n_3n_4}(\mathbf{q},\omega) = K^{\alpha\alpha'}_{n_1n_2,n_3n_4}(\mathbf{q},\omega) + \sum_{n_5,n_6,n_7,n_8} & K^{\alpha\alpha'}_{n_1n_2,n_5n_6}(\mathbf{q},\omega) \\ \times W^{\alpha\alpha'}_{n_5n_6,n_7n_8} & R^{(4)\alpha\alpha'}_{n_7n_8,n_3n_4}(\mathbf{q},\omega). \end{aligned} \tag{3.3.11}$$

This is a matrix equation in pairs of Wannier indices which can be solved for the four-point response matrix by inversion, i.e., schematically

$$R^{(4)} = (1 - KW)^{-1}K. \tag{3.3.12}$$

The physically relevant two-point magnetic response function $R^{+-}(\mathbf{r}, \mathbf{r}'; \omega)$ is generated from the four-point function by the contraction

$$\begin{aligned} R^{+-}(\mathbf{r}, \mathbf{r}'; \omega) &= -2R^{(4)}_{\downarrow\uparrow}(\mathbf{r}, \mathbf{r}; \mathbf{r}', \mathbf{r}'; \omega) \\ &= -2 \sum_{\mathbf{R},\mathbf{R}'} \sum_{n_1,n_2,n_3,n_4} R^{(4)\downarrow\uparrow}_{\mathbf{R}n_1\mathbf{R}n_2,\mathbf{R}'n_3\mathbf{R}'n_4}(\omega)\Omega^{\downarrow\uparrow}_{\mathbf{R}n_1n_2}(\mathbf{r})\Omega^{\downarrow\uparrow *}_{\mathbf{R}'n_3n_4}(\mathbf{r}'), \end{aligned} \tag{3.3.13}$$

with the products of Wannier functions

$$\Omega^{\downarrow\uparrow}_{\mathbf{R}n_1n_2}(\mathbf{r}) = w^{\downarrow}_{\mathbf{R}n_1}(\mathbf{r})w^{\uparrow *}_{\mathbf{R}n_2}(\mathbf{r}). \tag{3.3.14}$$

The lattice Fourier transform

$$\Omega^{\downarrow\uparrow}_{\mathbf{q}n_1n_2}(\mathbf{r}) = \frac{1}{\sqrt{N}} \sum_{\mathbf{R}} e^{i\mathbf{q}\mathbf{R}}\Omega^{\downarrow\uparrow}_{\mathbf{R}n_1n_2}(\mathbf{r}) \tag{3.3.15}$$

allows to evaluate the contraction of the four-point magnetic response function by means of the solution to Eq. (3.3.11)

$$R^{+-}(\mathbf{r}, \mathbf{r}'; \omega) = -2 \sum_{\mathbf{q}} \sum_{n_1,n_2,n_3,n_4} R^{(4)\downarrow\uparrow}_{n_1n_2,n_3n_4}(\mathbf{q}, \omega)\Omega^{\downarrow\uparrow}_{\mathbf{q}n_1n_2}(\mathbf{r})\Omega^{\downarrow\uparrow *}_{\mathbf{q}n_3n_4}(\mathbf{r}'). \tag{3.3.16}$$

For a comparison with the spectrum measured in neutron scattering experiments, the imaginary part of the two-point magnetic response function is projected onto the plane wave $e^{i\mathbf{q}\mathbf{r}}$ from both sides, which gives the function $\mathrm{Im}R^{+-}(\mathbf{q}, \omega)$. In this function, well defined spin-wave excitations manifest themselves as sharp δ-like peaks. The spin-wave dispersion relation is obtained by plotting the energy values ω of these peaks against $\mathbf{q}$.

3.3.2 Sum Rules

The magnetic moment (3.2.5) and the transverse spin fluctuation (3.2.6) are both accessible by means of the magnetic response function. We calculate these sum rules by projecting the magnetic response function onto a constant function $|1\rangle_{\mathbf{R}}$ at lattice

site **R**. For this, we use the projection

$$\chi^{\downarrow\uparrow}_{\mathbf{R}}(\omega) = \sum_{n_1,n_2,n_3,n_4} {}_{\mathbf{R}}\langle 1|\Omega^{\downarrow\uparrow}_{\mathbf{R}n_1n_2}\rangle\langle\tilde{\Omega}^{\downarrow\uparrow}_{\mathbf{R}n_1n_2}|R^{+-}(\omega)|\tilde{\Omega}^{\downarrow\uparrow}_{\mathbf{R}n_3n_4}\rangle\langle\Omega^{\downarrow\uparrow}_{\mathbf{R}n_3n_4}|1\rangle_{\mathbf{R}}, \tag{3.3.17}$$

with the Wannier product functions $\Omega^{\downarrow\uparrow}_{\mathbf{R}n_1n_2}(\mathbf{r})$ defined in Eq. (3.3.14) and the biorthogonal functions $\tilde{\Omega}^{\downarrow\uparrow}_{\mathbf{R}n_1n_2}(\mathbf{r})$ defined such that the projector

$$\sum_{n_1,n_2} |\tilde{\Omega}^{\downarrow\uparrow}_{\mathbf{R}n_1n_2}\rangle\langle\Omega^{\downarrow\uparrow}_{\mathbf{R}n_1n_2}| = |1\rangle_{\mathbf{R}}\,{}_{\mathbf{R}}\langle 1| \tag{3.3.18}$$

is an identity at lattice site **R**, while it is zero at all other sites. The four-point magnetic response function that appears in Eq. (3.3.17) is accessible via the matrix inversion of the Bethe-Salpeter equation (3.3.11). The physically relevant two-point magnetic response function is related to its four-point generalization by the contraction (3.3.16). Its projection reads

$$\chi^{\downarrow\uparrow}_{\mathbf{R}}(\omega) = -\frac{2}{N}\sum_{\mathbf{q}}\sum_{n_1,n_2,n_3,n_4} {}_{\mathbf{R}}\langle 1|\Omega^{\downarrow\uparrow}_{\mathbf{R}n_1n_2}\rangle R^{(4)\downarrow\uparrow}_{n_1n_2,n_3n_4}(\mathbf{q},\omega)\langle\Omega^{\downarrow\uparrow}_{\mathbf{R}n_3n_4}|1\rangle_{\mathbf{R}}, \tag{3.3.19}$$

where we have used that, e.g., the projection from the right is given by

$$\sum_{n_1n_2}\langle\Omega^{\downarrow\uparrow}_{\mathbf{q}n_3n_4}|\tilde{\Omega}^{\downarrow\uparrow}_{\mathbf{R}n_1n_2}\rangle\langle\Omega^{\downarrow\uparrow}_{\mathbf{R}n_1n_2}|1\rangle_{\mathbf{R}} = \frac{1}{\sqrt{N}}e^{-i\mathbf{q}\mathbf{R}}\langle\Omega^{\downarrow\uparrow}_{\mathbf{R}n_3n_4}|1\rangle_{\mathbf{R}}. \tag{3.3.20}$$

The projection onto a constant function at lattice site **R** corresponds to the overlap of two Wannier orbitals that can be related to the spin off-diagonal overlap matrix of the Bloch wave functions by the definition of the Wannier functions (3.3.3)

$${}_{\mathbf{R}}\langle 1|\Omega^{\downarrow\uparrow}_{\mathbf{R},n_1n_2}\rangle = \langle w^{\uparrow}_{\mathbf{R}n_2}|w^{\downarrow}_{\mathbf{R}n_1}\rangle = \frac{1}{N}\sum_{\mathbf{k}}\sum_{m,m'} U^{\uparrow *}_{\mathbf{k}m',n_2}\langle\varphi^{\uparrow}_{\mathbf{k}m'}|\varphi^{\downarrow}_{\mathbf{k}m}\rangle U^{\downarrow}_{\mathbf{k}m,n_1}. \tag{3.3.21}$$

The spin off-diagonal overlap matrix of the wave functions $\langle\varphi^{\uparrow}_{\mathbf{k}m'}|\varphi^{\downarrow}_{\mathbf{k}m}\rangle$ is constructed by means of the FLAPW approach. With the definition (2.3.3) the overlap of two Bloch functions separates into the overlap in the muffin-tin (MT) spheres and the overlap in the interstitial region (IR)

$$\langle\varphi^{\uparrow}_{\mathbf{k}n}|\varphi^{\downarrow}_{\mathbf{k}n'}\rangle = \int \mathrm{d}\mathbf{r}\left[\sum_{u,u'}\left(\kappa^{\uparrow *}_{\mathbf{k}n,u}A^{\uparrow *}_{\mathbf{k},u}(\mathbf{r})A^{\downarrow}_{\mathbf{k},u'}(\mathbf{r})\kappa^{\downarrow}_{\mathbf{k}n',u'}\right) + \sum_{\mathbf{G},\mathbf{G}'}\left(\beta^{\uparrow *}_{\mathbf{k}n,\mathbf{G}}P^{\uparrow *}_{\mathbf{k},\mathbf{G}}(\mathbf{r})P^{\downarrow}_{\mathbf{k},\mathbf{G}'}(\mathbf{r})\beta^{\downarrow}_{\mathbf{k}n',\mathbf{G}'}\right)\right]. \tag{3.3.22}$$

The second term on the right-hand side of this equation is the integration of the interstitial region. If the integration of the interstitial region is extended to the whole space, this gives rise to a Kronecker $\delta_{\mathbf{G},\mathbf{G}'}$ coming from the orthogonality of the plane waves. The remainder, the integration of the plane waves in the muffin-tin sphere, can be evaluated using the Rayleigh expansion

$$e^{\mathrm{i}\mathbf{G}\mathbf{r}} = 4\pi \sum_{l,m} \mathrm{i}^l j_l(|\mathbf{G}||\mathbf{r}|) Y^*_{lm}(\hat{\mathbf{G}}) Y_{lm}(\hat{\mathbf{r}}), \tag{3.3.23}$$

where $j_l(z)$ denote the spherical Bessel functions and $Y_{lm}(\widehat{\mathbf{G}})$ describe the spherical harmonics. The angular integration of the spherical harmonics

$$\int \mathrm{d}\hat{\mathbf{r}}\, Y_{lm}(\hat{\mathbf{r}}) = \sqrt{4\pi}\, \delta_{l,0}\delta_{m,0} \tag{3.3.24}$$

gives a contribution only for $l = m = 0$. Therefore, the overlap of the plane waves in the interstitial region is given by

$$\frac{1}{V}\int_{\mathrm{IR}} \mathrm{d}\mathbf{r} \sum_{\mathbf{G},\mathbf{G}'} \beta^{\uparrow *}_{\mathbf{k}n,\mathbf{G}} \beta^{\downarrow}_{\mathbf{k}n',\mathbf{G}'} e^{\mathrm{i}(\mathbf{G}-\mathbf{G}')\mathbf{r}} = \sum_{\mathbf{G},\mathbf{G}'} \beta^{\uparrow *}_{\mathbf{k}n,\mathbf{G}} \left(\delta_{\mathbf{G},\mathbf{G}'} - 4\pi \int_{\mathrm{MT}} \mathrm{d}r\, j_0(|\mathbf{G}-\mathbf{G}'|r) \right) \beta^{\downarrow}_{\mathbf{k}n',\mathbf{G}'}. \tag{3.3.25}$$

The contribution of the muffin-tin spheres is calculated by making use of the orthogonality of the spherical harmonics

$$\int \mathrm{d}\hat{\mathbf{r}}\, Y^*_{lm}(\hat{\mathbf{r}})\, Y_{l'm'}(\hat{\mathbf{r}}) = \delta_{l,l'}\delta_{m,m'}, \tag{3.3.26}$$

which reduces the problem to calculating the radial integration of the atomic orbitals

$$\int \mathrm{d}\mathbf{r} \sum_{u,u'} \left(\kappa^{\uparrow *}_{\mathbf{k}n,u} A^{\uparrow *}_{\mathbf{k},u}(\mathbf{r}) A^{\downarrow}_{\mathbf{k},u'}(\mathbf{r}) \kappa^{\downarrow}_{\mathbf{k}n',u'} \right) = \frac{1}{N} \sum_{a,l,m,p,p'} \left[\kappa^{\uparrow *}_{\mathbf{k}n,alpm} \left(\int \mathrm{d}r\, \phi^{\uparrow *}_{alp}(r) \phi^{\downarrow}_{alp'}(r) \right) \kappa^{\downarrow}_{\mathbf{k}n',alp'm} \right], \tag{3.3.27}$$

where we have used that the orbitals overlap only if they are located at the same atom, which gives rise to an additional Kronecker $\delta_{a,a'}$. To sum up, the projector (3.3.21) is calculated by means of the overlap of the FLAPW Bloch functions (3.3.22) with the contribution of the muffin-tin spheres (3.3.27) and the interstitial region (3.3.25). This allows to calculate the sum rules of the magnetic response function

in terms of its projection onto a lattice site.

The magnetic moment projected onto a lattice site

$$m_{\mathbf{R}} = \sum_{n_1,n_2,n_3,n_4} {}_{\mathbf{R}}\langle 1|\Omega^{\downarrow\uparrow}_{\mathbf{R}n_1n_2}\rangle\langle\tilde{\Omega}^{\downarrow\uparrow}_{\mathbf{R}n_1n_2}|m|\tilde{\Omega}^{\downarrow\uparrow}_{\mathbf{R}n_3n_4}\rangle\langle\Omega^{\downarrow\uparrow}_{\mathbf{R}n_3n_4}|1\rangle_{\mathbf{R}}, \tag{3.3.28}$$

can be calculated from the projection of the magnetic response function (3.3.19). To this end, the commutation relation of the spin-ladder operators that equals the magnetic moment operator is constructed by means of the magnetic response function (3.2.5). The magnetic response function has to be Fourier transformed to the time domain such that the spin-ladder operators obey the correct time-ordering, i.e.,

$$m_{\mathbf{R}} = \frac{\mathrm{i}}{2\pi}\left(\lim_{\tau\to 0^+}\int_{-\infty}^{\infty}\mathrm{d}\omega\, e^{-\mathrm{i}\omega\tau}\chi^{\downarrow\uparrow}_{\mathbf{R}}(\omega) - \lim_{\tau\to 0^-}\int_{-\infty}^{\infty}\mathrm{d}\omega\, e^{-\mathrm{i}\omega\tau}\chi^{\downarrow\uparrow}_{\mathbf{R}}(\omega)\right). \tag{3.3.29}$$

The Fourier transformations are performed by means of a contour integration. For this, we use a Padé approximation to the magnetic response function. This allows to represent the magnetic response function as a sum of effective poles so that the integration can be performed analytically. The exponential factors $e^{-\mathrm{i}\omega\tau}$ together with the limit $\tau \to 0^{\pm}$ ensure that the arcs that close the contour integration paths do not contribute to the integral. In particular, the contour is closed in the lower half plane for $\tau \to 0^+$, and for $\tau \to 0^-$ the contour is closed in the upper half plane. The details of the frequency integration employing a Padé approximation are described in Appendix A.

The Lehman representation of the non-interacting magnetic response function (3.3.7) allows the magnetic-moment sum rule to be expressed explicitly. In this case, the magnetic moment projected onto a lattice site $\mathbf{R}$ reads

$$m_{\mathbf{R}} = \frac{2}{N}\sum_{\mathbf{k}m}^{\mathrm{occ.}}\sum_{n_1,n_2,n_3,n_4} {}_{\mathbf{R}}\langle 1|\Omega^{\uparrow\downarrow}_{\mathbf{R}n_1,n_2}\rangle\left[U^{\uparrow *}_{\mathbf{k}m,n_1}U^{\uparrow}_{\mathbf{k}m,n_3}\delta_{n_2,n_4} - U^{\downarrow}_{\mathbf{k}m,n_2}U^{\downarrow *}_{\mathbf{k}m,n_4}\delta_{n_1,n_3}\right] \times \langle\Omega^{\uparrow\downarrow}_{\mathbf{R}n_3,n_4}|1\rangle_{\mathbf{R}}. \tag{3.3.30}$$

Its value equals that of the magnetic moment obtained from the (renormalized) magnetic response function. This means the renormalization does not change the value of the magnetic moment. The reason is that the spectral weight of the magnetic response function does not change by the renormalization. As a consequence, the magnetic moment which equals the integrated spectral weight does not change, too. The calculated magnetic moments projected onto a lattice site by means of the non-

		non-interacting	renormalized
$m_{\mathbf{R}}\,[\mu_{\mathrm{B}}]$	Fe	2.19	2.19
	Co	1.60	1.60
	Ni	0.58	0.58
$2\langle S_{\mathrm{x}}^2 + S_{\mathrm{y}}^2\rangle_{\mathbf{R}}\,[\mu_{\mathrm{B}}^2]$	Fe	1.93	2.56
	Co	1.62	1.87
	Ni	1.20	1.35

Table 3.1: Magnetic moment and transverse spin fluctuations obtained from the sum rules (3.3.29) and (3.3.31) using the non-interacting and renormalized magnetic response function for the elementary ferromagnets. A local-spin-density approximation calculation using the parameterization of the exchange-correlation potential by Perdew and Zunger [90] served as starting point. The magnetic moments obtained within the muffin-tin spheres are $m_{\mathrm{Fe}} = 2.20\,\mu_{\mathrm{B}}$, $m_{\mathrm{Co}} = 1.62\,\mu_{\mathrm{B}}$, and $m_{\mathrm{Ni}} = 0.59\,\mu_{\mathrm{B}}$ for iron, cobalt, and nickel, respectively.

interacting and renormalized magnetic response function are summarized in Table 3.1. The magnetic moments are in accordance with the values obtained from the underlying Kohn-Sham system within the muffin-tin spheres. Minor differences among the magnetic moments can be attributed to the difference within the integration regions defined by the projection onto a lattice site in terms of the maximally localized Wannier functions and the muffin-tin spheres used in the density-functional theory calculation. In contrast to the magnetic moment, the spin fluctuation projected onto a lattice site $\mathbf{R}$

$$2\langle S_x^2 + S_y^2\rangle_{\mathbf{R}} = \frac{\mathrm{i}}{2\pi}\left(\lim_{\tau\to 0^+}\int_{-\infty}^{\infty}\mathrm{d}\omega\, e^{-\mathrm{i}\omega\tau}\chi_{\mathbf{R}}^{\downarrow\uparrow}(\omega) + \lim_{\tau\to 0^-}\int_{-\infty}^{\infty}\mathrm{d}\omega\, e^{-\mathrm{i}\omega\tau}\chi_{\mathbf{R}}^{\downarrow\uparrow}(\omega)\right) \tag{3.3.31}$$

does change due to the renormalization of the magnetic response function. The reason is that the transverse spin fluctuation depends on the distribution of the spectral weight, which undergoes a change due to the renormalization, cf. Table 3.1. In particular, the renormalization leads to an increase of the transverse spin fluctuations in the elementary ferromagnets.

3.4 Formal Discussion of the Goldstone-Mode Condition

In a ferromagnetic material without spin-orbit coupling the Goldstone-mode condition relates the magnetization of a material to its spin excitation spectrum. In the ferromagnetically ordered state the Goldstone mode is a consequence of the spontaneously broken spin-rotation symmetry. The spin-rotation symmetry is spon-

taneously broken because the spin polarization of the ferromagnetic ground state destroys the spin-rotational symmetry, while the many-body Hamiltonian is spin-rotationally invariant. According to the Goldstone theorem each spontaneously broken symmetry creates a long-range correlation which restores the broken symmetry. In the case of the ferromagnetic order the spin-rotational symmetry is restored by the magnons in the long-wavelength limit. These magnons lead to a homogeneous rotation of the spin system without a cost of energy. In other words, a homogeneous magnetic **B** field that acts as perturbation perpendicular to the spin polarization axis causes a collective rotation of all the spins towards the field direction. Without spin-orbit coupling the collective rotation can take place without a cost of energy, i.e., the spin-wave excitation energy vanishes in the limit $\mathbf{q} \to 0$. In practical *ab initio* calculations the Goldstone-mode condition is often violated. We investigate the Goldstone violation within the many-body perturbation theory.

In the following discussion we focus on the details of the spontaneous breaking of the spin-rotational symmetry and its relation to the Goldstone mode. In particular, we discuss the existence of the Goldstone mode in the view of the magnetic response function. As was shown for example by Kotani *et al.* [45] the magnetization is an eigenfunction of the inverse magnetic response function of the interacting system with eigenvalue zero. The time evolution of the time-ordered magnetic response function (3.2.4) is

$$\begin{aligned}\partial_\tau R^{+-}(\mathbf{r},\mathbf{r}';\tau) &= -\mathrm{i}\partial_\tau \langle \mathcal{T} S^+(\mathbf{r}\tau) S^-(\mathbf{r}'0)\rangle \\ &= \langle \mathcal{T}[H, S^+(\mathbf{r}\tau)] S^-(\mathbf{r}'0)\rangle - \mathrm{i}\langle [S^+(\mathbf{r}\tau), S^-(\mathbf{r}'0)]\rangle \delta(\tau), \quad (3.4.1)\end{aligned}$$

where $\tau = t - t'$ is the time difference between the action of the spin-raising and the spin-lowering operator. The spin operators obey the commutation relation

$$[S^i(\mathbf{r}t), S^j(\mathbf{r}'t')] = \mathrm{i}\sum_k \epsilon_{ijk} S^k(\mathbf{r}t)\delta(\mathbf{r}-\mathbf{r}')\delta(t-t'), \quad (3.4.2)$$

with the Levi-Civita symbol ϵ_{ijk} and $i, j, k \in \{\mathrm{x}, \mathrm{y}, \mathrm{z}\}$. The many-body Hamiltonian

$$H = H_0 + S^{\mathrm{z}} B(\mathbf{r}) \quad (3.4.3)$$

contains a Zeeman term that couples the spin space to the real space. With this, the

first term on the right-hand side of Eq. (3.4.1) evaluates to

$$\left\langle \mathcal{T}[H, S^+(\mathbf{r}\tau)]S^-(\mathbf{r}'0)\right\rangle = \left\langle \mathcal{T}S^+(\mathbf{r}\tau)S^-(\mathbf{r}'0)\right\rangle B(\mathbf{r}), \tag{3.4.4}$$

where the commutation relation of the spin-raising operator has been used. Similarly, the second term on the right-hand side of Eq. (3.4.1) is given by

$$\langle [S^+(\mathbf{r}\tau), S^-(\mathbf{r}'0)]\rangle \delta(\tau) = 2\langle S^z(\mathbf{r}\tau)\rangle \delta(\mathbf{r}-\mathbf{r}')\delta(\tau). \tag{3.4.5}$$

A Fourier transformation as well as a spatial integration of Eq. (3.4.1) yields a relation between the magnetic response function and the magnetization

$$-\omega \int \mathrm{d}\mathbf{r}'\, R^{+-}(\mathbf{r}, \mathbf{r}'; \omega) = \int \mathrm{d}\mathbf{r}'\, B(\mathbf{r})\, R^{+-}(\mathbf{r}, \mathbf{r}'; \omega) - m(\mathbf{r}). \tag{3.4.6}$$

This relation is satisfied for all values of ω. For the Goldstone-mode condition the limit $\omega \to 0$ is of special interest. The relation (3.4.6) allows to deduce the existence of the magnon as a gapless excitation in this limit. In the ferromagnetic order an infinitesimal magnetic perturbation fixes the spin-polarization axis of an interacting electron system. In the limit of $B(\mathbf{r}) \to 0$, the first term on the right-hand side of that relation vanishes. As a consequence, the response function $R^{+-}(\mathbf{r}, \mathbf{r}'; \omega)$ must contain a pole at zero frequency such that

$$m(\mathbf{r}) = \lim_{\omega \to 0} \omega \int \mathrm{d}\mathbf{r}'\, R^{+-}(\mathbf{r}, \mathbf{r}'; \omega). \tag{3.4.7}$$

The pole at zero frequency corresponds to the gapless magnon excitation. Therefore, the Eq. (3.4.7) is called the Goldstone-mode condition for the (interacting) magnetic response function. The Goldstone-mode condition implies that the magnetization is an eigenfunction of the inverse magnetic response function with eigenvalue zero.

For the derivation of Eq. (3.4.7) the limit $B(\mathbf{r}) \to 0$ has been taken first. If the magnetic field is finite, the magnetic response function does not contain a magnon pole in the limit $\omega \to 0$. As a consequence, the left-hand side of equation (3.4.6) cancels in the limit $\omega \to 0$ and the relation reduces to

$$m(\mathbf{r}) = \int \mathrm{d}\mathbf{r}'\, B(\mathbf{r})\, R^{+-}(\mathbf{r}, \mathbf{r}'; 0). \tag{3.4.8}$$

This relation states that the value of the magnetization depends on the size of the applied magnetic $B(\mathbf{r})$ field. In this case, the magnetic response function R^{+-} might be

considered as that of a mean-field system. An example is the spin-polarized Kohn-Sham system. In the Kohn-Sham system the spin-dependent exchange-correlation potential acts as an effective $B(\mathbf{r})$ field which drives the non-interacting system into its spin-polarized state, cf. Section 3.4.2. As a consequence, the non-interacting magnetic response function of a spin-polarized Kohn-Sham system does not contain a magnon pole. It turns out that the non-interacting magnetic response function of the Kohn-Sham system must obey a relation of the same form as Eq. (3.4.8) as a requirement for the renormalized response function to fulfill the Goldstone condition (3.4.7). Therefore, for the Goldstone-mode condition to be fulfilled Eqs. (3.4.8) and (3.4.7) have to be fulfilled simultaneously. As examples, we discuss the one-band Hubbard model, the Kohn-Sham system, and the Coulomb hole and screened exchange (COHSEX) mean-field system in the Sections 3.4.1 to 3.4.3.

3.4.1 One-Band Hubbard Model

The one-band Hubbard model is capable to describe itinerant ferromagnetic systems, and it allows to study the Goldstone condition in detail [148, 149]. The Hubbard Hamiltonian [17]

$$H = \sum_{\mathbf{R},\mathbf{R}'} \sum_{\alpha} t_{\mathbf{R}-\mathbf{R}'} c^{\dagger}_{\mathbf{R}\alpha} c_{\mathbf{R}'\alpha} + U \sum_{\mathbf{R}\alpha} n_{\mathbf{R}\alpha} n_{\mathbf{R}-\alpha} \tag{3.4.9}$$

contains the kinetic energy in form of a hopping parameter $t_{\mathbf{R}-\mathbf{R}'}$ between the lattice sites $\mathbf{R}$ and $\mathbf{R}'$ and an on-site electron-electron repulsion U. Here, $c^{\dagger}_{\mathbf{R}\alpha}$ and $c_{\mathbf{R}\alpha}$ are the electron creation and annihilation operators, respectively, for an electron at lattice site $\mathbf{R}$ with spin α, and $n_{\mathbf{R}\alpha} = c^{\dagger}_{\mathbf{R}\alpha} c_{\mathbf{R}\alpha}$ denotes the site occupation number. The magnetic response function is defined in analogy to Eq. (3.2.4) by

$$\chi^{+-}(\mathbf{R},\mathbf{R}';\tau) = -\mathrm{i}\langle \mathcal{T} S^{+}_{\mathbf{R}}(\tau) S^{-}_{\mathbf{R}'}(0)\rangle \tag{3.4.10}$$

with the spin creation $S^{+}_{\mathbf{R}} = c^{\dagger}_{\mathbf{R}\uparrow} c_{\mathbf{R}\downarrow}$ and annihilation operator $S^{-}_{\mathbf{R}} = c^{\dagger}_{\mathbf{R}\downarrow} c_{\mathbf{R}\uparrow}$ at lattice site $\mathbf{R}$. In a mean-field ansatz the interaction term of the Hubbard Hamiltonian (3.4.9) is replaced by

$$U \sum_{\mathbf{R}\alpha} n_{\mathbf{R}\alpha} n_{\mathbf{R}-\alpha} \to U \sum_{\mathbf{R}\alpha} n_{\mathbf{R}\alpha} \langle n_{\mathbf{R}-\alpha}\rangle, \tag{3.4.11}$$

where $\langle n_{\mathbf{R}-\alpha}\rangle$ is the average occupation number at lattice site $\mathbf{R}$ with spin $-\alpha$. With the mean-field approximation for the one-band Hubbard model the equation of mo-

tion (3.4.1) of the non-interacting magnetic response function is given by

$$-\omega \sum_{\mathbf{R}'} \chi_0^{+-}(\mathbf{R}, \mathbf{R}'; \omega) = Um \sum_{\mathbf{R}'} \chi_0^{+-}(\mathbf{R}, \mathbf{R}'; \omega) - m, \tag{3.4.12}$$

with the site magnetization m. In the non-interacting case, the magnetic response function does not contain a magnon pole. This is because the electrons do not interact with each other so that a homogeneous magnetic perturbation perpendicular to the spin polarization axis does not lead to a collective rotation of the spin system. Therefore, in the Goldstone limit $\mathbf{q} \to 0$ and $\omega \to 0$ the relation (3.4.12) reduces to

$$\chi_0^{+-}(\mathbf{q} \to 0, \omega \to 0) = \frac{1}{U}. \tag{3.4.13}$$

If the interaction between the electrons is taken into account in the Hartree-Fock approximation, the interacting magnetic response function is

$$\chi^{+-}(\mathbf{q}, \omega) = \frac{\chi_0^{+-}(\mathbf{q}, \omega)}{1 - U\chi_0^{+-}(\mathbf{q}, \omega)}. \tag{3.4.14}$$

Obviously, the non-interacting magnetic response function which obeys the relation (3.4.13) ensures the fulfillment of the Goldstone condition as the magnetic response function (3.4.14) has a pole in the Goldstone limit. On the other hand, the explicit expression of the non-interacting magnetic response function in the Hartree-Fock approximation is given by

$$\chi_0^{+-}(\mathbf{q}, \omega) = \frac{1}{N} \sum_{\mathbf{k}} \frac{n_{\mathbf{k}\downarrow} - n_{\mathbf{k}-\mathbf{q}\uparrow}}{\omega - \epsilon_{\mathbf{k}-\mathbf{q}} + \epsilon_{\mathbf{k}} - E_{\mathrm{ex}} - i\eta}. \tag{3.4.15}$$

In the Goldstone limit the non-interacting magnetic response function χ_0^{+-} reduces to

$$\chi_0^{+-}(\mathbf{q} \to 0, \omega \to 0) = \frac{m}{E_{\mathrm{ex}}}. \tag{3.4.16}$$

Thus, the Goldstone condition is fulfilled only if Eq. (3.4.13) and Eq. (3.4.16) are fulfilled simultaneously. Therefore, the Goldstone-mode condition leads to an intimate relation between the on-site interaction U, the site magnetization m, and the exchange splitting E_{ex}. If the non-interacting magnetic response function χ_0^{+-} (3.4.15) is calculated consistently in the Hartree-Fock approximation, in which $E_{\mathrm{ex}} = Um$, the Goldstone condition is identically fulfilled.

3.4.2 Local-Spin-Density Approximation

The spin density-functional theory in the local-spin-density approximation (LSDA) is a standard approach to describe magnetic materials. In view of the previous discussion the question arises how the ferromagnetic state described within the LSDA relates to the Goldstone condition. The exchange-correlation potential $v_{\mathrm{xc}}^{\alpha}(\mathbf{r})$ is the functional derivative of the exchange-correlation energy $E_{\mathrm{xc}}[n_{\uparrow}(\mathbf{r}), n_{\downarrow}(\mathbf{r})]$ with respect to the spin density $n_{\alpha}(\mathbf{r})$ and, thus, depends on the spin state α, i.e., it differs for the majority and the minority states. The spin-dependent exchange-correlation potential acts as an effective magnetic field. The exchange-correlation potential can be written as a sum of a spin-independent potential $v_{\mathrm{xc}}^{0}(\mathbf{r}) = 1/2(v_{\mathrm{xc}}^{\uparrow}(\mathbf{r}) + v_{\mathrm{xc}}^{\downarrow}(\mathbf{r}))$ and a Zeeman term $S^{z}B_{\mathrm{xc}}(\mathbf{r})$ with

$$B_{\mathrm{xc}}(\mathbf{r}) = \frac{1}{2}\left(v_{\mathrm{xc}}^{\uparrow}(\mathbf{r}) - v_{\mathrm{xc}}^{\downarrow}(\mathbf{r})\right), \tag{3.4.17}$$

which drives the non-interacting electron system into a spin-polarized state. Due to the non-interacting nature of the auxiliary Kohn-Sham system, it is the finite exchange-correlation magnetic field $B_{\mathrm{xc}}(\mathbf{r})$ introduced through the spin-dependent exchange-correlation potential that is responsible for the formation of a spin-polarized state. The magnetic response function of the non-interacting Kohn-Sham system is

$$\chi_{\mathrm{KS}}^{ij}(\mathbf{r}, \mathbf{r}'; \tau) = \frac{\delta m^{i}(\mathbf{r}t)}{\delta B_{\mathrm{eff}}^{j}(\mathbf{r}'t')}, \tag{3.4.18}$$

with the magnetization density $m^{i}(\mathbf{r}t)$ and the effective magnetic field

$$B_{\mathrm{eff}}^{i}(\mathbf{r}t) = B_{\mathrm{ext}}^{i}(\mathbf{r}t) + B_{\mathrm{xc}}^{i}(\mathbf{r}t), \tag{3.4.19}$$

which depends on an external magnetic field $B_{\mathrm{ext}}^{i}(\mathbf{r}t)$. The Kohn-Sham magnetic response function is the response of a system of non-interacting particles. The Kohn-Sham Hamiltonian, implicitly defined in Eq. (2.2.11), allows to derive a relation among the magnetization, the exchange-correlation B_{xc} field, and the non-interacting magnetic response function in analogy to the Goldstone condition (3.4.8)

$$m(\mathbf{r}) = \int \mathrm{d}\mathbf{r}'\, B_{\mathrm{xc}}(\mathbf{r})\, \chi_{\mathrm{KS}}^{+-}(\mathbf{r}, \mathbf{r}'; 0). \tag{3.4.20}$$

The condition implies that the non-interacting Kohn-Sham response does not contain a gapless magnon pole because of the finite-valued exchange-correlation mag-

netic field B_{xc}. In other words, the effective magnetic field introduced through the exchange-correlation potential breaks the invariance of the Kohn-Sham Hamiltonian under a transversal spin rotation. This is, in fact, the case for every mean-field Hamiltonian describing a spin-polarized state. In order to describe spin excitations of the interacting system within the framework of density-functional theory, the magnetic response function [158–161] can be calculated within the time-dependent density-functional theory (TDDFT) [34, 42, 162–164]. The response function of the interacting system

$$\chi^{ij}(\mathbf{r},\mathbf{r}';\tau) = \frac{\delta m^i(\mathbf{r}t)}{\delta B^j_{\mathrm{ext}}(\mathbf{r}'t')} \tag{3.4.21}$$

accounts for the self-consistently induced response by the system due to an external magnetic perturbation. The magnetic response function obeys a Dyson-like equation

$$\chi^{ij}(\mathbf{r},\mathbf{r}';\tau)^{-1} = \chi^{ij}_{\mathrm{KS}}(\mathbf{r},\mathbf{r}';\tau)^{-1} - f^{ij}_{\mathrm{xc}}(\mathbf{r},\mathbf{r}';\tau), \tag{3.4.22}$$

where the interaction among the electron-hole pairs is described by the exchange-correlation kernel $f^{ij}_{\mathrm{xc}}(\mathbf{r},\mathbf{r}';\tau)$. Usually, TDDFT calculations [34, 42, 162–164] make use of the adiabatic local-density approximation (ALDA) [165] to the exchange-correlation kernel, i.e., its time dependence is neglected. In the case of collinear magnetism, the linear-response function as well as the exchange-correlation kernel separates into a longitudinal and a transversal component. The transverse magnetic response function $\chi^{+-} = \delta m^+ / \delta B^+_{\mathrm{ext}}$ implies the transverse exchange-correlation kernel $f^{+-}_{\mathrm{xc}} = \delta B^+_{\mathrm{xc}} / \delta m^+$ with $\delta m^+ = \delta m^{\mathrm{x}} + \mathrm{i}\delta m^{\mathrm{y}}$ and $\delta B^+ = \delta B^{\mathrm{x}} + \mathrm{i}\delta B^{\mathrm{y}}$. In the ALDA the transverse exchange-correlation kernel [42] evaluates to

$$f^{+-}_{\mathrm{xc}}(\mathbf{r},\mathbf{r}';\tau) = \frac{v^{\uparrow}_{\mathrm{xc}}(\mathbf{r}) - v^{\downarrow}_{\mathrm{xc}}(\mathbf{r})}{m(\mathbf{r})}\delta(\mathbf{r}-\mathbf{r}')\delta(\tau). \tag{3.4.23}$$

The Goldstone condition demands that the response function diverges in the Goldstone limit $(\mathbf{q},\omega) \to (\mathbf{0},0)$. In this limit, the magnetization density is an eigenfunction of the inverse magnetic response function with eigenvalue zero

$$\int \mathrm{d}\mathbf{r}'\,\mathrm{d}\tau\,\chi^{+-}(\mathbf{r},\mathbf{r}';\tau)^{-1}\,m(\mathbf{r}') = 0. \tag{3.4.24}$$

Therefore, for the Goldstone-mode condition to be fulfilled the Dyson equation of the magnetic response function (3.4.22) requires that the transverse exchange-correlation

kernel and the inverse Kohn-Sham response function are related such that

$$\int \mathrm{d}\mathbf{r}' \, \mathrm{d}\tau \, \chi_{\mathrm{KS}}^{+-}(\mathbf{r}, \mathbf{r}'; \tau)^{-1} \, m(\mathbf{r}') = \int \mathrm{d}\mathbf{r}' \, \mathrm{d}\tau \, f_{\mathrm{xc}}^{+-}(\mathbf{r}, \mathbf{r}'; \tau) \, m(\mathbf{r}'). \tag{3.4.25}$$

This relation should be compared with the Goldstone-mode condition for the non-interacting Kohn Sham response function (3.4.20). The Goldstone-mode condition is fulfilled if the Kohn-Sham response function and the exchange-correlation kernel fulfill the relations (3.4.20) and (3.4.25) simultaneously. In numerical implementations the Kohn-Sham magnetic response and the exchange-correlation kernel usually derive from different ground-state calculations [38]. As a result the Goldstone-mode condition is numerically violated in these calculations. Lounis *et al.* [38] ensure the Goldstone-mode condition by deriving the exchange-correlation kernel from a magnetic sum rule instead of calculating it explicitly from Eq. (3.4.23), such that Eq. (3.4.20) and Eq. (3.4.25) are fulfilled at the same time.

3.4.3 Coulomb Hole and Screened Exchange Approximation

The derivation of the magnetic response function in many-body perturbation theory requires that the Green function is a self-consistent solution to the Dyson equation (3.2.7) with respect to a chosen self-energy approximation. We employ the *GW* approximation with an additional static approximation for the screened interaction. Therefore, the resulting magnetic response function can be derived from the Coulomb hole (COH) and screened exchange (SEX) self-energy, which is the static limit of the *GW* approximation. A derivation of the COHSEX self-energy is presented in the Appendix B. The Coulomb hole contribution

$$\Sigma_{\mathrm{COH}}(\mathbf{r}, \mathbf{r}'; \omega = 0) = \frac{1}{2} \delta(\mathbf{r} - \mathbf{r}') W_c(\mathbf{r}, \mathbf{r}'; 0) \tag{3.4.26}$$

acts as a local and spin-independent potential. It is the potential induced by the static polarization cloud of a quasiparticle. In contrast, the screened exchange self-energy acts as a nonlocal and spin-dependent potential

$$\Sigma_{\mathrm{SEX}}^{\alpha}(\mathbf{r}, \mathbf{r}'; \omega = 0) = -\sum_{\mathbf{k}}^{\mathrm{BZ}} \sum_{m}^{\mathrm{occ}} \varphi_{\mathbf{k}m}^{\alpha}(\mathbf{r}) \varphi_{\mathbf{k}m}^{\alpha *}(\mathbf{r}') W(\mathbf{r}, \mathbf{r}'; 0). \tag{3.4.27}$$

The COHSEX self-energy

$$\Sigma_{\mathrm{COHSEX}}^{\alpha}(\mathbf{r}, \mathbf{r}') = \Sigma_{\mathrm{COH}}(\mathbf{r}, \mathbf{r}'; \omega = 0) + \Sigma_{\mathrm{SEX}}^{\alpha}(\mathbf{r}, \mathbf{r}'; \omega = 0) \tag{3.4.28}$$

is a static self-energy approximation, and, therefore, it is a Hermitian self-energy operator. It corresponds to the Hartree-Fock exchange operator with the bare Coulomb interaction replaced by the static screened interaction. Without spin-orbit coupling the Coulomb hole contribution couples only charge degrees of freedom. It is the screened exchange contribution which is responsible for the spin polarization. This becomes apparent when the COHSEX self-energy is separated in a spin-independent and a spin-dependent contribution by means of a Zeeman-like term

$$\Sigma^{\alpha}_{\mathrm{COHSEX}}(\mathbf{r},\mathbf{r}') = \Sigma^{0}_{\mathrm{COHSEX}}(\mathbf{r},\mathbf{r}') + S^{z} B_{\mathrm{COHSEX}}(\mathbf{r},\mathbf{r}'). \tag{3.4.29}$$

The nonlocal magnetic B_{COHSEX} field corresponds to the difference of the screened exchange potential for the majority and minority states

$$B_{\mathrm{COHSEX}}(\mathbf{r},\mathbf{r}') = -\sum_{\mathbf{k}}^{\mathrm{BZ}} \sum_{m}^{\mathrm{occ}} \left(\varphi^{\uparrow}_{\mathbf{k}m}(\mathbf{r}) \varphi^{\uparrow *}_{\mathbf{k}m}(\mathbf{r}') - \varphi^{\downarrow}_{\mathbf{k}m}(\mathbf{r}) \varphi^{\downarrow *}_{\mathbf{k}m}(\mathbf{r}') \right) W(\mathbf{r},\mathbf{r}'). \tag{3.4.30}$$

In other words, the screened exchange contribution brings the mean-field system into its spin-polarized state. In contrast, the spin-independent Coulomb hole part does not contribute to the effective magnetic field. The effective magnetic field allows to derive a condition for the non-interacting magnetic response K^{+-} of the COHSEX mean-field system in analogy to Eq. (3.4.8). The generalization of the Goldstone condition to the nonlocal effective magnetic field of the COHSEX mean-field system reads

$$m(\mathbf{r}) = \int \mathrm{d}\mathbf{r}'\, B_{\mathrm{COHSEX}}(\mathbf{r},\mathbf{r}')\, K^{+-}(\mathbf{r},\mathbf{r}';0). \tag{3.4.31}$$

The non-interacting magnetic response function K^{+-} is conveniently calculated from the Kohn-Sham Green function, e.g. by using the LSDA. This, however, brings a fundamental inconsistency into the formulation of the magnetic response function. Obviously, the relation (3.4.31) is not fulfilled if the non-interacting magnetic response function is calculated from a Kohn-Sham Green function. In this work, we have lifted this fundamental inconsistency by calculating the non-interacting magnetic response function from the properly renormalized Green function by means of the COHSEX self-energy.

In addition to Eq. (3.4.31), the Goldstone condition of the magnetic response function R^{+-} requires that the magnetization is an eigenfunction to the inverse magnetic

response function, i.e.,

$$\int \mathrm{d}\mathbf{r}'\, R^{+-}(\mathbf{r},\mathbf{r}';0)^{-1} m(\mathbf{r}') = 0. \tag{3.4.32}$$

We make use of a Wannier function approach to calculate the magnetic response function by means of an auxiliary four-point function as this allows to solve the Bethe-Salpeter equation (3.3.12) by matrix inversion. The magnetic response function is obtained from the auxiliary four-point magnetic response function by the contraction (3.3.16). The Goldstone-mode condition (3.4.32) requires that at least one eigenvalue of the matrix $1 - KW$ vanishes in the Goldstone limit. If this is not the case, a gap error occurs in the Goldstone limit of the spin-wave dispersion. As we will see, even though the fundamental inconsistency of using the Kohn-Sham Green function is lifted, approximations in the numerical scheme cause a remaining gap error. This numerical violation of the Goldstone condition might be caused by several reasons: **k**-point set issues, basis set issues, and the on-site approximation of the screened interaction to name a few. The influence of the **k**-point set is minimized by employing the same **k**-point set and the same **k**-point integration method at every stage of the calculation of the magnetic response function. The next section presents the results of the investigation of the violation of the Goldstone-mode condition.

3.5 Results

3.5.1 Computational Details

In the framework of many-body perturbation theory the calculation of the magnetic response function is a multi-stage process. First, a self-consistent field calculation provides the electronic ground state within density-functional theory. The calculations are performed with the local-spin-density approximation (LSDA) for the exchange-correlation potential in the parameterization by Perdew and Zunger [90]. Alternatively, we use the generalized gradient approximation (GGA) in the parameterization by Perdew, Burke, and Ernzerhof [91]. We calculate the elementary ferromagnetic materials iron, cobalt, and nickel with the lattice constants 2.87 Å, 3.54 Å, and 3.53 Å, respectively. At every stage of the calculation we sample the Brillouin zone (BZ) with a $14 \times 14 \times 14$ **k**-point grid. The BZ integrations are performed with the tetrahedron method [157]. Next, the on-site static screened interaction is calculated in the random-phase approximation (RPA). For this, the screened interaction is

calculated in the mixed-product basis [72, 108] using the LSDA or the GGA starting point. To obtain the on-site contribution the screened interaction is projected onto a Wanner product basis. The Lehman representation of the two-particle propagator K allows its evaluation directly in the Wannier product basis [43, 166], cf. Eq. (3.3.7). The Wannier functions which form the Wannier product basis must fulfill two conditions: first, they must be sufficiently localized to enable an efficient real-space truncation [43, 166], and second the set of Wannier functions must reproduce the relevant energetic subspace properly. The electronic d states close to the Fermi level are most important for the formation of the spin-wave excitations. Therefore, it is that energy region which is relevant for the magnetic response. To put it another way, the set of Wannier functions must be chosen such that the electron and the hole Green function attaching to the vertices of the four-point quantities can couple properly. To this end, we have chosen a set of nine maximally localized Wannier functions [46, 47] of s, p, and d character for each material. For their construction we employ the 18 energetically lowest mean-field single-particle states $\varphi^{\alpha}_{\mathbf{k}n}(\mathbf{r})$. The choice of the number of bands is a compromise. On the one hand, the two-particle propagator is built from the empty states and therefore the number of bands should not be too small to ensure its adequate description. On the other hand, the set of Wannier functions has to describe the low-energy electronic bands sufficiently accurately. Therefore, the number of bands should not exceed the number of Wannier functions too much. We have performed test calculations with two different sets employing the 12 or 24 lowest mean-field single-particle states which give very similar results. The Wannier product basis is used to present the four-point quantities $R^{(4)}$ and K as well as the on-site screened interaction W. This allows to solve for the magnetic response function (3.3.12) by matrix inversion.

We consider the starting-point dependence of the spin-wave spectra for the elementary bulk ferromagnets iron, cobalt, and nickel. We refer here to the Green function with which the two-particle propagator K is calculated. In particular, we compare the spin-wave spectra calculated with the LSDA, the GGA, and the Coulomb hole screened exchange (COHSEX) Green function.

3.5.2 Coulomb Hole and Screened Exchange Approximation

The Bethe-Salpeter equation of the magnetic response function is derived under the assumption that the Green function is the solution of the Dyson equation (3.2.7). This means that the theoretical framework relies on a Green function that is a self-

consistent solution to the self-energy Σ. We employ the self-energy in the *GW* approximation (3.2.10) which leads via $\delta\Sigma/\delta B$ (3.2.17) to the magnetic response function in the ladder approximation (3.2.19), cf. Fig. 3.1. The relationship between the screened interaction W and the two-particle propagator K is also apparent from the Bethe-Salpeter equation (3.3.12) of the magnetic response function. To fulfill the Goldstone-mode condition at least one eigenvalue of the matrix $(1 - KW)$ must vanish exactly. Therefore, the two-particle propagator $K = -iGG$ has to be related to the screened interaction W. And, in fact, they are related if the Green function is the self-consistent solution to the Dyson equation. In this case, the screened interaction which is part of the self-energy enters the self-consistent solution of G. The particular construction of the screened interaction, however, does not enter the Bethe-Salpeter equation of the magnetic response function. Therefore, it is irrelevant that the screened interaction in the random-phase approximation (RPA) itself is constructed using the Green function as the screened interaction merely appears as a parameter. Thus, a consistent implementation of the underlying theory requires to use the Green function that is self-consistently renormalized with the self-energy. At first sight, the *GW* self-energy (3.2.10) appears to be the proper self-energy. However, the implementation of the magnetic response function makes use of a static approximation for the screened interaction. For this reason, the proper self-energy has to be constructed with the static screened interaction. This means, a proper choice of the self-energy replaces the dynamical screened interaction $W(\mathbf{r}, \mathbf{r}'; \tau)$ of the *GW* approximation (3.2.10) by an instantaneous interaction whose Fourier transform would be the static screened interaction $W(\mathbf{r}, \mathbf{r}') = W(\mathbf{r}, \mathbf{r}'; \omega = 0)$. The resulting screened exchange (SEX) self-energy $\Sigma^{\alpha}_{\mathrm{SEX}}(\mathbf{r}, \mathbf{r}')$ (3.4.27) corresponds to the Fock-term of the Hartree-Fock theory with the bare Coulomb interaction replaced by the static screened interaction. The SEX self-energy is, however, not a good approximation. Instead, we can use the static limit of the *GW* approximation. The static limit of the *GW* approximation involves, in addition to the SEX self-energy, a Coulomb hole (COH) self-energy $\Sigma_{\mathrm{COH}}(\mathbf{r}, \mathbf{r}')$ (3.4.26). The static limit of the *GW* approximation [71] is known as the Coulomb hole and screened exchange (COHSEX) self-energy (3.4.28). The Coulomb hole term acts as a local and spin-independent potential. If spin-orbit coupling is set aside, the COH self-energy couples only charge degrees of freedom. As a consequence, it does not affect the transverse magnetic response function. It is the SEX term which enters the derivation of the Bethe-Salpeter equation with $\delta\Sigma/\delta G = \mathrm{i}W(0)$. This leads to a Bethe-Salpeter equation of the same

form as Eq. (3.2.19). But, the dynamic screened interaction is replaced by the static one, i.e., the additional static approximation to the screened interaction is not needed anymore as the static limit is already taken in the COHSEX self-energy.

To obtain the properly renormalized Green function in terms of the COHSEX self-energy, we must solve the Dyson equation self-consistently. Technically, the LSDA solution forms the starting point of this procedure. We construct the Green function, the polarization function, and the static screened interaction which, in turn, are used to calculate the COHSEX self-energy from the LSDA energies and wave functions. The COHSEX self-energy is, due to its frequency independence, a Hermitian operator which defines a new mean-field system. This allows to calculate the quasiparticle equations

$$h_0(\mathbf{r})\varphi^{\alpha}_{\mathbf{k}m}(\mathbf{r}) + \int \mathrm{d}\mathbf{r}'\, \Sigma^{\alpha}_{\mathrm{COHSEX}}(\mathbf{r},\mathbf{r}')\varphi^{\alpha}_{\mathbf{k}m}(\mathbf{r}') = E^{\alpha}_{\mathbf{k}m}\varphi^{\alpha}_{\mathbf{k}m}(\mathbf{r}) \tag{3.5.1}$$

in a very similar way as the single-particle equations of the Kohn-Sham density-functional theory. In particular, the single-particle equations are iterated while the matrix

$$\langle \varphi^{\alpha}_{\mathbf{k}m} | \Sigma^{\alpha}_{\mathrm{COHSEX}} - v^{\alpha}_{\mathrm{xc}} | \varphi^{\alpha}_{\mathbf{k}m'} \rangle \tag{3.5.2}$$

remains fixed. This process updates the density and the local effective potential in each iteration. The resulting new set of wave functions and energies are then used to construct a new Green function, polarization function, screened interaction, and COHSEX self-energy. These steps are repeated until self-consistency is reached.

For the calculation of the magnetic response function we employ the LSDA, the GGA, or the COHSEX mean-field solution of the 3*d* ferromagnets bcc iron, fcc cobalt, and fcc nickel as starting point. The density of states (DOS) for the three elementary ferromagnets is shown in Fig. 3.4 for all three starting points. The DOS spectra look similar and all approaches describe the three materials qualitatively correct as ferromagnetic metals. However, there are quantitative difference among the three approaches. Strikingly, for all three materials the minority 3*d* states appear higher in energy within the GGA approach compared to the LSDA and the COHSEX approach. The LSDA occupied-band width shrinks, in particular for Co and Ni, compared to the COHSEX occupied-band width. In addition, the majority spin and minority spin states are relatively shifted to lower values. The exchange splittings, listed in Table 3.2 for selected single-particle states, support these observations. The exchange splittings found with the COHSEX approach are systematically smaller than

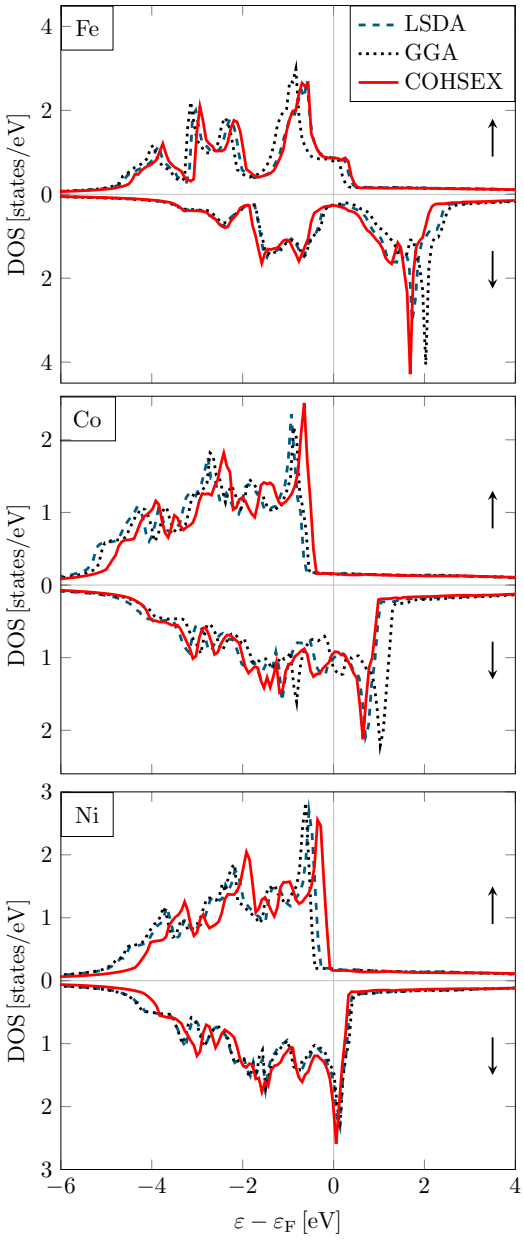

Figure 3.4: Density of states for the bulk 3*d* elementary ferromagnets iron, cobalt, and nickel employing the LSDA (blue dashed line), the GGA (black dotted line), and the COHSEX (red solid line) approach. The upper and lower panel show the majority and minority spin channel, respectively. The Fermi level is set to zero.

			LSDA	LSDA corr.	GGA	GGA corr.	COHSEX	Expt.
$m\,[\mu_B]$	Fe		2.19	2.16	2.26	2.13	2.10	2.08[a]
	Co		1.60	1.49	1.68	1.51	1.46	1.52[a]
	Ni		0.58	0.51	0.62	0.50	0.45	0.52[a]
$E_{ex}\,[eV]$	Fe	Γ'_{25}	1.8	1.7	2.0	1.6	1.5	2.1[b]
		H_{25}	2.1	2.0	2.3	1.9	1.7	1.8[c]
		P_4	1.4	1.3	1.4	1.0	1.1	1.5[d]
	Co	Γ_{12}	1.7	1.3	1.6	1.0	1.1	1.1[e]
		Γ'_{25}	1.4	1.0	2.0	1.4	1.2	1.1[e]
	Ni	L_3	0.5	0.3	0.6	0.3	0.4	0.3[d]
		X_2	0.6	0.4	0.6	0.2	0.3	0.2[f]

Table 3.2: The spin magnetic moment m and the exchange splitting E_{ex} calculated within the LSDA, the GGA and the self-consistent COHSEX approach and corresponding experimental values for the 3*d* transition metals. In addition, the values LSDA corr. and GGA corr. are given which correspond to the corrected LSDA and the corrected GGA Green function which yield spin-wave dispersions respecting the Goldstone condition. Magnetic moments are obtained from the sum rule (3.3.29). Parts of this table were published [51], ©2016 American Physical Society. Experimental values are taken from references [a] [167, 168], [b] [169–172], [c] [172], [d] [173], [e] [174], and [f] [175].

the LSDA and GGA ones. In most cases, the GGA exchange splittings are larger than the LSDA values. The magnetic moments found with the three approaches show a similar behavior. While the LSDA and the GGA approach, both slightly overestimate the magnetic moments, the COHSEX approach corrects the magnetic moment to smaller values even slightly too small in the case of cobalt and nickel. The DOS spectra for the three ferromagnets suggest that the LSDA results are closer to those obtained with the COHSEX approach compared to the GGA approach, cf. Fig. 3.4. The magnetic moment and the exchange splittings, shown in Table 3.2, support this presumption. Recently, the electronic structure of iron and nickel has been investigated by means of a one-shot COHSEX self-energy calculation using the linearized muffin-tin orbital (LMTO) method [176]. Our results support their findings only partly. While their calculations yield a COHSEX magnetic moment smaller than the LSDA value in case of iron, for nickel they find the COHSEX magnetic moment to be larger than the LSDA value.

3.5.3 Spin-Wave Dispersions

Spin-wave dispersions calculated in the many-body perturbation theory depend on the chosen starting point. We analyze this starting-point dependence for the spin-

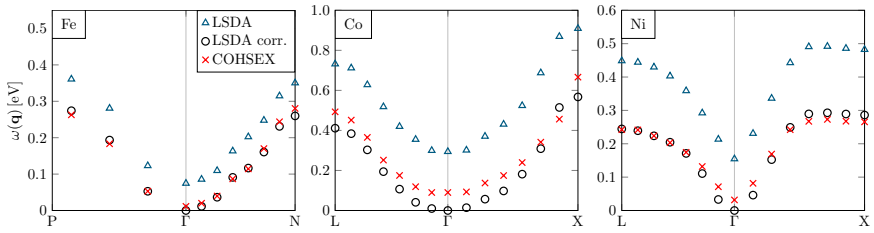

Figure 3.5: Starting-point dependence of the spin-wave spectra for Fe, Co, and Ni obtained with the LSDA (blue triangles), corrected LSDA (black circles), and COHSEX (red crosses) Green function. The spin-wave dispersion is shown along the high-symmetry line P $\rightarrow$ Γ $\rightarrow$ N and L $\rightarrow$ Γ $\rightarrow$ X for the bcc and fcc lattice structure, respectively. This figure was published recently [51], ©2016 American Physical Society.

wave spectra for the 3*d* elementary ferromagnetic metals iron, cobalt, and nickel. Here, we refer to the mean-field approximation with which the Green function and the two-particle propagator K is calculated. The first step of a spin-wave dispersion calculation is the calculation of the ground state conveniently obtained in the LSDA or the GGA. The ground-state calculation yields already a set of single-particle states which allows to calculate the Kohn-Sham Green function from the corresponding single-particle wave functions and energies. The spin-wave dispersions resulting from the LSDA Green function are shown in Fig. 3.5 as blue triangles for the 3*d* elementary ferromagnets. The dispersions correctly obey a quadratic behavior around the center of the BZ, though the dispersions also exhibit a gap error: the spin-wave excitation energy does not vanish at the Γ point as it should according to the Goldstone-mode condition. The violation of the Goldstone-mode condition might be caused by a number of reasons. First, the numerical realization of the magnetic response function makes use of an on-site approximation for the screened interaction. The on-site approximation does not allow the electron-hole pairs to separate further than one lattice site while they can propagate over arbitrarily many lattice sites. This means the electron-hole pairs interact with each other only if they are located at the same lattice site. The on-site approximation is justified if the screened interaction falls off sufficiently fast so that the off-site contribution to the interaction can be neglected. The assumption of the screened interaction's short-range behavior seems to be justified for the ferromagnetic metals Fe, Co, and Ni. We have tested the on-site approximation for those materials and we found that the nearest-neighbor interactions are typically 98% smaller than the corresponding on-site terms, cf. right panel of Fig. 3.2. Second, the numerical realization makes use of a formulation in a Wannier

	$\delta\omega_{\mathrm{LSDA}}$ [meV]	$\delta\omega_{\mathrm{GGA}}$ [meV]	$\delta\omega_{\mathrm{COHSEX}}$ [meV]
Fe	75	289	11
Co	294	457	90
Ni	155	242	32

Table 3.3: Starting-point dependence of the gap error $\delta\omega$ in the Goldstone limit $\mathbf{q} \to 0$ for Fe, Co, and Ni. The gap errors are given for three different starting points: LSDA in the parameterization of Perdew and Zunger [90], GGA in the parameterization of Perdew, Berke, and Enzerhof [91], and COHSEX [71] self-energy approximation. This table was published recently [51], ©2016 American Physical Society.

basis. The choice of the Wannier basis effectively restricts the band summation for the Green function as well as for the two-particle propagator K to those bands that are used in the construction of the Wannier functions. We have chosen the 18 energetically lowest single-particle states for the construction of the Wannier basis. The choice of the number of single-particle states is a compromise between an accurate description of the low-energy physical properties and the unoccupied band summation of the two-particle propagator. A third possible reason for the violation of the Goldstone mode is related to the Wannier basis. The Wannier product basis used to solve the Bethe-Salpeter equation of the four-point magnetic response function might be inappropriate for representing plane waves with small Bloch vector, in particular the constant function which is relevant for the Goldstone mode limit $\mathbf{q} \to 0$. In addition, convergence issues related to the $\mathbf{k}$-point set, the empty-state summation, *et cetera* might contribute to the gap error. Though there are a number of issues related to the numerical realization we focus, in the following, on a more fundamental inconsistency in the chosen approach. It is the choice of the starting point, i.e., the LSDA Green function which brings in a fundamental inconsistency. The Bethe-Salpeter equation of the magnetic response function is derived under the assumption that the Green function is the solution of the Dyson equation. The Bethe-Salpeter equation of the magnetic response function with a static screened interaction mediating the correlation among the electron-hole pairs derives from the Green function which is the self-consistent solution to the COHSEX self-energy. Consequently, to remain consistent with the theoretical framework, we must employ a Green function which is self-consistently renormalized by means of the COHSEX self-energy. The resulting spin-wave dispersions calculated from the COHSEX Green function are shown as red crosses in Fig. 3.5. The dispersions still show a gap error at the Γ point. But, the use of the self-consistent COHSEX Green function substantially reduces the gap error compared to the LSDA value. The reduction of the gap error is summarized

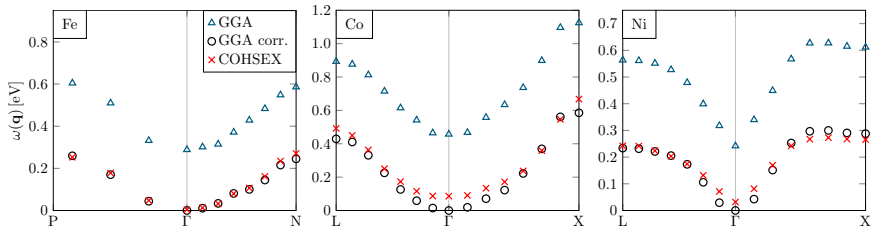

Figure 3.6: Same as Fig. 3.5 for a GGA starting point.

in Table 3.3 for the three materials. It amounts to 85%, 69%, and 79% in the case of bcc iron, fcc cobalt, and fcc nickel, respectively. As a comparison we have performed the same analysis for a GGA starting point with the exchange-correlation potential parameterized by the functional of Perdew, Berke, and Enzerhof (PBE) [91]. The resulting spin-wave dispersions, shown as blue triangles in Fig. 3.6, correctly obey a quadratic dispersion in the vicinity of the BZ center and again a gap error occurs. The gap errors are even larger than the LSDA values for all three materials, see Table 3.3.

The ansatz presented so far suffers from its unfavorable computational effort. It requires the self-consistent mean-field solution of the COHSEX self-energy calculated on a fine $\mathbf{k}$-point set as a prerequisite. Therefore, the ansatz is far more computational demanding than a Kohn-Sham starting point either in the LSDA or in the GGA. Despite the fact that the gap error strongly depends on the chosen starting point, the spin-wave dispersions obtained with the LSDA, the GGA, and the COHSEX Green function are very similar. The similarity of the spin-wave dispersions raises the question if the Kohn-Sham Green function can be corrected such that the spin-wave dispersion respects the Goldstone condition. The one-band Hubbard model allows to analyze the Goldstone-mode condition in detail, cf. Section 3.4.1. In the Hartree-Fock approximation the magnetic response function appears as a simple algebraic equation (3.4.14) in the form of Eq. (3.3.12) with the screened interaction W replaced by an on-site interaction parameter U. The Goldstone-mode condition obeys the simple relation

$$1 = \frac{U\,m}{E_{\mathrm{ex}}}, \tag{3.5.3}$$

where we have used that the two-particle propagator simplifies to $K = m/E_{\mathrm{ex}}$ in the Goldstone limit, with the site magnetization m and the exchange splitting E_{ex}. The Goldstone-mode condition is identically fulfilled if the two-particle propagator is calculated in the Hartree-Fock approximation in which the exchange splitting is

$E_{\mathrm{ex}} = U\,m$. The simplicity of the Goldstone-mode condition within the one-band Hubbard model invites to use one of its constituents as an adjustable parameter. The on-site interaction parameter U plays the role of the screened interaction W, which is a matrix obtained within the RPA. Thus, the screened interaction cannot be corrected easily by a single parameter. The magnetization m results from a self-consistent field calculation employing either the LSDA or the GGA. Therefore, the magnetization cannot be changed straightforwardly. In contrast, the exchange splitting E_{ex}, which can be regarded as the difference between the majority and minority bands, can be changed easily. The band alignment can be adjusted once a Kohn-Sham solution has been found. The adjustment of the exchange splitting changes the Kohn-Sham Green function via the adjustment of the Kohn-Sham energies, while the screened interaction remains unchanged. In Section 3.5.2 we found that an essential effect of a self-consistent COHSEX calculation is the renormalization of the exchange splitting of the LSDA solution and the GGA solution, respectively. Therefore, the adjustment of the exchange splitting can be hoped to mimic the effect of the renormalization of the Green function. We choose the exchange splitting as an adjustable parameter by rigidly shifting the majority and minority bands relative to each other

$$\tilde{\epsilon}^{\uparrow/\downarrow}_{\mathbf{k}m} = \epsilon^{\uparrow/\downarrow}_{\mathbf{k}m} \pm \frac{\Delta E_{\mathrm{ex}}}{2} \tag{3.5.4}$$

in such a way that the Goldstone-mode condition is fulfilled. The two-particle propagator K is then constructed with the Kohn-Sham Green function corrected by means of the adjustment of the exchange splitting. Karlsson *et al.* [44] and Şaşıoğlu *et al.* [43] have also used the adjustment of the exchange splitting for the calculation of the spin-wave dispersion. They have applied it, however, as an *ad hoc* correction in order to fit the exchange splitting to the experimental value. However, Şaşıoğlu *et al.* [43] anticipates that a self-consistent calculation of the proper mean-field solution would bring about an adjustment of the exchange splitting. Our results of the self-consistent calculation of the COHSEX Green function, see Section 3.5.2, confirm this conjecture.

The spin-wave dispersion calculated with the corrected Kohn-Sham Green function respect the Goldstone condition and also they are close to the COHSEX results for the three materials as shown in Fig. 3.5 for the corrected LSDA and in Fig. 3.6 for the corrected GGA Green function. The relative shift of the majority spin and minority spin band alignment is such that the exchange splittings decrease, see Table 3.4. The adjustment of the exchange splitting that is needed to correct the GGA Green function is systematically larger than that of the LSDA Green function. This corre-

	$\Delta E_{\mathrm{ex}}^{\mathrm{LSDA}}$ [meV]	$\Delta E_{\mathrm{ex}}^{\mathrm{GGA}}$ [meV]
Fe	0.10	0.40
Co	0.39	0.60
Ni	0.21	0.34

Table 3.4: Adjustment of the exchange splitting ΔE_{ex} for the LSDA and GGA Green function that is applied so that the spin-wave dispersions fulfill the Goldstone-mode condition. The relative shift in the band energies is such that the exchange splittings decrease.

sponds to our finding that among the LSDA, the GGA, and the COHSEX approach the exchange splittings are largest in the GGA approach followed by the LSDA approach, cf. Table 3.2. The adjustment of the exchange splittings leads, in turn, to an adjustment of the Fermi level. As a consequence, the correction scheme affects the ground state magnetic properties as well. Interestingly, the resulting magnetic moments and exchange splittings of the corrected Kohn-Sham Green function turn out to be very close to the corresponding COHSEX values, see Table 3.2. The proximity of COHSEX and the corrected LSDA as well as the corrected GGA values can be regarded as an *a posteriori* justification of the adjustment of the exchange splitting (3.5.4).

Among the three elementary ferromagnets, fcc cobalt appears as a problematic case. First, its gap error is largest for all mean-field starting points. Second, the COHSEX spin-wave dispersion shows an unusually flat behavior at the Γ point. For example, if the lattice constant is decreased by less than 1% the curvature of the spin-wave dispersion can even turn slightly negative when employing the GGA Green function indicating a magnetic instability. Similar peculiarities of the magnetic properties of fcc cobalt have been found in earlier density-functional theory studies. For example Janak [177] report two competing magnetic ground states with low and high magnetic moment. In addition, Moruzzi *et al.* [178, 179] found a strong dependence of the magnetic properties on the lattice constant. They showed that a reduction of the lattice constant by 5% leads to a collapse of the magnetic moment.

Şaşıoğlu *et al.* [43] have employed a different correction scheme to enforce the Goldstone condition. As a pragmatic approach they used a scaling parameter λ to change the screened interaction $W \to \lambda W$ such that the Goldstone-mode condition is fulfilled. The on-site approximation leads to a $\mathbf{q}$ independent screened interaction and therefore, their correction scheme affects the spin-wave dispersion throughout the BZ. The scaling of the screened interaction is a simple *a posteriori* correction scheme. In contrast, the adjustment of the exchange splitting changes the Green

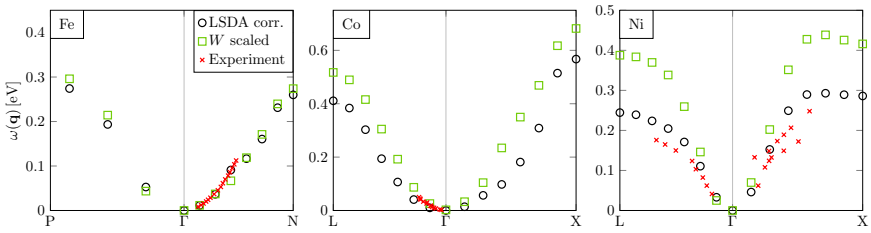

Figure 3.7: Spin-wave spectra for Fe, Co, and Ni that have been calculated with two different Goldstone-mode correction schemes: by adjusting the exchange splitting (black circles) and by scaling the screened interaction W (green squares) as suggested in Ref. [43]. Experimental values [151,180,181] are shown for comparison. This figure was published recently [51], ©2016 American Physical Society.

function itself. The adjustment of the exchange splitting leads to a change of the Fermi level, which requires to recalculate the Green function in an iterative way. Additionally, the scaling of the screened interaction lacks a theoretical justification as the screened interaction matrix is calculated from the RPA and it cannot be changed easily by a simple scaling parameter. Nevertheless, it is worthwhile to compare the spin-wave dispersions resulting from the different correction schemes. Figure 3.7 shows the spin-wave dispersions obtained with the corrected LSDA Green function, the LSDA results with a scaled interaction and experimental data from neutron scattering experiments. The two correction schemes yield rather similar spin-wave dispersions with the exception of Ni. In this case, the adjustment of the exchange splitting yields a spin-wave dispersion which is closer to experiment. The result is in accordance with previous findings by Karlsson *et al.* [44] and Şaşıoğlu *et al.* [43]. Moreover, the spin-wave dispersions resulting from the scaling of the screened interaction W tend to be stiffer, in particular for nickel and, to a lesser degree, for cobalt.

3.6 Summary

In this chapter we have discussed the dynamical magnetic response function in the many-body perturbation theory (MBPT), which is implemented in the all-electron full-potential linearized augmented-plane-wave (FLAPW) method. The magnetic response function in the ladder approximation derives from the *GW* approximation with an additional static approximation for the screened interaction. Within the ladder approximation the magnetic response function is the solution of a Bethe-Salpeter equation. Its first principles calculation allows to access single-particle Stoner exci-

tations and collective spin-wave excitations on the same footing. We have focussed our discussion on the long-wavelength limit of the spin-wave spectra for the bulk elementary ferromagnetic metals iron, cobalt, and nickel. The long-wavelength limit is of special importance as it is related to the Goldstone theorem. The Goldstone theorem states that due to the spontaneously broken spin-rotation symmetry in ferromagnetic materials there exists a gapless excitation in the long-wavelength limit $\mathbf{q} \to 0$. We discussed the Goldstone theorem in the view of the magnetic response function. It turned out that the Goldstone-mode condition for the magnetic response function implies a condition for the non-interacting magnetic response function. In *ab initio* calculations the Goldstone-mode condition is usually numerically violated giving rise to a gap error in the spin-wave dispersion. We have figured out that the choice of the starting point might bring a fundamental inconsistency into the underlying theory. A consistent numerical realization must use the self-consistently renormalized Green function by means of the Coulomb hole and screened exchange (COHSEX) self-energy, which is the static limit of the *GW* self-energy. The self-consistent COHSEX calculations bring about an overall reduction of the exchange splittings compared to the Kohn-Sham values, often leading to a better agreement with experiment. We have shown that the gap error is indeed substantially reduced when using the COHSEX Green function instead of either the local spin-density approximation (LSDA) or the generalized gradient approximation (GGA) one. A correction scheme, motivated by the spin-wave solution of the one-band Hubbard model in the Hartree-Fock approximation, allows to cure the fundamental inconsistency of choosing a Kohn-Sham Green function. The correction scheme uses the exchange splitting of the Kohn-Sham system as an adjustable parameter. The Kohn-Sham Green function is changed in such a way that the spin-wave dispersion fulfills the Goldstone condition. The resulting spin-wave dispersions are closer to the corresponding COHSEX than to the original LSDA or rather the original GGA results. The same can be said about the magnetic properties, i.e., the magnetic moment and the exchange splittings, of the corrected LSDA and the corrected GGA Green function. The corrected Kohn-Sham Green function comes at the numerical cost of an ordinary Kohn-Sham mean-field calculation. The Kohn-Sham Green function corrected in such a way that the Goldstone-mode condition is fulfilled opens up the possibility of efficient *ab initio* many-body perturbation theory calculations of spin excitations. We use this correction scheme for the calculation of the electron-magnon interaction within the *GT* self-energy approximation in the elementary bulk ferromagnets.

4. Electron-Magnon Scattering

4.1 Introduction

The theoretical understanding of realistic materials has gained a lot of insight from *ab initio* density-functional theory (DFT) calculations. Its implementation employing (semi-) local-density approximations (LDA) is exact in the limit of a homogeneous electron gas. The properties of weakly correlated materials are reproduced well in the LDA approach. Angle-resolved photoelectron spectroscopy (ARPES) measurements, however, give evidence that even in simple cases there exists a systematic difference between the experimental band structure and its prediction by means of a LDA calculation. In the case of bulk sodium the measured band width is 2.5 eV [182] and 2.65 eV [183], respectively, while LDA predicts a band width of 3.2 eV. It turned out that many-body corrections to the LDA substantially reduce the band width [184]. Employing the *GW* approximation, the band width is in good agreement with the experiment [185,186]. Yet, the *GW* approximation underestimates the measured quasiparticle lifetimes in sodium. To account for this, Lischner *et al.* [187] employed a self-energy correction beyond the *GW* approximation that accounts for spin fluctuations. While the spin fluctuations hardly affect the occupied-band width, they give an important contribution to the quasiparticle lifetime. This demonstrates even for simple metals such as sodium the importance of many-body effects for a comprehensive understanding of material properties.

The 3*d* transition metals form a class of intermediately correlated materials in which localized *d* states close to the Fermi level are embedded in a free-electron-like band structure. The stronger the correlation among the electrons the more pronounced are the systematic differences of LDA to experiment. Among the 3*d* transition metals Ni is a prominent example as the results from the local-spin-density

approximation (LSDA) approach show considerable deviations from experiment. While the ground-state properties such as the magnetic moment [188] obtained from LSDA are in rather good agreement with experiment, the LSDA band structure significantly deviates from ARPES measurements. The measured 3*d*-band width is about 30% smaller than the DFT prediction [173, 189–192]. In iron, the experimental band width [193–195] is 10% smaller than the DFT prediction [176]. The LSDA also overestimates the exchange splitting. Nickel is again an extreme case where the exchange splitting is twice as large as measured in experiment [173, 190–192]. In addition, x-ray photoemission spectroscopy (XPS) reveals satellite structures in the density of states (DOS) of nickel and iron at 6 eV [191, 196–198] and 3.2 eV [199] binding energy, respectively. These satellites are not reproduced in the LSDA approach. Furthermore, experiments indicate a strong broadening of the quasiparticle peaks at the bottom of the *d* bands due to many body effects, which are not accessible in an independent-electron theory such as DFT. In cobalt, the majority spin quasiparticle peaks disappear for binding energies larger than 2 eV [61]. The strong broadening of the quasiparticle peaks as well as the satellite structures in the density of states emphasize the importance of many-body effects for the transition metals. The *GW* approximation partly cures the shortcomings of the LSDA approach. Aryasetiawan [200] has shown that treating nickel within the *GW* approximation yields a 3*d*-band width in good agreement with experiment. This result has been confirmed by Friedrich *et al.* [72]. They find a reduction of the band width from 4.0 eV in LSDA to 3.2 eV in the *GW* approach in accordance with the experimental finding [173, 189–192]. In iron, the situation is similar. While the band width, experimentally found to be 3.3 eV [193–195], is overestimated in the LSDA approach, the *GW* result is in good agreement with experiment [176]. The *GW* approximation, however, does not account for the description of satellites and also the exchange splitting is hardly improved. Aryasetiawan [200] argues that the overestimation of the exchange splitting and the missing satellite structure are related features that need a treatment beyond the *GW* approximation taking into account particle-particle scattering. Penn [201] and Liebsch [202] have shown within the Hubbard model employing a *T*-matrix formulation that the hole-hole scattering leads to the occurence of the 6 eV satellite in nickel and, furthermore, it gives rise to a reduction of the exchange splitting. Springer *et al.* [203] have applied an *ab initio T*-matrix theory to the 6 eV satellite of nickel. Indeed they found the satellite structure due to multiple hole-hole scattering processes and a significant reduction of the exchange splitting.

Zhukov *et al.* [67–70,204] employed a combined *GW* and *T*-matrix (*GW*+*T*) approach that accounts for non-spin-flip and spin-flip excitations in metallic systems to study lifetime effects of excited electrons. They found that the non-spin-flip scattering gives an important contribution to the inverse lifetime of the minority excited electrons. While the spin-flip scattering of electronic states in nickel appears to be weak and independent of the spin state, in iron the spin-flip scattering causes a strong reduction of the lifetimes of the minority states compared to the majority states. Zhukov *et al.* [67] conclude that the inclusion of spin-flip processes improves the agreement of the minority spin lifetimes in iron between theory and experiment [60]. Interestingly, they find that free-electron-like minority states and all the majority excited electron states are weakly affected by spin-flip scattering in iron.

Recent high-resolution ARPES measurements reveal further correlation effects in the transition metals which are not fully accounted for in the *GW* approach and which have not been studied yet within the *GW*+*T* approach. Higashiguchi *et al.* [205] conducted a high-resolution ARPES measurement of ferromagnetic nickel. They observed a kink structure in the energy band dispersion at 40 meV binding energy, which they attributed to the electron-phonon interaction. They emphasize, however, that the observed effective-mass enhancement indicates many-body effects beyond the electron-phonon interaction. While the occurrence of kink structures due to the coupling of electrons to phonons is well understood, there is an ongoing debate on the origin of kink structures at higher binding energies. Hofmann *et al.* [59] found a kink structure at an unusually high binding energy of 300 meV. Schäfer *et al.* [58] found a similar kink structure for a surface state of iron at 160 meV binding energy. In both cases, the kink structures are attributed to a coupling mechanism of the electrons to spin-wave excitations. Schäfer *et al.* [206] found in a subsequent ARPES study on bulk iron a strong effective-mass enhancement of bulk states when compared to a DFT calculation employing the generalized gradient approximation (GGA). They discuss the experimentally measured effective masses in view of correlation effects and the coupling of electrons to magnetic excitations.

In strongly correlated materials, on the other hand, kink structures have been found which are not related to an electron-boson coupling mechanism. Calculations based on pure electron-electron interactions employing the dynamical mean-field theory (DMFT) [207–209] predicted a kink structure in the electron dispersion for any (strongly) correlated material, showing two separate regimes of quasiparticle renormalization [210]. Held *et al.* [211] explain the physical mechanism behind the

emergence of such kinks. The combined LDA+DMFT approach [212–215] applied to $SrVO_3$ yields a kink structure at the energy of 150 meV below the Fermi level [216] as observed experimentally [217]. The LDA+DMFT approach can be viewed as the dynamic extension of the LDA+U approach [212], which was an early attempt to correct the LDA by a static mean-field Hubbard U term for localized states. Unfortunately, the LDA+U approach and the LDA+DMFT approach rely on additional parameters, most notably the Hubbard U. Its calculation from first principles relies, usually, on one of two approaches, either on the constrained LDA [218] or the constrained random-phase approximation [219, 220].

The application of the LDA+DMFT approach to iron leads to a strong damping of the majority quasiparticle states below 1 eV binding energy [65]. A combined analysis of an ARPES experiment and a LDA+DMFT calculation on iron conducted by Sánchez-Barriga *et al.* [62] indicates that the LDA+DMFT approach improves the description of correlation effects. The mass renormalization, however, is too small within the LDA+DMFT approach. A subsequent investigation of Fe, Co, and Ni [63, 64] revealed that for a quantitative agreement between experiment and theory more sophisticated many-body calculations are needed. In particular, the linewidth of the quasiparticle peaks obtained within a LDA+DMFT approach tends to be underestimated compared to experiment. Grechnev *et al.* [66] found in a LDA+DMFT study for Fe, Co, and Ni that the main correlation effects are present in the majority spin channel. In particular, they find a strong quasiparticle broadening for the majority hole states. While the LDA+DMFT approach improves the description of correlation effects, it has conceptual problems such as a double-counting correction and the dependence on parameters. Biermann *et al.* [221] proposed a GW+DMFT scheme, which is derived from a free-energy functional introduced by Almbladh [222]. In a self-consistent implementation of the GW+DMFT scheme the Hubbard U interaction and the double-counting correction are uniquely defined. A first application of the GW+DMFT approach to real materials has been achieved by Tomczak *et al.* [223]. Their study of $SrVO_3$ and subsequent investigations [224–226] show that the GW+DMFT scheme inherits the advantages of both theories. The nonlocal GW self-energy accounts for the reduction of the band width, overestimated in the LDA+DMFT scheme, and the local self-energy leads to a renormalization of the quasiparticle energies with the emergence of kink structures in the vicinity of the Brillouin zone (BZ) center.

The DMFT approach, either combined with LDA or with GW, is capable of de-

scribing kink structures in strongly correlated materials. In intermediately correlated systems such as the transition metals, however, the emergence of kink structures has not been reported, yet. Just as well, kink structures have not been studied within the *GW*+*T* theory so far. So, it remains an open question what the origin of the kink structures in the transition metals [58,59] is. Moreover, the reason for the strong mass renormalization as well as the strong quasiparticle broadening observed experimentally [61–64,206] in these materials is still under debate. In the following, we address these questions by means of a *T*-matrix approach. The next section gives a derivation of the *T*-matrix formulation of the self-energy beyond the *GW* approximation. Section 4.3 lays out the details of the implementation. The quasiparticle concept is reviewed in Section 4.4, and a formal discussion of the previously introduced *GT* self-energy is given in Section 4.5. The computational details of the calculations are presented in Section 4.6. We show results for iron, cobalt, and nickel in Section 4.7, and finally Section 4.8 concludes our findings.

4.2 Theory

The *GW* approximation has become a standard method in electronic structure calculations. It successfully reproduces many of the excited-state properties of a wide range of materials and usually improves over the results obtained from LDA calculations. Nevertheless, the *GW* approximation has also some shortcomings, e.g. one-shot *GW* calculations of the transition metals neither improve the exchange splitting nor do they give rise to satellite structures. In addition, plasmarons, which are plasmons dressed with clouds of eletrons and which were predicted by Hedin and Lundqvist [74, 227–230], appear at the wrong energetic position within the *GW* approximation. To account for this, one needs to go beyond the *GW* approximation. One alternative is to combine many-body perturbation theory with the DMFT, which adds a local self-energy to the *GW* approximation in the so-called *GW*+DMFT approach [221]. To go beyond the *GW* approximation within the framework of many-body perturbation theory one can either improve the Green function itself or employ additional self-energy diagrams.

The cumulant expansion [231–233] is a diagrammatic expansion of the Green function. It is an intuitive way to describe an electron-boson coupling mechanism. The cumulant expansion has first been applied to study x-ray spectra of core electrons [234–236]. Bergersen *et al.* [237], Minnhagen [238], and Hedin [231] extended

the formalism to valence electrons. The *GW* plus cumulant approach applied to sodium and aluminum metal [232] and to semiconductors [233] gives rise to multiple plasmon satellites, which are also called plasmarons, electronic polarons [239, 240], or plasmonic polarons [241, 242]. Recently, Caruso *et al.* [241, 242] have shown that the electron-plasmon coupling in the *GW* plus cumulant approach leads to the occurrence of a plasmonic polaron band structure. These new bands appear blueshifted by the plasmon energy from the electronic band structure and strongly broadened.

The diagrammatic expansion of the self-energy itself is another alternative to go beyond the *GW* approximation. The *GW* approximation results from the first iteration of the Hedin equations, where vertex corrections are neglected. The application of first-order vertex corrections to silicon and diamond [243, 244] indicates that vertex corrections are small in these materials. Recently, Ren *et al.* [245] have proposed a second-order screened exchange (SOSEX) correction to the *GW* approximation which improves the highest occupied and lowest unoccupied molecular orbitals in benzene and tetracyanoethylene. Strinati [246] was one of the first who introduced the *T*-matrix approach to study optical properties of semiconductors. The *T*-matrix approach is nowadays routinely applied to study particle-hole excitations, i.e., exciton excitations [247–252] and spin-wave excitations [43, 166, 253]. The *T*-matrix approach has also been employed as a vertex correction to the self-energy [67–69, 203, 204] known as the *GW*+*T* approach. These vertex corrections, however, entail double-counting corrections to account for diagrams present in the *GW* self-energy as well as in the additional *GT* self-energy. Romaniello *et al.* [254] gave an alternative derivation of the *T*-matrix approach to the self-energy allowing to combine the *GW* approximation and higher-order diagrams without the need of double-counting corrections.

We propose a self-energy relying on the *T*-matrix approach that accounts explicitly for spin-flip processes motivated by the expansion of the Hedin self-energy that allows a combination with the *GW* approximation without the need of double-counting corrections. The self-consistent solution of the Hedin equations [71], a set of five integro-differential equations, solves the many-body problem exactly. The self-energy takes the form

$$\Sigma_{\alpha\beta}(12) = \mathrm{i}\sum_{\gamma}\int \mathrm{d}3\,\mathrm{d}4\, G_{\alpha\gamma}(14)W(1^{+}3)\Gamma_{\gamma\beta}(42;3), \tag{4.2.1}$$

where the vertex function is defined as

$$\Gamma_{\alpha\beta}(12;3) = -\frac{\delta G^{-1}_{\alpha\beta}(12)}{\delta U_{\text{eff}}(3)} = \delta(12)\delta(13)\delta_{\alpha\beta} + \frac{\delta\Sigma_{\alpha\beta}(12)}{\delta U_{\text{eff}}(3)} \tag{4.2.2}$$

with the total effective potential U_{eff} (2.1.28), cf. Eqs. (2.1.30) and (2.1.31). Spin indices are denoted by Greek characters. Neglecting vertex corrections $\delta\Sigma/\delta U_{\text{eff}}$ leads to the *GW* approximation (2.1.36). In this approximation the screened interaction W is calculated in the random-phase approximation (RPA) [255–257]. This means that the polarization of the system is approximated by non-interacting electron-hole pairs

$$P(12) = -\mathrm{i}\sum_{\alpha,\beta} G_{\alpha\beta}(12)G_{\beta\alpha}(21^+). \tag{4.2.3}$$

In the following, the self-energy is expanded in terms of the RPA screened interaction, i.e., while vertex corrections are considered for the self-energy, they are neglected for the polarization of the system. Inserting the vertex function (4.2.2) into the self-energy expression (4.2.1) yields

$$\Sigma_{\alpha\beta}(12) = \mathrm{i}G_{\alpha\beta}(12)W(1^+2) + \mathrm{i}\sum_{\gamma}\int \mathrm{d}3\,\mathrm{d}4\, G_{\alpha\gamma}(14)W(1^+3)\frac{\delta\Sigma_{\gamma\beta}(42)}{\delta U_{\text{eff}}(3)}, \tag{4.2.4}$$

the *GW* self-energy plus an additional self-energy contribution that contains the functional derivative of the self-energy with respect to the effective potential. The successive reinsertion of the self-energy on the right-hand side generates self-energies of ever increasing order in the screened interaction W. The functional derivative of the self-energy involves the response of the Green function

$$\frac{\delta G_{\alpha\beta}(12)}{\delta U_{\text{eff}}(3)} = -\sum_{\gamma,\delta}\int \mathrm{d}4\,\mathrm{d}5\, G_{\alpha\gamma}(14)\left(\delta(45)\delta(43)\delta_{\gamma\delta} + \frac{\delta\Sigma_{\gamma\delta}(45)}{\delta U_{\text{eff}}(3)}\right)G_{\delta\beta}(52), \tag{4.2.5}$$

as well as a functional derivative of the screened interaction, which is

$$\frac{\delta W(12)}{\delta U_{\text{eff}}(3)} = \int \mathrm{d}4\,\mathrm{d}5\, W(14)\frac{\delta P(45)}{\delta U_{\text{eff}}(3)}W(52), \tag{4.2.6}$$

where the variation of the polarization function in the random-phase approximation is

$$\frac{\delta P(12)}{\delta U_{\text{eff}}(3)} = -\mathrm{i}\sum_{\alpha,\beta}\left(\frac{\delta G_{\alpha\beta}(12)}{\delta U_{\text{eff}}(3)}G_{\beta\alpha}(21^+) + G_{\alpha\beta}(12)\frac{\delta G_{\beta\alpha}(21^+)}{\delta U_{\text{eff}}(3)}\right). \tag{4.2.7}$$

The Eqs. (4.2.5) - (4.2.7) together with Eq. (4.2.4) result in the desired expansion of

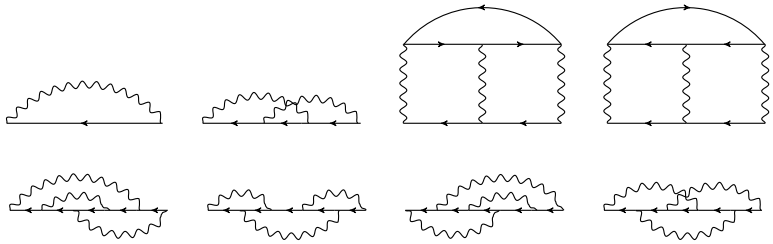

Figure 4.1: Feynman diagrams of the expansion of the Hedin self-energy up to the third order in the screened interaction (wiggly line). The Green function is denoted by an arrow.

the self-energy. The following discussion of the self-energy contributions focuses on collinear magnetic systems in which the Green function is diagonal in spin space $G_{\alpha\beta}(12) = G_\alpha(12)\delta_{\alpha\beta}$ with $\alpha = \{\uparrow, \downarrow\}$. The expansion of the self-energy up to the third order in the screened interaction is shown in terms of Feynman diagrams in Fig. 4.1. It has been discussed by Hedin and Lundqvist [71, 74] already. The expansion constitutes of two distinct types of diagrams: exchange diagrams and diagrams called direct terms that contain a loop formed by Green functions. The *GW* self-energy is an exchange self-energy in which the exchange process is mediated by the screened interaction. It occurs as the first-order self-energy $\Sigma_\alpha^{(1)}$ expanded in the screened interaction. The next higher-order contribution is the second-order screened exchange (SOSEX) self-energy

$$\Sigma_\alpha^{(2)}(12) = \int \mathrm{d}3\,\mathrm{d}4\, G_\alpha(14)W(13)G_\alpha(43)W(42)G_\alpha(32). \tag{4.2.8}$$

The SOSEX self-energy is an exchange self-energy in which the effective interaction takes the form of a particle-particle (pp) T matrix

$$T_{\alpha\alpha}^{(2),\mathrm{pp}}(13,42) = -W(13)K_{\alpha\alpha}^{\mathrm{pp}}(13,42)W(42) \tag{4.2.9}$$

with the non-interacting particle-particle propagation

$$K_{\alpha\alpha'}^{\mathrm{pp}}(12,34) = \mathrm{i}G_\alpha(13)G_{\alpha'}(24). \tag{4.2.10}$$

In collinear magnetic systems, exchange diagrams do not contain spin-flip processes. The reason is that exchange is a quantum mechanical effect that stems from the indistinguishability of the electrons. In a collinear magnetic system, two electrons are

indistinguishable only if they have the same spin. Consequently, an exchange contribution to the self-energy is only non-zero in collinear magnetic systems if the spin is equal. This can also be seen from the Feynman diagrams in Fig. 4.1. In an exchange diagram, all Green functions contained in it are directly connected to each other. In collinear magnetic systems, these Green functions are diagonal in spin-space so that the spin of the connected Green functions must be the same for a non-vanishing contribution. Therefore, the SOSEX self-energy

$$\Sigma_{\alpha}^{(2)}(12) = \mathrm{i}\int \mathrm{d}3\,\mathrm{d}4\, G_{\alpha}(43) T_{\alpha\alpha}^{(2),\mathrm{pp}}(13,42) \tag{4.2.11}$$

as well as all the exchange self-energies of the third order, see lower row of Fig. 4.1, do not contain spin-flip processes. We search, however, for a self-energy beyond the *GW* approximation that explicitly takes into account spin-flip processes. Besides the exchange self-energies, two non-exchange self-energies, so-called direct terms, occur in the expansion of the self-energy. These direct terms are shown as the third and the fourth diagram in the upper row of Fig. 4.1. In contrast to an exchange self-energy, a direct term contains spin-flip processes as the Green functions which are solely connected by the screened interaction can have different spins. The direct terms can be formulated in the T-matrix approach similar to that of the SOSEX. The effective interaction in the direct diagrams involves a particle-hole (ph) propagator

$$K_{\alpha\alpha'}^{\mathrm{ph}}(12,34) = \mathrm{i}G_{\alpha}(13)G_{\alpha'}(42) \tag{4.2.12}$$

in addition to the particle-particle propagator (4.2.10). The effective interaction corresponds to a particle-particle and particle-hole scattering that reads

$$T_{\alpha\alpha'}^{(3),\mathrm{pp/ph}}(13,24) = -\int \mathrm{d}5\,\mathrm{d}6\, W(13) K_{\alpha\alpha'}^{\mathrm{pp/ph}}(13,56) W(56) K_{\alpha\alpha'}^{\mathrm{pp/ph}}(56,24) W(24) \tag{4.2.13}$$

formulated in terms of a particle-particle and a particle-hole T matrix, respectively. The corresponding self-energies

$$\Sigma_{\alpha}^{(3)}(12) = -\mathrm{i}\sum_{\alpha'}\int \mathrm{d}3\,\mathrm{d}4\, \left[T_{\alpha\alpha'}^{(3),\mathrm{ph}}(13,24)G_{\alpha'}(34) + T_{\alpha\alpha'}^{(3),\mathrm{pp}}(13,24)G_{\alpha'}(43)\right] \tag{4.2.14}$$

contain contributions from non-spin-flip ($\alpha = \alpha'$) and spin-flip ($\alpha = -\alpha'$) processes. In summary, the expansion of the Hedin self-energy in terms of the RPA screened interaction yields self-energies of two different types. The exchange diagrams like the

GW self-energy, the SOSEX self-energy, and the higher-order exchange self-energies do not account for spin-flip processes in collinear magnetic systems. Therefore, these diagrams are irrelevant to describe the effect of spin-flip scattering on the electronic spectrum. In contrast, direct terms can take spin-flip processes into account. The expansion of the self-energy leads to a vertex correction in the flavor of the *GW*+*T* approach that does not require a double-counting correction. The particle-particle T matrix has been used for the investigation of the 6 eV satellite in nickel [203]. The non-spin-flip contribution of the particle-hole channel accounts for excitonic effects, which are important for the optical properties of semiconductors [240, 246, 258]. It is the spin-flip part of the particle-hole channel with opposite spins $\alpha = -\alpha'$

$$\Sigma^{(3)}_{\alpha}(12) = -\mathrm{i} \int \mathrm{d}3\, \mathrm{d}4\, T^{(3)}_{\alpha\alpha'}(13,24) G_{\alpha'}(34) \tag{4.2.15}$$

that is expected to be particularly important for ferromagnetic materials. The third-order *GT* self-energy (4.2.15) accounts for the coupling of electrons to spin-flip excitations. Collective spin-wave excitations, however, are not fully accounted for in the T matrix of third order. They arise from the correlated motion of electron-hole pairs with opposite spins. The diagram of the third-order T matrix has the characteristic form of a ladder diagram where the rungs of the ladder correspond to the interaction and its rails correspond to the electron and hole propagation. The ladder approximation sums up the ladder diagrams to infinite order in the interaction. Thereby, it extends the third-order T matrix to a multiple-scattering T matrix, which accounts for the single-particle excitations and the collective spin-wave excitations. The ladder approximation has been employed in the magnetic response function, in which the collective spin-wave excitations show up as sharp peaks in its spectral function, see Section 3.2. In the ladder approximation, the multiple-scattering T matrix is the solution of the Bethe-Salpeter equation

$$T_{\alpha\alpha'}(12,34) = T^{(3)}_{\alpha\alpha'}(12,34) + \int \mathrm{d}5\, \mathrm{d}6\, W(12) K_{\alpha\alpha'}(12,56) T_{\alpha\alpha'}(56,34). \tag{4.2.16}$$

The T matrix is an effective interaction driven by spin-flip excitations and, in particular, the collective spin-wave excitations, also known as magnons, play an important role. We refer to the multiple-scattering electron-hole T matrix with opposite spins as the magnon-induced effective interaction. We employ this effective interaction in the self-energy expression (4.2.15) instead of the third-order T matrix. The resulting

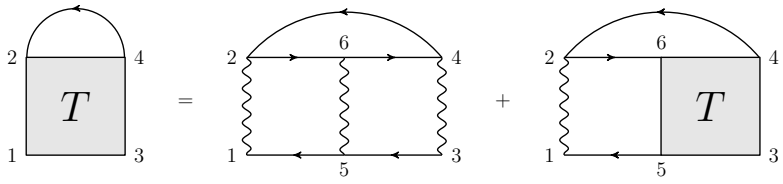

Figure 4.2: Feynman diagram of the electron-magnon self-energy in the ladder approximation. Notation as in Fig. 4.1.

self-energy, whose diagram is shown in Fig. 4.2,

$$\Sigma_\alpha(13) = -\mathrm{i}\int \mathrm{d}2\,\mathrm{d}4\, T_{\alpha\alpha'}(12,34)G_{\alpha'}(24) \tag{4.2.17}$$

is referred to as the *GT* approximation in the present context. By using the term *GT* self-energy we implicitly assume opposite spins $\alpha = -\alpha'$. The *GT* approximation does not require a double-counting correction if it is combined with the *GW* approximation. The *GT* approximation generally takes into account the coupling of electrons to spin-flip excitations. In particular, it accounts for the coupling of electrons to magnons, which is expected to be of special importance in ferromagnetic materials. Therefore, the *GT* self-energy is also referred to as the electron-magnon self-energy.

The *GT* approximation describes the electron-magnon scattering in terms of magnon exchange processes, which is formally similar to the electron-phonon self-energy where phonon exchange processes are described. In case of the electron-phonon interaction it was shown by Migdal [259] that phonon exchange processes in first order, i.e., without vertex corrections, are sufficient to describe the electron-phonon scattering despite the strength of the electron-phonon interaction. The Migdal theorem states that vertex corrections to the electron-phonon self-energy are proportional to the inverse square root of the mass of the nuclei in atomic units and are therefore negligible. The question arises what is the importance of vertex corrections for the electron-magnon self-energy. The vertex corrections to the electron-magnon self-energy in the *GT* approximation leads to similar diagrams as in Fig. 4.1 with the screened interaction W replaced by the magnon propagator T. Analyzing these vertex corrections up to the third order in the magnon propagator one notices that the second-order exchange diagram, shown as the second diagram in the top row of that figure, and all third-order diagrams except one vanish without spin-orbit coupling. The only non-vanishing vertex correction yields an exchange self-energy contribution of third order in the magnon propagator T, it has the shape of the last

self-energy diagram in the lower row of Fig. 4.1 with W replaced by T. This self-energy diagram describes a propagating particle that undergoes several spin flips of which at least one is a minority spin flip. In the case of strong ferromagnetism where only majority spin flips are possible the corresponding contribution would vanish. While in general also minority spin flips are possible in ferromagnetic materials, these processes are much more unlikely than majority spin flips. Therefore, such a self-energy contribution is expected to be considerably less important than the GT self-energy (4.2.17) and is neglected in the following.

Another important question is how the GT self-energy relates to commonly employed realizations of the dynamical mean-field theory (DMFT). In the framework of the DMFT [209,214,215] the interacting many-body problem is mapped onto a (single site) quantum impurity model, which is embedded in a bath system and is subject to a self-consistency condition. The quantum impurity model lies at the heart of the DMFT and various impurity solvers have been implemented. For the description of the transition metals within the DMFT [62–66] the spin-polarized T-matrix fluctuation exchange (SPTF) approximation proposed by Katsnelson *et al.* [65, 260, 261] is often used. The fluctuation exchange (FLEX) approximation is a perturbative expansion of the self-energy in powers of the interaction U that resums ladder diagrams treating particle-particle and particle-hole excitations on the same footing [262–264]. Thereby, the FLEX self-energy accounts for the interaction of (longitudinal and transversal) spin, charge, and particle-particle fluctuations, i.e., the FLEX approximation contains the Hartree diagram, the GW approximation, the SOSEX self-energy, and higher-order diagrams in terms of the T-matrix approach. The SPTF approximation [65, 260, 261] refines the symmetric treatment of the particle-particle and particle-hole channel within the FLEX approximation. That is, the SPTF approximation makes use of the fact that the main correlation effects in magnetism stem from the electron-hole channel while the particle-particle channel is essential for the renormalization of the effective interactions. To this end, the bare interaction U that mediates the correlation among the electron-hole pairs is replaced by the static limit of the spin-polarized particle-particle T matrix. In this work, we include a subset of the scattering channels accounted for in the SPTF. In particular, the electron-magnon scattering in the GT approximation is combined with the static limit of the GW approximation. On the other hand the self-energy calculated within single site DMFT is purely local and extensions to cluster methods yield at most a limited access to the momentum dependence of the self-energy in practice. Thus, the DMFT approach

does not permit to study phenomena which stem from nonlocal self-energy effects. In the many-body perturbation theory, however, the full $\mathbf{k}$ dependence of the self-energy is taken into account and, therefore, nonlocal effects are treated naturally. In particular, the GT self-energy allows to investigate phenomena which might arise from the spatial extension of the spin-wave excitations. Indeed, we find features in the renormalized quasiparticle band dispersions for the elementary ferromagnets, which have not been reported by DMFT calculations and which can be attributed to the nonlocal treatment of the self-energy. The discussion proceeds with a presentation of the implementation of the GT approximation.

4.3 Implementation

The GT self-energy approximation contains the multiple-scattering spin-flip T matrix. The T matrix is a four-point function as it depends on four space and time variables just as the four-point magnetic response function discussed in Section 3.3. For a practical implementation, the GT self-energy (4.2.17) is too complex. To reduce its complexity, we apply the same approximations that have been used already for the implementation of the magnetic response function. First, the implementation makes use of the fact that the Hamiltonian is not explicitly time dependent. As a consequence, the number of independent time variables reduces to three. Since the spin-wave excitations are low-energy excitations, it is reasonable to approximate the screened interaction for all frequencies by its static limit. This implies that the interaction is instantaneous in time, i.e., $W(12) = W(\mathbf{r}_1, \mathbf{r}_2)\delta(t_1 - t_2)$. As a result of the static approximation, the self-energy (4.2.17) depends on a single time or frequency argument

$$\Sigma_\alpha(\mathbf{r}_1, \mathbf{r}_3; \omega) = \frac{-\mathrm{i}}{2\pi} \int_{-\infty}^{\infty} \mathrm{d}\omega' \int \mathrm{d}\mathbf{r}_2 \, \mathrm{d}\mathbf{r}_4 \, G_{\alpha'}(\mathbf{r}_2, \mathbf{r}_4; \omega - \omega') \, T_{\alpha\alpha'}(\mathbf{r}_1, \mathbf{r}_2; \mathbf{r}_3, \mathbf{r}_4; \omega'). \tag{4.3.1}$$

For the evaluation of the frequency convolution two different methods have been implemented. One of the methods makes use of the Green function's Lehman representation, which allows to perform a contour integration. As an alternative approach, the self-energy calculated as a function of an imaginary frequency argument is analytically continued to real frequencies. Besides the frequency integration, which is discussed in Section 4.3.2, the dependence of the T matrix on four space variables is a major challenge in terms of the numerical demand. A formulation in a Wannier

basis [46, 47] allows an efficient truncation of the T matrix in real space.

4.3.1 Formulation in a Wannier Basis

A formulation in a Wannier basis allows an efficient treatment of the real space integrations, necessary for the evaluation of the self-energy. The self-energy is calculated starting from a mean-field solution, e.g., a density-functional theory calculation may serve as starting point. Under the assumption that the single-particle wave functions are a good approximation to the quasiparticle wave functions, the self-energy matrix represented in the single-particle states is practically diagonal. The self-energy (4.3.1) represented with respect to a single-particle state $\varphi^{\alpha}_{\mathbf{q}n}(\mathbf{r})$ with Bloch-momentum $\mathbf{q}$, band n, and spin α reads

$$\Sigma^{\alpha}_{\mathbf{q}n}(\omega) = \frac{-\mathrm{i}}{2\pi}\int_{-\infty}^{\infty}\mathrm{d}\omega' \int \mathrm{d}\mathbf{r}_1\,\mathrm{d}\mathbf{r}_2\,\mathrm{d}\mathbf{r}_3\,\mathrm{d}\mathbf{r}_4 \times \varphi^{\alpha *}_{\mathbf{q}n}(\mathbf{r}_1) G_{\alpha'}(\mathbf{r}_2,\mathbf{r}_4;\omega-\omega')\, T_{\alpha\alpha'}(\mathbf{r}_1,\mathbf{r}_2;\mathbf{r}_3,\mathbf{r}_4;\omega')\varphi^{\alpha}_{\mathbf{q}n}(\mathbf{r}_3). \quad (4.3.2)$$

The evaluation of the self-energy is a challenging task, in particular, the T matrix, which explicitly depends on four space arguments, makes the real space integrations costly. The T matrix is treated in the ladder approximation where the interaction between the electron-hole pairs is the screened interaction W within the random-phase approximation. In metallic systems, which are of central interest in the present work, screening is very efficient and consequently the interaction is short-range. The short-rangeness of W allows to employ an on-site approximation for the interaction. The on-site approximation means that electron-hole pairs located on the same atomic site interact with each other, while off-site interactions are neglected, cf. Fig. 3.2. The short-rangeness of W motivates to formulate the theory in a basis of maximally localized Wannier functions [46, 47]. Wannier functions are given by the Fourier transforms of the single-particle wave functions, cf. Eq. (3.3.3). The T matrix is truncated in real space by employing a set of Wannier orbitals, denoted by n_i, for its representation

$$T_{\alpha\alpha'}(\mathbf{r}_1,\mathbf{r}_2;\mathbf{r}_3,\mathbf{r}_4;\omega) = \sum_{\mathbf{R},\mathbf{R}'}\sum_{n_1,n_2,n_3,n_4} w^{\alpha}_{\mathbf{R}n_1}(\mathbf{r}_1) w^{\alpha' *}_{\mathbf{R}n_2}(\mathbf{r}_2) \times T^{\alpha\alpha'}_{\mathbf{R}n_1\mathbf{R}n_2,\mathbf{R}'n_3\mathbf{R}'n_4}(\omega) w^{\alpha *}_{\mathbf{R}'n_3}(\mathbf{r}_3) w^{\alpha'}_{\mathbf{R}'n_4}(\mathbf{r}_4). \quad (4.3.3)$$

The set of Wannier functions has to be chosen such that the physical properties are represented appropriately. In particular, the T matrix describes the collective spin-wave excitations. In the elementary ferromagnets these excitations arise mainly from the states close to the Fermi level. Therefore, it is that energy subspace which is most important. The states close to the Fermi level have predominantly d character and a minimal Wannier basis set should contain at least the five d orbitals. Combining the T matrix represented in such a way with the Lehman representation of the non-interacting Green function (3.3.4) reduces the four real-space integrations in the self-energy expression (4.3.2) to a summation over the lattice sites $\mathbf{R}$ and $\mathbf{R}'$ of the supercell as well as a sum of the set of Wannier orbitals n_i

$$\Sigma^{\alpha}_{\mathbf{q}n}(\omega) = \frac{-\mathrm{i}}{2\pi N}\int_{-\infty}^{\infty}\mathrm{d}\omega' \sum_{\mathbf{k}}\sum_{m}^{\text{all}}\sum_{\mathbf{R},\mathbf{R}'}\sum_{n_1,n_2,n_3,n_4} e^{-\mathrm{i}(\mathbf{q}-\mathbf{k})(\mathbf{R}-\mathbf{R}')} \times \frac{T^{\alpha\alpha'}_{\mathbf{R}n_1\mathbf{R}n_2,\mathbf{R}'n_3\mathbf{R}'n_4}(\omega') U^{\alpha}_{\mathbf{q}n,n_1} U^{\alpha'*}_{\mathbf{k}m,n_2} U^{\alpha*}_{\mathbf{q}n,n_3} U^{\alpha'}_{\mathbf{k}m,n_4}}{\omega - \omega' - \epsilon^{\alpha'}_{\mathbf{k}m} + \mathrm{i}\eta\mathrm{sgn}(\epsilon^{\alpha'}_{\mathbf{k}m} - \epsilon_{\mathrm{F}})}. \quad (4.3.4)$$

The T matrix depends only on the difference of the lattice site position $\Delta\mathbf{R} = \mathbf{R} - \mathbf{R}'$. Therefore, the summations over all lattice sites $\mathbf{R}$ and $\mathbf{R}'$ correspond to a lattice Fourier transformation from the space of lattice sites to the space of lattice momenta

$$\Sigma^{\alpha}_{\mathbf{q}n}(\omega) = \frac{-\mathrm{i}}{2\pi}\int_{-\infty}^{\infty}\mathrm{d}\omega' \sum_{\mathbf{k}'}\sum_{m}^{\text{all}}\sum_{n_1,n_2,n_3,n_4} \times \frac{T^{\alpha\alpha'}_{n_1n_2,n_3n_4}(\mathbf{k}',\omega') U^{\alpha}_{\mathbf{q}n,n_1} U^{\alpha'*}_{\mathbf{q}-\mathbf{k}'m,n_2} U^{\alpha*}_{\mathbf{q}n,n_3} U^{\alpha'}_{\mathbf{q}-\mathbf{k}'m,n_4}}{\omega - \omega' - \epsilon^{\alpha'}_{\mathbf{q}-\mathbf{k}'m} + \mathrm{i}\eta\mathrm{sgn}(\epsilon^{\alpha'}_{\mathbf{q}-\mathbf{k}'m} - \epsilon_{\mathrm{F}})}, \quad (4.3.5)$$

where the summation over the Brillouin zone has been shifted by $\mathbf{k} = \mathbf{q} - \mathbf{k}'$ for convenience. The summation over states m is practically restricted to the number of single-particle wave functions which are used within the construction of the Wannier functions. The self-energy (4.3.5) is amenable for a numerical treatment. The next section addresses the convolution of the Green function and the T matrix in the frequency domain.

4.3.2 Frequency Integration

The calculation of the GT self-energy (4.3.5) requires the evaluation of the convolution of the Green function G and the T matrix in the frequency domain. To this end, two methods, the contour-integration method and the analytic-continuation method, have been implemented.

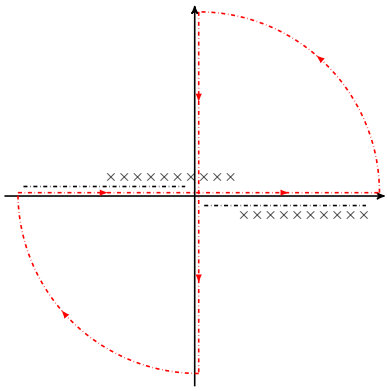

Figure 4.3: The contour integration path that is used for the evaluation of the convolution of the electronic Green function G and the T matrix in the frequency domain. Crosses depict the poles of the Green function and the dash-dotted line indicates the pole distribution of the T matrix.

Contour-Integration Method

The contour-integration method has been introduced by Godby *et al.* [265] as an efficient way to calculate self-energy operators. Since then the contour integration has been routinely applied to the calculation of the *GW* self-energy. We have adapted the contour-integration method to evaluate the convolution of the Green function and the T matrix in the frequency domain. The integrand, consisting of G and T, has a lot of structure along the real frequency axis. For this reason, to obtain accurate results an explicit evaluation of the integral along the real frequency axis would require an excessive computational effort. The contour-integration method bypasses this problem. It makes use of the fact that the distribution of the integrand's poles are known, see Fig. 4.3. The poles of the Green function are known exactly, these are located at the single-particle energies shifted with respect to the frequency argument of the self-energy. The poles of the T matrix are not known exactly, but their distribution is known. The poles lie in the upper half plane for negative real frequencies and in the lower half plane for positive real frequencies. These pieces of information are sufficient to replace the integration along the real frequency axis by the contour integration shown in Fig. 4.3. It relates the integration along the real frequency axis to an integration along the imaginary frequency axis plus the sum over the poles of the Green function falling into the contour path. According to Cauchy's integral formula, the sum of the Green function's poles demands the evaluation of

the T matrix at those poles. One alternative could be to evaluate the T matrix as a function of real frequencies and obtain the T matrix at the Green function's pole by an interpolation scheme. This approach, however, demands the T matrix to be calculated on a dense mesh of real frequencies. Therefore, an alternative approach is employed which makes use of the imaginary frequency axis. There, the T matrix is a smooth function which permits a Padé approximation for the T matrix calculated for an exponential imaginary frequency mesh of the form

$$\omega_i = \frac{x^i - x}{x^n - x}\,\omega_{\max}, \tag{4.3.6}$$

where x determines the exponentially increasing distance between the n mesh points with a maximal frequency $\omega_{\max}$. The Padé approximation is a representation of the T matrix as a sum of effective poles. The Padé approximation, in turn, allows to obtain the value of the T matrix at the real-valued poles of the Green function by means of an analytic continuation. In addition, the Padé approximation allows to perform the integration along the imaginary frequency axis analytically. The technical details of the Padé approximation and its use within the contour-integration method are described in the Appendix A.

Analytic-Continuation Method

The method of analytic continuation [266, 267] allows the evaluation of self-energy operators in the frequency domain, it is an alternative to the contour-integration method. The analytic continuation avoids the integration along the real-frequency axis entirely. To this end, the T matrix and the Green function are evaluated along the imaginary frequency axis. There, the integrand is a smooth function which allows an efficient calculation of the self-energy. The self-energy as a function of imaginary frequencies $z = \mathrm{i}\omega$ is connected to the time domain by means of a Laplace transformation

$$\Sigma_\alpha(\mathbf{r}_1, \mathbf{r}_3; z) = -\mathrm{i}\int_0^\infty \mathrm{d}\tau \int \mathrm{d}\mathbf{r}_2\,\mathrm{d}\mathbf{r}_4\, e^{-z\tau}\, G_{\alpha'}(\mathbf{r}_2, \mathbf{r}_4; \tau)\, T_{\alpha\alpha'}(\mathbf{r}_1, \mathbf{r}_2; \mathbf{r}_3, \mathbf{r}_4; \tau). \tag{4.3.7}$$

The inverse Laplace transformation

$$T_{\alpha\alpha'}(\mathbf{r}_1, \mathbf{r}_2; \mathbf{r}_3, \mathbf{r}_4; \tau) = \frac{1}{2\pi\mathrm{i}}\int_{\eta-\mathrm{i}\infty}^{\eta+\mathrm{i}\infty} \mathrm{d}z'\, e^{z'\tau} T_{\alpha\alpha'}(\mathbf{r}_1, \mathbf{r}_2; \mathbf{r}_3, \mathbf{r}_4; z') \tag{4.3.8}$$

with a positive infinitesimal $\eta \to 0^+$ yields the self-energy as a function of complex frequencies

$$\Sigma_\alpha(\mathbf{r}_1, \mathbf{r}_3; z) = \frac{-1}{2\pi} \int_{\eta - i\infty}^{\eta + i\infty} \mathrm{d}z' \int \mathrm{d}\mathbf{r}_2 \, \mathrm{d}\mathbf{r}_4 \, G_{\alpha'}(\mathbf{r}_2, \mathbf{r}_4; z - z') \, T_{\alpha\alpha'}(\mathbf{r}_1, \mathbf{r}_2; \mathbf{r}_3, \mathbf{r}_4; z'). \tag{4.3.9}$$

In the Wannier-basis formulation the diagonal element of the self-energy as a function of imaginary frequencies is

$$\Sigma^\alpha_{\mathbf{q}n}(z) = \frac{-1}{2\pi} \int_{\eta - \mathrm{i}\infty}^{\eta + \mathrm{i}\infty} \mathrm{d}z' \sum_{\mathbf{k}'} \sum_{m}^{\text{all}} \sum_{n_1, n_2, n_3, n_4} \times \frac{T^{\alpha\alpha'}_{n_1 n_2, n_3 n_4}(\mathbf{k}', z') U^{\alpha}_{\mathbf{q}n, n_1} U^{\alpha' *}_{\mathbf{q}-\mathbf{k}'m, n_2} U^{\alpha *}_{\mathbf{q}n, n_3} U^{\alpha'}_{\mathbf{q}-\mathbf{k}'m, n_4}}{z - z' - \epsilon^{\alpha'}_{\mathbf{q}-\mathbf{k}'m}}. \tag{4.3.10}$$

This expression corresponds to the self energy (4.3.5) analytically continued to the imaginary frequency axis. The poles of the integrand, the Green function, and the T matrix are located close to the real axis. As a consequence, the integrand has a lot of structure as a function of real frequencies. In contrast, along the imaginary frequency axis the integrand is a smooth function so that the integration along that axis can be done efficiently using a coarse frequency mesh. For the integration, a Padé approximation of the T matrix is employed that, in turn, allows to perform the integration analytically. The corresponding formulas are shown in the Appendix A. The self-energy as a function of imaginary frequencies has no significance on its own. The physically meaningful self-energy is a function of real frequencies. It is obtained by an analytic continuation of the self-energy (4.3.10). The procedure of the analytic continuation is depicted in Fig. 4.4. In practice, the analytic continuation is done by means of a Padé approximation of the self-energy. That is, the self-energy as a function of imaginary frequencies is represented by a sum of effective poles. This allows to perform the analytic continuation by replacing $\mathrm{i}\omega \to \omega$. The process of analytic continuation must avoid crossing the poles of the self-energy operator. Therefore, the analytic continuation is performed such that the self-energy of positive real frequencies is obtained from the self-energy defined on the positive imaginary axis and vice-versa for the negative axis.

The analytic-continuation method has been implemented as an alternative to the contour-integration method to evaluate the convolution of the Green function and the T matrix in the frequency domain that appears in the self-energy operator (4.3.1). The computational details and a comparison of both methods is discussed in Sec-

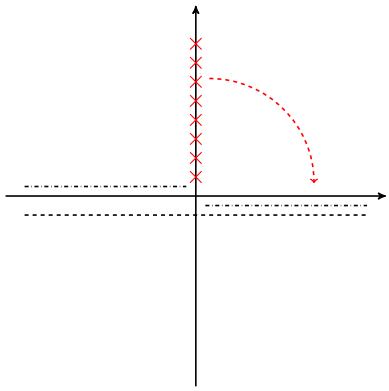

Figure 4.4: The analytic continuation of the self-energy given as a function of imaginary frequencies (red crosses) is performed by means of a Padé approximation. The effective poles of the Padé approximation are depicted as dashed line. The analytic continuation is performed such that no pole of the actual self-energy represented as dash-dotted line is crossed.

tion 4.6. Prior to that, the next section reviews the quasiparticle concept and Section 4.5 gives a formal discussion of the GT self-energy.

4.4 Quasiparticle Concept

4.4.1 Quasiparticle Equation

The Green function formulation of the many-body problem [82, 83] allows to calculate the quasiparticle energies [268,269]. For this, one needs to solve the quasiparticle equation

$$h_0(\mathbf{r})\psi^{\alpha}_{\mathbf{q}n}(\mathbf{r}) + \int \mathrm{d}\mathbf{r}'\, \Sigma_{\alpha}(\mathbf{r},\mathbf{r}';E^{\alpha}_{\mathbf{q}n})\, \psi^{\alpha}_{\mathbf{q}n}(\mathbf{r}') = E^{\alpha}_{\mathbf{q}n}\, \psi^{\alpha}_{\mathbf{q}n}(\mathbf{r}), \tag{4.4.1}$$

with the Hartree Hamiltonian $h_0(\mathbf{r})$ defined in Eq. (2.1.23), the quasiparticle wavefunction $\psi^{\alpha}_{\mathbf{q}n}(\mathbf{r})$, the quasiparticle energy $E^{\alpha}_{\mathbf{q}n}$, and the exchange-correlation self-energy $\Sigma_{\alpha}(\mathbf{r},\mathbf{r}';\omega)$, which acts as a nonlocal and energy-dependent potential. A convenient starting point is the Kohn-Sham system, which is the solution of the Kohn-Sham equation

$$[h_0(\mathbf{r}) + v^{\alpha}_{\mathrm{xc}}(\mathbf{r})]\ \varphi^{\alpha}_{\mathbf{q}n}(\mathbf{r}) = \epsilon^{\alpha}_{\mathbf{q}n}\, \varphi^{\alpha}_{\mathbf{q}n}(\mathbf{r}) \tag{4.4.2}$$

of the density-functional theory with a (semi-) local-density approximation to the exchange-correlation potential $v^{\alpha}_{\mathrm{xc}}(\mathbf{r})$, the Kohn-Sham eigenfunction $\varphi^{\alpha}_{\mathbf{q}n}(\mathbf{r})$, and the Kohn-Sham energy $\epsilon^{\alpha}_{\mathbf{q}n}$, cf. Section 2.2.1. The exchange-correlation potential can be

seen as a local and energy-independent approximation to the exchange-correlation self-energy that gives the correct ground-state density of the interacting system. Provided that the correction of the self-energy approximation is small compared to the chosen Kohn-Sham starting point, the Kohn-Sham eigenfunctions and Kohn-Sham eigenvalues will be sufficiently close to the quasiparticle solution to apply first-order perturbation theory to solve the quasiparticle equation

$$\begin{aligned}&\left[h_0(\mathbf{r}) + v_{\mathrm{xc}}^{\alpha}(\mathbf{r})\right]\, \varphi_{\mathbf{q}n}^{\alpha}(\mathbf{r}) \\ &\qquad + \int \mathrm{d}\mathbf{r}'\, \left[\Sigma_{\alpha}(\mathbf{r},\mathbf{r}';E_{\mathbf{q}n}^{\alpha}) - v_{\mathrm{xc}}^{\alpha}(\mathbf{r}')\delta(\mathbf{r}-\mathbf{r}')\right]\, \varphi_{\mathbf{q}n}^{\alpha}(\mathbf{r}') = E_{\mathbf{q}n}^{\alpha}\, \varphi_{\mathbf{q}n}^{\alpha}(\mathbf{r}). \quad (4.4.3)\end{aligned}$$

Usually, the off-site elements ($n \neq n'$) of the self-energy matrix are small compared to the diagonal elements. Therefore, the quasiparticle energies are often calculated by considering only the diagonal elements of the self-energy

$$E_{\mathbf{q}n}^{\alpha} = \epsilon_{\mathbf{q}n}^{\alpha} + \int \mathrm{d}\mathbf{r}\,\mathrm{d}\mathbf{r}'\, \varphi_{\mathbf{q}n}^{\alpha *}(\mathbf{r})\, \left[\Sigma_{\alpha}(\mathbf{r},\mathbf{r}';E_{\mathbf{q}n}^{\alpha}) - v_{\mathrm{xc}}^{\alpha}(\mathbf{r}')\delta(\mathbf{r}-\mathbf{r}')\right]\, \varphi_{\mathbf{q}n}^{\alpha}(\mathbf{r}'). \quad (4.4.4)$$

The linearized solution of the quasiparticle equation is found by expanding the self-energy up to the first order in the quasiparticle energy

$$E_{\mathbf{q}n}^{\alpha} = \epsilon_{\mathbf{q}n}^{\alpha} + Z_{\mathbf{q}n}^{\alpha} \int \mathrm{d}\mathbf{r}\,\mathrm{d}\mathbf{r}'\, \varphi_{\mathbf{q}n}^{\alpha *}(\mathbf{r})\, \left[\Sigma_{\alpha}(\mathbf{r},\mathbf{r}';\epsilon_{\mathbf{q}n}^{\alpha}) - v_{\mathrm{xc}}^{\alpha}(\mathbf{r}')\delta(\mathbf{r}-\mathbf{r}')\right]\, \varphi_{\mathbf{q}n}^{\alpha}(\mathbf{r}'), \quad (4.4.5)$$

where the renormalization factor is given by

$$Z_{\mathbf{q}n}^{\alpha} = \left(1 - \int \mathrm{d}\mathbf{r}\,\mathrm{d}\mathbf{r}'\, \varphi_{\mathbf{q}n}^{\alpha *}(\mathbf{r}) \frac{\mathrm{d}\Sigma_{\alpha}(\mathbf{r},\mathbf{r}';\epsilon_{\mathbf{q}n}^{\alpha})}{\mathrm{d}\omega} \varphi_{\mathbf{q}n}^{\alpha}(\mathbf{r}')\right)^{-1}. \quad (4.4.6)$$

The quasiparticle energies obtained in such a way can be compared with the excitation spectrum measured in photoemission experiments.

4.4.2 Spectral Function

A photoemission experiment uses photons to excite electrons out of the crystal. Analyzing the angle resolved energy and momentum distribution of the excited electrons allows to deduce information about the hole left behind in the probe. Thereby, a photoemission experiment yields information about the occupied states in the solid [270]. In contrast, an inverse photoemission experiment uses electrons to probe the unoccupied states of the solid by analyzing the outcoming photons [271–273]. The pho-

toemission intensity measured experimentally is intimately connected to the spectral function of the electronic Green function. Within many-body perturbation theory the Green function is a solution of the Dyson equation

$$G_\alpha(\mathbf{r},\mathbf{r}';\omega)^{-1} = G_{0,\alpha}(\mathbf{r},\mathbf{r}';\omega)^{-1} - \Sigma_\alpha(\mathbf{r},\mathbf{r}';\omega), \tag{4.4.7}$$

with the non-interacting Green function $G_{0,\alpha}$ that solves the Hartree Hamiltonian $h_0(\mathbf{r})$ with eigenenergies $\epsilon^\alpha_{0,\mathbf{q}n}$. The Green function contains the true excitation energies and its spectral function

$$A_\alpha(\mathbf{q},\omega) = \frac{1}{\pi}\left|\mathrm{Im}\sum_n^{\text{all}}\int \mathrm{d}\mathbf{r}\,\mathrm{d}\mathbf{r}'\,\varphi^{\alpha *}_{\mathbf{q}n}(\mathbf{r})G_\alpha(\mathbf{r},\mathbf{r}';\omega)\varphi^\alpha_{\mathbf{q}n}(\mathbf{r}')\right| \tag{4.4.8}$$

is the distribution of the quasiparticle poles at these excitation energies $\omega = E^\alpha_{\mathbf{q}n}$. Employing the linearized solution of the quasiparticle equation (4.4.5), the spectral function of a single quasiparticle

$$A^\alpha_{\mathbf{q}n}(\omega) = \frac{1}{\pi}\frac{\left|\mathrm{Im}Z^\alpha_{\mathbf{q}n}\,\mathrm{Re}\left[\omega - \left(\epsilon^\alpha_{0,\mathbf{q}n} + \Sigma^\alpha_{\mathbf{q}n}(E^\alpha_{\mathbf{q}n})\right)\right]\right| + \left|\mathrm{Re}Z^\alpha_{\mathbf{q}n}\,\mathrm{Im}\Sigma^\alpha_{\mathbf{q}n}(E^\alpha_{\mathbf{q}n})\right|}{\left|\omega - \left(\epsilon^\alpha_{0,\mathbf{q}n} + \mathrm{Re}\Sigma^\alpha_{\mathbf{q}n}(E^\alpha_{\mathbf{q}n})\right)\right|^2 + \left|\mathrm{Im}\Sigma^\alpha_{\mathbf{q}n}(E^\alpha_{\mathbf{q}n})\right|^2}, \tag{4.4.9}$$

takes the form of an asymmetric Breit-Wigner distribution. Usually, the renormalization of the single-particle state is small and, in the limiting case $\mathrm{Im}Z^\alpha_{\mathbf{q}n} \to 0$, the spectral function (4.4.9) reduces to a symmetric Lorentzian-shaped quasiparticle peak located at the quasiparticle energy $E^\alpha_{\mathbf{q}n}$. The width of such a quasiparticle peak is associated with the inverse lifetime of that state and originates from the finite imaginary part of the self-energy $\mathrm{Im}\Sigma^\alpha_{\mathbf{q}n}(E^\alpha_{\mathbf{q}n})$. The lifetime arises from the fact that the quasiparticle state is not a discrete eigenstate of the interacting Hamiltonian, corresponding to a single-particle state dressed with a manifold of excited states. If the lifetime is long, i.e., the imaginary part of the quasiparticle solution is small, the quasiparticle is a coherent state of the many-body system. In contrast, if the quasiparticle lifetime is short, the spectral function exhibits a broad feature. This means that the quasiparticle is an incoherent state of the many-body system [74].

4.4.3 Effective Mass

The interaction between the electrons within a solid leads to the formation of quasiparticles, provided that the quasiparticle picture is applicable. Usually, the quasiparticle mass differs from the mass m_e of a free electron. In the vicinity of the Fermi

level many materials exhibit a quadratic band dispersion just as the dispersion of free electrons. This allows to define an effective mass m_* of the quasiparticles, which is related to the inverse curvature of the dispersion relation. There are two experimental techniques routinely employed to determine the effective mass. On the one hand, angle-resolved photoemission spectroscopy (ARPES) experiments measure the band structure directly. For example, recent ARPES measurements indicate a strong renormalization of the effective masses for the three elementary ferromagnets bcc Fe [58, 62, 206], hcp Co [61], and for fcc Ni [59, 274–277]. On the other hand, the de Haas-van Alphen (dHvA) experiment, which allows to image the Fermi surface, has been used to study mass renormalization [278–280]. The mass renormalization is, usually, calculated by comparing the measured effective mass with a theoretically predicted mass m_0, e.g., from a band dispersion obtained by density-functional theory. The effective masses of the (quasi-)particles is inversely proportional to the curvature of the band dispersion. An estimate of the mass renormalization is given by the ratio of the single particle's and the quasiparticle's velocity, i.e.,

$$\frac{m_*}{m_0} = \frac{\nabla_{\mathbf{q}}\, \epsilon^{\alpha}_{\mathbf{q}n}}{\nabla_{\mathbf{q}}\, E^{\alpha}_{\mathbf{q}n}}. \tag{4.4.10}$$

The quasiparticle velocity is derived from the quasiparticle equation (4.4.4)

$$\nabla_{\mathbf{q}}\, E^{\alpha}_{\mathbf{q}n} = \nabla_{\mathbf{q}}\, \epsilon^{\alpha}_{\mathbf{q}n} + \nabla_{\mathbf{q}}\, E^{\alpha}_{\mathbf{q}n}\, \left.\frac{\mathrm{d}\Sigma^{\alpha}_{\mathbf{q}n}(\omega)}{\mathrm{d}\omega}\right|_{\omega=E^{\alpha}_{\mathbf{q}n}} + \nabla_{\mathbf{q}}\, \left.\Sigma^{\alpha}_{\mathbf{q}n}(\omega)\right|_{\omega=E^{\alpha}_{\mathbf{q}n}}, \tag{4.4.11}$$

so that the mass-renormalization is given by

$$\frac{m_*}{m_0} = \frac{\nabla_{\mathbf{q}}\, \epsilon^{\alpha}_{\mathbf{q}n}}{Z^{\alpha}_{\mathbf{q}n}\left(\nabla_{\mathbf{q}}\, \epsilon^{\alpha}_{\mathbf{q}n} + \nabla_{\mathbf{q}}\, \left.\Sigma^{\alpha}_{\mathbf{q}n}(\omega)\right|_{\omega=E^{\alpha}_{\mathbf{q}n}}\right)}, \tag{4.4.12}$$

with the renormalization factor $Z^{\alpha}_{\mathbf{q}n}$ defined in Eq. (4.4.6) but evaluated at the quasiparticle energy instead of at the Kohn-Sham energy. Provided that the dispersion of the self-energy is negligible, the mass renormalization reduces to the inverse of the quasiparticle renormalization factor

$$\frac{m_*}{m_0} = \frac{1}{Z^{\alpha}_{\mathbf{q}n}}. \tag{4.4.13}$$

An example for such a case is the electron-phonon self-energy. It has been shown by Migdal [259] that the self-energy is essentially independent of the momentum $\mathbf{q}$.

Nakajima and Watabe [281,282] figured out that the variation of the electron-phonon self-energy with respect to the energy is two orders of magnitude larger than its variation with respect to the momentum.

4.4.4 Satellites

The solution to the quasiparticle equation (4.4.4) usually gives rise to a well defined quasiparticle peak in the spectral function. This quasiparticle represents an electron or a hole dressed with virtual many-body excitations. However, there might occur an additional quasiparticle solution giving rise to a second peak in the spectral function. This is because the quasiparticle equation (4.4.4) is nonlinear. The second quasiparticle solution represents a bound state of a real many-body excitation dressed with electrons or holes. In case of the *GW* approximation such an additional quasiparticle state corresponds to a bound state of plasmons with an electron or a hole. This new state is called a *plasmaron* and was predicted by Hedin and Lundqvist [227–230].

The additional quasiparticle peak is referred to as a satellite peak. Usually, satellites are not well described by *GW* calculations and the full satellite spectrum is inaccessible due to the missing vertex corrections. The cumulant expansion is a way to partially sum higher-order diagrams. It has been shown to be suitable to describe an electron-boson coupling in terms of a polaron Hamiltonian [232]. Therefore, the bound states of plasmons with an electron or a hole, introduced by Hedin and Lundqvist as plasmarons, are also referred to as *electronic polarons* [239, 240] or *plasmonic polarons* [241, 242]. Nozières and de Dominicis [235] as well as Langreth [236] used the cumulant expansion to study singularities in the x-ray spectra of metallic core states. Later the method has been applied to conduction electrons by Bergersen [237], Minnhagen [238], and Hedin [231]. This type of expansion sums boson type diagrams describing the emission and reabsorption of plasmons. Aryasetiawan *et al.* [232] have shown that the cumulant expansion is able to reproduce multiple plasmon satellites in Na and Al as seen experimentally. Photoemission experiments also measure multiple satellites in semiconductors, which are reproduced by the cumulant expansion of the *GW* approximation [233]. Caruso *et al.* [241, 242] have shown that the cumulant expansion is capable of describing plasmonic polaron bands, which occur in materials such as silicon and group IV transition-metal dichalcogenides with well-defined plasmon resonances.

The coupling of electrons to magnons, as described by the *GT* self-energy, might also lead to the occurrence of new structures in the single-particle spectrum. These

satellites are, however, different in their nature compared to the plasmaron state occurring in the GW plus cumulant expansion. For a qualitative description of these new states, the Brillouin-Wigner perturbation theory is employed. For this, we follow the approach employed by Lundqvist [227] for the description of the plasmaron state and apply it to the electron-magnon coupling. The electron-magnon coupling is described by the effective Hamiltonian [283, 284]

$$H_{\text{eff}} = \sum_{\mathbf{k}} \sum_{\alpha} \epsilon^{\alpha}_{\mathbf{k}} c^{\dagger}_{\mathbf{k}\alpha} c_{\mathbf{k}\alpha} + \sum_{\mathbf{q}} \omega_{\mathbf{q}} b^{\dagger}_{\mathbf{q}} b_{\mathbf{q}} + \sum_{\mathbf{k},\mathbf{q}} \left(\gamma^{\uparrow\downarrow}_{\mathbf{q}} c^{\dagger}_{\mathbf{k}+\mathbf{q}\uparrow} c_{\mathbf{k}\downarrow} b^{\dagger}_{\mathbf{q}} + \gamma^{\downarrow\uparrow}_{\mathbf{q}} c^{\dagger}_{\mathbf{k}-\mathbf{q}\downarrow} c_{\mathbf{k}\uparrow} b_{\mathbf{q}} \right), \quad (4.4.14)$$

where $c^{\dagger}_{\mathbf{k}\alpha}, c_{\mathbf{k}\alpha}$ and $b^{\dagger}_{\mathbf{q}}, b_{\mathbf{q}}$ are creation and annihilation operator for electrons with spin α and energy $\epsilon^{\alpha}_{\mathbf{k}}$ and magnons with excitation energy $\omega_{\mathbf{q}}$, respectively. The coupling strength between electrons and magnons is taken into account by the coupling constant $\gamma^{\alpha\alpha'}_{\mathbf{q}}$. Excited states, which are formed out of the ground state $|0\rangle$ by the creation of electron or hole states, are coupled to magnon excitations. For example a majority hole state $c_{\mathbf{k}\uparrow}|0\rangle$ is coupled to a product state of minority holes and magnons $c_{\mathbf{k}-\mathbf{q}\downarrow} b^{\dagger}_{\mathbf{q}}|0\rangle$. The coupling of the majority hole with the magnons leads to a renormalization of the unperturbed hole state $c_{\mathbf{k}\uparrow}|0\rangle$. In particular, the new state vector is a linear combination of the unperturbed majority hole and a product state consisting of minority holes and magnons, i.e.

$$|\Psi^{\uparrow}_{\mathbf{k}}\rangle = \frac{1}{\mathcal{N}} \left[c_{\mathbf{k}\uparrow} + \sum_{\mathbf{q}} \gamma^{\uparrow\downarrow}_{\mathbf{q}} \frac{c_{\mathbf{k}-\mathbf{q}\downarrow} b^{\dagger}_{\mathbf{q}}}{E - \epsilon^{\downarrow}_{\mathbf{k}-\mathbf{q}} + \omega_{\mathbf{q}}} \right] |0\rangle, \quad (4.4.15)$$

with a properly chosen normalization constant $\mathcal{N}$. The energy of the perturbed majority hole obeys an implicit equation

$$E = \epsilon^{\uparrow}_{\mathbf{k}} + \sum_{\mathbf{q}} |\gamma^{\uparrow\downarrow}_{\mathbf{q}}|^2 \frac{1}{E - \epsilon^{\downarrow}_{\mathbf{k}-\mathbf{q}} + \omega_{\mathbf{q}}}, \quad (4.4.16)$$

which is formally identical to the quasiparticle equation (4.4.4). Usually, its solution corresponds to a well-defined quasiparticle, which is the hole state that experiences a weak renormalization due to the perturbation of the hole-magnon excitations. If the electron-magnon coupling is sufficiently strong, i.e., $\gamma^{\uparrow\downarrow}_{\mathbf{q}}$ is large, there might appear an additional solution to the implicit equation (4.4.16). As a consequence, the perturbed state (4.4.15) has two main contributions depending on the energy E and momentum $\mathbf{k}$. The two contributions are (strongly) mixed many-body states. The additional peak appears due to the mixing of the majority hole state with a bound

state of minority holes and magnon excitations. This means the many-body state corresponds to a majority hole which is superimposed by a coherent linear combination of minority holes bound to magnon excitations. A similar mixed many-body state appears for minority electrons. In this case, the mixed many-body state corresponds to a superposition of a minority electron with a coherent bound state of majority electrons and magnon excitations. We refer to the bound states of single-particle and magnon excitations as *magnarons* in analogy to the concept of plasmarons. In principle, such magnarons could be formed out of majority electrons and the minority holes, too. The ferromagnetic state, however, inherently leads to strong and weak spin-flip excitations. The spin-flip scattering of the majority electrons and the minority holes proceeds via excitations that flip a minority spin, which is an unlikely process. Therefore, the coupling of these states to the spin-flip excitations are presumably not strong enough to cause the appearance of a magnaron. The magnaron state was discussed for itinerant strong ferromagnets by Edwards and Hertz [149] as *magnetic polaron*. Irkhin and Katsnelson [285–288] studied a state corresponding to a superposition of a minority electron with a majority electron plus a magnon in half-metallic ferromagnets which is called a *spin polaron*.

4.5 Formal Discussion of the Electron-Magnon Self-Energy

This section provides a formal discussion and a mathematical analysis of the qualitative behavior of the electron-magnon self-energy in ferromagnets. The qualitative behavior of the electron-magnon self-energy has been studied a lot in the literature. Early studies by Phillips *et al.* [289] and Davis *et al.* [283] focused on the renormalization of states close to the Fermi level. They found an effective-mass renormalization as large as that due to the electron-phonon interaction. Brandt [290] used the Hubbard model and derives a conserving T-matrix approach to study a model ferromagnet. In case of a completely polarized system he found a large damping of the single-particle states and a new type of quasiparticle at low excitation energies that gives rise to a satellite feature in the spectral function. Hertz *et al.* [148, 149] studied the electron-magnon coupling and its impact on the quasiparticle states. They concluded that the electron-magnon interaction leads to a reduction of the exchange splitting in the vicinity of the Fermi energy. In addition, Hertz *et al.* discuss the possibility of satellite features, i.e., additional quasiparticle solutions due to the electron-magnon interaction. They derive an expression for the self-energy that is equivalent

to the T-matrix approach used by Liebsch [202]. Liebsch showed that the coupling of the electrons to a magnon-induced interaction leads to a narrowing of the d-band width and a slight reduction of the exchange splitting in nickel. The following consideration adopts the GT self-energy expression derived by Hertz *et al.* [148, 149] for the one-band Hubbard model within the T-matrix approach

$$\Sigma_{\alpha}(\mathbf{q},\omega) = \frac{-\mathrm{i}}{2\pi}\sum_{\mathbf{k}}\int_{-\infty}^{\infty}\mathrm{d}\omega'\, G_{\alpha'}(\mathbf{q}-\mathbf{k},\omega-\omega')\, T_{\alpha\alpha'}(\mathbf{k},\omega'), \tag{4.5.1}$$

which is a special case of the more general expression (4.2.17). The GT approximation is, mathematically speaking, the convolution of the electronic Green function G and the multiple-scattering T matrix in the momentum and the frequency domain. The multiple-scattering T matrix describes the correlated motion of an electron-hole pair with opposite spins. Thereby, it describes the single-particle Stoner excitations, the magnon excitations, and combinations thereof on equal footing. In the interacting many-body system these excitations merge and, strictly speaking, the so-called single-particle excitations cannot be distinguished from the collective ones. Therefore, we generally refer to these excitations as spin-flip or magnon excitations in the following. Accordingly, we refer to the multiple-scattering T matrix as the magnon-induced effective interaction. Besides the magnon-induced interaction the self-energy depends on the electronic spectrum via the Green function G. The Green function describes the spin-polarized state of a ferromagnetic system with its majority and minority states. The spin polarization leads to the occurrence of strong and weak magnon excitations meaning the spectral weight of the strong magnon excitations is larger than that of the weak magnon excitations, see Fig. 4.5. While the strong magnon excitations involve majority holes and minority electrons, the weak magnon excitations form out of the majority electrons and minority holes.

The GT self-energy (4.5.1) allows an interpretation in terms of a magnon-induced scattering process, i.e., the GT self-energy describes the scattering of electrons while magnon excitations are emitted or absorbed. The corresponding Feynman diagram is shown in Fig. 4.6. The strong and weak magnon excitations reflect themselves in the spin-dependent distribution of the poles of the T matrix. With the spectral representation of the magnon-induced interaction

$$T_{\alpha\alpha'}(\mathbf{k},\omega) = \int_{-\infty}^{\infty}\mathrm{d}\omega'\,\frac{t_{\alpha\alpha'}(\mathbf{k},\omega')}{\omega-\omega'+\mathrm{i}\eta\mathrm{sgn}(\omega')}, \tag{4.5.2}$$

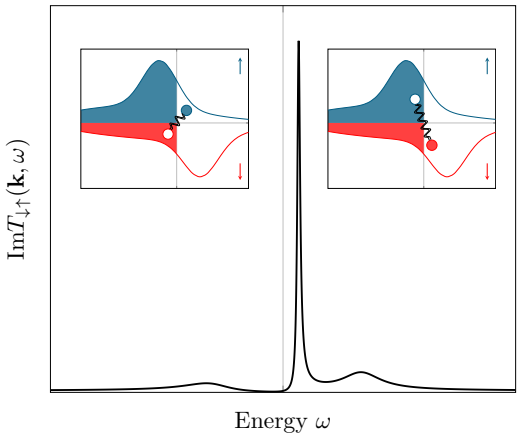

Figure 4.5: Schematic behavior of the spectral function of the T matrix for finite momenta as a function of real frequencies. The spin polarization of a ferromagnetic material, shown as insets, leads to the occurence of weak (left) and strong (right) magnon excitations. A weak magnon excitation involves majority electron and minority hole states as depicted in the left inset. In contrast, a strong magnon excitation involves majority hole and minority electron states, see inset on the right.

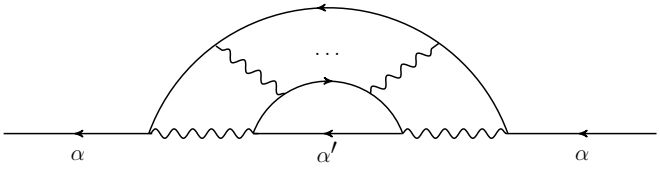

Figure 4.6: Feynman diagram of the electron-magnon scattering process accounted for in the GT self-energy, cf. Fig. 4.2. The scattering of the incoming particle with spin α by a magnon excitation leads to a spin-flip of the propagating particle $\alpha = -\alpha'$. The magnon excitation is described by the multiple-scattering T matrix as the correlated motion of an electron-hole pair with opposite spins.

and the spectral representation of the Green function

$$G_\alpha(\mathbf{k},\omega) = \int_{-\infty}^{\infty} \mathrm{d}\omega' \, \frac{g_\alpha(\mathbf{k},\omega')}{\omega - \omega' + \mathrm{i}\eta \mathrm{sgn}\omega'}, \tag{4.5.3}$$

where $t_{\alpha\alpha'}(\mathbf{k},\omega)$ and $g_\alpha(\mathbf{k},\omega)$ is the spectral function of the T matrix and the Green function, respectively, the self-energy (4.5.1) decomposes into the contribution of the strong and the weak magnon excitations

$$\begin{aligned}\Sigma_\alpha(\mathbf{q},\omega) = \sum_{\mathbf{k}} \int_0^{\infty} \mathrm{d}\omega' \, \mathrm{d}\omega'' \, \frac{g_{\alpha'}(\mathbf{q}-\mathbf{k},\omega') t_{\alpha\alpha'}(\mathbf{k},\omega'')}{\omega - \omega' - \omega'' + \mathrm{i}\eta} \\ + \sum_{\mathbf{k}} \int_{-\infty}^{0} \mathrm{d}\omega' \, \mathrm{d}\omega'' \, \frac{g_{\alpha'}(\mathbf{q}-\mathbf{k},\omega') t_{\alpha\alpha'}(\mathbf{k},\omega'')}{\omega - \omega' - \omega'' - \mathrm{i}\eta}.\end{aligned} \tag{4.5.4}$$

The strong magnon excitation appears in the spectral function of the T matrix as a well defined δ-like quasiparticle peak, schematically shown in Fig. 4.5. The strong magnon excitation dominates the spectral function of the T matrix, and consequently it essentially determines the properties of the GT self-energy. For example, if the spectral function of the T matrix is approximated to solely contain the strong magnon excitation its impact on the GT self-energy can be evaluated. To this end, the spectral function is written as $t_{\downarrow\uparrow}(\mathbf{k},\omega) = a(\mathbf{k})\delta(\omega - \omega(\mathbf{k}))$, where $\omega(\mathbf{k}) \geq 0$ is the spin-wave excitation energy disregarding spin-wave lifetime effects, and $a(\mathbf{k})$ accounts for the fact that the spectral weight of the spin-wave excitations decreases from the Brillouin zone center to its boundary. Which states are predominantly influenced by the strong magnon excitations depends on the spin state under consideration. The contribution of the strong magnon excitations to the minority spin self-energy is

$$\tilde{\Sigma}_\downarrow(\mathbf{q},\omega) = \sum_{\mathbf{k}} \int_0^{\infty} \mathrm{d}\omega' \, \frac{g_\uparrow(\mathbf{q}-\mathbf{k},\omega') a(\mathbf{k})}{\omega - \omega' - \omega(\mathbf{k}) + \mathrm{i}\eta}. \tag{4.5.5}$$

The expression describes the magnon-induced scattering involving the strong magnon excitations, which proceeds via the unoccupied majority states. As a consequence, the strong magnon excitations predominantly influence the unoccupied minority states. In contrast, its contribution to the majority spin self-energy is

$$\tilde{\Sigma}_\uparrow(\mathbf{q},\omega) = \sum_{\mathbf{k}} \int_{-\infty}^{0} \mathrm{d}\omega' \, \frac{g_\downarrow(\mathbf{q}-\mathbf{k},\omega') a(\mathbf{k})}{\omega - \omega' + \omega(\mathbf{k}) - \mathrm{i}\eta}, \tag{4.5.6}$$

i.e., the strong magnon excitations affect the occupied majority states. The processes involving the strong magnon excitations are schematically shown in Fig. 4.7. The ex-

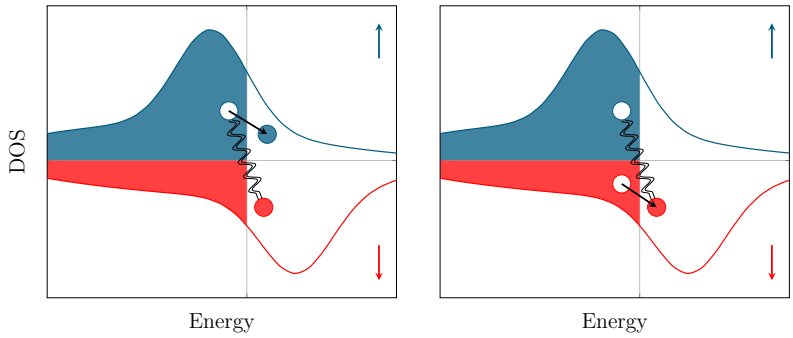

Figure 4.7: Schematic spin-polarized density of states representing magnon-induced electron scattering processes in a ferromagnetic material. Left: an additional minority electron becomes part of a strong magnon while a majority electron-hole pair is excited. Right: an additional majority hole state becomes part of a strong magnon while a minority electron-hole pair is excited. The magnon is depicted as the double-wiggly line representing the multiple scattering of electron-hole pairs with opposite spins.

istence of strong magnon excitations has two important consequences for the renormalization of the electronic spectrum. First, the self-energy yields a spin-asymmetric renormalization of the quasiparticles, and, second, the self-energy leads to a particle-hole asymmetric renormalization, i.e., occupied and unoccupied states experience a different renormalization. While in the majority spin channel the hole states are mostly affected, in the minority spin channel the electronic states above the Fermi level experience a renormalization due to the strong magnon excitation. Under the assumption that the spin-wave excitation energies that are important for the coupling of electrons to magnons is much smaller than the energy scale of the electronic spectrum, the self-energy becomes practically independent of the momentum. For example the dispersion of an electronic band spans typically an energy range of the order of eVs. In contrast, the characteristic energy scale of the spin-wave dispersion is of the order of meVs. In the case that the spin-wave dispersion can be approximated by a single excitation energy ω_0, i.e., the spectral function of the T matrix takes the form $t_{\downarrow\uparrow}(\mathbf{k}, \omega) = a\delta(\omega - \omega_0)$ with a momentum independent spectral weight a, the self-energies (4.5.5) and (4.5.6) become independent of the momentum. Based on similar arguments, the momentum insensitivity of the electron-magnon self-energy was discussed by Edwards and Hertz for a strong ferromagnet within the Hubbard model [149]. We will later see that the GT self-energy is close to this limiting case for the elementary ferromagnets iron, cobalt, and nickel.

4.6 Computational Details

The *GT* approximation for the electron-magnon self-energy is implemented in the SPEX code [72], which utilizes the full-potential linearized augmented-plane-wave (FLAPW) basis set. The non-interacting Green function that serves as starting point for the self-energy calculation is provided by the FLEUR code [92], which is a FLAPW implementation of the density-functional theory [18, 19]. The implementation of the *GT* self-energy makes use of the T matrix, which is formulated in a Wannier basis. We employ a set of nine maximally localized Wannier functions [46, 47] with s, p, and d orbital character. These Wannier functions are constructed from the 18 energetically lowest mean-field single-particle states $\varphi^{\alpha}_{\mathbf{k}m}(\mathbf{r})$.

The calculation of the *GT* self-energy requires the calculation of several other properties in advance. First, a self-consistent-field calculation of the electronic ground state within density-functional theory is needed. The exchange-correlation potential is chosen in the local-spin-density approximation (LSDA) using the parameterization of Perdew and Zunger [90]. The results for the three elementary ferromagnets iron, cobalt, and nickel are obtained with the lattice constants 2.87 Å, 3.54 Å, and 3.53 Å, respectively. All calculations employ a $14 \times 14 \times 14$ $\mathbf{k}$-point grid. For the Brillouin zone (BZ) integration we use the tetrahedron method [157]. The static screened interaction, which mediates the correlation among the electron-hole pairs of opposite spins, is projected onto a Wannier product basis after it is calculated within the mixed product basis [72, 108, 166]. The electron-hole pair propagator $K = \mathrm{i}GG$ is evaluated directly in the Wannier product basis by utilizing its Lehman representation, see Section 3.3.1. The calculation of the screened interaction W and the electron-hole pair propagator K are the most time-consuming steps. Therefore, W and K are stored on the disk, once they are calculated, to accelerate subsequent calculations. In order to fulfill the Goldstone-mode condition the exchange splitting of the LSDA result is corrected [51]. For iron, cobalt, and nickel the exchange splitting is adjusted by 0.10 eV, 0.39 eV, and 0.21 eV respectively. The corrected LSDA solution serves as starting point for the *GT* self-energy calculation as an alternative to the COHSEX starting point. The adjustment of the exchange splitting mimics the effect of the self-consistently renormalized Green function with respect to the COHSEX self-energy, see Section 3.5.2. We consider the starting-point dependence of the *GT* self-energy in Section 4.6.2. The next section summarizes the computational details of the frequency convolution of G and T.

4.6.1 Frequency Integration

The evaluation of the GT self-energy (4.3.1) requires the calculation of the convolution of the Green function and the T matrix in the frequency domain. We have implemented two methods for the frequency integration, the contour-integration method and the analytic-continuation method, for details see Section 4.3.2.

Contour-Integration Method

The contour-integration method enables to perform the frequency integration accurately. It is performed by evaluating the self-energy on an equidistant frequency mesh around the Fermi level. For example, the self-energy is evaluated within an interval from -7 eV to 7 eV around the Fermi level with a frequency spacing of 25 meV, which corresponds to 560 frequencies. To evaluate the self-energy, the contour integration is carried out for each of these frequencies. While the contour integration is the most precise method to evaluate self-energy operators, it is also computationally the most demanding. Technically, the integration is done by using a Padé approximation for the T matrix. To this end, the T matrix is evaluated as a function of imaginary frequencies. We use an exponential mesh of the form (4.3.6), with $n = 30$ mesh points, $\omega_{\max} = 0.5\,\text{htr}$ maximum energy, and an exponential factor of $x = 1.02$. The Padé approximant represents the T matrix as a sum of effective poles. With the given poles, the contour integration is performed analytically, the corresponding formulas are shown in the Appendix A. Results of the GT self-energy calculation obtained with the contour-integration method for the cases Fe, Co, and Ni are shown in Fig. 4.8. Clearly, the results exhibit a very spiky form of the self-energy in all three cases. The spikes result from the difficulty to properly converge the BZ sampling of the δ-like quasiparticle peaks present in the T matrix. These δ-like quasiparticle peaks are associated with the strong magnon excitations. Accordingly, the self-energy is especially spiky where the strong magnons affect the self-energy, i.e., for the majority states below the Fermi level and for the minority states above the Fermi level, cf. the formal discussion of the electron-magnon interaction in Section 4.5. In principle, the spikes in the self-energy can be converged by increasing the number of $\mathbf{k}$ points until the results are smooth. However, the numerical effort of a GT self-energy calculation does not allow to increase the $\mathbf{k}$-point set further at the moment. As a consequence, the $\mathbf{k}$-point convergence issue currently hinders to solve the quasiparticle equation accurately with the self-energy obtained by means of the

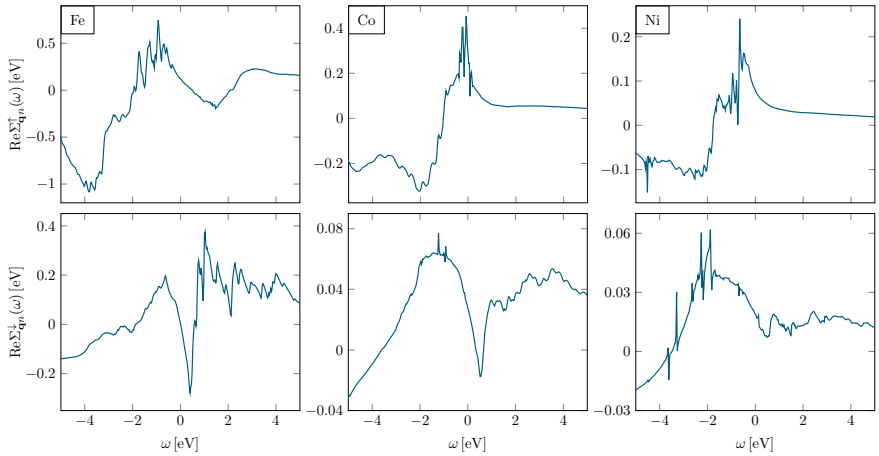

Figure 4.8: The real part of the self-energy evaluated using the contour-integration method. The self-energy for a majority (minority) spin state is shown in the upper (lower) row for the three cases Fe, Co, and Ni (from left to right). The self-energy is evaluated for the single-particle state $\epsilon^{\uparrow}_{\Gamma,5} = (-0.89, -1.09, -0.99)\,\mathrm{eV}$ and $\epsilon^{\downarrow}_{\Gamma,4} = (-0.49, -1.14, -0.66)\,\mathrm{eV}$ for iron, cobalt, and nickel, respectively. The Fermi level is set to zero.

contour-integration method.

Analytic-Continuation Method

The analytic continuation relies entirely on the calculation along the imaginary frequency axis, i.e., the self-energy is evaluated as a function of imaginary frequencies. An analytic continuation at the end of the calculation yields the self-energy as a function of real frequencies. The integration along the imaginary frequency axis is performed by using a Padé approximant to the T matrix as done in the contour-integration method. The method of analytic continuation is computationally less demanding compared to the contour-integration method. In contrast to the contour integration, the analytic-continuation method requires the evaluation of the self-energy for only $n = 20 \ldots 30$ imaginary frequencies. We employ an exponential frequency mesh of the form (4.3.6). The analytic continuation is performed by using a Padé approximant to the self-energy. Results for the elementary ferromagnets are shown in Fig. 4.9. Clearly, these results do not show any spiky behavior as in the case of the contour-integration method. The results obtained from the analytic-continuation method appear as a smooth self-energy following the same overall trend as obtained by means of the contour-integration method, cf. Fig. 4.8.

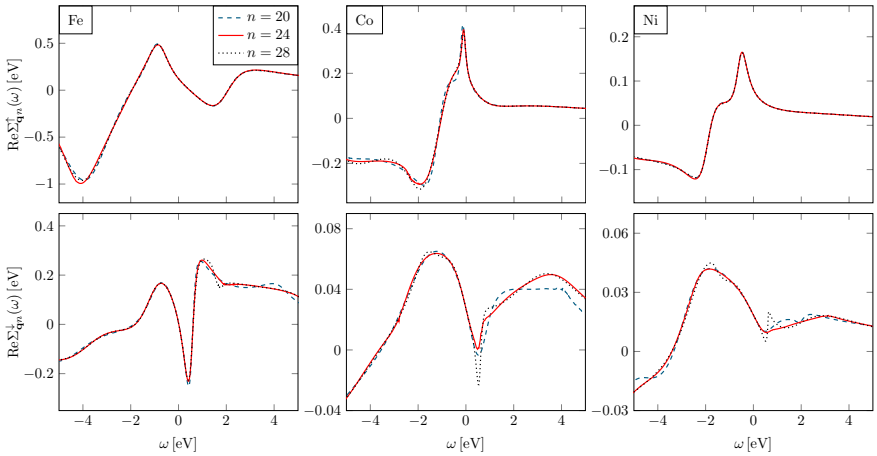

Figure 4.9: The real part of the self-energy evaluated using the analytic-continuation method. The self-energy for a majority (minority) spin state is shown in the upper (lower) row for the three cases Fe, Co, and Ni (from left to right). The blue dashed, red solid, and black dotted curves represent the result using $n = 20$, $n = 24$, and $n = 28$ mesh points on the imaginary frequency axis respectively. The self-energy is evaluated for the same states as in Fig. 4.8. The Fermi level is set to zero.

The choice of a proper imaginary frequency mesh, which is used for the analytic-continuation method, is a delicate task. Usually, it is possible to converge a calculation with respect to its parameters. In case of the analytic continuation, however, there is no systematic way to converge the imaginary frequency mesh. In Fig. 4.9 the self-energy that is obtained by means of three different frequency meshes is shown. Although, there is no way to converge the frequency mesh, practical experience gives a rule of thumb. The choice of the frequency mesh is a compromise between accuracy and stability of the Padé approximation. If, on the one hand, a very coarse frequency mesh is chosen the resulting self-energy might miss some essential features. On the other hand, with a very fine frequency mesh the Padé approximation might become unstable. The number of poles present in the Padé approximation increases with the number of frequencies. Therefore, increasing the number of frequencies also increases the number of effective poles of the Padé approximant. The additional poles in turn might lead to spurious features in the self-energy. We have tested various meshes for the evaluation of the GT self-energy and we found that a frequency mesh with $n = 20 \ldots 30$ frequencies with a maximal energy in the range of $\omega_{\mathrm{max}} = 1.5\mathrm{i} \ldots 2.5\mathrm{i}\,\mathrm{htr}$, and an exponential factor of $x = 1.01 \ldots 1.05$ gives stable results, see Fig. 4.9.

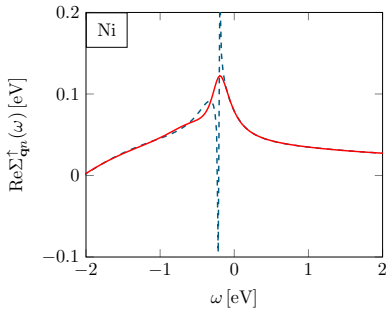

Figure 4.10: The analytic continuation of a Padé approximation can lead to spurious peaks in the result in rare cases (blue dashed line). To smoothen such numerical artifacts the result of multiple Padé approximations is averaged (red solid line).

The analytic continuation, which relies on a single Padé approximation to the self-energy, can lead to spurious peaks in the self-energy in rare cases. An example of such a case is shown as the blue dashed line in Fig. 4.10. The reason for this is the following: the Padé approximation represents a function with an infinite number of poles by a finite number of effective poles. Therefore, the analytic continuation of such a function is an ill-posed problem. The Padé approximation is sensitive to small errors in the data so that spurious features in the analytically continued function might arise. For example, if a Padé approximation contains effective poles located close to the real frequency axis, the analytically continued function exhibits a spurious feature in a small energy interval while being in good agreement with the function elsewhere. Such a problem is also known from the analytic continuation of quantum Monte Carlo data. Silver *et al.* [291] proposed the maximum-entropy method which has been widely used in the analysis of experimental data before. The maximum-entropy method is an image reconstruction approach. In case of the analytic continuation, the image corresponds to the analytically continued function and the Monte Carlo data provides the function on the imaginary frequency or time axis. The maximum-entropy method defines an entropy function which accounts for the properties of the analytically continued function, e.g., sum rules, positivity, *et cetera*. Nowadays, the maximum-entropy method is widely used in the field of condensed-matter theory [292–295]. Data obtained by a Monte Carlo algorithm is prone to two types of errors: random noise and numerical errors. For such cases, an image reconstruction approach is appropriate. In contrast, the self-energy as calculated in the present implementation might contain numerical errors while random

noise does not occur. Numerical errors are smaller than random noise present in Monte Carlo data. Therefore, we employ a pragmatic approach to smoothen the Padé approximation. Instead of employing a single Padé approximation for the analytic continuation, we use multiple approximations and the result is averaged over the resulting analytically continued self-energies. For each of the Padé approximations we add artificially a random noise to the imaginary frequency mesh. In particular, the frequency mesh points are changed randomly using a uniform distribution in the interval $[-5, 5] \cdot 10^{-9}\mathrm{i}\,\mathrm{htr}$. This procedure hinders the Padé approximation to give the same effective poles in each repetition. As a result the analytic continuation does not give spurious features as these are averaged out by the repetition of the Padé approximation. The red curve in Fig. 4.10 is an example where 10000 analytic continuations have been used each with a Padé approximation. A similar approach has been implemented recently by Schött *et al.* [296]. They perform the analytic continuation by averaging Padé approximants in which the number of input data points is changed. Their algorithm performs well compared to the maximum-entropy method even if the noise of the input data is increased beyond the magnitude of numerical errors. For the calculation of the self-energy as a function of imaginary frequencies, we use a frequency mesh with $n = 24$ frequencies and a maximum frequency of $2\mathrm{i}\,\mathrm{htr}$.

4.6.2 Starting-Point Dependence

In practice, a self-energy calculation is usually performed perturbatively, which is often called a one-shot calculation. Such a self-energy calculation is based on a prior self-consistent mean-field calculation, which serves as the starting point. The results of the subsequent self-energy calculation generally depend on the chosen starting point, e.g., published results obtained from one-shot *GW* calculations, known as the G_0W_0 procedure, show occasionally large deviations among themselves [297]. The impact of the starting point on G_0W_0 calculations has been analyzed, also with regard to the numerical treatment [297–301]. To get rid of the starting-point dependence the Dyson equation (2.1.27) must be iterated until self-consistency is reached. For example, the quasiparticle self-consistent *GW* (QS*GW*) scheme [144–147] allows to iterate the Dyson equation by means of a best mean-field approximation to the *GW* self-energy. It leads to the independence of *GW* calculations from the chosen starting point [302, 303]. However, self-consistent self-energy calculations demand a tremendous computational effort, so that many calculations are limited to one-shot procedures because of their practicality.

Springer *et al.* [203] and Zhukov *et al.* [67–69,204] were among the first who implemented the *GW*+*T* theory for real materials from first principles. These implementations used the LSDA as starting point and their self-energy results were obtained by means of a one-shot calculation. In these implementations, the *GT* self-energy is combined with the *GW* approximation in order to account for many-body effects which are not present in the *GW* approximation. The present implementation employs the *GT* approximation as an extension to the chosen starting point. This means, the single-particle energies $\epsilon^{\alpha}_{\mathbf{q}n}$ of the starting point are assumed to contain the many-body effects except for those of the *GT* approximation. The quasiparticle energies are obtained by adding the contribution of the *GT* self-energy

$$E^{\alpha}_{\mathbf{q}n} = \epsilon^{\alpha}_{\mathbf{q}n} + \int \mathrm{d}\mathbf{r}\,\mathrm{d}\mathbf{r}'\,\varphi^{\alpha *}_{\mathbf{q}n}(\mathbf{r})\Sigma^{\alpha}_{GT}(\mathbf{r},\mathbf{r}';E^{\alpha}_{\mathbf{q}n})\,\varphi^{\alpha}_{\mathbf{q}n}(\mathbf{r}'). \tag{4.6.1}$$

For an extension in the flavor of the *GW*+*T* theory, the starting point must be the result of a (self-consistent) *GW* self-energy calculation. However, it should be noted that the multiple-scattering *T* matrix, as it is implemented, derives from the static limit of the *GW* approximation. Consequently, the self-consistent COHSEX self-energy, i.e., the self-consistent solution to the static limit of the *GW* self-energy, is an even better starting point for a subsequent *GT* self-energy calculation than a self-consistent *GW* calculation. Therefore, we use the COHSEX Green function as starting point for the *GT* self-energy. However, the self-consistent scheme is computationally very demanding and it does not allow to perform calculations for **k** points different from the ones in the initially chosen set ($14 \times 14 \times 14$ in our case).

As an alternative to the COHSEX Green function, the corrected LSDA Green function can be used as a starting point. The use of the corrected LSDA Green function for the calculation of the *GT* self-energy has a couple of practical advantages. The calculation of the corrected LSDA Green function comes at the cost of a usual LSDA calculation, i.e., it is computationally much less demanding than a self-consistent COHSEX self-energy calculation. Furthermore, the corrected LSDA Green function allows to extend the chosen **k**-point set by additional **k** points. This enables the calculation of the self-energy beyond the **k**-point set employed for the calculation, i.e., fine details of the band structure can also be investigated. The question is, however, if there is a justification for the use of the corrected LSDA Green function. In this respect, the investigation of the starting-point dependence of the spin-wave dispersion revealed that the spin-wave dispersion starting from the corrected LSDA Green function resembles that of the COHSEX Green function in the case of Fe, Co, and Ni,

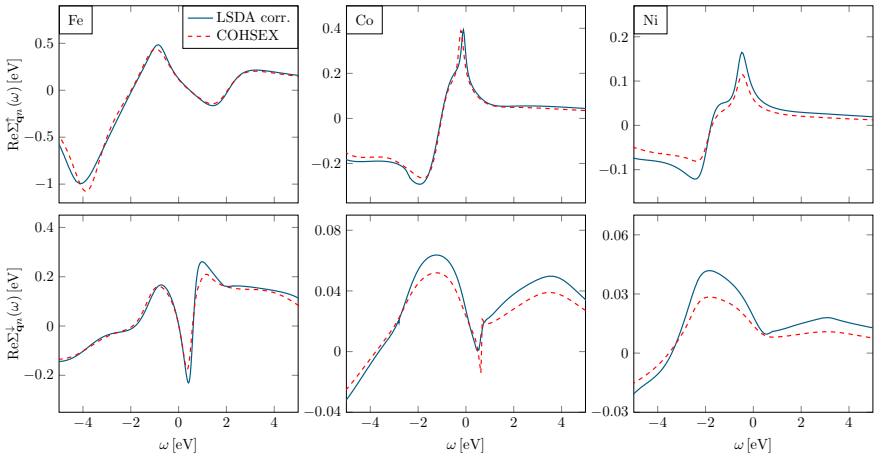

Figure 4.11: The real part of the self-energy evaluated using either the corrected LSDA (blue solid line) or the COHSEX (red dashed line) Green function as starting point. The self-energy for a majority (minority) spin state is shown in the upper (lower) row for the three cases Fe, Co, and Ni (from left to right). The *GT* approximation to the self-energy is evaluated for the same states as in Fig. 4.8. The Fermi level is set to zero.

compare Section 3.5.3. This indicates that the multiple-scattering T matrix, which is part of the magnetic response function, exhibits practically the same behavior for the corrected LSDA and the COHSEX Green function in those materials. However, the use of the LSDA solution comes with a drawback as it hides all its many-body effects in the exchange-correlation potential. Therefore, it is not possible to define a double-counting term that accounts for many-body effects present in the exchange-correlation potential as well as in the *GT* self-energy. From a practical point of view, however, the advantages of the corrected LSDA Green function approach outweigh its drawbacks if the difference between both starting points is small. The results for the *GT* self-energy calculated with the corrected LSDA and the COHSEX Green function, presented in Fig. 4.11, actually support this viewpoint. In particular, the results for iron and cobalt are encouraging. The self-energies are practically on top of each other except for mild deviations for the minority states. In case of nickel the amplitude of the self-energy seems to be reduced slightly when using the self-consistent COHSEX Green function compared to the corrected LSDA one. Nevertheless, also in the case of nickel the main features of the self-energy appear at the same energies for both Green functions. This indicates that both self-energies, starting from either the corrected LSDA or the COHSEX Green function, lead qualitatively to the same

renormalization. The next section analyzes the results of the *GT* self-energy calculations for the transition metals iron, cobalt, and nickel. In the course of this analysis, we give more details about the starting-point dependence of the *GT* self-energy with respect to the corrected LSDA and the COHSEX Green function.

4.7 Results

The *GT* approximation to the electronic self-energy has been calculated for the elementary bulk ferromagnets Fe, Co, and Ni. As a mean-field starting point, we employ the COHSEX Green function if not stated otherwise. The *GT* self-energy calculated for the three elementary ferromagnets share a number of common features. For example the self-energy is found to be weakly momentum dependent, i.e., the self-energy of a single-particle state $\varphi^{\alpha}_{\mathbf{q}n}(\mathbf{r})$ hardly changes with respect to a change of its Bloch vector $\mathbf{q}$. The self-energies of both spin channel, shown in Figure 4.12 for the cases Fe, Co, and Ni, are typical examples where the self-energy hardly changes for various states along a specific band. The weak momentum dependence of the *GT* self-energy can be understood by a gedankenexperiment. The magnon excitation energies are typically of the order of meVs, i.e., the excitation energies are much smaller than the energy scale of electronic excitations. Therefore, the spin-wave dispersion, i.e., the change of the spin-wave excitation energy with respect to a change of its momentum plays a subordinate role. Under the assumption that the spin-wave dispersion can be approximated by a single excitation energy $\omega(\mathbf{k}) = \omega_0$, the self-energy becomes momentum independent. In this limit, the self-energy depends only on the constant magnon excitation energy and the electronic density of states, compare Eqs. (4.5.5) and (4.5.6) and the discussion thereafter. The *GT* self-energy is close to the limiting case of a momentum independent self-energy. However, the weak momentum dependence in combination with the strong frequency dependence might lead to important renormalization effects.

In addition, the *GT* self-energy exhibits a particle-hole asymmetry for the three cases iron, cobalt, and nickel, meaning that the *GT* self-energy leads to a substantially different renormalization of electron and hole states, compare the self-energies in Fig. 4.12 above and below the Fermi level $\omega = 0$. The particle-hole asymmetry stems from the difference between the strong and the weak magnons. Strong magnons involve the spin-flip of a majority spin, which is much more likely than the spin-flip of a minority spin contained in the weak magnons. The strong magnons

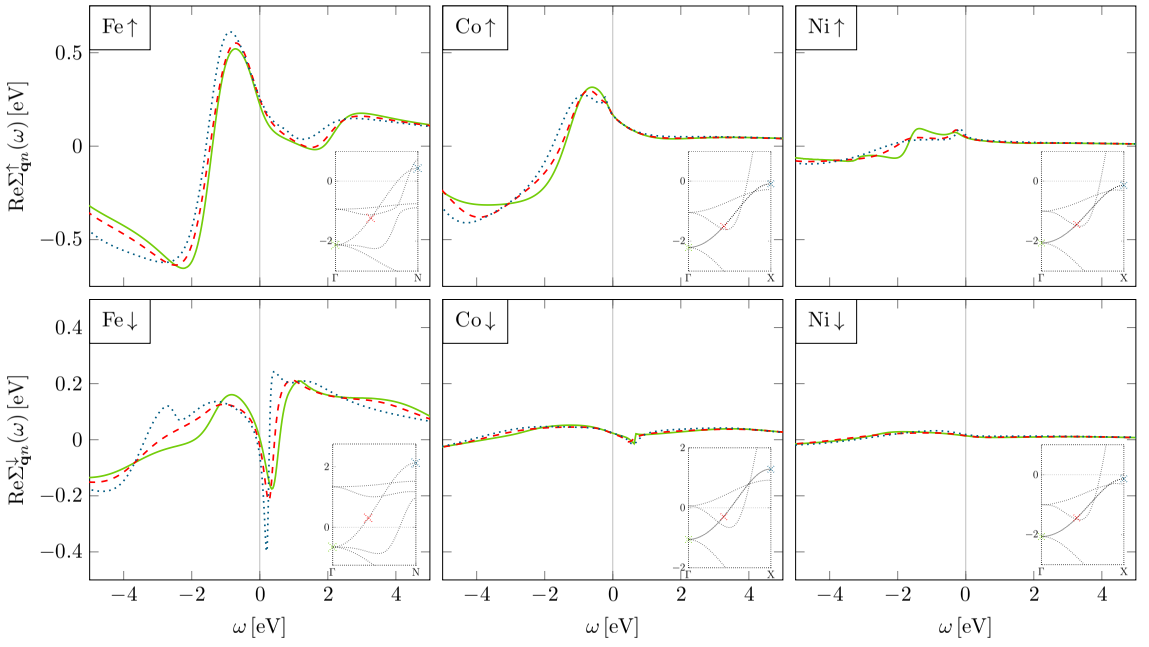

Figure 4.12: Real part of the self-energy calculated for three different **k** points along the Γ to N and Γ to X direction for the bcc and fcc structure, respectively. The calculated states are shown in the insets. The *GT* approximation is i) weakly dependent on the Bloch momentum **q** (compare green solid, red dashed, and blue dotted curves within each panel), ii) it exhibits a characteristic particle-hole asymmetry (compare self-energy above and below $\omega = 0$), and iii) it is strongly spin dependent leading to a spin-asymmetric renormalization (compare upper and lower row). In addition, the self-energy decreases in the series of the elementary ferromagnets Fe, Co, and Ni (from left to right).

are important for the self-energy of majority holes and minority electrons, the corresponding scattering processes are depicted in Fig. 4.7. The particle-hole asymmetry is particularly pronounced in iron as well as for the majority spin channel of cobalt and nickel, see Fig. 4.12. In iron, the effect of the strong magnon on the minority spin self-energy manifests itself as a pronounced dip in the self-energy just above the Fermi level $\omega = 0$. This effect seems to be suppressed in the case of cobalt and almost absent in the case of nickel. The scattering of a minority electron that involves a strong magnon proceeds via the unoccupied majority states of which the d states are most important. In cobalt and nickel practically all majority d states are occupied so that this causes the suppression of the self-energy, cf. density of states in Fig. 3.4.

Furthermore, the GT self-energy is strongly spin dependent, i.e., the self-energy of a majority state is substantially different from that of a minority state, compare upper and lower row of Fig. 4.12. The reason is that the magnon-induced interaction T couples both spin channels. As a consequence, the self-energy of a majority state is determined by the density of minority states and vice versa. If we again consider the influence of the strong magnon as an example, see Fig. 4.7, the self-energy of a majority hole state is determined by the density of occupied minority states. In contrast, it is the density of unoccupied majority states that is important for the self-energy of a minority electron state. As a result, the self-energy yields a spin-dependent renormalization.

Finally, the amplitude of the self-energies shown in Fig. 4.12 decreases in the series iron, cobalt, and nickel. We ascribe this trend to the fact that the minority d-state occupation increases in the series of the elementary ferromagnets Fe, Co, and Ni. The unoccupied minority d states are important for the formation of the strong magnon. Consequently, an increase of the minority d-state occupation leads to a decrease of the spectral weight of the strong magnon. This, in turn, results in the decrease of the self-energies in the series of the elementary ferromagnets.

In the following, we analyze the GT self-energy and the resulting electronic spectral function individually for each of the three elementary ferromagnets. We find for all the elementary ferromagnets anomalies in the spectral function, in particular in the case of iron, we find a pronounced additional peak indicating the appearance of new quasiparticle states to which we refer as magnaron states, see Section 4.4.4. In addition, we analyze lifetime effects of the self-energy on the single-particle states.

4.7.1 Iron

Iron has often been investigated experimentally and the measurements show some clear deviations from the theoretical predictions. Iron is the ferromagnetic material in which the de Haas-van Alphen (dHvA) effect was measured first [304]. The dHvA effect enables to measure the Fermi surface and the effective masses. Lonzarich [278] found effective masses in the range of 3 to 6 times larger than the free electron mass for most Fermi surface sheets. Compared to band structure calculations he reported mass enhancement factors in the range of 1.5 to 3.0. In a recent angle-resolved photoemission spectroscopy (ARPES) experiment, Schäfer *et al.* [58, 206] found similar mass enhancement factors. In addition, they observed a band width reduction for shallow bands of 30%. Older ARPES studies [169, 173] for occupied states and inverse photoemission spectroscopy (IPS) studies [172] for unoccupied states provide additional data of the experimental band structure. These experiments report a 10% narrowing of the *d* bands. Time-resolved two-photon photoemission (TR-2PPE) experiments reveal that the spin-averaged relaxation times in iron are shortest among the elementary ferromagnets [60]. The ratio of majority and minority relaxation times $\tau_\uparrow/\tau_\downarrow$ is in the range between 1 and 2. Sánchez-Barriga *et al.* [62, 64] performed ARPES studies on iron and compared their results to a LDA+DMFT and three-body scattering approximation calculation. They found that both approaches, the LDA+DMFT approach and the three-body scattering approximation approach, improve the description of correlation effects in iron over that of plain LDA. However, the effective masses and the line width of the photoemission peaks are underestimated. An early DMFT study by Katsnelson *et al.* [65] found a strong damping of the quasiparticle states beyond 1 eV binding energy. Similarly, Grechnev *et al.* [66] conducted a LDA+DMFT study revealing that the main correlation effects are present in the majority spin channel. Zhukov *et al.* [67, 69, 70] performed GW+T calculations to study the influence of the magnon excitations on the electron states in iron. They found that the electron-magnon interaction yields an essential reduction of the lifetime of the minority *d* states. In comparison, the influence of the electron-magnon interaction on the free-electron-like minority electrons and all the majority electrons is found to be much smaller.

We have performed an electron-magnon self-energy calculation in the GT approximation starting from the self-consistent COHSEX Green function. The electron-magnon self-energy and the corresponding spectral function is shown in Figs. 4.13 and 4.14 for majority and minority states along the Γ to N direction, respectively.

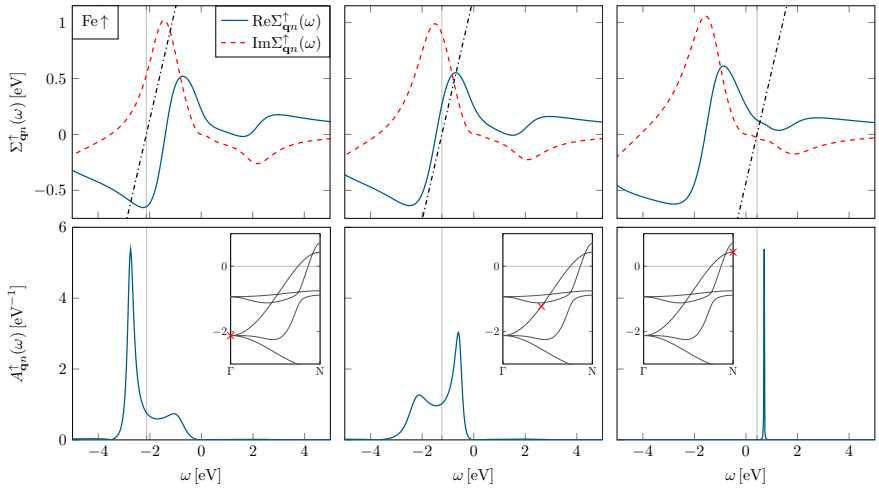

Figure 4.13: Self-energy (upper row) and the corresponding spectral function (lower row) for three majority states of a band along the Γ to N direction in iron. The insets of the spectral function show the band structure along that $\mathbf{k}$ direction and the considered state is indicated as a red cross. The single-particle energy is indicated as a grey thin vertical line in the upper and lower panel. The dash-dotted line (upper panel) corresponds to $\omega - \epsilon^{\uparrow}_{\mathbf{q}n}$ and its intersection with the self-energy indicates a quasiparticle solution. The self-consistent COHSEX Green function serves as starting point for the GT self-energy calculation. The Fermi level is set to zero.

The coupling of the electronic spectrum to strong magnons, which proceeds via the scattering processes schematically shown in Fig. 4.7, leads to a resonant feature in the self-energy. These resonances manifest themselves as a peak in the imaginary part of the self-energy, accompanied by a corresponding strong variation in the real part. The resonances within the self-energy indicate the energy range in which the electron-magnon interaction is particularly effective. In other words, the more effective the electron-magnon interaction, the larger the imaginary part of the self-energy. The resonance of the electron-magnon interaction depends on the spin state. While the majority spin self-energy exhibits the resonance below the Fermi level at binding energies larger than 1 eV, the resonance occurs just above the Fermi level for the minority spin states, cf. Figs. 4.13 and 4.14. If the electron-magnon interaction is weak, this causes a mixing of a single-particle state with magnon excitations forming a quasiparticle that manifests itself in a well-defined quasiparticle peak in the spectral function. In case of iron, however, we find, besides the well-defined quasiparticle peaks, additional peaks in the spectral function due to the electron-magnon interaction, see lower row of Figs. 4.13 and 4.14. The additional peak occurs if the

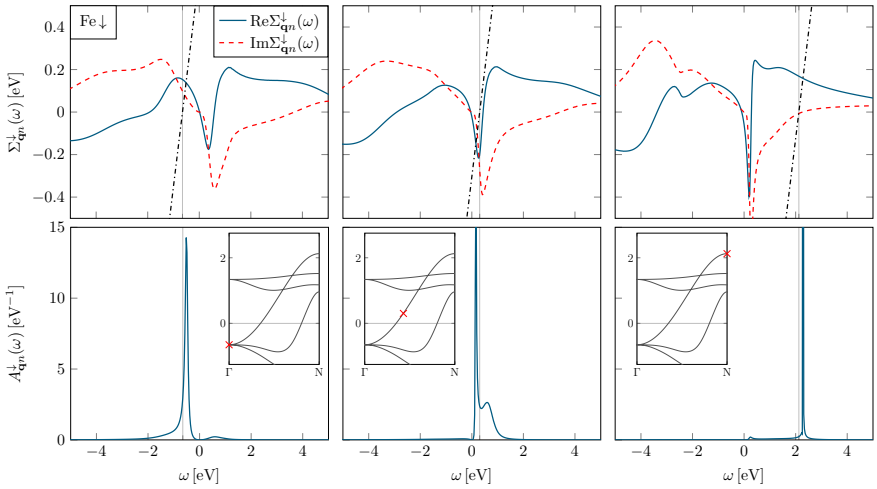

Figure 4.14: Same as Fig. 4.13 for a minority band along the Γ to N direction in iron. The dash-dotted line in the upper panel corresponds to $\omega - \epsilon^{\downarrow}_{\mathbf{q}n}$.

electron-magnon interaction is sufficiently strong. It results from the mixing of a quasiparticle state with a many-body state to which we refer to as a *magnaron* state, a coherently bound state of single-particle and magnon excitations. The many-body character of the magnaron state depends on the spin channel. In case of the majority spin channel, the additional peak appears due to the coupling of a majority hole to a coherent superposition of minority holes and strong magnon excitations. In case of the minority spin channel, the additional peaks appears due to the coupling of a minority electron to a coherent superposition of majority electrons and strong magnon excitations. We have discussed these magnaron states in details in Section 4.4.4.

The magnaron state is intimately connected to the properties of the self-energy as it appears energetically at the resonance of the self-energy. Therefore, the weak momentum dependence of the self-energy transfers to a weak momentum dependence of the magnaron state and consequently the magnaron state forms a flat band, schematically shown as green dotted line in the right panel of Fig. 4.15. If an electronic band, depicted as red dashed line in that figure, crosses the flat band of the magnaron state, the electron-magnon interaction causes a mixing of these states leading to additional peaks in the spectral function. The electronic bands, considered in Figs. 4.13 and 4.14, are examples thereof. The additional peaks can also be seen in the quasiparticle dispersion. The left panel of Fig. 4.15 exemplarily shows the majority quasiparticle dispersion of the band considered in Fig. 4.13. Along the band

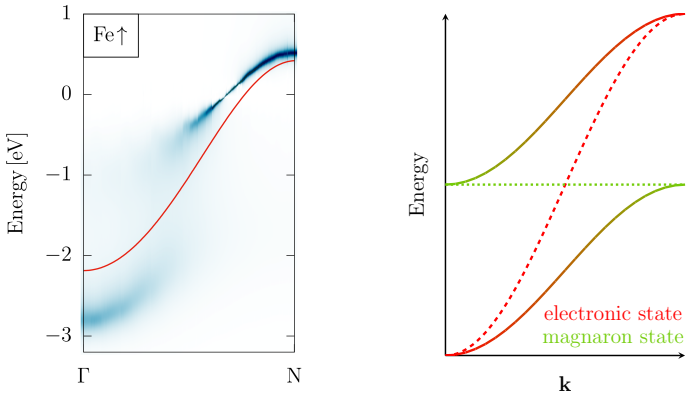

Figure 4.15: Additional quasiparticle peak in the spectral functions indicating the emergence of a new quasiparticle to which we refer as the *magnaron* state. Left: majority single-particle band (red line) along the Γ to N direction in iron and its renormalized spectral functions shown as blue color-coded map calculated with the corrected LSDA Green function. The Fermi level is set to zero. Right: schematic representation of the mixing of an electron state (red dashed) and a magnaron state (green dotted). The hybrid states change their many-body character (color gradient along the bands shown as solid line) between electronic and magnaron-like state depending on the momentum **k**.

the many-body character of the two quasiparticle states change due to the electron-magnon interaction and so spectral weight is transfered from one peak to the other. The change of the many-body character is schematically represented as the color gradient along the bands shown as solid lines in the right panel of Fig. 4.15. A similar effect can be seen in the band structure of the minority spin channel, shown in the right panel of Fig. 4.18, for the band considered in Fig. 4.14. The mixing of the electronic quasiparticle state and the magnaron state leads to an energetic splitting and a broadening of the corresponding quasiparticle peaks. The splitting as well as the broadening of the quasiparticle peaks is particularly strong in the majority spin channel. The two quasiparticle peaks are separated by approximately 1.8 eV. In contrast, the separation of the two minority quasiparticle solutions amounts to approximately 0.6 eV. The reason for the difference between the majority and minority spin channel comes from the shape of the corresponding self-energies. The mixing and, by this, the splitting of the quasiparticle solutions is determined by the resonance features of the self-energy. While the real-part of the majority spin self-energy exhibits a broad resonance feature below the Fermi level, cf. upper row of Fig. 4.13, the resonance feature for the minority states is a narrow dip, cf. upper row of Fig. 4.14. This, in turn,

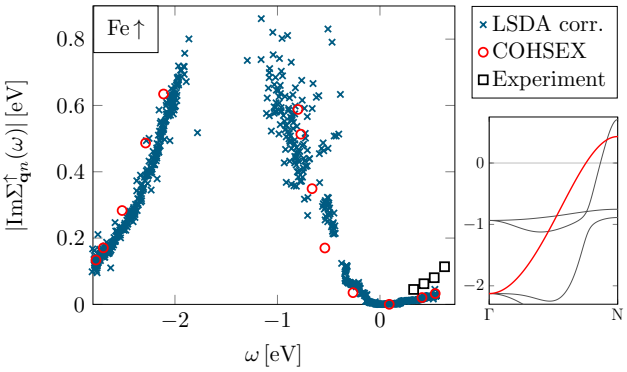

Figure 4.16: Starting-point dependence of the quasiparticle inverse lifetime employing the corrected LSDA (blue crosses) and the COHSEX Green function (red circles) compared to experimental values (black squares) taken from Knorren *et al.* [60]. The quasiparticle inverse lifetime is calculated for a majority band along the Γ to N direction shown as the red thick line in the inset.

leads to the wide and narrow splitting of the mixed quasiparticle states within the majority and minority spin channel, respectively.

The broadening of the majority quasiparticles and minority quasiparticles, which is inversely proportional to their lifetime, is shown in Figs. 4.16 and 4.17, respectively. The results are obtained with the COHSEX Green function, shown as red circles, and with the corrected LSDA Green function, shown as blue crosses, compared to the results of a TR-2PPE experiment [60]. The inverse lifetimes obtained with the corrected LSDA Green function are in good agreement to the data obtained with the COHSEX starting point. This indicates that the corrected LSDA Green function can be employed for the calculation of the *GT* self-energy alternatively to the COHSEX one. The corrected LSDA Green function has the practical advantage that it allows to calculate the self-energy at arbitrary **k** points easily.

The inverse lifetimes increase quadratically around the Fermi level for both spin channels. The electron-magnon scattering involving the strong magnon excitations causes the imaginary part of the majority and minority quasiparticle solution to increase strongly below and above the Fermi level, respectively. The different shapes of the imaginary part of the quasiparticle solution as a function of the binding energy are a consequence of the spin asymmetry of the self-energy. In case of the majority spin channel, the inverse lifetime attains values larger than 0.6 eV, see Fig. 4.16. Apparently, the larger the imaginary part of the quasiparticle solution, the larger the scatter within the obtained data. There are a number of reasons for this. First,

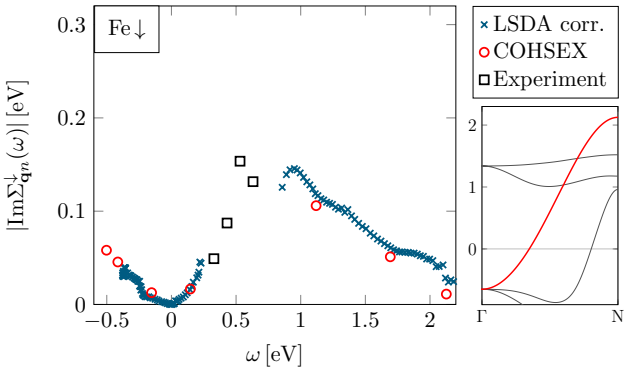

Figure 4.17: Same as Fig. 4.16 for a minority band along the Γ to N direction.

the quasiparticle equation is solved by a fitting procedure. The fitting procedure is particularly stable if the imaginary part of the self-energy is small. Second, in the presence of two mixed quasiparticle states a large imaginary part leads to an overlap of the corresponding quasiparticle peaks so that a unique determination of the two quasiparticle solutions is complicated further. In addition, the self-energy varies strongly with respect to the binding energy, which is another reason why the solution of the quasiparticle equation is difficult to be found numerically. In spite of the scatter within the data, the results clearly indicate the trend of the quasiparticle solution's imaginary part resembling the imaginary part of the self-energy taken for a single state shown in Fig. 4.13. Near the binding energy of 1.5 eV there exists no quasiparticle solution, this is a result of the splitting of the mixed quasiparticle states. The large imaginary part at that binding energy indicates that the quasiparticle solutions are overdamped leading to a complete loss of the quasiparticle peaks, cf. left panel of Fig. 4.15. This is because the electron-magnon scattering is resonant in that energy region. We find a very similar behavior for the minority spin channel, see Fig. 4.17. Above the Fermi level there exists an energy range, between 0.2 eV and 0.8 eV, where no quasiparticle solution exists. This energy range corresponds to the separation of the mixed quasiparticles. It is the energy range where the resonance of the self-energy occurs, i.e., the real part of the self-energy exhibits the pronounced dip and its imaginary part increases drastically.

The Figs. 4.16 and 4.17 show in addition to the calculated inverse lifetimes experimentally measured results. In case of the minority spin channel the experimentally observed inverse lifetime is obtained just in that energy range where the calculations do not yield a quasiparticle solution. The maximal inverse lifetime agrees well

with the experimental value, although at slightly lower energies than obtained from the self-energy calculation. We conclude that the spin-flip scattering process is an important scattering channel for the unoccupied minority states close to the Fermi level. In comparison, the lifetime of the unoccupied majority states are affected less by the electron-magnon self-energy. This is a consequence of the spin asymmetry of the self-energy. The comparison of the inverse lifetime of the majority states with the experimental data indicates that the spin-flip processes, described by the GT self-energy, give a significant contribution to the total inverse lifetime. Yet, the experimental inverse lifetime is considerably larger than the contribution coming from the spin-flip processes. Our findings are in accordance with the GW+T calculations by Zhukov *et al.* [67, 69, 70], they report that the inclusion of the spin-flip scattering processes are important for the minority electron states to improve the agreement between theory and experiment. Additionally, they find that spin-flip scattering affects the majority electron states much less compared to the minority spin channel. It is important to note that the GT self-energy accounts for the spin-flip processes, while other scattering processes affecting the quasiparticle's lifetime are missing. For example the contribution from the GW self-energy, particle-particle scattering, electron-phonon scattering, defect scattering, *et cetera* are not accounted for in the present approach. Therefore, missing many-body effects in the GT approximation might give a valuable contribution to lifetime effects. The mismatch between experiment and theory for the lifetime of the majority states might be attributed to the missing many-body effects in the GT self-energy. The missing many-body effects are also the reason why the inverse lifetimes, shown in Figs. 4.16 and 4.17, decrease below $-2\,\mathrm{eV}$ and above $1\,\mathrm{eV}$ for the majority and minority states, respectively. In these energy regions the electron-magnon scattering becomes less effective and other scattering processes might become important.

As a conclusion of our analysis for iron, we discuss the renormalization of the band structure calculated with the corrected LSDA Green function. The band structure gives an overview of the GT self-energy renormalization of the single-particle states. The quasiparticle energies and lifetimes are shown as a blue color-coded map in Fig. 4.18 together with the corrected LSDA band structure shown as the red line. The left and right panel of that figure show the majority and minority states, respectively. The particle-hole asymmetry and the spin asymmetry of the self-energy is clearly visible in the renormalized band structure. Both spin channels experience a strong renormalization due to the GT self-energy in the vicinity of the Fermi level.

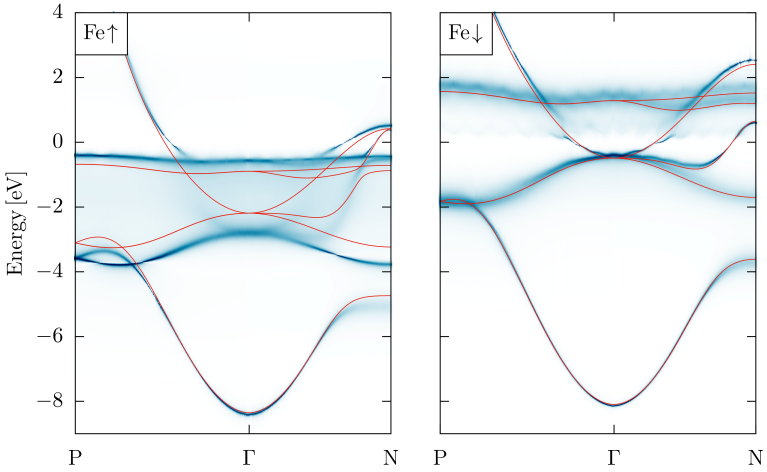

Figure 4.18: Band structure of bcc iron along the high-symmetry line P $\rightarrow$ Γ $\rightarrow$ N for the majority (left) and the minority (right) states. The corrected LSDA band structure is shown as the red solid line. The corresponding renormalized quasiparticle bands including lifetime effects are shown as a blue color-coded map. The Fermi level of the corrected LSDA Green function is set to zero.

While the majority spin states are affected most below the Fermi level, the minority spin states are particularly renormalized above the Fermi level. The *GT* self-energy leads to strong lifetime effects for the majority spin channel for binding energies larger than 0.5 eV. Towards stronger binding energies the mixing of the electron and magnaron state yields a strong increase of the inverse lifetime, which can even lead to a complete loss of the quasiparticle peaks. In both spin channels the mixing of electrons and magnarons leads to a splitting of the band and a strong broadening of the quasiparticle states. This can be seen in the quadratic bands around the Γ point considered along the Γ to N direction in Figs. 4.16 and 4.17. The curvature of these quadratic free-electron-like bands flattens at the Fermi level indicating a renormalization of the effective mass. We find for both spin channels effective-mass renormalizations (4.4.13) in the range of $1.5 - 1.6$ along the Γ to N direction. These values compare fairly well with the mass renormalization ratios of 1.8 ± 0.4 and 2.0 ± 0.4 reported by Schäfer *et al.* [206] for the minority and majority band, respectively. In addition, Schäfer *et al.* [206] found a reduction of the occupied-band width compared to a generalized gradient approximation calculation. They observe experimentally a majority state at the P point at 0.57 eV binding energy. We find that this state, which

appears in the corrected LSDA starting point at 0.68 eV binding energy, is renormalized qualitatively correct to a lower binding energy of 0.37 eV. The same can be said about the experimentally observed band width reduction in the minority spin channel. At the Γ point the binding energy is reduced from 0.49 eV to 0.34 eV. However, these binding energies have to be taken with caution as we do not account for a new Fermi level alignment.

As mentioned earlier, we find that the electron-magnon interaction gives an important contribution to the minority electron lifetimes yielding values in good agreement with experiment [60]. Zhukov *et al.* [67] drew the same conclusions from their *GW*+*T* calculations. For the majority electron states the electron-magnon interaction is less effective. However, it gives a significant contribution to the experimentally measured lifetimes. Our results compare well with DMFT studies of ferromagnetic iron. For example, Katsnelson *et al.* [65] and Grechnev *et al.* [66] report a strong damping of the majority quasiparticle states beyond 1 eV binding energy. The spectral functions shown by Sánchez-Barriga *et al.* [62, 64] are in very good agreement with our data. They also obtain a strong broadening of the majority quasiparticle peaks in the energy range of -1 eV to -3 eV, but they do not discuss additional peaks in the spectral function. We find magnaron states in the majority and minority spin channel. We note that in the minority spin channel the quasiparticle dispersion of the flat band at approximately $1.5 - 1.8$ eV above the Fermi level extending from the P to the N point exhibits an artificial oscillatory behavior. We ascribe this oscillatory behavior to a numerical artifact due to the analytic-continuation method used for the frequency integration.

4.7.2 Cobalt

In the case of cobalt, experimental band structure data is scarce in the literature [174, 305]. The overall *d*-band width is found to be 20% narrower compared to the prediction by a LSDA calculation. There is an ongoing debate over the quasiparticle lifetime effects in cobalt. A recent low-energy high-resolution ARPES study by Monastra *et al.* [61] found a quenching of the quasiparticle states for binding energies larger than 2 eV. In contrast, Mulazzi *et al.* [306] found in a soft x-ray angle resolved photoemission spectroscopy (SX-ARPES) measurement for bulk ferromagnetic cobalt that the spectral peak widths are narrower than previously observed in the low-energy ARPES experiment by Monastra *et al.* [61]. Mulazzi *et al.* traced the overestimation of the spectral peak width back to the final-state broadening. The

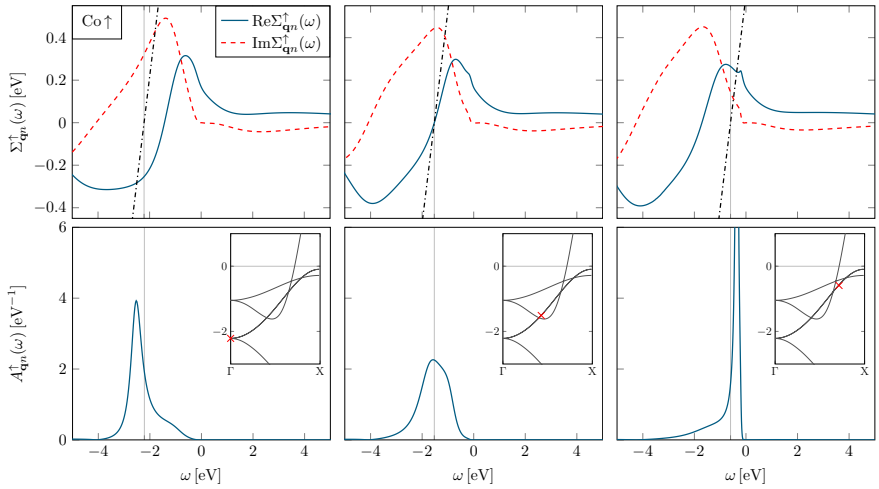

Figure 4.19: Same as Fig. 4.13 for a majority band along the Γ to X direction in cobalt.

dominance of the final state in the photoemission mapping of the Fermi surface of cobalt was shown earlier by Gao *et al.* [307]. In a TR-2PPE experiment by Knorren *et al.* [60] it was found that in fcc cobalt the spin-averaged lifetime of electron states is longest among the elementary ferromagnets. Cinchetti *et al.* [308] performed a time-resolved magneto-optical Kerr effect as well as a spin-, energy-, and time-resolved two-photon photoemission experiment on a thin cobalt film. They found that the electron-magnon interaction gives a significant contribution to the spin dynamics of single electrons excited close to the Fermi level. A review on hot electron lifetimes in ferromagnetic metals by TR-2PPE can be found in [309]. The LDA+DMFT study by Grechnev *et al.* [66] and the combined ARPES and LDA+DMFT study by Sánchez-Barriga *et al.* [63,64] find a strong spin-dependent lifetime effect for binding energies larger than $\simeq 1$ eV.

We study cobalt in the fcc crystal structure. Figures 4.19 and 4.20 show the self-energy and the corresponding spectral function for a majority and minority band along the Γ to X direction as characteristic examples. The self-energies, shown in the upper row of these figures, exhibit a particle-hole asymmetry very similar to that of iron. However, the effect of spin-flip scattering for the minority spins seems to be suppressed, both in comparison to that of the majority spin states, and also in comparison to the minority spin self-energy of iron, cf. Figs. 4.14 and 4.20. The difference between iron and cobalt might be attributed to the different occupations of the *d* states. While iron is classified as a weak ferromagnet as the majority *d* states are not

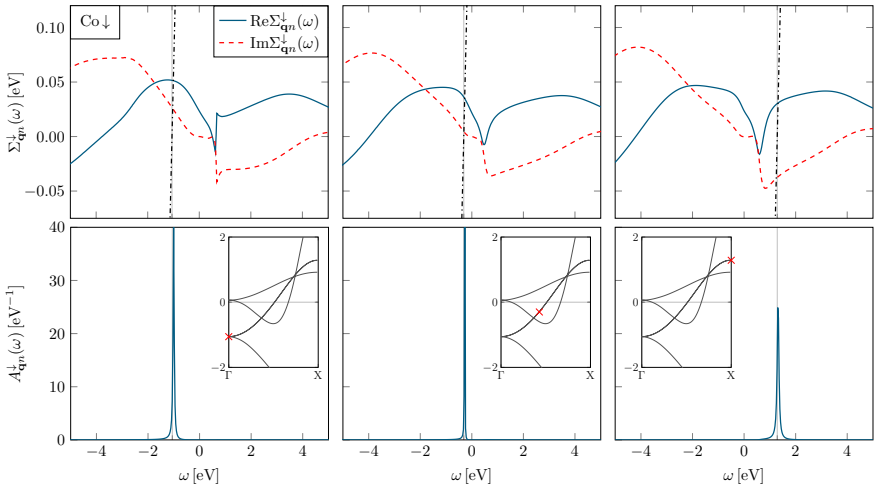

Figure 4.20: Same as Fig. 4.14 for a minority band along the Γ to X direction in cobalt.

fully occupied, cobalt (and also nickel) is a strong ferromagnet in the sense that all majority *d* states are occupied. A strong-magnon process of a minority spin state involves the excitation of electron-hole pairs in the majority spin channel. The *d* states are particularly important for the formation of collective spin-wave excitations. Consequently, the lack of unoccupied majority *d* states in cobalt leads to a suppression of such spin-flip scattering processes resulting in a weak minority spin self-energy. In the vicinity of the Fermi level, the real part of the minority spin self-energies ranges from −20 meV to 50 meV, hardly changing the single-particle energies. Just as well, the self-energy gives only a small contribution to the quasiparticle lifetimes. As a consequence the self-energy hardly affects the minority states in cobalt leading to well defined quasiparticle peaks in the spectral function, see lower row of Fig. 4.20. The electron-magnon self-energy cannot account for the inverse lifetimes of minority electrons measured in a TR-2PPE measurement [60] that observes inverse lifetimes larger than 150 meV at 1 eV above the Fermi level. In contrast to the minority spin channel, the renormalization of the majority states is strong. The self-energy of the majority states yields a pronounced quasiparticle renormalization, particularly strong for hole states. In the case of cobalt, the majority spin self-energy is practically featureless above the Fermi level, see Figure 4.19. This is a consequence of the majority *d*-state occupation, i.e., unoccupied majority *d* states are scarce so that weak-magnon scattering processes, which determine the self-energy above the Fermi level, are suppressed. The strong-magnon scattering leads to a resonance feature in

the self-energy below the Fermi level very similar to that of iron, cf. Figs. 4.13 and 4.19. However, in cobalt the resonance feature extends over a larger energy range compared to iron, i.e., the imaginary part of the self-energy is a rather broad function meaning that it attains large values in a comparatively large energy range. This, in turn, leads to asymmetric quasiparticle peaks of the Breit-Wigner form over a wide range of binding energies. The spectral functions in the lower panel of Fig. 4.19 are examples for this. In contrast to iron, in which we found two peaks in the spectral function, the quasiparticle peaks in cobalt exhibit strongly broadened Breit-Wigner shaped peaks but no double-peak structures. At energies near 1.5 eV where the imaginary part of the self-energy is maximal, the quasiparticle peak is strongly damped, see middle column of Fig. 4.19. The damping of the quasiparticle indicates that the electron-magnon interaction is particularly strong in that energy region leading to incoherent many-body states. At the bottom and the top of the band the quasiparticle peaks have shoulder structures above and below the main peak, respectively. These shoulders indicate a mixing of the majority hole states with the magnaron state, schematically shown in the right panel of Fig. 4.15, similar to the mixing effect found in iron. However, the electron-magnon interaction is not strong enough to lead to the appearance of a distinct second peak in the spectral function as in the case of iron. Instead, the hybrid states manifest themselves as a quasiparticle peak plus a shoulder structure that occurs above or below the main peak.

In addition, we find a dispersion anomaly in a free-electron-like majority band crossing the Fermi level in the Γ to K direction, see Fig. 4.21. The dispersion anomaly is accompanied by a flattening of the band dispersion with an effective-mass renormalization (4.4.13) of $\simeq 1.2$ at the Fermi level. Below the Fermi level, the inverse lifetimes of the quasiparticle increase strongly (left panel) yielding a rapid increase of the broadening of the quasiparticle peaks that can be seen in the spectral functions (right panel). The quasiparticle broadening superimposes the renormalization of the band dispersion so that with increasing binding energies a clear interpretation of the band dispersion becomes increasingly difficult. However, for low binding energies a kink structure is observable in the quasiparticle dispersion that exhibits a maximal deviation from the single-particle dispersion near 200 meV binding energy. At this energy the inverse lifetime jumps to approximately 220 meV and remain almost constant up to a binding energy of 300 meV. For larger binding energies the broadening of the quasiparticle peaks increases further leading to a strong smearing of the band dispersion, see spectral functions in the right panel of Fig. 4.21. In contrast, the

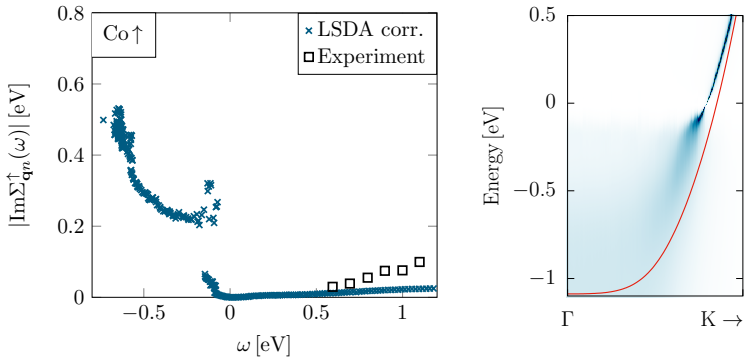

Figure 4.21: Quasiparticle lifetime broadening and dispersion anomaly caused by the electron-magnon interaction for a majority band in cobalt which crosses the Fermi level along the Γ to K direction. Left: imaginary part of the quasiparticle solution (blue crosses) compared to experimental data [60] (black squares). Right: single-particle band (red line) and its renormalized spectral functions shown as a blue color-coded map. The corrected LSDA Green function serves as starting point, the Fermi level is set to zero.

electron-magnon interaction is much less effective above the Fermi level and it can only account partly for the experimentally measured inverse lifetimes. At 1 eV above the Fermi level the imaginary part of the quasiparticle solution amounts to $\simeq 20$ meV while in experiment a value of $\simeq 80$ meV is observed.

In summary, we find a pronounced spin-dependent quasiparticle renormalization in fcc cobalt. The band structure together with lifetime effects is shown in Fig. 4.22 for the majority spin (left) and the minority spin (right) states along the X $\rightarrow$ Γ $\rightarrow$ K direction. The renormalization of the minority spin states (right) is rather small and lifetime effects are almost equally important for occupied and unoccupied states. In contrast, the occupied majority states (left) are affected strongly by the electron-magnon interaction. The electron-magnon interaction leads to a strong broadening of the quasiparticle peaks. The quasiparticle damping sets in at binding energies higher than 0.5 eV. Our results are in accordance with a previous ARPES measurement and a three-body scattering study by Monastra *et al.* [61]. This measurement found that the quasiparticle peaks vanish for binding energies larger than 2 eV due to many-body effects. They found that the many-body effects are much stronger for the majority states than for the minority states. LDA+DMFT calculations by Grechnev *et al.* [66] and Sánchez-Barriga *et al.* [63,64] come to similar conclusions. The LDA+DMFT approach yields a strongly spin-dependent quasiparticle renormal-

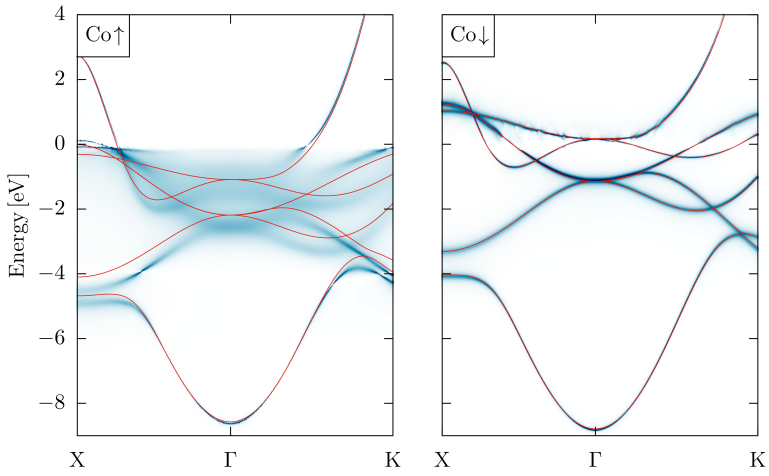

Figure 4.22: Same as Fig. 4.18 for fcc cobalt along the X → Γ → K direction.

ization in cobalt, where the majority hole states experience strong lifetime effects for binding energies larger than $\simeq 1\,\mathrm{eV}$.

For the unoccupied states we find that the electron-magnon interaction does only partly account for the quasiparticle lifetimes seen experimentally [60, 310]. For a quantitative agreement with experiment additional many-body effects like the *GW* self-energy, the particle-particle scattering, the electron-phonon interaction, *et cetera* might be important. We discussed the mixing of a magnaron state and the single-particle states leading to shoulder structures in the spectral functions and a strong damping of the quasiparticle peaks in the energy window $1.0 - 1.5\,\mathrm{eV}$ binding energy, cf. Fig. 4.19. It is that energy window, in which the spectral functions of the majority spin channel appear particularly smeared, see left panel of Fig. 4.22. In addition, we find a kink structure in the free-electron-like band along the Γ to K direction below the Fermi level. It manifests itself as a substantial change of the band dispersion, accompanied by a rapid increase of the quasiparticle broadening, cf. 4.21. The electron-magnon interaction becomes less effective for binding energies beyond $3\,\mathrm{eV}$ and with it the lifetime broadening decreases.

4.7.3 Nickel

Nickel has gained a lot of attention from an experimental point of view. Its Fermi surface and its band structure have been studied experimentally by dHvA experi-

ments [311–313] already in the 1960's. Early ARPES experiments [190, 192, 314] that measured the band structure and the exchange splitting of nickel revealed substantial differences between theory and experiment. For example the calculated exchange splitting is typically too large, and also the measured *d*-band width is 30% smaller than the calculated value. In addition, density-functional calculations do not account for the 6 eV satellite in the density of states that has been observed by XPS experiments [194, 196–198]. It has been shown [201–203] that hole-hole interactions are responsible for the 6 eV satellite.

More recent ARPES experiments revealed correlation effects in the band structure occurring near the Fermi level. For example, Higashiguchi *et al.* [205] found a kink structure in the dispersion of a minority band that originates from the electron-phonon interaction. They point out, however, that additional electron correlations contribute to the spectral features near the Fermi level. Hofmann *et al.* [59] performed an ARPES study of a minority band. They observed a renormalization when compared to a Gutzwiller calculation [315, 316] that shows a kink structure in the band dispersion at $250 - 300$ meV binding energy. In addition, a comparison of photoemission data to three-body scattering calculations revealed that local correlations are important for a realistic description of the electron states near the Fermi surface [275]. Knorren *et al.* [60] found in a TR-2PPE experiment that the spin-averaged electron lifetime is smaller than that of cobalt but larger than that of iron. Andres *et al.* [317] conducted a TR-2PPE experiment for a nickel thin film. They observed a low spin asymmetry in the decay rates of the photoexcited electrons. This is supported by a combined ARPES measurement and LDA+DMFT study perfromed by Sánchez-Barriga *et al.* [64]. They found a linewidth broadening in nickel that is approximately equal for both spin channels. Grechnev *et al.* [66] conducted LDA+DMFT calculations for Fe, Co, and Ni and they found that the spin-dependent behavior of the self-energy is less pronounced in nickel compared to iron and cobalt. In a *GW*+*T* calculation Zhukov *et al.* [67,69,70] have shown that the decay of electron states in nickel is only weakly affected by the electron-magnon interaction. However, a *GW* calculation including spin-orbit coupling [318] demonstrates that the spin mixing gives an important contribution to the spin-dependent lifetimes.

The majority and minority self-energy together with the resulting spectral functions is shown in Figs 4.23 and 4.24, respectively. The self-energy is calculated for a band dispersing along the Γ to X direction as indicated in the insets. In case of iron and cobalt we have found a weak dependence of the self-energy on the Bloch

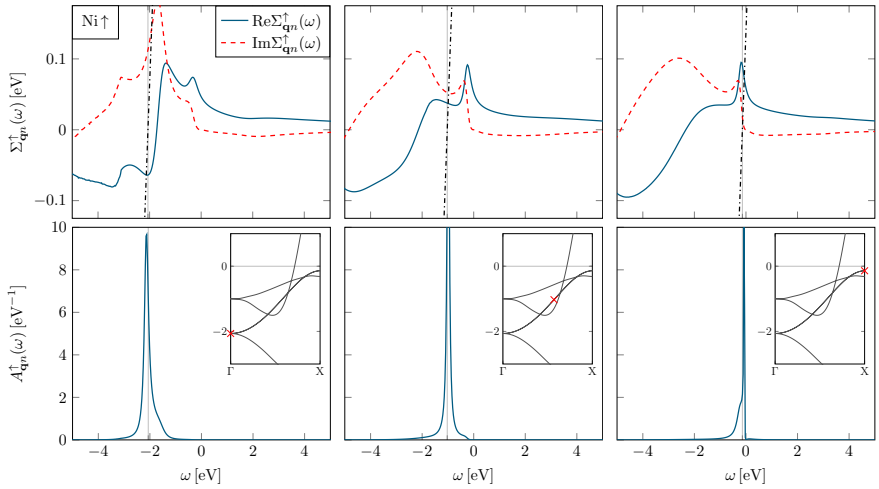

Figure 4.23: Same as Fig. 4.13 for a majority band along the Γ to X direction in nickel.

momentum. Differently to these cases, the self-energy of nickel shows a stronger momentum dependence. In particular, the majority self-energy has a comparatively strong momentum dependence that we explain with the density of states of nickel. The majority self-energy is determined by the minority density of states. In contrast to iron and cobalt, where the minority density of states is rather flat in the vicinity of the Fermi level, in nickel the minority density of states exhibits a peak just at the Fermi level, cf. Fig. 3.4. The peak in the density of states, in turn, leads to a strong variation of the number of available scattering states in the vicinity of the Fermi level leading to a stronger momentum dependence of the self-energy compared to that of iron or cobalt.

In addition, the pronounced dip in the real part of the minority spin self-energy just above the Fermi level as seen in iron and to a lesser degree in cobalt is absent in the case of nickel, compare the minority spin self-energies for iron, cobalt, and nickel in Figs. 4.14, 4.20, and 4.24, respectively. The minority spin self-energy of nickel is practically featureless above the Fermi level. The reason is that nickel has almost all d states filled. As a consequence the formation of strong magnon excitations as well as the spin-flip scattering is suppressed for minority electron states. The same argument explains why we find the energy scale of the self-energy to be smallest among the elementary ferromagnets.

In contrast to iron and cobalt, the particle-hole asymmetry of the minority spin self-energy is reversed for nickel. This means that differently to the minority states of

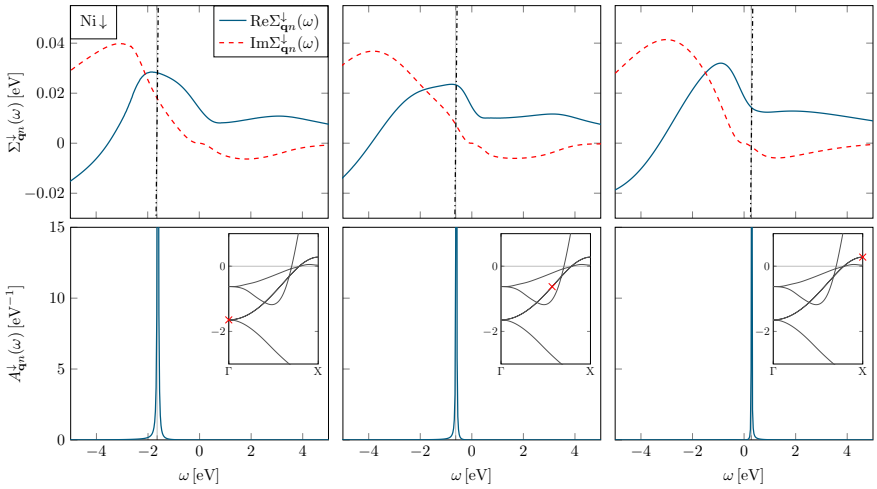

Figure 4.24: Same as Fig. 4.14 for a minority band along the Γ to X direction in nickel.

iron and cobalt, the minority self-energy in nickel yields a stronger renormalization for hole states than for electron states. Nevertheless, the electron-magnon interaction causes overall a mild renormalization of the minority single-particle states. The quasiparticle peaks, occurring in the spectral function shown in the lower panel of Fig. 4.24, are well defined having a symmetric Lorentzian shape. The imaginary part of the minority quasiparticle solutions of that band does not exceed 40 meV indicating that lifetime effects for the minority quasiparticles due to the electron-magnon interaction play a subordinate role. Compared to the other elementary ferromagnets we find that lifetime effects for these states are smallest in nickel.

Similarly, we find that the majority states of nickel are affected least by the electron-magnon interaction compared to iron and cobalt. The self-energy yields a moderate renormalization of the majority single-particle states leading to fairly well defined quasiparticle peaks. Nevertheless, also in the case of nickel the electron-magnon self-energy causes the appearance of anomalies within the quasiparticle peaks. For example, the quasiparticle peaks shown in the lower row of Fig. 4.23 exhibit shoulder structures besides the main peak. Close to the Fermi level, right column of that figure, the shoulder structure is distinctly visible in the main quasiparticle peak. The shoulder structure is an indication for the appearance of magnarons that mix with the electronic states. Similar shoulder structures, although more pronounced, are seen in the case of cobalt, cf. Fig. 4.19.

Moreover, we find a kink structure in the quasiparticle dispersion of a free-

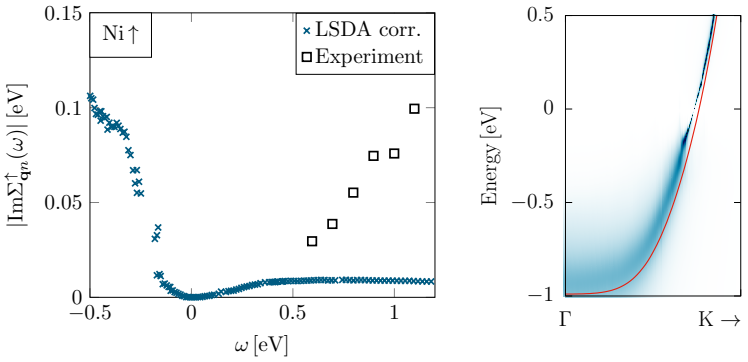

Figure 4.25: Same as Fig. 4.21 for a majority band along the Γ to K direction in nickel.

electron-like majority band crossing the Fermi level along the Γ to K direction, see Fig. 4.25. The dispersion anomaly is very similar to that in the case of cobalt, cf. Fig. 4.21. As in the case of cobalt, the quasiparticle dispersion flattens compared to the single-particle dispersion. However, the effective-mass renormalization (4.4.13) is smaller and amounts to $\simeq 1.12$ at the Fermi level. In the energy range of $-200 \ldots 200$ meV around the Fermi level, the inverse lifetimes grow quadratically and are approximately equal for electron and hole states. However, for binding energies larger than 200 meV the inverse lifetime increases rapidly. The behavior of the inverse quasiparticle lifetimes as a function of the binding energy is very similar to that of the free-electron-like band of cobalt considered in Fig. 4.21. In both cases the inverse lifetimes strongly increase beyond 200 meV binding energy. However, the broadening of the quasiparticle peaks in nickel is considerably smaller than that in cobalt. As a consequence the quasiparticle band dispersion can be seen also for binding energies higher than 500 meV, see right panel of Fig. 4.25. The real-part of the self-energy renormalization, which corresponds to the difference of the blue and the red curve in the right panel of Fig. 4.25, peaks at around 220 meV binding energy with an amplitude of approximately 70 meV.

Hofmann *et al.* [59] conducted an ARPES study of a minority band along the Γ to K direction. They found a deviation from the calculated band dispersion at the binding-energy range of $250 - 300$ meV that takes the form of a kink structure in the band dispersion. They attribute this kink structure, whose maximal deviation to the calculated band amounts to $\simeq 25$ meV, to the electron-magnon interaction. We find a shallow renormalization of the quasiparticle dispersion that increases rather monotonically from 20 meV at the Fermi level to 36 meV at 0.6 eV binding energy, see left

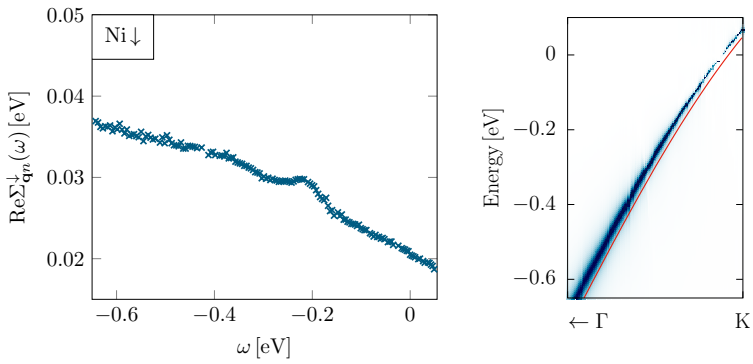

Figure 4.26: Renormalization of a minority quasiparticle band dispersion along the Γ to K direction in nickel. Left: real part of the self-energy correction. Right: single-particle band (red line) and its renormalized spectral functions shown as a blue color-coded map. The corrected LSDA Green function serves as starting point, the Fermi level is set to zero.

panel of Fig. 4.26. Interestingly, at approximately $200 - 250$ meV binding energy a noticeable deviation from the overall renormalization trend occurs. The amplitude of the deviation, however, amounts only to a few meVs and cannot explain the experimentally observed deviation [59]. Important to note is that the renormalization of the quasiparticle dispersion, shown in the right panel of Fig. 4.26, is calculated with respect to the corrected LSDA Green function. The experimentally observed deviation of $\simeq 25$ meV is calculated with respect to a Gutzwiller [315,316] reference.

The majority states above the Fermi level hardly change due to the electron-magnon interaction. Above 0.5 eV the inverse lifetimes of the majority quasiparticles are almost constant, see Fig. 4.25. The spin-flip scattering does not contribute significantly to the experimentally observed inverse lifetimes of the majority quasiparticles [60, 309]. The same can be said about the minority states (not shown in that figure). We find similar self-energy effects for the minority electrons underestimating the experimental inverse lifetimes. In particular, the renormalization of the electron states shows a low spin asymmetry, i.e., the renormalization of majority and minority states are fairly similar, compare the spin channels within the band structure shown in Fig. 4.27. These results are in accordance with the *GW*+*T* calculations by Zhukov *et al.* [67]. They conclude that the effect of spin-flip scattering on electron states in nickel is generally weak. Although the experimentally observed inverse lifetimes cannot be explained by the electron-magnon interaction, the low spin asymmetry is also seen experimentally [60, 317]. Differently to iron and cobalt, in nickel

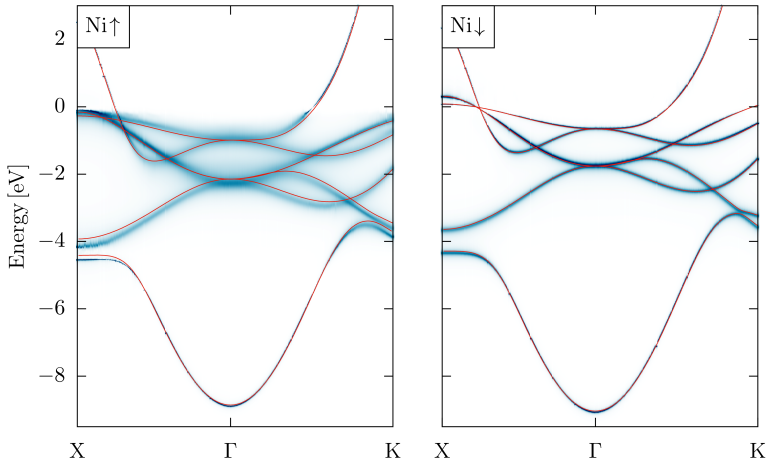

Figure 4.27: Same as Fig. 4.18 for fcc Ni along the X → Γ → K direction.

we find that the minority hole states are renormalized slightly stronger than the electron states. Nevertheless, the renormalization of minority states is weak and we find that the quasiparticle energies are hardly affected and the electron-magnon interaction gives a small contribution to the quasiparticle lifetimes. The kink structure in the minority band crossing the Fermi level in the vicinity of the K point observed by Hofmann *et al.* [59] is not clearly seen within our approach. Nevertheless, we find also a noticeable deviation within the band renormalization that appears at $200 - 250$ meV binding energy, cf. Fig. 4.26.

The majority hole states experience a pronounced lifetime broadening compared to the electron states. Still, lifetime effects are smallest in nickel among the elementary ferromagnets. Along the high-symmetry line Γ to K we find a kink structure in the band dispersion below the Fermi level. The kink structure peaks at approximately 220 meV binding energy, cf. Fig. 4.25. The kink structure is accompanied by a jump of the quasiparticle inverse lifetime. A similar kink structure was found in cobalt.

4.8 Summary

We have implemented the electron-magnon interaction in the *GT* approximation to the self-energy within the many-body perturbation theory utilizing the full-potential

linearized augmented-plane-wave (FLAPW) method. The *GT* approximation is complementary to the *GW* approximation by explicitly accounting for spin-flip excitations. The *GW* approximation is the self-energy approximation that results from the Hedin equations if vertex corrections are neglected. We have formulated the *GT* self-energy such that it can be combined with the *GW* approximation without the need of double-counting corrections. For this, the self-energy of the Hedin equations is expanded in the screened interaction. We have figured out that the *GT* diagrams start with the third order in *W* in the self-energy expansion, while lower orders are considered in the Hartree and *GW* diagrams. This self-energy corresponds to a self-energy diagram in which the correlated propagation of the electron-hole pairs with opposite spins is described by a ladder diagram with three rungs. In order to take also all higher-order interactions into account, which are important for the description of the collective spin-wave excitations, we employ the ladder approximation. The ladder approximation accounts for the interaction between the electron-hole pairs from the third to infinite order by employing the multiple-scattering T matrix, which is the solution of a Bethe-Salpeter equation. We use this T matrix to formulate the *GT* self-energy approximation so that it can be combined with the *GW* approximation without the need of double-counting corrections.

The multiple-scattering T matrix describes single-particle and collective spin-wave excitations on the same footing. The multiple-scattering T matrix is formulated in a basis of maximally localized Wannier function [46, 47], which allows an efficient truncation in real space. The evaluation of the *GT* self-energy requires to calculate the convolution of the Green function and the T matrix in the frequency domain. To this end, we have implemented two methods: the contour-integration method [265] and the analytic continuation method [266, 267]. The contour-integration method is known to be the most precise and computationally most demanding technique. However, the contour-integration method applied to the *GT* approximation leads to spiky self-energies due to **k**-point convergence issues, see Fig. 4.8. Compared to that, the analytic-continuation method allows to efficiently calculate the self-energy. For this, the self-energy is evaluated as a function of imaginary frequencies and analytically continued to real frequencies at the end of the calculation. The analytic continuation is performed by means of a Padé approximation, which is a representation of the self-energy in terms of a sum of effective poles. The analytic continuation performed with a single Padé approximation to the self-energy might yield spurious features in the self-energy in rare cases. To prevent these spurious features, we have

refined the analytic-continuation method.

The GT self-energy contribution is added as a correction to the single-particle energies of the starting point. This is done under the assumption that the starting point accounts for many-body effects except for those of the GT self-energy. We have applied the GT self-energy to the $3d$ bulk transition metals iron, cobalt, and nickel. The self-consistently renormalized Green function with respect to the COHSEX self-energy serves as starting point. Alternatively, we use the corrected LSDA Green function as starting point, that is the LSDA Green function which is corrected for its exchange splitting such that the acoustic magnon excitation energy vanishes in the long-wavelength limit, see discussion on the starting-point dependence of the spin-wave dispersions in Section 3.5.3. The starting-point dependence of the GT self-energy, employing either the COHSEX Green function or the corrected LSDA Green function, is found to be weak in these materials.

The application of the GT self-energy to the bulk elementary ferromagnets Fe, Co, and Ni can have important effects. In particular, we have seen strong lifetime effects for all materials for the majority hole states and for iron also for the minority electron states. In some cases, the lifetime broadening leads to a complete loss of the quasi-particle peaks. We have found that the effect of the self-energy on the electronic spectrum weakens in the series iron, cobalt, and nickel. We ascribe this weakening to the increasing d-state occupation as the unoccupied d states are particularly important for the electron-magnon interaction. The qualitative behavior of the GT self-energy can be explained by density-of-states arguments for these materials. The characteristics of ferromagnetic materials, i.e., the presence of majority and minority spin states leads to the fact that the spin-flip of a majority spin is much more likely than that of a minority spin. As a consequence, the T matrix that mediates spin-flip processes exhibits a pronounced spin asymmetry. The spin asymmetry of the T matrix has a number of consequences for the GT self-energy. First, the self-energy inherits the spin asymmetry of the T matrix, i.e., the self-energy leads to a substantially different renormalization of the majority and minority states. The reason is that the T matrix couples opposite spin states. For example the renormalization of a majority state depends on the minority states via spin excitations and vice versa. Second, the spin asymmetry of the T matrix leads to a particle-hole asymmetric renormalization, i.e., the renormalization of particle and hole states is substantially different depending on the considered spin state. While majority hole states typically experience a strong renormalization, the effect for the corresponding electron states is weak. To the op-

posite, the renormalization of the minority electrons is much more pronounced than that of the minority holes in most cases. The momentum dependence of the *GT* self-energy is found to be weak, an effect that we ascribe to the low excitation energies of the magnons compared to typical electronic excitation energies.

We found that the electron-magnon interaction leads to the emergence of an additional quasiparticle that is a coherently bound state of electron and magnon excitations to which we refer as the *magnaron* state. The magnarons form a fairly flat band in the Brillouin zone inheriting the weak momentum dependence of the self-energy. As a consequence, the crossing of an electronic band with that of a magnaron results in a mixing of these states. In iron, the mixed many-body states manifest themselves as two peaks in the electronic spectral function. The mixing leads to a splitting of the quasiparticle states that is clearly visible in the band structure. In cobalt and nickel, in which the electron-magnon interaction is weaker than in iron, the mixing of electron and magnaron states leads to shoulder structures instead of additional peaks in the spectral functions. In addition, we found that the electron-magnon interaction can lead to anomalies in the quasiparticle dispersion. For example, we found kink structures in the quasiparticle dispersion of free-electron-like bands appearing in cobalt and nickel at binding energies larger than 200 meV. The implementation of the *GT* self-energy opens up the possibility to study spin-dependent renormalization effects of the electronic spectrum. In particular, the *GT* self-energy is able to describe the spin-dependent lifetime broadening seen experimentally. Interestingly, in the vicinity of the Fermi energy our results are in good qualitative agreement with LDA+DMFT studies of the elementary ferromagnets [62–66] employing the spin-polarized T-matrix fluctuation exchange approximation. This allows the conclusion that the electron-magnon scattering is a very important scattering channel in this energy range for these materials. In the *GT* approximation, the coupling of electrons to spin-flip excitations leads to the emergence of kink structures in the quasiparticle dispersion, which can be attributed to the nonlocal treatment of the collective spin-wave excitations and which, therefore, cannot be described within DMFT. Thus, the *GT* self-energy can help in clarifying the origin of kink structures seen experimentally.

5. Conclusions

The central aim of this thesis has been the first-principles investigation of spin-wave excitations and the electron-magnon scattering in elementary ferromagnets on the basis of the many-body perturbation theory (MBPT). To study spin excitations, the central quantity of interest is the dynamical magnetic response function that allows to access the entire spin excitation spectrum, i.e., single-particle Stoner excitations and collective spin-wave excitations, on the same footing. In the framework of the *GW* approximation the magnetic response function is the solution of a Bethe-Salpeter equation including a multiple-scattering T matrix, which describes the correlated motion of the electron-hole pairs with opposite spins in the ladder approximation. The Bethe-Salpeter equation is solved with the help of an auxiliary four-point magnetic response function. We have used a recently established computational scheme within the full-potential linearized augmented-plane-wave method (FLAPW) employing a Wannier-function basis for the explicit representation of the four-point scattering matrices [43, 166]. The contraction of the four-point magnetic response function yields the physically relevant two-point magnetic response function. A convenient choice, though an approximation, for the Green function of the non-interacting system is the local-spin-density approximation Green function calculated from the Kohn-Sham wave functions and energies. For the description of collective spin excitations the magnetic response function of the non-interacting system is renormalized by solving the Bethe-Salpeter equation. Since spin-wave excitations are low energy excitations, the screened interaction, which describes the interaction between the electron-hole pairs, is approximated by its static limit. The correlated motion of electron-hole pairs of opposite spins, in turn, leads to the formation of collective spin excitations as well as a renormalization of the single-particle Stoner excitations. The screened interaction W in the random-phase approximation is short-range in metal-

lic systems. This motivates a formulation of the magnetic response function in a basis of maximally localized Wannier functions, which allows an efficient truncation of the four-point functions in real space. The short-range behavior of the screened interaction is utilized by employing an on-site approximation, in which off-site contributions of the interaction between electron-hole pairs are neglected.

The so-calculated magnetic response function leads to a gap error in the spin-wave dispersion of collinear magnetic materials, i.e., the spin-wave excitation energy does not vanish in the long-wavelength limit as it should according to the Goldstone theorem. The Goldstone theorem states that the $\mathbf{q} \to 0$ limit of the acoustic magnon excitation energy must vanish in collinear magnetic systems as a consequence of the spontaneously broken spin-rotation symmetry. We have suspected that part of the gap error could be attributed to the choice of the Kohn-Sham Green function for the treatment of the non-interacting system. As the magnetic response function derives from the *GW* approximation with an additional static approximation for the screened interaction, a consistent numerical realization must use the self-consistently renormalized Green function with respect to that self-energy.

We have calculated the Green function for the elementary ferromagnets iron, cobalt, and nickel from a self-consistent Coulomb hole and screened exchange (COHSEX) self-energy [71], which is the static limit of the *GW* approximation, and studied their spin-wave dispersions. The self-consistent COHSEX calculation brings about an overall reduction of the exchange splitting compared to a local-spin-density approximation (LSDA) or a generalized gradient approximation (GGA) in the parameterization of Perdew-Zunger [90] and Perdew, Burke, and Ernzerhof [91], often leading to a better agreement with experiment. We have found, indeed, that the use of the properly renormalized Green function substantially reduces the gap error compared to when the Kohn-Sham Green functions are employed. The remaining gap error is attributed to approximations in the numerical scheme, e.g., the use of the on-site approximation, the formulation in a Wannier basis, empty-state summations, *et cetera*. In addition, we have introduced a correction scheme motivated by the one-band Hubbard model that cures the fundamental inconsistency of using the Kohn-Sham Green function. To this end, the exchange splitting of the Kohn-Sham solution is adjusted such that the spin-wave excitation energy vanishes in accordance with the Goldstone theorem. The resulting spin-wave dispersions as well as the magnetic moments and the exchange splittings of the corrected Kohn-Sham systems are closer to the corresponding COHSEX results for the materials than to the original Kohn-Sham

results. The correction scheme enables to efficiently calculate spin excitations that respect the Ward identity of spin conservation within the many-body perturbation theory.

In this work, we have developed and implemented a self-energy approximation that describes the electron-magnon scattering. To this end, we have used the description of the spin excitations within the multiple-scattering T-matrix approach. The self-energy is constructed such that it can be combined with the GW approximation without the need of a double-counting correction. The GW approximation accounts for the interaction of electrons with charge fluctuations, known as plasmons, where the screened interaction W corresponds to the propagator of the plasmon excitations. In the GT approximation the multiple-scattering T matrix, which describes the (collective) spin-excitation spectrum, can be seen as the propagator of the magnon excitations. In order to combine the GW and the GT approximation one has to avoid double-counting terms. We accomplish this by leaving out the first- and second-order diagram of the GT approximation as these diagrams are already contained in the Hartree term and the GW approximation. In fact, analyzing the Hedin equations reveals that the leading order of GT-like diagrams is the third order in the screened interaction.

We have calculated the GT self-energy contribution for iron, cobalt, and nickel in combination with the self-consistent COHSEX Green function. Comparing these results with calculations employing the corrected LSDA Green function as starting point we have found generally a good agreement. For Fe, Co, and Ni the GT self-energy gives rise to a particle-hole asymmetric renormalization meaning that either hole or electron states are predominantly renormalized. In addition, the self-energy exhibits a spin asymmetry, i.e., while in the majority spin channel the hole states are more strongly renormalized than the electron states, it is the other way around in the minority spin channel.

We have found that the renormalization due to the GT self-energy decreases in the series Fe, Co, and Ni, an effect that we ascribe to the increase of the d-state occupation. In iron the renormalization gives rise to a strong lifetime broadening of majority holes and minority electrons, to the extent that the quasiparticle character is virtually lost in certain energy regions. We have found that the spin-flip scattering in iron affects the majority electron lifetimes, though to a smaller degree than observed experimentally [60]. For the minority electron states the renormalization by the GT self-energy is considerably stronger, and the calculated lifetimes

are in fairly good agreement with the experimentally observed values. In addition, we found additional peaks in the electronic spectral function for both spin channels indicating the presence of an additional quasiparticle. An analysis by means of the Brillouin-Wigner perturbation theory reveals that the additional quasiparticle is a bound many-body state that is formed by a superposition of single-particle and magnon excitations, to which we refer as a *magnaron* state. The magnaron state forms a flat band inheriting the weak momentum dependence of the self-energy. We have observed a strong coupling of electronic bands with the magnaron state, which is accompanied by a strong lifetime broadening. In cobalt and nickel we have found similar renormalization effects in the spectral function of the majority spin channel, though less pronounced than in iron. Moreover, we have seen that the GT self-energy yields kink structures in the majority quasiparticle band dispersions in cobalt and nickel, a result that we attribute to the spatially extended nature of the spin-wave excitation, requiring a $\mathbf{k}$-dependent description of the self-energy. Hofmann *et al.* [59] investigated a minority quasiparticle band in nickel by means of an angle-resolved photoemission spectrocopy (ARPES) experiment. They observed a kink structure in the band dispersion of the order of 30 meV at a binding energy of $250 - 300$ meV. At approximately the same binding energy we have found a kink-like renormalization, but the renormalization is smaller than seen in the experiment. The contribution of spin-flip scattering on electron states in cobalt and nickel is generally weak. However, the GT self-energy gives rise to a strong lifetime broadening of majority hole states in cobalt and to a lesser degree in nickel. Our results are in good qualitative agreement with LDA+DMFT studies [62–66] in the vicinity of the Fermi energy and our calculated electron lifetimes for iron and nickel compare well with the spin-flip contribution obtained from calculations based on diagrammatic techniques [67–70].

At the current stage the electron-magnon interaction in the GT approximation is combined with the COHSEX self-energy, which is the static limit of the GW approximation. A promising next step is the extension to a GW+T approximation. A seamless combination of the GW and the GT self-energies would put us in the position to make quantitative comparisons with high-resolution ARPES measurements. Furthermore, the GT self-energy is calculated perturbatively at the moment, assuming that the single-particle states of the self-consistent COHSEX calculations are good approximations to the quasiparticle amplitudes. The investigation of the full self-energy matrix of a combined GW+T approximation would open up the possibility to study also very fine details of quasiparticle renormalizations measured experimen-

tally. In order to enable the study of more complex crystal structures, a formulation of the T matrix beyond the on-site approximation, which is currently employed for the screened interaction, would be desirable. The investigation of the electron-magnon scattering in the iron-based superconductors, in which the spin-fluctuations are supposed to be the mediating bosons for the attractive interaction leading to the superconductivity, is interesting in its own right. Moreover, the T-matrix approach also allows to treat optical excitations. For this, the present implementation of the electron-hole T matrix could be extended to excitonic excitations, which opens up the possibility to calculate a self-energy in the flavor of a GT approximation that accounts for electron-exciton scattering effects. However, typical excitonic excitation energies are of the order of eVs and thus much larger than typical magnon excitation energies. Consequently, empty-state summations are presumably more important for the description of excitonic effects than for magnons. A systematic band convergence is, however, problematic in the Wannier-function approach. As an alternative, a formulation in terms of a two-particle Hamiltonian, which makes use of the basis of Bloch functions could be used. Apart from the self-energy diagrams discussed so far, there are other potentially important diagrams that are worth mentioning. The leading order correction to the GW approximation is the second-order screened exchange (SOSEX) self-energy, which has been recently implemented and applied in a G_0W_0+SOSEX scheme to molecular systems by Ren *et al.* [245]. A systematic treatment of self-energy corrections beyond the GW approximation would require the consideration of the SOSEX self-energy, in addition to higher-order exchange terms and also self-energies of the GT form that account for the particle-particle scattering channel.

A. Padé Approximation

In the present thesis we deal with functions, e.g., the magnetic response function, which contain poles corresponding to excitation energies of the system. Typically, a power series expansion is not suitable to represent such a function. Superior to this is an approximation that expands the function as a ratio of two power series known as Padé approximation. If the degree of the polynomial of the denominator is by one larger than that of the nominator the function has a characteristic $1/\omega$ behavior for $\omega \in \mathbb{C}$ as needed for, e.g., the magnetic response function. This kind of rational function allows to represent a given pole structure. The SPEX code utilizes the Thiele algorithm to obtain the Padé approximant [319]. The Thiele algorithm uses the continued fraction representation of a rational function

$$f(\omega) = \cfrac{1}{c_0 + \cfrac{\omega - \omega_0}{c_1 + \cfrac{\omega - \omega_1}{c_2 + \ldots}}}. \tag{A.0.1}$$

and determines the complex-valued parameters c_i recursively. If the number of sampling points is odd, additional constraints reflecting the properties of the actual function are needed. The Padé approximation can be written as a sum of poles

$$f(\omega) = \sum_{\nu=1}^{n} \frac{a_\nu}{\omega - \Omega_\nu}, \quad \mathrm{Re}(\omega) > 0 \tag{A.0.2}$$

with residues $a_\nu \in \mathbb{C}$ and position of the poles $\Omega_\nu = \omega_\nu + \mathrm{i}\Gamma_\nu$, where $\omega_\nu \in \mathbb{R}$ and $\Gamma_\nu < 0$ for positive real frequencies. For negative real frequencies the function $f(\omega)$

is obtained by

$$f(\omega) = \sum_{\nu=1}^{n} \frac{a_\nu^*}{\omega - \Omega_\nu^*}, \quad \mathrm{Re}(\omega) < 0. \tag{A.0.3}$$

A function represented by a Padé approximation has to be continuously differentiable at $\omega = 0$. For this the residues and the their corresponding poles need to meet two conditions. The first condition is $f(\omega)|_{\omega=0} = f(-\omega)|_{\omega=0}$ ensuring the continuity of the function itself. With Eqs. (A.0.2) and (A.0.3), this condition is

$$\mathrm{Im} \sum_{\nu=1}^{n} \frac{a_\nu}{\Omega_\nu} = 0. \tag{A.0.4}$$

Similarly, for the continuity of the derivative one finds

$$\mathrm{Im} \sum_{\nu=1}^{n} \frac{a_\nu}{\Omega_\nu^2} = 0. \tag{A.0.5}$$

The real part of the function that is represented by a Padé approximation has a characteristic $1/\omega$ behavior. The imaginary part of such a function obtains a $1/\omega^2$ behavior. To this end, the imaginary part of the Padé approximation

$$\mathrm{Im}f(\omega) = \sum_{\nu=1}^{n} \frac{\mathrm{Im}\left[(\omega - \Omega_\nu^*)a_\nu\right]}{(\omega - \Omega_\nu)(\omega - \Omega_\nu^*)} = \sum_{\nu=1}^{n} \frac{\Gamma_\nu \mathrm{Re}(a_\nu) + (\omega - \omega_\nu)\mathrm{Im}(a_\nu)}{(\omega - \Omega_\nu)(\omega - \Omega_\nu^*)}. \tag{A.0.6}$$

leads to the condition

$$\mathrm{Im} \sum_{\nu=1}^{n} a_\nu = 0, \tag{A.0.7}$$

which ensures the correct behavior of $\mathrm{Im}f(\omega) \propto 1/\omega^2$.

Integrating a Padé Approximant

The Padé approximant is used in the present work to evaluate different kinds of frequency integrations. The pole representation of a function defined on the real frequency axis $\omega \in \mathbb{R}$ using the Padé approximation reads

$$f(\omega) = \sum_{\nu=1}^{n} \frac{a_\nu}{\omega - \Omega_\nu} \Theta(\omega) + \sum_{\nu=1}^{n} \frac{a_\nu^*}{\omega - \Omega_\nu^*} \Theta(-\omega), \tag{A.0.8}$$

with $\Omega_\nu = \omega_\nu + \mathrm{i}\Gamma_\nu$ describing the pole position in the complex plane and a_ν the corresponding residue of the pole. In the following we describe two different kinds of integrals which are of special interest: the Fourier transformation and the con-

volution of two functions in the frequency domain. The Fourier transformation is needed for the evaluation of the sum rules (3.3.29) and (3.3.31) of the magnetic response function. The evaluation of the convolution of two functions in the frequency domain is used for the evaluation of the GT self-energy.

Fourier Transformation

The Fourier transformation

$$\mathcal{F}(\tau) = \frac{1}{2\pi} \int_{-\infty}^{\infty} \mathrm{d}\omega \, e^{-\mathrm{i}\omega\tau} \, f(\omega) \tag{A.0.9}$$

of a Padé approximant employing the special form of the pole representation (A.0.8) splits into the two integrals, i.e.

$$\begin{aligned} \mathcal{F}_{1,\nu}(\tau) &= \frac{1}{2\pi} \int_{0}^{\infty} \mathrm{d}\omega \, e^{-\mathrm{i}\omega\tau} \frac{a_\nu}{\omega - \Omega_\nu} \\ &= \frac{a_\nu \, e^{-\mathrm{i}\Omega_\nu\tau}}{2\pi} \left[-2\pi\mathrm{i} \, \Theta\left(\omega_\nu\right) \mathrm{sgn}(\omega_\nu\tau) \Theta(-\Gamma_\nu\tau) + E_1(-\mathrm{i}\Omega_\nu\tau) \right], \end{aligned} \tag{A.0.10}$$

and

$$\begin{aligned} \mathcal{F}_{2,\nu}(\tau) &= \frac{1}{2\pi} \int_{-\infty}^{0} \mathrm{d}\omega \, e^{-\mathrm{i}\omega\tau} \frac{a_\nu^*}{\omega - \Omega_\nu^*} \\ &= \frac{a_\nu^* \, e^{-\mathrm{i}\Omega_\nu^*\tau}}{2\pi} \left[2\pi\mathrm{i} \, \Theta\left(-\omega_\nu\right) \mathrm{sgn}(\omega_\nu\tau) \Theta(\Gamma_\nu\tau) - E_1(-\mathrm{i}\Omega_\nu^*\tau) \right], \end{aligned} \tag{A.0.11}$$

where the exponential integral function is defined as

$$E_1(z) = \int_{z}^{\infty} \mathrm{d}t \, \frac{e^{-t}}{t}, \quad |\arg(z)| < \pi. \tag{A.0.12}$$

A detailed discussion on the exponential integral function can be found in [320]. The Fourier transformation is then obtained by the sum of the integrals (A.0.10) and (A.0.11)

$$\mathcal{F}(\tau) = \sum_{\nu=1}^{n} \mathcal{F}_{1,\nu}(\tau) + \mathcal{F}_{2,\nu}(\tau). \tag{A.0.13}$$

The evaluation of the magnetic moment and the spin fluctuations, cf. Eqs. (3.3.29) and (3.3.31), involve the calculation of the limit $\tau \to 0^{\pm}$ of the Fourier transform (A.0.13). In these cases, special care must be taken for the exponential integral function, resulting in

$$\mathcal{F}(\tau \to 0^{+}) - \mathcal{F}(\tau \to 0^{-}) = \frac{-\mathrm{i}}{2} \sum_{\nu=1}^{n} (a_\nu + a_\nu^*), \tag{A.0.14}$$

and

$$\mathcal{F}(\tau \to 0^+) + \mathcal{F}(\tau \to 0^-) = \sum_{\nu=1}^{n} \left[\frac{\mathrm{i}(a_\nu + a_\nu^*)}{\pi} \arctan\left(\frac{\omega_\nu}{\Gamma_\nu}\right) - \frac{a_\nu - a_\nu^*}{2\pi} \ln\left(\omega_\nu^2 + \Gamma_\nu^2\right) \right]. \quad \text{(A.0.15)}$$

Convolution along the Real Frequency Axis

The evaluation of the GT self-energy (4.3.1) requires the calculation of the convolution of the electronic Green function and the T matrix in the frequency domain. To this end, the contour-integration method and the analytic-continuation method have been implemented. Both methods make use of the Padé approximation. While the contour-integration method makes use of a convolution along the real frequency axis, the analytic-continuation method relies on the convolution along the imaginary frequency axis. For the contour-integration method integrals of the form

$$\mathcal{C}(\omega) = \int_{-\infty}^{\infty} \mathrm{d}\omega' \, \frac{1}{\omega - \omega' - \epsilon + \mathrm{i}\eta \mathrm{sgn}(\epsilon)} f(\omega'). \quad \text{(A.0.16)}$$

have to be solved. Here, ϵ denotes a single-particle energy relative to the Fermi level and the function $f(\omega)$ is represented by means of a Padé approximation. We solve these integrals for each pole of the Padé approximation, i.e.

$$\mathcal{C}(\omega) = \sum_{\nu=1}^{n} \mathcal{C}_{1,\nu}(\omega) + \mathcal{C}_{2,\nu}(\omega), \quad \text{(A.0.17)}$$

with

$$\mathcal{C}_{1,\nu}(\omega) = \int_{-\infty}^{0} \mathrm{d}\omega' \, \frac{1}{\omega - \omega' - \epsilon + \mathrm{i}\eta \mathrm{sgn}(\epsilon)} \frac{a_\nu^*}{\omega' - \Omega_\nu^*}, \quad \text{(A.0.18)}$$

and

$$\mathcal{C}_{2,\nu}(\omega) = \int_{0}^{\infty} \mathrm{d}\omega' \, \frac{1}{\omega - \omega' - \epsilon + \mathrm{i}\eta \mathrm{sgn}(\epsilon)} \frac{a_\nu}{\omega' - \Omega_\nu}. \quad \text{(A.0.19)}$$

A partial fraction decomposition together with the standard integral

$$\int_{z_1}^{z_2} \mathrm{d}\omega \, \frac{1}{\omega - z_0} = \left[\ln\left(|\omega - z_0|\right) + \mathrm{i} \arg(\omega - z_0) \right]_{z_1}^{z_2} \quad \text{(A.0.20)}$$

allow to evaluate the integrals easily. In the case of $\eta \to 0^+$ the results of the convolutions are given by

$$\mathcal{C}_{1,\nu}(\omega) = \frac{a_\nu^*}{\Omega_\nu^* - \omega + \epsilon}\Bigg[\ln\left(|\epsilon - \omega|\right) + \mathrm{i}\pi\mathrm{sgn}(\epsilon)\Theta(\epsilon - \omega) - \frac{1}{2}\ln(\omega_\nu^2 + \Gamma_\nu^2) + \mathrm{i}(\pi\mathrm{sgn}(\Gamma_\nu) - \arg(-\Omega_\nu^*))\Bigg] \quad \text{(A.0.21)}$$

and

$$\mathcal{C}_{2,\nu}(\omega) = \frac{a_\nu}{\Omega_\nu - \omega + \epsilon}\Bigg[-\ln\left(|\epsilon - \omega|\right) + \mathrm{i}\pi\mathrm{sgn}(\epsilon)\Theta(\omega - \epsilon) + \frac{1}{2}\ln(\omega_\nu^2 + \Gamma_\nu^2) + \mathrm{i}\arg(-\Omega_\nu)\Bigg]. \quad \text{(A.0.22)}$$

Convolution along the Imaginary Frequency Axis

The analytic-continuation method makes use of the convolution along the imaginary frequency axis

$$\mathcal{C}(z) = \int_{\eta - \mathrm{i}\infty}^{\eta + \mathrm{i}\infty} \mathrm{d}z' \, \frac{1}{z - z' - \epsilon} f(z') \quad \text{(A.0.23)}$$

for the evaluation of the self-energy as a function of imaginary frequencies. We assume for its imaginary frequency argument $z = \mathrm{i}\omega$ that $\omega \geq 0$. The convolution along the imaginary frequency axis can be evaluated following exactly the same steps as in the case of the convolution along the real frequency axis, see previous section. The result for the integration along the negative imaginary axis from $\eta - \mathrm{i}\infty$ to 0 is given by

$$\mathcal{C}_{1,\nu}(i\omega) = \frac{a_\nu^*}{\Omega_\nu^* - \mathrm{i}\omega + \epsilon}\Bigg[\frac{1}{2}\ln\left(\epsilon^2 + \omega^2\right) + \mathrm{i}\arg(\mathrm{i}\omega - \epsilon) - 2\pi\mathrm{i}\Theta(-\omega_\nu)\Theta(\Gamma_\nu) + \mathrm{i}\pi\mathrm{sgn}(\Gamma_\nu) - \frac{1}{2}\ln(\omega_\nu^2 + \Gamma_\nu^2) - \mathrm{i}\arg(-\Omega_\nu^*)\Bigg]. \quad \text{(A.0.24)}$$

Performing the integration along the positive imaginary frequency axis from 0 to $\eta + \mathrm{i}\infty$ yields

$$\mathcal{C}_{2,\nu}(\mathrm{i}\omega) = \frac{a_\nu}{\Omega_\nu - \mathrm{i}\omega + \epsilon}\Bigg[-\frac{1}{2}\ln\left(\epsilon^2 + \omega^2\right) - \mathrm{i}\arg(\mathrm{i}\omega - \epsilon) + \mathrm{i}\pi\mathrm{sgn}(\omega) - 2\pi\mathrm{i}\Theta(-\epsilon)\Theta(\omega) + 2\pi\mathrm{i}\Theta(\omega_\nu)\Theta(\Gamma_\nu) + \frac{1}{2}\ln(\omega_\nu^2 + \Gamma_\nu^2) + \mathrm{i}\arg(-\Omega_\nu)\Bigg]. \quad \text{(A.0.25)}$$

B. Coulomb Hole and Screened Exchange Self-Energy

The Coulomb hole and screened exchange (COHSEX) self-energy is the static limit of the *GW* approximation

$$\Sigma_\alpha(\mathbf{r},\mathbf{r}';\omega) = \frac{\mathrm{i}}{2\pi}\int_{-\infty}^{\infty} \mathrm{d}\omega'\, e^{\mathrm{i}\eta\omega'} G_\alpha(\mathbf{r},\mathbf{r}';\omega+\omega')W(\mathbf{r},\mathbf{r}';\omega'), \tag{B.0.1}$$

which can be formally rewritten in the contributions coming from the poles of the Green function and the contribution of the (plasmon) poles of the screened interaction. This kind of decomposition was first done by Hedin [71] and allows to derive the COHSEX self-energy approximation. To this end, the Green function

$$G_\alpha(\mathbf{r},\mathbf{r}';\omega) = \int_{-\infty}^{\infty} \mathrm{d}\omega' \,\frac{A_\alpha(\mathbf{r},\mathbf{r}';\omega')}{\omega-\omega'+\mathrm{i}\eta\mathrm{sgn}(\omega')}. \tag{B.0.2}$$

is written in terms of its spectral function

$$A_\alpha(\mathbf{r},\mathbf{r}';\omega) = \sum_{\mathbf{k}}^{\mathrm{BZ}}\sum_{m}^{\mathrm{all}} \varphi^\alpha_{\mathbf{k}m}(\mathbf{r})\varphi^{\alpha\,*}_{\mathbf{k}m}(\mathbf{r}')\delta(\omega-\epsilon^\alpha_{\mathbf{k}m}). \tag{B.0.3}$$

The screened interaction can also be written in terms of its spectral function. For this, the frequency independent bare Coulomb interaction is separated from the remainder part

$$W(\mathbf{r},\mathbf{r}';\omega) = v(\mathbf{r},\mathbf{r}') + W_c(\mathbf{r},\mathbf{r}';\omega), \tag{B.0.4}$$

which can be represented as

$$W_c(\mathbf{r},\mathbf{r}';\omega) = \int_{-\infty}^{\infty} \mathrm{d}\omega' \,\frac{D(\mathbf{r},\mathbf{r}';\omega')}{\omega-\omega'+\mathrm{i}\eta\mathrm{sgn}(\omega')}, \tag{B.0.5}$$

where $D(\mathbf{r},\mathbf{r}';\omega)$ is the spectral function of the screened interaction. The spectral function obeys the symmetry relation $D(\mathbf{r},\mathbf{r}';\omega) = -D(\mathbf{r},\mathbf{r}';-\omega)$. The dynamical screened exchange contribution

$$\tilde{\Sigma}^{\alpha}_{\mathrm{SEX}}(\mathbf{r},\mathbf{r}';\omega) = -\sum_{\mathbf{k}}^{\mathrm{BZ}}\sum_{m}^{\mathrm{occ}} \varphi^{\alpha}_{\mathbf{k}m}(\mathbf{r})\varphi^{\alpha\,*}_{\mathbf{k}m}(\mathbf{r}')W(\mathbf{r},\mathbf{r}';\epsilon^{\alpha}_{\mathbf{k}m}-\omega) \tag{B.0.6}$$

arise from the poles of the Green function. It takes into account exchange processes via the dynamical screened interaction. The poles of the screened interaction leads to the dynamical Coulomb hole part

$$\tilde{\Sigma}^{\alpha}_{\mathrm{COH}}(\mathbf{r},\mathbf{r}';\omega) = \sum_{\mathbf{k}}^{\mathrm{BZ}}\sum_{m}^{\mathrm{all}} \varphi^{\alpha}_{\mathbf{k}m}(\mathbf{r})\varphi^{\alpha\,*}_{\mathbf{k}m}(\mathbf{r}') \int_0^{\infty} \mathrm{d}\omega' \, \frac{D(\mathbf{r},\mathbf{r}';\omega')}{\omega - \epsilon^{\alpha}_{\mathbf{k}m} - \omega' + \mathrm{i}\eta\mathrm{sgn}(\epsilon^{\alpha}_{\mathbf{k}m})}. \tag{B.0.7}$$

For states close to the Fermi energy the Coulomb hole has the physical interpretation of the interaction of a quasiparticle with the induced potential due to the dynamical screening. The Eqs. (B.0.6) and (B.0.7) are exact and their sum corresponds to the *GW* approximation. Under the assumption that the most important contribution of the spectral function $A^{\alpha}(\mathbf{r},\mathbf{r}';\omega)$ comes from the energy region in the vicinity of the Fermi level $\omega \simeq 0$, the screened exchange self-energy can be approximated by

$$\Sigma^{\alpha}_{\mathrm{SEX}}(\mathbf{r},\mathbf{r}';\omega=0) = -\sum_{\mathbf{k}}^{\mathrm{BZ}}\sum_{m}^{\mathrm{occ}} \varphi^{\alpha}_{\mathbf{k}m}(\mathbf{r})\varphi^{\alpha\,*}_{\mathbf{k}m}(\mathbf{r}')W(\mathbf{r},\mathbf{r}';0). \tag{B.0.8}$$

In this limit, the Coulomb hole contribution simplifies to a local and spin independent potential

$$\Sigma^{\alpha}_{\mathrm{COH}}(\mathbf{r},\mathbf{r}';\omega=0) = \frac{1}{2}\delta(\mathbf{r}-\mathbf{r}')W_c(\mathbf{r},\mathbf{r}';0). \tag{B.0.9}$$

The obtained self-energy approximation

$$\Sigma^{\alpha}_{\mathrm{COHSEX}}(\mathbf{r},\mathbf{r}') = \Sigma^{\alpha}_{\mathrm{COH}}(\mathbf{r},\mathbf{r}';\omega=0) + \Sigma^{\alpha}_{\mathrm{SEX}}(\mathbf{r},\mathbf{r}';\omega=0) \tag{B.0.10}$$

is a static self-energy approximation known as the COHSEX approximation. As the COHSEX approximation is frequency independent, it corresponds to a Hermitian self-energy operator.

List of Abbreviations

ALDA	adiabatic local-density approximation.
ARPES	angle-resolved photoemission spectroscopy.
BLS	Brillouin light scattering.
BZ	Brillouin zone.
COH	Coulomb hole.
COHSEX	Coulomb hole and screened exchange.
CMOS	complementary metal-oxide-semiconductor.
DFT	density-functional theory.
dHvA	de Haas-van Alphen.
DMFT	dynamical mean-field theory.
DOS	density of states.
FLAPW	full-potential linearized augmented-plane-wave.
FLEX	fluctuation exchange.
GGA	generalized gradient approximation.
GMR	giant magnetoresistance.
HDD	hard disk drive.
INS	inelastic neutron scattering.
IPS	inverse photoemission spectroscopy.
IR	interstitial region.

KS	Kohn-Sham.
LDA	local-density approximation.
LMTO	linearized muffin-tin orbital.
LSDA	local-spin-density approximation.
MBPT	many-body perturbation theory.
MT	muffin-tin.
PBE	Perdew-Burke-Ernzerhof.
PZ	Perdew-Zunger.
QS*GW*	quasiparticle self-consistent *GW*.
RPA	random-phase approximation.
SEX	screened exchange.
SOSEX	second-order screened exchange.
SPTF	spin-polarized T-matrix fluctuation exchange.
SX-ARPES	soft x-ray angle-resolved photoemission spectroscopy.
TAS	triple-axis spectroscopy.
TDDFT	time-dependent density-functional theory.
TMR	tunneling magnetoresistance.
TR-2PPE	time-resolved two-photon photoemission.
xc	exchange correlation.
XPS	x-ray photoemission spectroscopy.

Bibliography

[1] R. Waser, *Nanoelectronics and Information Technology* (Wiley Subscription Services, Inc., A Wiley Company, 2012)

[2] R. Waser, in *Memristive Phenomena - From Fundamental Physics to Neuromorphic Computing*, edited by R. Waser and M. Wuttig (Forschungszentrum Jülich GmbH IAS, ICS, JCNS, PGI, 2016) pp. 15–37

[3] G. Binasch, P. Grünberg, F. Saurenbach, and W. Zinn, *Enhanced magnetoresistance in layered magnetic structures with antiferromagnetic interlayer exchange*, Phys. Rev. B **39**, 4828 (1989)

[4] M. N. Baibich, J. M. Broto, A. Fert, F. N. Van Dau, F. Petroff, P. Etienne, G. Creuzet, A. Friederich, and J. Chazelas, *Giant Magnetoresistance of (001)Fe/(001)Cr Magnetic Superlattices*, Phys. Rev. Lett. **61**, 2472 (1988)

[5] P. A. Grünberg, *Nobel Lecture: From spin waves to giant magnetoresistance and beyond**, Rev. Mod. Phys. **80**, 1531 (2008)

[6] P. Grünberg, R. Schreiber, Y. Pang, M. B. Brodsky, and H. Sowers, *Layered Magnetic Structures: Evidence for Antiferromagnetic Coupling of Fe Layers across Cr Interlayers*, Phys. Rev. Lett. **57**, 2442 (1986)

[7] D. D. Awschalom and M. E. Flatte, *Challenges for semiconductor spintronics*, Nat. Phys. **3**, 153 (2007)

[8] A. V. Chumak, A. A. Serga, and B. Hillebrands, *Magnon transistor for all-magnon data processing*, Nat. Commun. **5**, (2014)

[9] A. V. Chumak, V. I. Vasyuchka, A. A. Serga, and B. Hillebrands, *Magnon spintronics*, Nat. Phys. **11**, 453 (2015)

[10] P. Pirro, T. Brächer, A. V. Chumak, B. Lägel, C. Dubs, O. Surzhenko, P. Görnert, B. Leven, and B. Hillebrands, *Spin-wave excitation and propagation in microstructured waveguides of yttrium iron garnet/Pt bilayers*, Applied Physics Letters **104**, 012402 (2014)

[11] V. Cherepanov, I. Kolokolov, and V. L'vov, *The saga of YIG: Spectra, thermodynamics, interaction and relaxation of magnons in a complex magnet*, Physics Reports **229**, 81 (1993)

[12] J. S. Plant, *Spinwave dispersion curves for yttrium iron garnet*, Journal of Physics C: Solid State Physics **10**, 4805 (1977)

[13] P. Rovillain, R. de Sousa, Y. Gallais, A. Sacuto, M. A. Méasson, D. Colson, A. Forget, M. Bibes, A. Barthélémy, and M. Cazayous, *Electric-field control of spin waves at room temperature in multiferroic $BiFeO_3$*, Nat Mater **9**, 975 (2010)

[14] S. Demokritov, B. Hillebrands, and A. Slavin, *Brillouin light scattering studies of confined spin waves: linear and nonlinear confinement*, Physics Reports **348**, 441 (2001)

[15] R. Lowde and C. Windsor, *On the magnetic excitations in nickel*, Advances in Physics **19**, 813 (1970)

[16] S. W. Lovesey, *Theory of Neutron Scattering from Condensed Matter - Nuclear Scattering* (Clarendon Press, Oxford, 1986)

[17] S. W. Lovesey, *Theory of Neutron Scattering from Condensed Matter - Polarization effects and magnetic scattering* (Clarendon Press, Oxford, 1986)

[18] P. Hohenberg and W. Kohn, *Inhomogeneous Electron Gas*, Phys. Rev. **136**, B864 (1964)

[19] W. Kohn and L. J. Sham, *Self-Consistent Equations Including Exchange and Correlation Effects*, Phys. Rev. **140**, A1133 (1965)

[20] N. M. Rosengaard and B. Johansson, *Finite-temperature study of itinerant ferromagnetism in Fe, Co, and Ni*, Phys. Rev. B **55**, 14975 (1997)

[21] S. V. Halilov, A. Y. Perlov, P. M. Oppeneer, and H. Eschrig, *Magnon spectrum and related finite-temperature magnetic properties: A first-principle approach*, Europhysics Letters **39**, 91 (1997)

[22] S. V. Halilov, H. Eschrig, A. Y. Perlov, and P. M. Oppeneer, *Adiabatic spin dynamics from spin-density-functional theory: Application to Fe, Co, and Ni*, Phys. Rev. B **58**, 293 (1998)

[23] M. van Schilfgaarde and V. P. Antropov, *First-principles exchange interactions in Fe, Ni, and Co*, Journal of Applied Physics **85**, 4827 (1999)

[24] M. Pajda, J. Kudrnovský, I. Turek, V. Drchal, and P. Bruno, *Ab initio calculations of exchange interactions, spin-wave stiffness constants, and Curie temperatures of Fe, Co, and Ni*, Phys. Rev. B **64**, 174402 (2001)

[25] P. H. Dederichs, S. Blügel, R. Zeller, and H. Akai, *Ground States of Constrained Systems: Application to Cerium Impurities*, Phys. Rev. Lett. **53**, 2512 (1984)

[26] R. B. Muniz and D. L. Mills, *Theory of spin excitations in Fe(110) monolayers*, Phys. Rev. B **66**, 174417 (2002)

[27] R. B. Muniz and D. L. Mills, *Local spin dynamics of magnetic moments on metal surfaces*, Phys. Rev. B **68**, 224414 (2003)

[28] A. T. Costa, R. B. Muniz, and D. L. Mills, *Theory of large-wave-vector spin waves in ultrathin ferromagnetic films: Sensitivity to electronic structure*, Phys. Rev. B **70**, 054406 (2004)

[29] A. T. Costa, R. B. Muniz, and D. L. Mills, *Ground State of Magnetic Dimers on Metal Surfaces*, Phys. Rev. Lett. **94**, 137203 (2005)

[30] A. T. Costa, R. Bechara Muniz, and D. L. Mills, *Ferromagnetic resonance linewidths in ultrathin structures: A theoretical study of spin pumping*, Phys. Rev. B **73**, 054426 (2006)

[31] A. T. Costa, R. B. Muniz, S. Lounis, A. B. Klautau, and D. L. Mills, *Spin-orbit coupling and spin waves in ultrathin ferromagnets: The spin-wave Rashba effect*, Phys. Rev. B **82**, 014428 (2010)

[32] A. A. Khajetoorians, S. Lounis, B. Chilian, A. T. Costa, L. Zhou, D. L. Mills, J. Wiebe, and R. Wiesendanger, *Itinerant Nature of Atom-Magnetization Excitation by Tunneling Electrons*, Phys. Rev. Lett. **106**, 037205 (2011)

[33] S. Y. Savrasov, *Linear Response Calculations of Spin Fluctuations*, Phys. Rev. Lett. **81**, 2570 (1998)

[34] P. Buczek, *Spin dynamics of complex itinerant magnets*, Ph.D. thesis, Martin-Luther-Universität Halle Wittenberg (2009)

[35] P. Buczek, A. Ernst, P. Bruno, and L. M. Sandratskii, *Energies and Lifetimes of Magnons in Complex Ferromagnets: A First-Principle Study of Heusler Alloys*, Phys. Rev. Lett. **102**, 247206 (2009)

[36] P. Buczek, A. Ernst, and L. M. Sandratskii, *Interface Electronic Complexes and Landau Damping of Magnons in Ultrathin Magnets*, Phys. Rev. Lett. **106**, 157204 (2011)

[37] P. Buczek, A. Ernst, and L. M. Sandratskii, *Different dimensionality trends in the Landau damping of magnons in iron, cobalt, and nickel: Time-dependent density functional study*, Phys. Rev. B **84**, 174418 (2011)

[38] S. Lounis, A. T. Costa, R. B. Muniz, and D. L. Mills, *Dynamical Magnetic Excitations of Nanostructures from First Principles*, Phys. Rev. Lett. **105**, 187205 (2010)

[39] S. Lounis, A. T. Costa, R. B. Muniz, and D. L. Mills, *Theory of local dynamical magnetic susceptibilities from the Korringa-Kohn-Rostoker Green function method*, Phys. Rev. B **83**, 035109 (2011)

[40] S. Lounis, M. dos Santos Dias, and B. Schweflinghaus, *Transverse dynamical magnetic susceptibilities from regular static density functional theory: Evaluation of damping and g shifts of spin excitations*, Phys. Rev. B **91**, 104420 (2015)

[41] M. dos Santos Dias, B. Schweflinghaus, S. Blügel, and S. Lounis, *Relativistic dynamical spin excitations of magnetic adatoms*, Phys. Rev. B **91**, 075405 (2015)

[42] B. Rousseau, A. Eiguren, and A. Bergara, *Efficient computation of magnon dispersions within time-dependent density functional theory using maximally localized Wannier functions*, Phys. Rev. B **85**, 054305 (2012)

[43] E. Şaşıoğlu, A. Schindlmayr, C. Friedrich, F. Freimuth, and S. Blügel, *Wannier-function approach to spin excitations in solids*, Phys. Rev. B **81**, 054434 (2010)

[44] K. Karlsson and F. Aryasetiawan, *A many-body approach to spin-wave excitations in itinerant magnetic systems*, Journal of Physics: Condensed Matter **12**, 7617 (2000)

[45] T. Kotani and M. van Schilfgaarde, *Spin wave dispersion based on the quasiparticle self-consistent GW method: NiO, MnO and α-MnAs*, Journal of Physics: Condensed Matter **20**, 295214 (2008)

[46] N. Marzari and D. Vanderbilt, *Maximally localized generalized Wannier functions for composite energy bands*, Phys. Rev. B **56**, 12847 (1997)

[47] A. A. Mostofi, J. R. Yates, Y.-S. Lee, I. Souza, D. Vanderbilt, and N. Marzari, *wannier90: A tool for obtaining maximally-localised Wannier functions*, Computer Physics Communications **178**, 685 (2008)

[48] E. Wimmer, H. Krakauer, M. Weinert, and A. J. Freeman, *Full-potential self-consistent linearized-augmented-plane-wave method for calculating the electronic structure of molecules and surfaces:* O_2 *molecule*, Phys. Rev. B **24**, 864 (1981)

[49] M. Weinert, E. Wimmer, and A. J. Freeman, *Total-energy all-electron density functional method for bulk solids and surfaces*, Phys. Rev. B **26**, 4571 (1982)

[50] H. J. F. Jansen and A. J. Freeman, *Total-energy full-potential linearized augmented-plane-wave method for bulk solids: Electronic and structural properties of tungsten*, Phys. Rev. B **30**, 561 (1984)

[51] M. C. T. D. Müller, C. Friedrich, and S. Blügel, *Acoustic magnons in the long-wavelength limit: Investigating the Goldstone violation in many-body perturbation theory*, Phys. Rev. B **94**, 064433 (2016)

[52] I. Žutić, J. Fabian, and S. Das Sarma, *Spintronics: Fundamentals and applications*, Rev. Mod. Phys. **76**, 323 (2004)

[53] A. H. MacDonald, T. Jungwirth, and M. Kasner, *Temperature Dependence of Itinerant Electron Junction Magnetoresistance*, Phys. Rev. Lett. **81**, 705 (1998)

[54] T. Balashov, A. F. Takács, W. Wulfhekel, and J. Kirschner, *Magnon Excitation with Spin-Polarized Scanning Tunneling Microscopy*, Phys. Rev. Lett. **97**, 187201 (2006)

[55] T. Balashov, A. F. Takács, M. Däne, A. Ernst, P. Bruno, and W. Wulfhekel, *Inelastic electron-magnon interaction and spin transfer torque*, Phys. Rev. B **78**, 174404 (2008)

[56] B. Schweflinghaus, M. dos Santos Dias, A. T. Costa, and S. Lounis, *Renormalization of electron self-energies via their interaction with spin excitations: A first-principles investigation*, Phys. Rev. B **89**, 235439 (2014)

[57] B. Schweflinghaus, *First-principles investigation of inelastic magnetic excitations in nanostructures deposited on surfaces*, Ph.D. thesis, RWTH Aachen (2016)

[58] J. Schäfer, D. Schrupp, E. Rotenberg, K. Rossnagel, H. Koh, P. Blaha, and R. Claessen, *Electronic Quasiparticle Renormalization on the Spin Wave Energy Scale*, Phys. Rev. Lett. **92**, 097205 (2004)

[59] A. Hofmann, X. Y. Cui, J. Schäfer, S. Meyer, P. Höpfner, C. Blumenstein, M. Paul, L. Patthey, E. Rotenberg, J. Bünemann, F. Gebhard, T. Ohm, W. Weber, and R. Claessen, *Renormalization of Bulk Magnetic Electron States at High Binding Energies*, Phys. Rev. Lett. **102**, 187204 (2009)

[60] R. Knorren, K. H. Bennemann, R. Burgermeister, and M. Aeschlimann, *Dynamics of excited electrons in copper and ferromagnetic transition metals: Theory and experiment*, Phys. Rev. B **61**, 9427 (2000)

[61] S. Monastra, F. Manghi, C. A. Rozzi, C. Arcangeli, E. Wetli, H.-J. Neff, T. Greber, and J. Osterwalder, *Quenching of Majority-Channel Quasiparticle Excitations in Cobalt*, Phys. Rev. Lett. **88**, 236402 (2002)

[62] J. Sánchez-Barriga, J. Fink, V. Boni, I. Di Marco, J. Braun, J. Minár, A. Varykhalov, O. Rader, V. Bellini, F. Manghi, H. Ebert, M. I. Katsnelson, A. I. Lichtenstein, O. Eriksson, W. Eberhardt, and H. A. Dürr, *Strength of Correlation Effects in the Electronic Structure of Iron*, Phys. Rev. Lett. **103**, 267203 (2009)

[63] J. Sánchez-Barriga, J. Minár, J. Braun, A. Varykhalov, V. Boni, I. Di Marco, O. Rader, V. Bellini, F. Manghi, H. Ebert, M. I. Katsnelson, A. I. Lichtenstein, O. Eriksson, W. Eberhardt, H. A. Dürr, and J. Fink, *Quantitative determination of spin-dependent quasiparticle lifetimes and electronic correlations in hcp cobalt*, Phys. Rev. B **82**, 104414 (2010)

[64] J. Sánchez-Barriga, J. Braun, J. Minár, I. Di Marco, A. Varykhalov, O. Rader, V. Boni, V. Bellini, F. Manghi, H. Ebert, M. I. Katsnelson, A. I. Lichtenstein, O. Eriksson, W. Eberhardt, H. A. Dürr, and J. Fink, *Effects of spin-dependent quasiparticle renormalization in Fe, Co, and Ni photoemission spectra:An experimental and theoretical study*, Phys. Rev. B **85**, 205109 (2012)

[65] M. I. Katsnelson and A. I. Lichtenstein, *LDA++ approach to the electronic structure of magnets: correlation effects in iron*, Journal of Physics: Condensed Matter **11**, 1037 (1999)

[66] A. Grechnev, I. Di Marco, M. I. Katsnelson, A. I. Lichtenstein, J. Wills, and O. Eriksson, *Theory of bulk and surface quasiparticle spectra for Fe, Co, and Ni*, Phys. Rev. B **76**, 035107 (2007)

[67] V. P. Zhukov, E. V. Chulkov, and P. M. Echenique, *Lifetimes of Excited Electrons In Fe And Ni: First-Principles GW and the T-Matrix Theory*, Phys. Rev. Lett. **93**, 096401 (2004)

[68] V. P. Zhukov, O. Andreyev, D. Hoffmann, M. Bauer, M. Aeschlimann, E. V. Chulkov, and P. M. Echenique, *Lifetimes of excited electrons in Ta: Experimental time-resolved photoemission data and first-principles* GW + T *theory*, Phys. Rev. B **70**, 233106 (2004)

[69] V. P. Zhukov, E. V. Chulkov, and P. M. Echenique, *GW + T theory of excited electron lifetimes in metals*, Phys. Rev. B **72**, 155109 (2005)

[70] V. P. Zhukov, E. V. Chulkov, and P. M. Echenique, *Lifetimes and inelastic mean free path of low-energy excited electrons in Fe, Ni, Pt, and Au: Ab initio* GW + T *calculations*, Phys. Rev. B **73**, 125105 (2006)

[71] L. Hedin, *New Method for Calculating the One-Particle Green's Function with Application to the Electron-Gas Problem*, Phys. Rev. **139**, A796 (1965)

[72] C. Friedrich, S. Blügel, and A. Schindlmayr, *Efficient implementation of the GW approximation within the all-electron FLAPW method*, Phys. Rev. B **81**, 125102 (2010)

[73] M. Born and R. Oppenheimer, *Zur Quantentheorie der Molekeln*, Annalen der Physik **389**, 457 (1927)

[74] L. Hedin and S. Lundqvist, *Effects of Electron-Electron and Electron-Phonon Interactions on the One-Electron States of Solids*, Solid State Physics **23**, 1 (1969)

[75] R. O. Jones and O. Gunnarsson, *The density functional formalism, its applications and prospects*, Rev. Mod. Phys. **61**, 689 (1989)

[76] R. O. Jones, *Density functional theory: Its origins, rise to prominence, and future*, Rev. Mod. Phys. **87**, 897 (2015)

[77] J. C. Slater, *Note on Hartree's Method*, Phys. Rev. **35**, 210 (1930)

[78] V. Fock, *Näherungsmethode zur Lösung des quantenmechanischen Mehrkörperproblems*, Zeitschrift für Physik **61**, 126 (1930)

[79] C. Møller and M. S. Plesset, *Note on an Approximation Treatment for Many-Electron Systems*, Phys. Rev. **46**, 618 (1934)

[80] R. J. Bartlett, *Coupled-cluster approach to molecular structure and spectra: a step toward predictive quantum chemistry*, The Journal of Physical Chemistry **93**, 1697 (1989)

[81] F. Bloch, *Über die Quantenmechanik der Elektronen in Kristallgittern*, Zeitschrift für Physik **52**, 555 (1929)

[82] V. M. Galitskii and A. B. Migdal, *Application of Quantum Field Theory Methods to the Many Body Problem*, Soviet Physics JETP **7**, 96 (1958)

[83] V. M. Galitskii, *The Energy Spectrum of a Non-ideal Fermi Gas*, Soviet Physics JETP **7**, 104 (1958)

[84] H. Lehmann, *Über Eigenschaften von Ausbreitungsfunktionen und Renormierungskonstanten quantisierter Felder*, Il Nuovo Cimento (1943-1954) **11**, 342 (1954)

[85] P. C. Martin and J. Schwinger, *Theory of Many-Particle Systems. I*, Phys. Rev. **115**, 1342 (1959)

[86] M. Levy, *Universal variational functionals of electron densities, first-order density matrices, and natural spin-orbitals and solution of the v-representability problem*, Proceedings of the National Academy of Sciences **76**, 6062 (1979)

[87] M. Levy, *Electron densities in search of Hamiltonians*, Phys. Rev. A **26**, 1200 (1982)

[88] R. O. Jones, in *Computational Nanoscience: Do It Yourself*, Vol. 31, edited by J. Grotendorst, S. Blügel, and D. Marx (Forschungszentrum Jülich GmbH, John von Neumann Institute for Computing, 2006) pp. 45–70

[89] U. von Barth and L. Hedin, *A local exchange-correlation potential for the spin polarized case. i*, Journal of Physics C: Solid State Physics **5**, 1629 (1972)

[90] J. P. Perdew and A. Zunger, *Self-interaction correction to density-functional approximations for many-electron systems*, Phys. Rev. B **23**, 5048 (1981)

[91] J. P. Perdew, K. Burke, and M. Ernzerhof, *Generalized Gradient Approximation Made Simple*, Phys. Rev. Lett. **77**, 3865 (1996)

[92] `http://www.flapw.de`

[93] P. F. Baumeister, *Real-Space Finite-Difference PAW Method for Large-Scale Applications on Massively Parallel Computers*, Ph.D. thesis, RWTH Aachen (2012)

[94] S. Blügel and G. Bihlmayer, in *Computational Nanoscience: Do It Yourself*, Vol. 31, edited by J. Grotendorst, S. Blügel, and D. Marx (Forschungszentrum Jülich GmbH, John von Neumann Institute for Computing, 2006) pp. 85–129

[95] J. A. Pople, *Nobel Lecture: Quantum chemical models*, Rev. Mod. Phys. **71**, 1267 (1999)

[96] G. B. Bachelet, D. R. Hamann, and M. Schlüter, *Pseudopotentials that work: From H to Pu*, Phys. Rev. B **26**, 4199 (1982)

[97] D. Vanderbilt, *Soft self-consistent pseudopotentials in a generalized eigenvalue formalism*, Phys. Rev. B **41**, 7892 (1990)

[98] P. E. Blöchl, *Projector augmented-wave method*, Phys. Rev. B **50**, 17953 (1994)

[99] G. Kresse and D. Joubert, *From ultrasoft pseudopotentials to the projector augmented-wave method*, Phys. Rev. B **59**, 1758 (1999)

[100] J. C. Slater, *Wave Functions in a Periodic Potential*, Phys. Rev. **51**, 846 (1937)

[101] G. Michalicek, M. Betzinger, C. Friedrich, and S. Blügel, *Elimination of the linearization error and improved basis-set convergence within the FLAPW method*, Computer Physics Communications **184**, 2670 (2013)

[102] G. Michalicek, *Extending the precision and efficiency of the all-electron full-potential linearized augmented plane-wave density-functional theory method*, Ph.D. thesis, RWTH Aachen (2014)

[103] D. Singh, *Ground-state properties of lanthanum: Treatment of extended-core states*, Phys. Rev. B **43**, 6388 (1991)

[104] C. Friedrich, A. Schindlmayr, S. Blügel, and T. Kotani, *Elimination of the linearization error in GW calculations based on the linearized augmented-plane-wave method*, Phys. Rev. B **74**, 045104 (2006)

[105] M. Betzinger, C. Friedrich, S. Blügel, and A. Görling, *Local exact exchange potentials within the all-electron FLAPW method and a comparison with pseudopotential results*, Phys. Rev. B **83**, 045105 (2011)

[106] M. Betzinger, *Orbital-dependent exchange-correlation functionals in density-functional theory realized by the FLAPW method*, Ph.D. thesis, RWTH Aachen University (2011)

[107] C. Friedrich, M. C. Müller, and S. Blügel, *Band convergence and linearization error correction of all-electron GW calculations: The extreme case of zinc oxide*, Phys. Rev. B **83**, 081101 (2011)

[108] C. Friedrich, M. Betzinger, M. Schlipf, S. Blügel, and A. Schindlmayr, *Hybrid functionals and GW approximation in the FLAPW method*, Journal of Physics: Condensed Matter **24**, 293201 (2012)

[109] S. Doniach and S. Engelsberg, *Low-Temperature Properties of Nearly Ferromagnetic Fermi Liquids*, Phys. Rev. Lett. **17**, 750 (1966)

[110] T. Moriya and A. Kawabata, *Effect of Spin Fluctuations on Itinerant Electron Ferromagnetism*, Journal of the Physical Society of Japan **34**, 639 (1973)

[111] T. Moriya, *Spin Fluctuations in Itinerant Electron Magnetism* (Springer Berlin Heidelberg, 1985)

[112] D. S. Dessau, B. O. Wells, Z.-X. Shen, W. E. Spicer, A. J. Arko, R. S. List, D. B. Mitzi, and A. Kapitulnik, *Anomalous spectral weight transfer at the superconducting transition of* $Bi_2Sr_2CaCu_2O_{8+\delta}$, Phys. Rev. Lett. **66**, 2160 (1991)

[113] M. Randeria, H. Ding, J.-C. Campuzano, A. Bellman, G. Jennings, T. Yokoya, T. Takahashi, H. Katayama-Yoshida, T. Mochiku, and K. Kadowaki, *Momentum Distribution Sum Rule for Angle-Resolved Photoemission*, Phys. Rev. Lett. **74**, 4951 (1995)

[114] M. R. Norman, H. Ding, J. C. Campuzano, T. Takeuchi, M. Randeria, T. Yokoya, T. Takahashi, T. Mochiku, and K. Kadowaki, *Unusual Dispersion and Line Shape of the Superconducting State Spectra of* $Bi_2Sr_2CaCu_2O_{8+\delta}$, Phys. Rev. Lett. **79**, 3506 (1997)

[115] J. Rossat-Mignod, L. Regnault, C. Vettier, P. Bourges, P. Burlet, J. Bossy, J. Henry, and G. Lapertot, *Neutron scattering study of the* $YBa_2Cu_3O_{6+x}$ *system*, Physica C: Superconductivity **185**, 86 (1991)

[116] H. A. Mook, M. Yethiraj, G. Aeppli, T. E. Mason, and T. Armstrong, *Polarized neutron determination of the magnetic excitations in* $YBa_2Cu_3O_7$, Phys. Rev. Lett. **70**, 3490 (1993)

[117] H. F. Fong, B. Keimer, P. W. Anderson, D. Reznik, F. Doğan, and I. A. Aksay, *Phonon and Magnetic Neutron Scattering at 41 meV in* $YBa_2Cu_3O_7$, Phys. Rev. Lett. **75**, 316 (1995)

[118] H. F. Fong, B. Keimer, D. Reznik, D. L. Milius, and I. A. Aksay, *Polarized and unpolarized neutron-scattering study of the dynamical spin susceptibility of* $YBa_2Cu_3O_7$, Phys. Rev. B **54**, 6708 (1996)

[119] P. Dai, M. Yethiraj, H. A. Mook, T. B. Lindemer, and F. Doğan, *Magnetic Dynamics in Underdoped* $YBa_2Cu_3O_{7-x}$*: Direct Observation of a Superconducting Gap*, Phys. Rev. Lett. **77**, 5425 (1996)

[120] H. F. Fong, B. Keimer, D. L. Milius, and I. A. Aksay, *Superconductivity-Induced Anomalies in the Spin Excitation Spectra of Underdoped* $YBa_2Cu_3\ O_{6+x}$, Phys. Rev. Lett. **78**, 713 (1997)

[121] M. Eschrig and M. R. Norman, *Neutron Resonance: Modeling Photoemission and Tunneling Data in the Superconducting State of* $Bi_2Sr_2CaCu_2O_{8+\delta}$, Phys. Rev. Lett. **85**, 3261 (2000)

[122] M. Eschrig and M. R. Norman, *Effect of the magnetic resonance on the electronic spectra of* high $-$ T_c *superconductors*, Phys. Rev. B **67**, 144503 (2003)

[123] M. Eschrig, *The effect of collective spin-1 excitations on electronic spectra in* high $-$ T_c *superconductors*, Advances in Physics **55**, 47 (2006)

[124] P. Richard, T. Sato, K. Nakayama, S. Souma, T. Takahashi, Y.-M. Xu, G. F. Chen, J. L. Luo, N. L. Wang, and H. Ding, *Angle-Resolved Photoemission Spectroscopy of the Fe-Based* $Ba_{0.6}K_{0.4}Fe_2As_2$ *High Temperature Superconductor: Evidence for an Orbital Selective Electron-Mode Coupling*, Phys. Rev. Lett. **102**, 047003 (2009)

[125] A. Heimes, R. Grein, and M. Eschrig, *Effect of spin fluctuations on the electronic structure in iron-based superconductors*, Phys. Rev. B **86**, 064528 (2012)

[126] L. Shan, J. Gong, Y.-L. Wang, B. Shen, X. Hou, C. Ren, C. Li, H. Yang, H.-H. Wen, S. Li, and P. Dai, *Evidence of a Spin Resonance Mode in the Iron-Based Superconductor* $Ba_{0.6}K_{0.4}Fe_2As_2$ *from Scanning Tunneling Spectroscopy*, Phys. Rev. Lett. **108**, 227002 (2012)

[127] D. V. Evtushinsky, V. B. Zabolotnyy, T. K. Kim, A. A. Kordyuk, A. N. Yaresko, J. Maletz, S. Aswartham, S. Wurmehl, A. V. Boris, D. L. Sun, C. T. Lin, B. Shen, H. H. Wen, A. Varykhalov, R. Follath, B. Büchner, and S. V. Borisenko, *Strong electron pairing at the iron* $3d_{xz,yz}$ *orbitals in hole-doped* $BaFe_2As_2$ *superconductors revealed by angle-resolved photoemission spectroscopy*, Phys. Rev. B **89**, 064514 (2014)

[128] D. F. Xu, D. W. Shen, D. Zhu, J. Jiang, B. P. Xie, Q. S. Wang, B. Y. Pan, P. Dudin, T. K. Kim, M. Hoesch, J. Zhao, X. G. Wan, and D. L. Feng, *Electronic structure of* YFe_2Ge_2 *studied by angle-resolved photoemission spectroscopy*, Phys. Rev. B **93**, 024506 (2016)

[129] E. Dagotto, *Correlated electrons in high-temperature superconductors*, Rev. Mod. Phys. **66**, 763 (1994)

[130] D. Scalapino, *The case for* $d_{x^2-y^2}$ *pairing in the cuprate superconductors*, Physics Reports **250**, 329 (1995)

[131] K. Sasmal, B. Lv, B. Lorenz, A. M. Guloy, F. Chen, Y.-Y. Xue, and C.-W. Chu, *Superconducting Fe-Based Compounds* $(A_{1-x}Sr_x)Fe_2As_2$ *with* $A =$ K *and Cs with Transition Temperatures up to 37 K*, Phys. Rev. Lett. **101**, 107007 (2008)

[132] T. Dahm, V. Hinkov, S. V. Borisenko, A. A. Kordyuk, V. B. Zabolotnyy, J. Fink, B. Büchner, D. J. Scalapino, W. Hanke, and B. Keimer, *Strength of the spin-fluctuation-mediated pairing interaction in a high-temperature superconductor*, Nature Physics **18**, 217 (2009)

[133] M. P. Kostylev, A. A. Serga, T. Schneider, B. Leven, and B. Hillebrands, *Spin-wave logical gates*, Applied Physics Letters **87**, 153501 (2005)

[134] K. L. Wang, Z. Zhao, and A. Khitun, *Spintronics for nanoelectronics and nanosystems*, Thin Solid Films **517**, 184 (2008)

[135] L. Van Hove, *Time-Dependent Correlations between Spins and Neutron Scattering in Ferromagnetic Crystals*, Phys. Rev. **95**, 1374 (1954)

[136] T. Izuyama, D.-J. Kim, and R. Kubo, *Band Theoretical Interpretation of Neutron Diffraction Phenomena in Ferromagnetic Metals*, Journal of the Physical Society of Japan **18**, 1025 (1963)

[137] T. G. Phillips and H. M. Rosenberg, *Spin waves in ferromagnets*, Reports on Progress in Physics **29**, 285 (1966)

[138] S. Doniach, *Theory of inelastic neutron scattering in nearly ferromagnetic metals*, Proceedings of the Physical Society **91**, 86 (1967)

[139] S. W. Lovesey and D. E. Rimmer, *The theory of elastic scattering of neutrons by magnetic salts*, Reports on Progress in Physics **32**, 333 (1969)

[140] R. D. Lowde, R. M. Moon, B. Pagonis, C. H. Perry, J. B. Sokoloff, R. S. Vaughan-Watkins, M. C. K. Wiltshire, and J. Crangle, *A polarised-neutron scattering demonstration of deviations from Stoner-theory behaviour in nickel*, Journal of Physics F: Metal Physics **13**, 249 (1983)

[141] J. F. Cooke, *Neutron Scattering from Itinerant-Electron Ferromagnets*, Phys. Rev. B **7**, 1108 (1973)

[142] J. F. Cooke, J. W. Lynn, and H. L. Davis, *Calculations of the dynamic susceptibility of nickel and iron*, Phys. Rev. B **21**, 4118 (1980)

[143] J. F. Cooke, J. A. Blackman, and T. Morgan, *New Interpretation of Spin-Wave Behavior in Nickel*, Phys. Rev. Lett. **54**, 718 (1985)

[144] S. V. Faleev, M. van Schilfgaarde, and T. Kotani, *All-Electron Self-Consistent GW Approximation: Application to Si, MnO, and NiO*, Phys. Rev. Lett. **93**, 126406 (2004)

[145] M. van Schilfgaarde, T. Kotani, and S. Faleev, *Quasiparticle Self-Consistent GW Theory*, Phys. Rev. Lett. **96**, 226402 (2006)

[146] T. Kotani, M. van Schilfgaarde, and S. V. Faleev, *Quasiparticle self-consistent GW method: A basis for the independent-particle approximation*, Phys. Rev. B **76**, 165106 (2007)

[147] T. Kotani, M. van Schilfgaarde, S. V. Faleev, and A. Chantis, *Quasiparticle self-consistent GW method: a short summary*, Journal of Physics: Condensed Matter **19**, 365236 (2007)

[148] J. A. Hertz and D. M. Edwards, *Electron-magnon interactions in itinerant ferromagnetism. I. Formal theory*, Journal of Physics F: Metal Physics **3**, 2174 (1973)

[149] D. M. Edwards and J. A. Hertz, *Electron-magnon interactions in itinerant ferromagnetism. II. Strong ferromagnetism*, Journal of Physics F: Metal Physics **3**, 2191 (1973)

[150] J. W. Lynn and H. A. Mook, *Temperature dependence of the dynamic susceptibility of nickel*, Phys. Rev. B **23**, 198 (1981)

[151] H. A. Mook and D. M. Paul, *Neutron-Scattering Measurement of the Spin-Wave Spectra for Nickel*, Phys. Rev. Lett. **54**, 227 (1985)

[152] T. G. Perring, A. T. Boothroyd, D. M. Paul, A. D. Taylor, R. Osborn, R. J. Newport, J. A. Blackman, and H. A. Mook, *High-energy spin waves in bcc iron*, Journal of Applied Physics **69**, 6219 (1991)

[153] A. Boothroyd, T. Perring, A. Taylor, D. Paul, and H. Mook, *High energy spin waves in iron measured by neutron scattering*, Journal of Magnetism and Magnetic Materials **104 - 107**, 713 (1992)

[154] T. G. Perring, G. Aeppli, S. M. Hayden, S. A. Carter, J. P. Remeika, and S.-W. Cheong, *Spin Waves throughout the Brillouin Zone of a Double-Exchange Ferromagnet*, Phys. Rev. Lett. **77**, 711 (1996)

[155] F. Aryasetiawan and K. Karlsson, *Green's function formalism for calculating spin-wave spectra*, Phys. Rev. B **60**, 7419 (1999)

[156] G. D. Mahan, *Many-Particle Physics* (Springer US, 2000)

[157] J. Rath and A. J. Freeman, *Generalized magnetic susceptibilities in metals: Application of the analytic tetrahedron linear energy method to Sc*, Phys. Rev. B **11**, 2109 (1975)

[158] E. Runge and E. K. U. Gross, *Density-Functional Theory for Time-Dependent Systems*, Phys. Rev. Lett. **52**, 997 (1984)

[159] W. Kohn, *Density-functional theory for excited states in a quasi-local-density approximation*, Phys. Rev. A **34**, 737 (1986)

[160] K. L. Liu and S. H. Vosko, *A time-dependent spin density functional theory for the dynamical spin susceptibility*, Canadian Journal of Physics **67**, 1015 (1989)

[161] M. Petersilka, U. J. Gossmann, and E. K. U. Gross, *Excitation Energies from Time-Dependent Density-Functional Theory*, Phys. Rev. Lett. **76**, 1212 (1996)

[162] K. Capelle, G. Vignale, and C. A. Ullrich, *Spin gaps and spin-flip energies in density-functional theory*, Phys. Rev. B **81**, 125114 (2010)

[163] F. Wang and T. Ziegler, *Time-dependent density functional theory based on a non-collinear formulation of the exchange-correlation potential*, The Journal of Chemical Physics **121**, 12191 (2004)

[164] M. Niesert, *Ab initio calculation of spin-wave excitation spectra from time-dependent density functional theory*, Ph.D. thesis, RWTH Aachen University (2011)

[165] E. Gross and W. Kohn, in *Density Functional Theory of Many-Fermion Systems*, Advances in Quantum Chemistry, Vol. 21, edited by P.-O. Löwdin (Academic Press, 1990) pp. 255 – 291

[166] C. Friedrich, E. Şaşıoğlu, M. Müller, A. Schindlmayr, and S. Blügel, in *First Principles Approaches to Spectroscopic Properties of Complex Materials*, Topics in Current Chemistry, Vol. 347, edited by C. Di Valentin, S. Botti, and M. Cococcioni (Springer Berlin Heidelberg, 2014) pp. 259–301

[167] M. B. Stearns, in *Magnetic Properties in Metals*, New Series, Vol. III, edited by H. Wijn and Landolt-Börnstein (Springer Berlin, 1986)

[168] D. Bonnenberg, K. Hempel, and H. Wijn, in *Magnetic Properties in Metals*, New Series, Vol. III, edited by H. Wijn and Landolt-Börnstein (Springer Berlin, 1986)

[169] A. M. Turner, A. W. Donoho, and J. L. Erskine, *Experimental bulk electronic properties of ferromagnetic iron*, Phys. Rev. B **29**, 2986 (1984)

[170] E. Kisker, K. Schröder, W. Gudat, and M. Campagna, *Spin-polarized angle-resolved photoemission study of the electronic structure of Fe(100) as a function of temperature*, Phys. Rev. B **31**, 329 (1985)

[171] Y. Sakisaka, T. Rhodin, and D. Mueller, *Angle-resolved photoemission from Fe(110): Determination of* $E(\vec{k})$, Solid State Communications **53**, 793 (1985)

[172] A. Santoni and F. J. Himpsel, *Unoccupied energy bands, exchange splitting, and self-energy of iron*, Phys. Rev. B **43**, 1305 (1991)

[173] D. E. Eastman, F. J. Himpsel, and J. A. Knapp, *Experimental Exchange-Split Energy-Band Dispersions for Fe, Co, and Ni*, Phys. Rev. Lett. **44**, 95 (1980)

[174] F. J. Himpsel and D. E. Eastman, *Experimental energy-band dispersions and magnetic exchange splitting for cobalt*, Phys. Rev. B **21**, 3207 (1980)

[175] R. Raue, H. Hopster, and R. Clauberg, *Spin-polarized photoemission study on the temperature dependence of the exchange splitting of Ni*, Zeitschrift für Physik B Condensed Matter **54**, 121 (1984)

[176] A. Yamasaki and T. Fujiwara, *Electronic Structure of Transition Metals Fe, Ni and Cu in the GW Approximation*, Journal of the Physical Society of Japan **72**, 607 (2003)

[177] J. Janak, *Itinerant ferromagnetism in fcc cobalt*, Solid State Communications **25**, 53 (1978)

[178] P. Marcus and V. Moruzzi, *Equilibrium properties of the cubic phases of cobalt*, Solid State Communications **55**, 971 (1985)

[179] V. L. Moruzzi, P. M. Marcus, K. Schwarz, and P. Mohn, *Ferromagnetic phases of bcc and fcc Fe, Co, and Ni*, Phys. Rev. B **34**, 1784 (1986)

[180] J. W. Lynn, *Temperature dependence of the magnetic excitations in iron*, Phys. Rev. B **11**, 2624 (1975)

[181] R. N. Sinclair and B. N. Brockhouse, *Dispersion Relation for Spin Waves in a fcc Cobalt Alloy*, Phys. Rev. **120**, 1638 (1960)

[182] E. Jensen and E. W. Plummer, *Experimental Band Structure of Na*, Phys. Rev. Lett. **55**, 1912 (1985)

[183] I.-W. Lyo and E. W. Plummer, *Quasiparticle band structure of Na and simple metals*, Phys. Rev. Lett. **60**, 1558 (1988)

[184] E. L. Shirley, *Self-consistent GW and higher-order calculations of electron states in metals*, Phys. Rev. B **54**, 7758 (1996)

[185] J. E. Northrup, M. S. Hybertsen, and S. G. Louie, *Theory of quasiparticle energies in alkali metals*, Phys. Rev. Lett. **59**, 819 (1987)

[186] J. E. Northrup, M. S. Hybertsen, and S. G. Louie, *Quasiparticle excitation spectrum for nearly-free-electron metals*, Phys. Rev. B **39**, 8198 (1989)

[187] J. Lischner, T. Bazhirov, A. H. MacDonald, M. L. Cohen, and S. G. Louie, *Effect of spin fluctuations on quasiparticle excitations: First-principles theory and application to sodium and lithium*, Phys. Rev. B **89**, 081108 (2014)

[188] C. S. Wang and J. Callaway, *Energy bands in ferromagnetic nickel*, Phys. Rev. B **15**, 298 (1977)

[189] H. Höchst, S. Hüfner, and A. Goldmann, *The XPS valence band of nickel metal*, Zeitschrift für Physik B Condensed Matter **26**, 133 (1977)

[190] F. J. Himpsel, J. A. Knapp, and D. E. Eastman, *Experimental energy-band dispersions and exchange splitting for Ni*, Phys. Rev. B **19**, 2919 (1979)

[191] W. Eberhardt and E. W. Plummer, *Angle-resolved photoemission determination of the band structure and multielectron excitations in Ni*, Phys. Rev. B **21**, 3245 (1980)

[192] P. Heimann, F. Himpsel, and D. Eastman, *Experimental energy bands, exchange splittings, and lifetimes for Ni in the vicinity of the x-point*, Solid State Communications **39**, 219 (1981)

[193] R. Kirby, E. Kisker, F. King, and E. Garwin, *The ferromagnetic to paramagnetic phase transition of Fe studied by x-ray photoelectron spectroscopy*, Solid State Communications **56**, 425 (1985)

[194] H. Höchst, A. Goldmann, and S. Hüfner, *X-ray photoelectron emission from iron metal*, Zeitschrift für Physik B Condensed Matter **24**, 245 (1976)

[195] H. Höchst, S. Hüfner, and A. Goldmann, *XPS-valence bands of iron, cobalt, palladium and platinum*, Physics Letters A **57**, 265 (1976)

[196] S. Hüfner, G. Wertheim, N. Smith, and M. Traum, *XPS density of states of copper, silver, and nickel*, Solid State Communications **11**, 323 (1972)

[197] S. Hüfner and G. Wertheim, *Multielectron effects in the XPS spectra of nickel*, Physics Letters A **51**, 299 (1975)

[198] C. Guillot, Y. Ballu, J. Paigné, J. Lecante, K. P. Jain, P. Thiry, R. Pinchaux, Y. Pétroff, and L. M. Falicov, *Resonant Photoemission in Nickel Metal*, Phys. Rev. Lett. **39**, 1632 (1977)

[199] S. Hüfner, S.-H. Yang, B. S. Mun, C. S. Fadley, J. Schäfer, E. Rotenberg, and S. D. Kevan, *Observation of the two-hole satellite in Cr and Fe metal by resonant photoemission at the* $2p$ *absorption energy*, Phys. Rev. B **61**, 12582 (2000)

[200] F. Aryasetiawan, *Self-energy of ferromagnetic nickel in the GW approximation*, Phys. Rev. B **46**, 13051 (1992)

[201] D. Penn, *Effect of Bound Hole Pairs on the d-Band Photoemission Spectrum of Ni*, Phys. Rev. Lett. **42**, 921 (1979)

[202] A. Liebsch, *Ni d-band self-energy beyond the low-density limit*, Phys. Rev. B **23**, 5203 (1981)

[203] M. Springer, F. Aryasetiawan, and K. Karlsson, *First-Principles T-Matrix Theory with Application to the 6 eV Satellite in Ni*, Phys. Rev. Lett. **80**, 2389 (1998)

[204] V. P. Zhukov, E. V. Chulkov, P. M. Echenique, A. Marienfeld, M. Bauer, and M. Aeschlimann, *Excited electron dynamics in bulk ytterbium: Time-resolved two-photon photoemission and* GW + T *ab initio calculations*, Phys. Rev. B **76**, 193107 (2007)

[205] M. Higashiguchi, K. Shimada, K. Nishiura, X. Cui, H. Namatame, and M. Taniguchi, *Energy band and spin-dependent many-body interactions in ferromagnetic Ni(110): A high-resolution angle-resolved photoemission study*, Phys. Rev. B **72**, 214438 (2005)

[206] J. Schäfer, M. Hoinkis, E. Rotenberg, P. Blaha, and R. Claessen, *Fermi surface and electron correlation effects of ferromagnetic iron*, Phys. Rev. B **72**, 155115 (2005)

[207] W. Metzner and D. Vollhardt, *Correlated Lattice Fermions in $d = \infty$ Dimensions*, Phys. Rev. Lett. **62**, 324 (1989)

[208] A. Georges and G. Kotliar, *Hubbard model in infinite dimensions*, Phys. Rev. B **45**, 6479 (1992)

[209] A. Georges, G. Kotliar, W. Krauth, and M. J. Rozenberg, *Dynamical mean-field theory of strongly correlated fermion systems and the limit of infinite dimensions*, Rev. Mod. Phys. **68**, 13 (1996)

[210] K. Byczuk, M. Kollar, K. Held, Y.-F. Yang, I. A. Nekrasov, T. Pruschke, and D. Vollhardt, *Kinks in the dispersion of strongly correlated electrons*, Nature Physics **3**, 168 (2007)

[211] K. Held, R. Peters, and A. Toschi, *Poor Man's Understanding of Kinks Originating from Strong Electronic Correlations*, Phys. Rev. Lett. **110**, 246402 (2013)

[212] V. I. Anisimov, F. Aryasetiawan, and A. I. Lichtenstein, *First-principles calculations of the electronic structure and spectra of strongly correlated systems: the LDA + U method*, Journal of Physics: Condensed Matter **9**, 767 (1997)

[213] A. I. Lichtenstein and M. I. Katsnelson, ***Ab initio*** *calculations of quasiparticle band structure in correlated systems: LDA++ approach*, Phys. Rev. B **57**, 6884 (1998)

[214] G. Kotliar, S. Y. Savrasov, K. Haule, V. S. Oudovenko, O. Parcollet, and C. A. Marianetti, *Electronic structure calculations with dynamical mean-field theory*, Rev. Mod. Phys. **78**, 865 (2006)

[215] K. Held, *Electronic structure calculations using dynamical mean field theory*, Advances in Physics **56**, 829 (2007)

[216] I. A. Nekrasov, K. Held, G. Keller, D. E. Kondakov, T. Pruschke, M. Kollar, O. K. Andersen, V. I. Anisimov, and D. Vollhardt, *Momentum-resolved spectral functions of* $SrVO_3$ *calculated by* LDA + DMFT, Phys. Rev. B **73**, 155112 (2006)

[217] T. Yoshida, K. Tanaka, H. Yagi, A. Ino, H. Eisaki, A. Fujimori, and Z.-X. Shen, *Direct Observation of the Mass Renormalization in* $SrVO_3$ *by Angle Resolved Photoemission Spectroscopy*, Phys. Rev. Lett. **95**, 146404 (2005)

[218] O. Gunnarsson, O. K. Andersen, O. Jepsen, and J. Zaanen, *Density-functional calculation of the parameters in the Anderson model: Application to Mn in CdTe*, Phys. Rev. B **39**, 1708 (1989)

[219] T. Kotani, *Ab initio random-phase-approximation calculation of the frequency-dependent effective interaction between 3d electrons: Ni, Fe, and MnO*, Journal of Physics: Condensed Matter **12**, 2413 (2000)

[220] E. Şaşıoğlu, C. Friedrich, and S. Blügel, *Effective Coulomb interaction in transition metals from constrained random-phase approximation*, Phys. Rev. B **83**, 121101 (2011)

[221] S. Biermann, F. Aryasetiawan, and A. Georges, *First-Principles Approach to the Electronic Structure of Strongly Correlated Systems: Combining the GW Approximation and Dynamical Mean-Field Theory*, Phys. Rev. Lett. **90**, 086402 (2003)

[222] C.-O. Almbladh, U. v. Barth, and R. v. Leeuwen, *Variational total energies from* Φ- *and* Ψ- *derivable theories*, International Journal of Modern Physics B **13**, 535 (1999)

[223] J. M. Tomczak, M. Casula, T. Miyake, F. Aryasetiawan, and S. Biermann, *Combined GW and dynamical mean-field theory: Dynamical screening effects in transition metal oxides*, Europhysics Letters **100**, 67001 (2012)

[224] C. Taranto, M. Kaltak, N. Parragh, G. Sangiovanni, G. Kresse, A. Toschi, and K. Held, *Comparing quasiparticle GW+DMFT and LDA+DMFT for the test bed material $SrVO_3$*, Phys. Rev. B **88**, 165119 (2013)

[225] R. Sakuma, P. Werner, and F. Aryasetiawan, *Electronic structure of $SrVO_3$ within GW+DMFT*, Phys. Rev. B **88**, 235110 (2013)

[226] J. M. Tomczak, M. Casula, T. Miyake, and S. Biermann, *Asymmetry in band widening and quasiparticle lifetimes in* $SrVO_3$*: Competition between screened exchange and local correlations from combined GW and dynamical mean-field theory GW + DMFT*, Phys. Rev. B **90**, 165138 (2014)

[227] B. I. Lundqvist, *Single-particle spectrum of the degenerate electron gas. I. The structure of the spectral weight function*, Physik der kondensierten Materie **6**, 193 (1967)

[228] B. I. Lundqvist, *Single-particle spectrum of the degenerate electron gas. II. Numerical results for electrons coupled to plasmons*, Physik der kondensierten Materie **6**, 206 (1967)

[229] L. Hedin, B. Lundqvist, and S. Lundqvist, *New structure in the single-particle spectrum of an electron gas*, Solid State Communications **5**, 237 (1967)

[230] B. I. Lundqvist, *Single-particle spectrum of the degenerate electron gas. III. Numerical results in the random phase approximation*, Physik der kondensierten Materie **7**, 117 (1968)

[231] L. Hedin, *Effects of Recoil on Shake-Up Spectra in Metals*, Physica Scripta **21**, 477 (1980)

[232] F. Aryasetiawan, L. Hedin, and K. Karlsson, *Multiple Plasmon Satellites in Na and Al Spectral Functions from Ab Initio Cumulant Expansion*, Phys. Rev. Lett. **77**, 2268 (1996)

[233] M. Guzzo, G. Lani, F. Sottile, P. Romaniello, M. Gatti, J. J. Kas, J. J. Rehr, M. G. Silly, F. Sirotti, and L. Reining, *Valence Electron Photoemission Spectrum of Semi-*

conductors: Ab Initio Description of Multiple Satellites, Phys. Rev. Lett. **107**, 166401 (2011)

[234] P. Nozières, J. Gavoret, and B. Roulet, *Singularities in the X-Ray Absorption and Emission of Metals. II. Self-Consistent Treatment of Divergences*, Phys. Rev. **178**, 1084 (1969)

[235] P. Nozières and C. T. de Dominicis, *Singularities in the X-Ray Absorption and Emission of Metals. III. One-Body Theory Exact Solution*, Phys. Rev. **178**, 1097 (1969)

[236] D. C. Langreth, *Singularities in the X-Ray Spectra of Metals*, Phys. Rev. B **1**, 471 (1970)

[237] B. Bergersen, F. W. Kus, and C. Blomberg, *Single Particle Green's Function in the Electron-Plasmon Approximation*, Canadian Journal of Physics **51**, 102 (1973)

[238] P. Minnhagen, *Aspects on diagrammatic expansion for models related to a homogeneous electron gas*, Journal of Physics C: Solid State Physics **8**, 1535 (1975)

[239] L. Hedin, *On correlation effects in electron spectroscopies and the GW approximation*, Journal of Physics: Condensed Matter **11**, R489 (1999)

[240] R. M. Martin, L. Reining, and D. Ceperley, *Interacting Electrons: Theory and Computational Approaches* (Camebridge University Press, 2016)

[241] F. Caruso, H. Lambert, and F. Giustino, *Band Structures of Plasmonic Polarons*, Phys. Rev. Lett. **114**, 146404 (2015)

[242] F. Caruso and F. Giustino, *Spectral fingerprints of electron-plasmon coupling*, Phys. Rev. B **92**, 045123 (2015)

[243] P. A. Bobbert and W. van Haeringen, *Lowest-order vertex-correction contribution to the direct gap of silicon*, Phys. Rev. B **49**, 10326 (1994)

[244] R. T. M. Ummels, P. A. Bobbert, and W. van Haeringen, *First-order corrections to random-phase approximation* GW *calculations in silicon and diamond*, Phys. Rev. B **57**, 11962 (1998)

[245] X. Ren, N. Marom, F. Caruso, M. Scheffler, and P. Rinke, *Beyond the GW approximation: A second-order screened exchange correction*, Phys. Rev. B **92**, 081104 (2015)

[246] G. Strinati, *Application of the Green's functions method to the study of the optical properties of semiconductors*, La Rivista del Nuovo Cimento **11**, 1 (1988)

[247] G. Onida, L. Reining, R. W. Godby, R. Del Sole, and W. Andreoni, *Ab Initio Calculations of the Quasiparticle and Absorption Spectra of Clusters: The Sodium Tetramer*, Phys. Rev. Lett. **75**, 818 (1995)

[248] S. Albrecht, G. Onida, and L. Reining, *Ab initio calculation of the quasiparticle spectrum and excitonic effects in* Li_2O, Phys. Rev. B **55**, 10278 (1997)

[249] S. Albrecht, L. Reining, R. Del Sole, and G. Onida, *Ab Initio Calculation of Excitonic Effects in the Optical Spectra of Semiconductors*, Phys. Rev. Lett. **80**, 4510 (1998)

[250] L. X. Benedict, E. L. Shirley, and R. B. Bohn, *Optical Absorption of Insulators and the Electron-Hole Interaction: An Ab Initio Calculation*, Phys. Rev. Lett. **80**, 4514 (1998)

[251] M. Rohlfing and S. G. Louie, *Electron-Hole Excitations in Semiconductors and Insulators*, Phys. Rev. Lett. **81**, 2312 (1998)

[252] G. Onida, L. Reining, and A. Rubio, *Electronic excitations: density-functional versus many-body Green's-function approaches*, Rev. Mod. Phys. **74**, 601 (2002)

[253] E. Şaşıoğlu, C. Friedrich, and S. Blügel, *Strong magnon softening in tetragonal FeCo compounds*, Phys. Rev. B **87**, 020410 (2013)

[254] P. Romaniello, F. Bechstedt, and L. Reining, *Beyond the GW approximation: Combining correlation channels*, Phys. Rev. B **85**, 155131 (2012)

[255] D. Bohm and D. Pines, *A Collective Description of Electron Interactions. I. Magnetic Interactions*, Phys. Rev. **82**, 625 (1951)

[256] D. Pines and D. Bohm, *A Collective Description of Electron Interactions: II. Collective* vs *Individual Particle Aspects of the Interactions*, Phys. Rev. **85**, 338 (1952)

[257] D. Bohm and D. Pines, *A Collective Description of Electron Interactions: III. Coulomb Interactions in a Degenerate Electron Gas*, Phys. Rev. **92**, 609 (1953)

[258] C. Faber, *Electronic, excitonic and polaronic properties of organic systems within the many-body GW and Bethe-Salpeter formalism: towards organic photovoltaics*, Ph.D. thesis, L'université de Grenoble (2014)

[259] A. B. Migdal, *Interaction between electrons and lattice vibrations in a normal metal*, Soviet Physics JETP **7**, 996 (1958)

[260] Katsnelson, M. I. and Lichtenstein, A. I., *Electronic structure and magnetic properties of correlated metals*, Eur. Phys. J. B **30**, 9 (2002)

[261] L. V. Pourovskii, M. I. Katsnelson, and A. I. Lichtenstein, *Correlation effects in electronic structure of actinide monochalcogenides*, Phys. Rev. B **72**, 115106 (2005)

[262] N. Bickers and D. Scalapino, *Conserving approximations for strongly fluctuating electron systems. I. Formalism and calculational approach*, Annals of Physics **193**, 206 (1989)

[263] N. E. Bickers, D. J. Scalapino, and S. R. White, *Conserving Approximations for Strongly Correlated Electron Systems: Bethe-Salpeter Equation and Dynamics for the Two-Dimensional Hubbard Model*, Phys. Rev. Lett. **62**, 961 (1989)

[264] N. E. Bickers and S. R. White, *Conserving approximations for strongly fluctuating electron systems. II. Numerical results and parquet extension*, Phys. Rev. B **43**, 8044 (1991)

[265] R. W. Godby, M. Schlüter, and L. J. Sham, *Self-energy operators and exchange-correlation potentials in semiconductors*, Phys. Rev. B **37**, 10159 (1988)

[266] H. N. Rojas, R. W. Godby, and R. J. Needs, *Space-Time Method for Ab Initio Calculations of Self-Energies and Dielectric Response Functions of Solids*, Phys. Rev. Lett. **74**, 1827 (1995)

[267] M. M. Rieger, L. Steinbeck, I. White, H. Rojas, and R. Godby, *The GW space-time method for the self-energy of large systems*, Computer Physics Communications **117**, 211 (1999)

[268] L. D. Landau, *The Theory of a Fermi Liquid*, Soviet Physics JETP **3**, 920 (1956)

[269] L. D. Landau, *Oscillations in a Fermi-liquid*, Soviet Physics JETP **5**, 101 (1957)

[270] A. Damascelli, *Probing the Electronic Structure of Complex Systems by ARPES*, Physica Scripta **2004**, 61 (2004)

[271] G. Borstel and G. Thörner, *Inverse photoemission from solids: Theoretical aspects and applications*, Surface Science Reports **8**, 1 (1988)

[272] P. D. Johnson and S. L. Hulbert, *Inverse photoemission*, Review of Scientific Instruments **61**, 2277 (1990)

[273] M. Donath, *Polarization effects in inversephotoemission spectra*, Progress in Surface Science **35**, 47 (1990)

[274] P. Aebi, T. J. Kreutz, J. Osterwalder, R. Fasel, P. Schwaller, and L. Schlapbach, *k -Space Mapping of Majority and Minority Bands on the Fermi Surface of Nickel below and above the Curie Temperature*, Phys. Rev. Lett. **76**, 1150 (1996)

[275] F. Manghi, V. Bellini, J. Osterwalder, T. J. Kreutz, P. Aebi, and C. Arcangeli, *Correlation effects in the low-energy region of nickel photoemission spectra*, Phys. Rev. B **59**, R10409 (1999)

[276] J. Bünemann, F. Gebhard, T. Ohm, R. Umstätter, S. Weiser, W. Weber, R. Claessen, D. Ehm, A. Harasawa, A. Kakizaki, A. Kimura, G. Nicolay, S. Shin, and V. N. Strocov, *Atomic correlations in itinerant ferromagnets: Quasi-particle bands of nickel*, Europhysics Letters **61**, 667 (2003)

[277] F. Manghi and V. Boni, *Quasiparticle band structure*, Journal of Electron Spectroscopy and Related Phenomena **200**, 181 (2015)

[278] G. G. Lonzarich, *Band structure and magnetic fluctuations in ferromagnetic or nearly ferromagnetic Metals*, Journal of Magnetism and Magnetic Materials **45**, 43 (1984)

[279] G. G. Lonzarich and L. Taillefer, *Effect of spin fluctuations on the magnetic equation of state of ferromagnetic or nearly ferromagnetic metals*, Journal of Physics C: Solid State Physics **18**, 4339 (1985)

[280] G. G. Lonzarich, *Quasiparticles and magnetic fluctuations in metals with large magnetic susceptibilities*, Journal of Magnetism and Magnetic Materials **70**, 445 (1987)

[281] S. Nakajima and M. Watabe, *On the Electron-Phonon Interaction in Normal Metals. I*, Progress of Theoretical Physics **29**, 341 (1963)

[282] S. Nakajima and M. Watabe, *On the Electron-Phonon Interaction in Normal Metals. II*, Progress of Theoretical Physics **30**, 772 (1963)

[283] L. C. Davis and S. H. Liu, *Electron-Magnon Interaction in Ferromagnetic Transition Metals*, Phys. Rev. **163**, 503 (1967)

[284] G. Bergmann, *The electron-magnon mass enhancement in ferromagnetic metals*, Journal of Magnetism and Magnetic Materials **4**, 211 (1977)

[285] V. Y. Irkhin and M. I. Katsnelson, *Spin waves in narrow band ferromagnet*, Journal of Physics C: Solid State Physics **18**, 4173 (1985)

[286] V. Y. Irkhin and M. I. Katsnelson, *Ground state and electron-magnon interaction in an itinerant ferromagnet: half-metallic ferromagnets*, Journal of Physics: Condensed Matter **2**, 7151 (1990)

[287] L. Chioncel, M. I. Katsnelson, R. A. de Groot, and A. I. Lichtenstein, *Nonquasiparticle states in the half-metallic ferromagnet NiMnSb*, Phys. Rev. B **68**, 144425 (2003)

[288] V. Y. Irkhin and M. I. Katsnelson, *Non-quasiparticle states in the core level spectra of ferromagnetic semiconductors and half-metallic ferromagnets*, Eur. Phys. J. B **43**, 479 (2005)

[289] J. C. Phillips and L. F. Mattheiss, *Many-Electron Effects and Exchange Splittings in Nickel*, Phys. Rev. Lett. **11**, 556 (1963)

[290] U. Brandt, *Modified T-matrix approximation in itinerant ferromagnets*, Zeitschrift für Physik **244**, 217 (1971)

[291] R. N. Silver, D. S. Sivia, and J. E. Gubernatis, *Maximum-entropy method for analytic continuation of quantum Monte Carlo data*, Phys. Rev. B **41**, 2380 (1990)

[292] W. von der Linden and D. M. Edwards, *Ferromagnetism in the Hubbard model*, Journal of Physics: Condensed Matter **3**, 4917 (1991)

[293] W. von der Linden, M. Donath, and V. Dose, *Unbiased access to exchange splitting of magnetic bands using the maximum entropy method*, Phys. Rev. Lett. **71**, 899 (1993)

[294] W. von der Linden, *Maximum-entropy data analysis*, Applied Physics A **60**, 155 (1995)

[295] W. von der Linden, R. Preuss, and W. Hanke, *Consistent application of maximum entropy to quantum Monte Carlo data*, Journal of Physics: Condensed Matter **8**, 3881 (1996)

[296] J. Schött, I. L. M. Locht, E. Lundin, O. Grånäs, O. Eriksson, and I. Di Marco, *Analytic continuation by averaging Padé approximants*, Phys. Rev. B **93**, 075104 (2016)

[297] F. Bruneval and M. A. L. Marques, *Benchmarking the Starting Points of the GW Approximation for Molecules*, Journal of Chemical Theory and Computation **9**, 324 (2013)

[298] F. Bruneval, N. Vast, and L. Reining, *Effect of self-consistency on quasiparticles in solids*, Phys. Rev. B **74**, 045102 (2006)

[299] P. Rinke, A. Qteish, J. Neugebauer, C. Freysoldt, and M. Scheffler, *Combining GW calculations with exact-exchange density-functional theory: an analysis of valence-band photoemission for compound semiconductors*, New Journal of Physics **7**, 126 (2005)

[300] F. Fuchs, J. Furthmüller, F. Bechstedt, M. Shishkin, and G. Kresse, *Quasiparticle band structure based on a generalized Kohn-Sham scheme*, Phys. Rev. B **76**, 115109 (2007)

[301] N. Marom, F. Caruso, X. Ren, O. T. Hofmann, T. Körzdörfer, J. R. Chelikowsky, A. Rubio, M. Scheffler, and P. Rinke, *Benchmark of GW methods for azabenzenes*, Phys. Rev. B **86**, 245127 (2012)

[302] I. Aguilera, C. Friedrich, G. Bihlmayer, and S. Blügel, *GW study of topological insulators Bi_2Se_3, Bi_2Te_3, and Sb_2Te_3: Beyond the perturbative one-shot approach*, Phys. Rev. B **88**, 045206 (2013)

[303] I. Aguilera, C. Friedrich, and S. Blügel, *Electronic phase transitions of bismuth under strain from relativistic self-consistent GW calculations*, Phys. Rev. B **91**, 125129 (2015)

[304] J. R. Anderson and A. V. Gold, *de Haas-van Alphen Effect and Internal Field in Iron*, Phys. Rev. Lett. **10**, 227 (1963)

[305] P. Heimann, E. Marschall, H. Neddermeyer, M. Pessa, and H. F. Roloff, *Photoemission and electronic structure of cobalt*, Phys. Rev. B **16**, 2575 (1977)

[306] M. Mulazzi, J. Miyawaki, A. Chainani, Y. Takata, M. Taguchi, M. Oura, Y. Senba, H. Ohashi, and S. Shin, *Fermi surface of Co(0001) and initial-state*

linewidths determined by soft x-ray angle-resolved photoemission spectroscopy, Phys. Rev. B **80**, 241106 (2009)

[307] X. Gao, A. N. Koveshnikov, R. H. Madjoe, R. L. Stockbauer, and R. L. Kurtz, *Dominance of the Final State in Photoemission Mapping of the Fermi Surface of* $\mathrm{Co/Cu}(001)$, Phys. Rev. Lett. **90**, 037603 (2003)

[308] M. Cinchetti, M. Sánchez Albaneda, D. Hoffmann, T. Roth, J.-P. Wüstenberg, M. Krauß, O. Andreyev, H. C. Schneider, M. Bauer, and M. Aeschlimann, *Spin-Flip Processes and Ultrafast Magnetization Dynamics in Co: Unifying the Microscopic and Macroscopic View of Femtosecond Magnetism*, Phys. Rev. Lett. **97**, 177201 (2006)

[309] M. Bauer, A. Marienfeld, and M. Aeschlimann, *Hot electron lifetimes in metals probed by time-resolved two-photon photoemission*, Progress in Surface Science **90**, 319 (2015)

[310] M. Aeschlimann, M. Bauer, S. Pawlik, W. Weber, R. Burgermeister, D. Oberli, and H. C. Siegmann, *Ultrafast Spin-Dependent Electron Dynamics in fcc Co*, Phys. Rev. Lett. **79**, 5158 (1997)

[311] A. S. Joseph and A. C. Thorsen, *de Haas-van Alphen Effect and Fermi Surface in Nickel*, Phys. Rev. Lett. **11**, 554 (1963)

[312] D. C. Tsui and R. W. Stark, *de Haas-van Alphen Effect in Ferromagnetic Nickel*, Phys. Rev. Lett. **17**, 871 (1966)

[313] D. C. Tsui, *de Haas-van Alphen Effect and Electronic Band Structure of Nickel*, Phys. Rev. **164**, 669 (1967)

[314] H. Mårtensson and P. O. Nilsson, *Investigation of the electronic structure of Ni by angle-resolved uv photoelectron spectroscopy*, Phys. Rev. B **30**, 3047 (1984)

[315] J. Bünemann, W. Weber, and F. Gebhard, *Multiband Gutzwiller wave functions for general on-site interactions*, Phys. Rev. B **57**, 6896 (1998)

[316] J. Bünemann, F. Gebhard, T. Ohm, S. Weiser, and W. Weber, *Spin-Orbit Coupling in Ferromagnetic Nickel*, Phys. Rev. Lett. **101**, 236404 (2008)

[317] B. Andres, P. Weiss, M. Wietstruk, and M. Weinelt, *Spin-dependent lifetime and exchange splitting of surface states on* $Ni(111)$, Journal of Physics: Condensed Matter **27**, 015503 (2015)

[318] S. Kaltenborn and H. C. Schneider, *Spin-orbit coupling effects on spin-dependent inelastic electronic lifetimes in ferromagnets*, Phys. Rev. B **90**, 201104 (2014)

[319] *The Padé Approximant in Theoretical Physics*, edited by G. A. Baker and J. L. Gammel, Mathematics in Science and Engineering, Vol. 71 (Elsevier, 1970)

[320] M. Abramowitz, *Handbook of Mathematical Functions, With Formulas, Graphs, and Mathematical Tables,* (Dover Publications, Incorporated, 1974)

List of Publications

- M. C. T. D. Müller, C. Friedrich, and S. Blügel, *Acoustic magnons in the long-wavelength limit: Investigating the Goldstone violation in many-body perturbation theory*, published in Phys. Rev. B **94**, 064433 (2016)
- C. Friedrich, E. Şaşıoğlu, M. Müller, A. Schindlmayr, and S. Blügel, *Spin Excitations in Solids from Many-Body Perturbation Theory*, published in *First Principles Approaches to Spectroscopic Properties of Complex Materials, Topics in Current Chemistry*, Vol. 347, edited by C. Di Valentin, S. Botti, and M. Cococcioni (Springer Berlin Heidelberg, 2014) pp. 259-301
- C. Friedrich, M. C. Müller, and S. Blügel, *Band convergence and linearization error correction of all-electron GW calculations: The extreme case of zinc oxide*, published in Phys. Rev. B **83**, 081101 (2011); Erratum Phys. Rev. B **84**, 039906 (2011)

Acknowledgment

A Ph.D. project is a long-term project and it cannot be carried out without the help and support of various people. To emphasize this, I have used the personal pronoun *we* in this work and it is my great pleasure to explicitly express my acknowledgment in the following.

First and foremost, I would like to thank Prof. Dr. Stefan Blügel for giving me the opportunity to write my Ph.D. thesis in his group at the Peter Grünberg Institut 1 in the Forschungszentrum Jülich GmbH. The Peter Grünberg Institut, which attracts many great scientists, together with Stefan's enthusiam and drive for science is an inspiring environment for doing a Ph.D.

I am also very grateful to Prof. Dr. Carsten Honerkamp for being the second referee of my thesis.

This thesis would have been impossible without the commitment of Dr. Christoph Friedrich, and I am very much obliged to him. I would like to thank him for countless discussions that guided me through the time of my Ph.D., for the explanations of the SPEX code that have put me in the position to carry out this work, and for the careful proof reading of this manuscript, which has improved it immensely.

In addition, I would like to thank Dr. Markus Betzinger, who has contributed significantly to the success of this work through numerous discussions and ongoing support. Especially, I would like to thank PD Dr. Hans Lustfeld for many fruitful discussions. His way to ask scientific questions has made it possible for me to rethink given problems in a totally different way. This was a great help during my Ph.D. Also, I thank Dr. Ersoy Şaşıoğlu as an expert on performing calculations with the SPEX code. I am obliged to Dr. Manuel dos Santos Dias, Dr. Julen Azpiroz, Dr. Benedikt Schweflinghaus, Dr. Giovanna Lani, and Dr. Gregor Michalicek for discussions on topics related to my Ph.D. thesis.

A special thanks goes to my office colleague and friend Dr. Rico Friedrich. He

was a great support during the time of my Ph.D. and he contributed to the success of this thesis by innumerable (scientific) discussions, encouragements, and a productive working atmosphere. Additionally, it was a great time to plan the Ph.D. seminar together with him. Also, I would like to acknowledge Dr. Martin Callsen with whom I have spent already the time of my master thesis and part of my Ph.D. in the same office for discussions about whatever was written to the white board. Finally, I would like to thank all the members of our institute for creating such a pleasant and enjoyable atmosphere. Among them I wish to thank Ute Winkler in particular. Without her it would be impossible to finish a Ph.D. while having to deal with all the administrative issues.

Jülich, November 2016 Mathias C.T.D. Müller

Band / Volume 132
Robot-Assisted Phenotyping of Genome-Reduced *Corynebacterium glutamicum* Strain Libraries to Draft a Chassis Organism
S. Unthan (2016), 122 pp
ISBN: 978-3-95806-169-9

Band / Volume 133
Characterization of amino acid ammonia lyases & aminomutases for the production of chiral α- and β-amino acids
A. Dreßen (2016), ix, 112 pp
ISBN: 978-3-95806-176-7

Band/Volume 134
7th Georgian-German School and Workshop in Basic Science
Kacharava, A. (Ed.) erscheint nur als CD (2016)
ISBN 978-3-95806-179-8

Band / Volume 135
Crystal growth and scattering studies on two ferrites
S. Adiga (2016), iv, 150 pp
ISBN: 978-3-95806-183-5

Band / Volume 136
Manipulating the Structural and Electronic Properties of Epitaxial $NaNbO_3$ Films via Strain and Stoichiometry
B. Cai (2016), VI, 114 pp
ISBN: 978-3-95806-185-9

Band / Volume 137
Surface Potential of Metallic Surfaces and Self-Assembling Organic Monolayers in Various Electrolytes
J. Wang (2016), ii, 58 pp
ISBN: 978-3-95806-188-0

Band / Volume 138
Ab initio investigation of hybrid molecular-metallic interfaces as a tool to design surface magnetic properties for molecular spintronics
R. Friedrich (2016), 277 pp
ISBN: 978-3-95806-194-1

Band / Volume 139
Topological Matter – Topological Insulators, Skyrmions and Majoranas
Lecture Notes of the 48th IFF Spring School 2017
27 March – 07 April 2017, Jülich, Germany
ed. by S. Blügel, Y. Mokrousov, T. Schäpers, Y. Ando (2017), ca 1000 pp
ISBN: 978-3-95806-202-3

Band / Volume 140
In situ studies of the growth and oxidation of complex metal oxides by pulsed laser deposition
C. Xu (2017), iv, 159 pp
ISBN: 978-3-95806-204-7

Band / Volume 141
Intrinsic and extrinsic spin-orbit torques from first principles
G. Géranton (2017), 122 pp
ISBN: 978-3-95806-213-9

Band / Volume 142
Magnetic Proximity Effects in Nanoparticle Composite Systems and Macrocrystals
G. Wilbs (2017), III, 230 pp
ISBN: 978-3-95806-233-7

Band / Volume 143
Etablierung eines Systems aus Cysteinmutanten der Phosphoglycerat-Kinase für Entfaltungsstudien mit Einzelmolekül-FRET
A. Schöne (2017), 137 pp
ISBN: 978-3-95806-237-5

Band / Volume 144
Structural and electronic characterization of hetero-organic NTCDA-CuPc adsorbate systems on Ag(111)
S. Schröder (2017), vi, 154 pp
ISBN: 978-3-95806-239-9

Band / Volume 145
Tailoring Molecular Magnetism
T. Esat (2017), viii, 163 pp
ISBN: 978-3-95806-240-5

Band / Volume 146
Spin-wave excitations and electron-magnon scattering in elementary ferromagnets from *ab initio* many-body perturbation theory
M. C. T. D. Müller (2017), vi, 174 pp
ISBN: 978-3-95806-242-9

Schlüsseltechnologien /
Key Technologies
Band / Volume 146
ISBN 978-3-95806-242-9